On the Development of a Multi-scale Modelling Framework to Study Plasticity and Damage through the Coupling of Finite Element Crystal Plasticity and Discrete Dislocation Plasticity

by

Yilun XU

A Thesis submitted to Imperial College London in fulfilment of the degree of Doctor of Philosophy and the diploma of Imperial College London

October 2015

Tribology Group

Applied Mechanics and Mechanics of Materials Section

Department of Mechanical Engineering

The Imperial College of Science, Technology and Medicine

London

© 2015 by Yilun XU. All rights reserved.

Printed by -, United Kingdom

ISSN 0000-0000
ISBN 000-00-0000000-0

To my parents

For their endless love, support and encouragement.

“Look deep into nature, and then you will understand everything better.”

— Albert Einstein

“That’s Life. Life is Tough and thus Beautiful.”
— Daniele Dini

Declaration of Originality

Except where otherwise stated, this thesis is the result of my own research. This research was conducted in the Design Engineering Group at Imperial College between November 2011 and July 2015. I certify that this thesis has not been submitted in whole or in parts as consideration for any other degree or qualification at this or any other institute of learning.

Yilun XU

29th October 2015

Copyright Declaration

The copyright of this thesis rests with the author and is made available under a Creative Commons Attribution Non-Commercial No Derivatives license. Researchers are free to copy, distribute or transmit the thesis on the condition that they attribute it, that they do not use it for commercial purposes and that they do not alter, transform or build upon it. For any reuse or redistribution, researchers must make clear to others the license terms of this work.

Yilun XU

29th October 2015

Abstract

The microstructure of polycrystalline materials crucially determines their mechanical performance in engineering applications. A multi-scale modelling approach is capable of representing the microstructure and thus capturing the material performance for various resolution requirement at different scales. Besides, the application of multi-scale modelling effectively reduces expense and improves efficiency of computations without loss of accuracy at sensitive zones.

A method of concurrent coupling of planar discrete dislocation plasticity (DDP) and a crystal plasticity finite element (CPFE) method was devised for simulating plastic deformation in large polycrystals with discrete dislocation resolution in a single grain or cluster of grains for computational efficiency; computation time using the coupling method can be reduced by an order of magnitude compared to DDP. The method is based on an iterative scheme initiated by a sub-model calculation, which ensures displacement and traction compatibility at all nodes at the interface between the DDP and CPFE domains.

The proposed coupling approach is demonstrated using two plane strain problems: (i) uniaxial tension of a bi-crystal film and (ii) indentation of a thin film on a substrate. The latter demonstrated that the rigid substrate assumption used in earlier discrete dislocation plasticity studies is inadequate for indentation depths that are large compared to the film thickness, i.e. the effect of the polycrystalline plastic substrate modelled using CPFE becomes important. The coupling method can be used to study a wider range of indentation depths than previously possible using DDP alone, without sacrificing the indentation size effect regime captured by DDP. A comprehensive indentation pressure formula has been developed by applying the proposed multi-scale modelling approach on a polycrystalline coating system.

Planar nano-sliding and fretting calculations have been performed on thin films modelling by CPFE and DDP at different scales. Results of CPFE simulations provide an understanding of the role of microstructure on the plasticity and crack initiation during a contact problem. Beside, a new DDP computational framework has been proposed for a nano-fretting problem which is able to capture the contact size effect, simulate the dislocation evolution and predict the surface profile variation of thin films. Calculations of DDP simulations potentially provide CPFE simulations with fatigue parameters that is of more physical significance.

The method is general and can be applied to any problem where finer resolution of dislocation mediated plasticity is required to study the mechanical response of polycrystalline materials, e.g. to capture size effects locally within a larger elastic/plastic boundary value problem. Also, the model described here will provide further opportunities for directly coupled, three-tiered multi-scale models compromising an overall macroscopic continua having embedded crystal plasticity and discrete dislocation plasticity models, respectively, as the length scale decreases in the area of interest. Finally, the methodology of the proposed coupling method will shed light on archiving a general compatibility of sub-regions and thus benefit other researchers who are working on coupling methods among other scales.

Acknowledgements

I would like to thank my principal supervisor Dr Daniele Dini for his guidance, his inspiration, and the great deal of time he has dedicated to supervise my research. I am afraid I could have been puzzled without his guidance, patience and encouragement, not only in academic but also ordinary life.

I also would like to express my gratitude to my co-supervisor Dr Daniel S Balint for the many advice and opportunities he offered me. His critical thinking, nicety deduction and enthusiasm in science inspire me to explore the engineering field with a more mathematical and physical understanding.

I would like to thank my parents, who mean the world to me, for their unconditioned support and encouragement. I cannot imagine my life without their love and blessings. Thank you mom and dad for trusting in me and giving me liberty to choose what I desired. I have been considering myself as the luckiest son in the world to have such great parents, standing behind me with their love and support.

I am grateful to my colleagues and friends at Tribology Group and Mechanics of Materials Section at Imperial College. They have made every day at the college unforgettable. In particular, I would like to express my gratitude to Prof. Jianguo LIN, who is my Early Stage Examiner, proposes critical questions and provides me with much significant advice during my PhD study.

I am also grateful to Prof. Chengen WANG, Dr. Rongxia QU and Dr. Dongliang CUI who have been educating and leading me to academia for me when I was studying for my Master and Bachelor degree in China.

I would like to acknowledge the financial and project support of Mechanical Engineering Department and Imperial College Trust.

Table of Contents

ABSTRACT **7**

ACKNOWLEDGEMENTS **9**

TABLE OF CONTENTS **10**

LIST OF FIGURES **18**

LIST OF TABLES **33**

NOMENCLATURE **35**

ABBREVIATION **38**

1 INTRODUCTION **1**

1.1 MOTIVATION **1**

1.1.1 Multi-scale modelling of materials *1*

1.1.2 Size Effect in Uniaxial Tension Tests *2*

1.1.3 Indentation Size Effect and Hardness Evolution *3*

1.1.4 Size Effects in Sliding and Crack Initiation in Contact Fatigue *3*

1.2 OBJECTIVES **3**

1.2.1 A General Multi-scale Modelling Framework *4*

1.2.2 Multi-scale Coupling Framework Applied to Uniaxial Tension *4*

1.2.3 Multi-scale Coupling Framework Applied to Indentation Problems and Coated Systems *4*

1.2.4 Apply Multi-scale Coupling Framework in Sliding and Fretting *5*

1.3 APPROACHES AND TOOLS **5**

1.3.1 Commercial Software Package and Subroutines *5*

1.3.2 Simulation Environment 6

1.4 THESIS OUTLINE 6

2 LITERATURE REVIEW: MECHANICAL BEHAVIOUR AND MODELLING OF MATERIALS 8

2.1 INTRODUCTION 8

2.2 MODELLING MATERIAL PLASTIC DEFORMATIONS USING FRAMEWORKS AT DIFFERENT SCALES 9

2.2.1 Macroscale plasticity 9

2.2.2 Strain gradient plasticity 10

2.2.3 Crystal plasticity 11

2.2.4 Discrete dislocation plasticity 15

2.2.5 Multi-scale plasticity and its modelling 18

2.3 MECHANICAL BEHAVIOUR OF MATERIALS UNDER DIFFERENT WORKING CONDITIONS 20

2.3.1 Uni-axial Tension 20

2.3.2 Indentation 21

2.3.3 Sliding 22

2.3.4 Fretting 24

2.4 SUMMARY 27

3 A GENERAL APPROACH TO STUDY PLASTICITY BY COUPLING CRYSTAL PLASTICITY FINITE ELEMENT AND DISCRETE DISLOCATION PLASTICITY 29

3.1 INTRODUCTION 29

3.2 CRYSTAL PLASTICITY FINITE ELEMENT 30

3.2.1 Mechanisms 30

3.2.2 CPFE formulation 31

3.2.3 Implementation 33

3.2.4 Adaption and improvements of the CPFE routines 36

3.3 DISCRETE DISLOCATION PLASTICITY 36

3.3.1 Mechanisms 36

3.3.2 Formulations 37

3.3.3 Implementation 38

3.3.4 Adaption and improvements of the DDP code 41

3.4 GENERAL COUPLING PHILOSOPHY 42

3.4.1 Problem definition 42

3.4.2 Material calibration 43

3.4.3 Mesh configuration 45

3.4.4 External boundary conditions 45

3.4.5 Sub-regions modelling 45

3.4.6 Interface coupling 46

3.4.7 Boundary conditions passing 46

3.4.8 Iterative scheme 47

3.4.9 Convergence issue 47

3.4.10 Implementation 48

3.5 SUMMARY 49

4 APPLICATION OF THE COUPLED MODELLING APPROACH: UNIAXIAL TENSION PROBLEM 50

4.1 INTRODUCTION 50

4.2 TENSION PROBLEM SOLVING WITH CRYSTAL PLASTICITY FINITE ELEMENT 50

4.2.1 Methodology 50

4.2.2 Problem definition 52

4.2.3 Results and discussion 53

4.2.4 Summary 59

4.3 TENSION PROBLEM SOLVING WITH DISCRETE DISLOCATION PLASTICITY 59

4.3.1 Methodology 59

4.3.2 Problem definition 61

4.3.3 Results 62

4.3.4 Discussion 70

4.4 COMPARISON BETWEEN RESPONSES OF CPFE AND DDP DESCRIPTIONS IN TENSION PROBLEM 71

4.5 TENSION PROBLEM SOLVING WITH THE COUPLING APPROACH 72

4.5.1 Coupling methodology 73

4.5.2 Numerical results 76

4.5.3 Computational efficiency 82

4.6 DISCUSSION 83

4.7 SUMMARY 85

5 INDENTATION PROBLEM: RESOLVING DIFFERENT SCALES 86

5.1 INTRODUCTION 86

5.2 INDENTATION PROBLEM SOLVED USING DISCRETE DISLOCATION PLASTICITY ... 86

5.2.1 Methodology and problem definition 87

5.2.2 Results 89

5.2.3 Quantitative analysis of indentation pressure evolution 100

5.2.4 Summary 106

5.3 INDENTATION PROBLEM SOLVED WITH CRYSTAL PLASTICITY FINITE ELEMENT 108

5.3.1 Methodology and problem definition 109

5.3.2 Results 110

5.3.3 Summary 121

5.4 COMPARISON BETWEEN RESPONSES OF CPFE AND DDP DESCRIPTIONS IN INDENTATION PROBLEM 123

5.5 SUMMARY 124

6 APPLICATION OF THE PROPOSED MULTI-SCALE COUPLING METHOD TO INDENTATION 126

6.1 INTRODUCTION 126

6.2 METHODOLOGY 128

6.2.1 Problem definition 128

6.2.2 Boundary conditions passing 130

6.2.3 Interface modelling 131

6.2.4 Implementation of the coupling strategy 132

6.3 RESULTS 133

6.3.1 Validation: DDP zone size effect 133

6.3.2 Computational efficiency 142

6.4 APPLICATION: INDENTATION PRESSURE EVOLUTION OF A COATING SYSTEM 143

6.4.1 Models with coupling boundary as static grain boundary 145

6.4.2 Models with coupling boundary transparent to dislocations passing 149

6.5 DISCUSSION 154

6.6 SUMMARY 155

7 NANO-SLIDING AND FRETTING PROBLEMS 156

7.1 INTRODUCTION 156

7.2 SLIDING AND FRETTING PROBLEMS SOLVED USING THE CRYSTAL PLASTICITY FINITE ELEMENT TECHNIQUE 157

7.2.1 Methodology 157

7.2.2 Problem definition 157

7.2.3 Results 161

7.2.4 Summary 177

7.3 SLIDING AND FRETTING PROBLEMS SOLVED WITH DISCRETE DISLOCATION PLASTICITY 178

7.3.1 Methodology 178

7.3.2 Problem definition 178

7.3.3 Results 182

7.3.4 Summary 213

7.4 LINKING DISLOCATION ACTIVITY TO CRACK INITIATION FOR SLIDING AND FRETTING PROBLEMS 215

7.5 SUMMARY 217

8 CONCLUSION AND FUTURE WORK 219

8.1 SUMMARY AND KEY CONTRIBUTIONS 219

8.2 DISCUSSION AND APPLICATIONS OF THE PROPOSED FRAMEWORK 222

8.3 LIMITATIONS 223

8.4 FUTURE WORK 224

8.5 CONCLUSIONS 224

REFERENCE 226

APPENDIXES 246

APPENDIX I: THE MATHEMATICAL REPRESENTATION OF EULER ANGLE NOTATION 246

APPENDIX II: SCHMID'S LAW 247

APPENDIX III: PARAMETRIC STUDY ON HARDENING PARAMETERS IN CPFE FORMULATIONS 247

APPENDIX IV: STEP-TIME CONFIGURATION FOR CPFE CALCULATIONS IN ABAQUS 250

APPENDIX V: SLIP SYSTEM EFFECT ON INDENTATION PRESSURE IN DD CALCULATIONS 251

APPENDIX VI: MATHEMATICAL ANALYSIS ON PARAMETERS IN THE PROPOSED INDENTATION PRESSURE FORMULA 252

APPENDIX VII: HARDNESS VALUE OF AN ELASTIC FILM 254

APPENDIX VIII: MATHEMATICAL ANALYSIS OF THE PROPOSED INDENTATION PRESSURE EVOLUTION 255

APPENDIX IX: DISLOCATION SOURCE DENSITY EFFECT ON SHEAR STRESS 256

APPENDIX X: OBSTACLE DENSITY EFFECT ON SHEAR STRESS 261

APPENDIX XI: DISLOCATION STRUCTURE EVOLUTION IN FRETTING SIMULATIONS WITH VARIOUS CONTACT SIZES 262

List of Figures

Figure 1.1. Size scales and corresponding modelling methods involved in the study and usage of a turbine fan analysis. (a) Component scale with finite element method, (b) Meso-scale with discrete dislocation plasticity, (c) Nano-scale with dislocation plasticity and atomistic models and (d) Quantum scale [5]..... 2

Figure 2.1. Stress-strain curve showing typical plastic behaviour of materials in uniaxial tension test 10

Figure 2.2. Flow stress and strain hardening of anisotropic crystalline materials 12

Figure 2.3. a schematic representation of the decomposition of total deformation gradient F. $\mathrm{m}\alpha$ *is the slip direction and* $\mathrm{n}\alpha$ *is the slip plane normal of slip system* α.. *13*

Figure 2.4. dislocation motion on a slip plane, taken from [88] 16

Figure 2.5. the hierarchy of length scales in structure material plasticity ranging from atoms to macroscale. The corresponding modelling methods are also reported for each scale. 18

Figure 3.1. The structure of a typical seeds file employed in crystal plasticity finite element method..... 33

Figure 3.2. The Voronoi tessellations microstructure and finite element mesh of a rectangular specimen with dimension $6 \times 2\mu\mathrm{m}$ *modelled with CPFE 34*

Figure 3.3. The general flow chart of the CPFE code employed in this project 35

Figure 3.4. An edge dislocation dipole nucleated from a Frank-Read source in the plane of the simulation..... 37

Figure 3.5. The linear superposition scheme..... 38

Figure 3.6. A tension IN file structure with explanation..... 39

Figure 3.7. Part of a DISL file structure used for generating dislocation information for the DDP specimen adopted for the uniaxial tension problem..... 39

Figure 3.8. The structure of a BCIN file used for the tension coupling problem..... 40

Figure 3.9. The general flow chart of the DDP code employed in this project..... 41

Figure 3.10. the boundary conditions passing process between CPFE and DDP domains in uniaxial tension problem..... 42

Figure 3.11. Schematic of the domain-decomposition strategy used for the DDP-CPFE coupling..... 43

Figure 3.12. Macroscopic stress–strain responses predicted by DDP and CPFE for the Al crystal after calibration of the CPFE constitutive parameters to produce the best match between the two simulations..... 44

Figure 3.13. the general flow chart of newly proposed multi-scale modelling approach 48

Figure 4.1. Sketch of the uniaxial tension boundary value problem analysed .The left region is modelled as elastic-plastic continuum material while the right region is modelled as CPFE..... 52

Figure 4.2. Stress strain response curve of the elastic-plastic material. This curve is fitted from the 0 degree CPFE crystal whose stress strain response curve is also included for reference..... 52

Figure 4.3. Crystal rotation with Euler angles notation $\phi 1$, Φ *and* $\phi 2$ *(a) the three-dimensional perspective (b) the view along the Z direction showing the two-dimensional rotation situation..... 54*

Figure 4.4. The stress strain response curves of four uniform values grain orientations of a single crystal specimen modelling (see Figure 4.1) with crystal plasticity finite element. The result of the response of single crystal specimen and a polycrystalline sample characterised by a micro structure with 20 random distributed grain orientations are shown. A 0.2% strain yield line is also included for reference..... 55

Figure 4.5. the Von Mises stress field generated by a 20-grain (a) 0 degree single crystal (b) polycrystalline structure with random orientations *56*

Figure 4.6. The stress strain response curves of three values different critical shear stress of a single crystal specimen modelling (see Figure 4.1) with crystal plasticity finite element. A 0.2% strain yield line is also included for reference *57*

Figure 4.7. The stress strain response curves of different values Z *of single crystals and specimen modelling with crystal plasticity finite element. Both grains are characterised by 9 MPa as its critical resolved shear stress, but 0 and 45 degree orientation are taken into consideration. A 0.2% strain yield line is also included for reference.* *57*

Figure 4.8. The stress strain response curves of three different values HF *of a single crystal specimen modelling with crystal plasticity finite element. The grain is with 9MPa as its critical resolved shear stress and 0 degree orientation. A 0.2% strain yield line is also included for reference.* *58*

Figure 4.9. Sketch of the uniaxial tension boundary value problem analysed using Dislocation Dynamics. Both BCC-like single and polycrystalline specimens are considered. *61*

Figure 4.10. The distribution of (a) dislocation nucleation source sites and (b) obstacles predefined in the single LSD crystal specimen ($\rho\mathrm{nuc} = \rho\mathrm{obs} = 56\mu\mathrm{m}\text{-}2$*) used in the DD uni-axial tension problem* *62*

Figure 4.11. Uniaxial tensile response curves of the LSD ($\rho\mathrm{nuc} = \rho\mathrm{obs} = 56\mu\mathrm{m}\text{-}2$*) single crystals. (a) Overall stress,* σ*, versus strain, U/L, and (b) evolution of the dislocation density with strain. Curves are shown for different values of the specimen size w with a fixed aspect ratio* $\mathrm{L/w} = 1.5$ *64*

Figure 4.12. Uniaxial tensile response curves of the LSD ($\rho\mathrm{nuc} = \rho\mathrm{obs} = 56\mu\mathrm{m}\text{-}2$*) single FCC crystals. (a) Overall stress,* σ*, versus strain, U/L, and (b) evolution of the dislocation density with strain. Curves are shown for different values of the specimen size w with a fixed length* $\mathrm{L} = 6\mu\mathrm{m}$ *65*

Figure 4.13. Uniaxial tensile response curves of the LSD ($\rho\mathrm{nuc} = \rho\mathrm{obs} = 56\mu\mathrm{m}\text{-}2$*) single FCC polycrystalline specimens with grain size* $\mathrm{d} = 0.5\mu\mathrm{m}$ *. (a) Overall stress,* σ*, versus strain, U/L, and (b) evolution of the dislocation density with strain. Curves are shown for different values of the specimen size w with a ratio* $\mathrm{L/w} = 1.5$ *66*

Figure 4.14. Uniaxial tensile stress strain response curves of single FCC crystals with four different values of dislocation nucleation source density. Curves are shown for different values of the same dimension $\mathrm{L} \times \mathrm{w} = 6\mu\mathrm{m} \times 2\mu\mathrm{m}$. *67*

Figure 4.15. Uniaxial tensile response curves of the HSD ($\rho\mathrm{nuc} = 200\mu\mathrm{m}\text{-}2$ $\rho\mathrm{obs} = 100\mu\mathrm{m}\text{-}2$*) single FCC crystals. (a) Overall stress,σ, versus strain, U/L, and (b) evolution of the dislocation density with strain. Curves are shown for different values of the specimen size w with a fixed length* $\mathrm{L} = 6\mu\mathrm{m}$. *68*

Figure 4.16. the dislocation structure with undeformed FE mesh of the HSD single crystal tension with the engineering strain level$\varepsilon = 1.0\%$*. A large amount of dislocations are found pinning (piling up) at left and right boundaries of the crystal.* *69*

Figure 4.17. Uniaxial tensile response curves of the LSD ($\rho\mathrm{nuc} = 56\mu\mathrm{m}\text{-}2$ $\rho\mathrm{obs} = 56\mu\mathrm{m}\text{-}2$*) single FCC crystals. (a) Overall stress,σ, versus strain, U/L, and (b) evolution of the dislocation density with strain. Curves are shown for specimens with a fixed geometry dimension* $\mathrm{L} \times \mathrm{w} = 6\mu\mathrm{m} \times 2\mu\mathrm{m}$ *but subjecting from different loading rates respectively.* *70*

Figure 4.18. The comparison of stress field between CPFE and DDP calculations *72*

Figure 4.19. The uniaxial tension DD-CPFE coupling example. *73*

Figure 4.20. The Flow chart of the coupling procedure applied to the uniaxial tension problem..... *74*

Figure 4.21. Macroscopic stress-strain curves at the right-hand side boundary for the non-iteratively coupled and fully coupled solutions. A comparison with the initial DDP and CPFE individual stress-strain responses is also shown. *76*

Figure 4.22. The iteration process with iteration points against the final response curve of the uniaxial specimen..... *77*

Figure 4.23. (a) Dislocation density evolution and (b) stress-strain curves at the coupling boundary for the DDP only solution, the non-iteratively coupled solution and the fully coupled solution..... *79*

Figure 4.24. the stress field (a) the normal stress S11 (b) the shear stress S12 in the two CPFE and discrete dislocation plasticity crystals at six different coupling steps..... *80*

Figure 4.25. The normal stress $\sigma 11$ *contour and the corresponding dislocation structure in the discrete dislocation plasticity region of the uniaxial tension problem solved by the proposed coupling approach. Results are shown for the engineering strain level (a)* $\varepsilon = 0.125\%$ *and (b)* $\varepsilon = 0.25\%$*.....82*

Figure 4.26. The macroscopic stress strain response of the discrete dislocation region, the crystal plasticity region and the coupling region. The results are obtained by another type of boundary condition passing where discrete dislocation region receives displacements and feedbacks tractions to crystal plasticity region.....84

Figure 5.1. (a) Sketch of the indentation boundary value problem solved using the DDP model. (b) The definitions of the actual contact area A*, the nominal contact area* AN*, the indentation depth* δ *and sink-in* δs *ignoring the surface roughness.....89*

Figure 5.2. The distribution of (a) dislocation nucleation source sites and (b) internal obstacles (c) internal and boundary obstacles predefined in the single reference crystal specimen. The parameters set for the generation of the dislocation structure and the film to be indented are $h = 2\mu m$ *and nucleation source and obstacle density* $\rho nuc = \rho obs = 42\mu m\text{-}2$*.....90*

Figure 5.3. (a) Reaction force F*; (b) Nominal,* AN*, and actual,* A*, contact area; (c) Actual indentation pressure,* pA*, curves versus applied indentation depth* δ *for a film characterised by thickness* $h = 10\ \mu m$ *with different indenter shapes (different values of indenting angle* ω *with respect to X axis). The films analysed here have the same dislocation structure.....91*

Figure 5.4. Indentation force versus applied indentation depth for $\omega = 5°$ *wedge. Results are shown for both elastic and discrete dislocation predictions for the material under investigation.....92*

Figure 5.5. Actual contact area A *versus applied indentation depth* δ *for the* $\omega = 5°$ *wedge. Results are shown for both the elastic and discrete dislocation predictions for the* $h = 10\ \mu m$ *film. The nominal contact area* AN *is also included for reference.....93*

Figure 5.6. Actual indentation pressure pA*versus applied indentation depth* δ *for the* $\omega = 5°$ *wedge. Results are shown for both the elastic and discrete dislocation predictions for* $h = 2\ \mu m$ *and* $h = 10\ \mu m$ *films respectively. 93*

Figure 5.7. the relation between actual contact length, A*, and indentation depth* δ *for indentation of the reference material with* $\omega = 5°$ *wedge. Results are shown for five films with different thicknesses* h*. Nominal contact area,* AN*, is also shown for reference (dotted line).* *94*

Figure 5.8. deformed mesh (displacements magnified by a factor of 1) with $\omega = 5°$ *wedge indentation of (a)* $h = 2\mu m$ *and (b)* $h = 10\ \mu m$ *films. Meshes are shown at the time when the applied indentation depth* $\delta = 0.3\ \mu m$. *95*

Figure 5.9. Actual indentation pressure evolution pA *curves versus the applied indentation depth* δ *for five films with different thicknesses indented by the* $\omega = 5°$ *wedge. Note that the films are also characterised by different values of dislocation nucleation density.* *96*

Figure 5.10. (a) Actual (b) nominal indentation pressure variation of films with different values of film thickness but identical nucleation source density *97*

Figure 5.11. (a) Actual (b) nominal indentation pressure variation of films of thickness $h = 10\mu m$ *but different nucleation source density* *99*

Figure 5.12. Sketch of the physical interpretation of the initial intrinsic material hardness Hi *101*

Figure 5.13. the linear relationship between fitting parameter a^* *against average source spacing* *102*

Figure 5.14. Hardness data and their corresponding best fit curves (in discrete data marker) in indentation size effect zone for three Cu single crystals obtained in nano-indentation experiment. *106*

Figure 5.15. Sketch of the boundary value problem of a CPFE crystal indented by a wedge-shaped indenter analysed *110*

Figure 5.16. Von Mises stress contour plot of the reference CPFE crystal under wedge-shaped indenter indentation when indentation depth achieves $\delta = 2\mu m$ *(i.e. the relative indentation depth* $\beta = 2\%$ *)* *111*

Figure 5.17. hardness evolution curve of the reference CPFE crystal against relative indentation depth, with the trend lines of two different stages in indentation process *112*

Figure 5.18. the relationship between hardness and Young's modulus of CPFE single crystal. Other CPFE material parameters are set as identical as the reference CPFE single crystal. Both hardness values and Young's modulus are normalized by the hardness value and Young's modulus value of reference CPFE single crystal. *113*

Figure 5.19. the relationship between hardness and value of critical resolved shear stress (CRSS) of CPFE single crystal. Other CPFE material parameters are set as identical as the reference CPFE single crystal. Both hardness value and critical resolved shear stress are normalized by the hardness value and Young's modulus value of reference CPFE single crystal *114*

Figure 5.20. the relationship between hardness and grain orientation of CPFE single crystal. Other CPFE material parameters are set as identical as the reference CPFE single crystal. Hardness values of different CPFE films are normalized by the hardness value of reference CPFE single crystal..... *115*

Figure 5.21. accumulated plastic strain contour of (a) a single crystal CPFE film (b) a 20 grains polycrystalline CPFE film under wedge shaped indenter indentation when indentation depth achieves $\delta = 2\mu m$ *(i.e. relative indentation depth* $\beta = 4\%$ *).*..... *116*

Figure 5.22. actual indentation pressure p *evolution curves versus applied indentation depth* δ *of a single crystal and a polycrystalline material under wedge indenter indentation. The indentation simulation process is carried out up to* $\delta = 2\mu m$. *116*

Figure 5.23. Sketch of a coating system indented by a wedge-shaped indenter analysed. The coating film of this coating system is modelled as CPFE single crystal while the substrate is modelled as a purely elastic material. *118*

Figure 5.24. hardness revolution of a coating system with the reference single crystal as its coating and purely elastic material as substrate. The best fitting hardness curve of this coating system with eq.(5.15) is also plotted for reference. *118*

Figure 5.25. Parametric study of the influence of fitting parameters (a) $\beta 0$ *and (b)* ε *of the proposed formula upon hardness transition between the coating film and substrate. Cases are shown with the condition that film is harder than substrate, i.e.* $Hf > Hs$ .. *120*

Figure 5.26. Micro (Buehler) and macro indentation data collected from a $3.5\mu m$ *TiN coating on M2 tool steel. A best fit curve using eq.(5.15) is also shown in blue line.* ... *121*

Figure 6.1. Schematic representation of the indentation DD-CPFE coupling problem. 129

Figure 6.2. The Flow chart of the coupling procedure between crystal plasticity finite element and dislocation dynamics on a displacement-controlled two-dimensional indentation problem..... 131

Figure 6.3. Two physical models adopted by describing the coupling boundary as (a) static grain boundary (b) transparent boundary to dislocations..... 132

Figure 6.4. Curves of indentation pressure p *versus applied indentation depth* δ *for two film thicknesses:* $\mathrm{h} = 2\mu\mathrm{m}$ *and* $\mathrm{h} = 10\mu\mathrm{m}$*..... 135*

Figure 6.5. Normalized stress $\sigma 22\tau 0$*and dislocation structure of the indentation problem solved by (a) DDP film on a rigid boundary (b) DDP film coupled with a CPFE substrate (c) DDP film on an elastic substrate. All stress contours are plotted at the instant* $\delta = 0.2\ \mu\mathrm{m}$*. 136*

Figure 6.6. The deformed contact surface in the $\omega = 5°$ *wedge indentation of the* $\mathrm{h} = 2\mu\mathrm{m}$ *film. The displacements are shown at the instant when the applied indentation depth* $\delta = 0.3\mu\mathrm{m}$*. The initial nucleation source density is set as* $\rho\mathrm{nuc} = 42\mu\mathrm{m}$-2*. The DDP only results are also included for reference. 137*

Figure 6.7. Dislocation density evolution curves of the indentation process on the coupling model with discrete dislocation plasticity region sizes (a) $\mathrm{l} \times \mathrm{h} = 30\ \mu\mathrm{m} \times 10\ \mu\mathrm{m}$ *and (b)* $\mathrm{l} \times \mathrm{h} = 30\ \mu\mathrm{m} \times 2\ \mu\mathrm{m}$ *. The dislocation density is averaged within the corresponding DDP sub-region..... 138*

Figure 6.8. The dislocation structure in the discrete dislocation plasticity region modelling by the DD-CPFE coupling approach with discrete dislocation plasticity region size (a) $\mathrm{l} \times \mathrm{h} = 30\ \mu\mathrm{m} \times 20\ \mu\mathrm{m}$ *(results are shown within* $\mathrm{h} = 10\ \mu\mathrm{m}$ *), (b)* $\mathrm{l} \times \mathrm{h} = 30\ \mu\mathrm{m} \times 10\ \mu\mathrm{m}$ *and (c)* $\mathrm{l} \times \mathrm{h} = 30\ \mu\mathrm{m} \times 2\ \mu\mathrm{m}$ *respectively. Results are obtained at the instant* $\delta = 0.3\ \mu\mathrm{m}$*. The distributions are shown on the undeformed film. 139*

Figure 6.9. The distribution of total slip contour Γ *in the* $\mathrm{h} = 10\ \mu\mathrm{m}$ *film modelled by (a) the proposed coupling method and (b) discrete dislocation dynamics plasticity indented by the* $\omega = 5°$ *wedge-shaped indenter. Results are obtained at the instant* $\delta = 0.3\ \mu\mathrm{m}$ *(the actual contact area* $\mathrm{A} \approx 7.2\mu\mathrm{m}$*).The distributions are shown on the undeformed film. 140*

Figure 6.10. The distribution of lattice rotations under the indenter tip in the $h = 10\ \mu m$ *film modelled by (a) the proposed coupling method and (b) discrete dislocation dynamics plasticity indented by the* $\omega = 5°$ *wedge-shaped indenter. Results are obtained at the instant* $\delta = 0.3\ \mu m$ *(the actual contact area*$A \approx 7.2\mu m$*..... 141*

Figure 6.11. Schematic illustration of the indentation pressure variation against relative indentation depth that is aimed to be solved applying the newly proposed multi-scale coupling approach on a coating system with (a) substrate harder than film and (b) film harder than substrate 144

Figure 6.12. The actual indentation pressure pA *curves versus the applied indentation depth* δ *for the film* $h = 2\mu m$ *indented by the* $\omega = 5°$ *wedge. Results are shown for discrete dislocation plasticity alone and the DDP-CPFE coupling method with the same mesh configuration..... 146*

Figure 6.13. Sketch of the coupling model where a static grain boundary pins dislocations. The deformed geometry boundary is also shown for reference. 146

Figure 6.14. The actual indentation pressure pA *curves versus the relative indentation depth* β *for the polycrystalline coating system with the coating film* $h = 2\mu m$ *and various substrates with different continuum hardness values indented by the* $\omega = 5°$ *wedge. Results of discrete dislocation plasticity alone with a rigid boundary with the same mesh configuration are also included for reference. 148*

Figure 6.15. the actual indentation pressure against the relative indentation depth of a polycrystalline coating system. Results are shown for both coupling simulations and the best fit curve with eq.(6.9). 149

Figure 6.16. The actual indentation pressure pA *evolution curve of a coating system without internal grain boundary against the applied indentation depth* δ*. Indentation pressure curves generated by other modelling methods are also included for reference. 150*

Figure 6.17. Sketch of the coupling model where a boundary transparent to dislocations presents. The stress field transfer is also illustrated..... 151

Figure 6.18. The actual indentation pressure against the relative indentation depth of a typical coating system. Results are shown for both coupling simulations and the best fit curve with eq.(6.11). The indentation pressure of discrete dislocation plasticity and crystal

plasticity finite element simulations are also included for reference. The prediction of the coating system using the traditional formula eq.(6.1) is also plotted in orange. *152*

Figure 6.19. The actual indentation pressure pA *curves versus the relative indentation depth* β *for the single crystal coating system with the coating film* $\mathrm{h} = 2\mu\mathrm{m}$ *and various substrates with different continuum hardness values indented by the* $\omega = 5°$ *wedge. Results of DDP alone with a process window* $\mathrm{h} = 10\ \mu\mathrm{m}$ *with same source density are also included for reference.* *153*

Figure 7.1. Sketch of the boundary value problem of a CPFE crystal under a sliding and fretting loading by a flat-shaped indenter *159*

Figure 7.2. Linear and exponential types of damage evolution based on the accumulated plastic strain in finite elements..... *161*

Figure 7.3. The nodal path definitions in sliding simulations solving with CPFE method. The horizontal path definitions labelled as a_1, a_2 *and* a_3 *represent surface, subsurface and bulk behaviour, while vertical path definitions labelled as* b_1 *and* b_2 *represent the trailing and leading edge behaviour.*..... *162*

Figure 7.4. A general plastic deformation contour of the specimen under flat contact sliding. Figure shows the accumulated plastic strain contour near the leading edge.. *163*

Figure 7.5. Accumulated plastic strain γ *computed at nodes along Path Surface, Path Subsurface and Path Bulk*..... *163*

Figure 7.6. The accumulated plastic strain γ *of nodes along Path Leading Edge and Path Trailing Edge.* *164*

Figure 7.7. Sliding index ζ *of nodes along Path Surface, Path Subsurface and Path Bulk.* *164*

Figure 7.8. The influence of coefficient of friction on the plastic deformation of nodes at different positions (a) nodes along the specimen surface (b) nodes along the leading edge *166*

Figure 7.9. Accumulated plastic strain γ *of nodes along Path Surface (a), Path Subsurface (b) and Path Bulk (c). Results are shown from films assigned single crystals with grain orientations (GO)* $0,\ \pi/8$ *and*$\pi/4$, *respectively.* *167*

Figure 7.10. A sketch of polycrystalline microstructure of the specimen under flat contact sliding. X represents potentially sensitive grains. *168*

Figure 7.11. Accumulated plastic strain γ along Path Surface. Results are shown for polycrystalline specimens with grains near the contact leading edge oriented at 0, 22.5 and 45 degree, respectively. *169*

Figure 7.12. Points of interest on the specimen in fretting simulations solving with CPFE method. A focused mesh is also shown for reference *170*

Figure 7.13. Evolution of accumulated plastic strain γ of nodes along Path Surface during three cycles of sliding. Results are obtained from a single crystal oriented 0 degree and coefficient of friction $\mathrm{f} = 0.2$ *between the indenter and specimen.* *171*

Figure 7.14. Evolution of accumulated plastic strain γ of nodes at the intersection between contact edges and (a) Path Surface, (b)Path Subsurface and (c)Path Bulk during three cycles of fretting. Results are obtained from simulations with a single crystal oriented 0 degree as specimen and 0.2 as the coefficient of friction between the specimen and indenter. *173*

Figure 7.15. Evolution of accumulated plastic strain γ of nodes at the intersection between contact edges and (a) Path Surface, (b)Path Subsurface and (c)Path Bulk during three cycles of fretting. Results are obtained from simulations with a single crystal oriented 22.5 degree as specimen and 0.2 as the coefficient of friction between the specimen and indenter. *174*

Figure 7.16. Contact between film and a rounded rectangular indenter with a fillet radius $\mathrm{R} = 1\mu\mathrm{m}$. *175*

Figure 7.17. Evolution of accumulated plastic strain γ of nodes at the most sensitive nodes during three cycles of sliding under contact edges with radius (a) $\mathrm{R} = 0.5\mu\mathrm{m}$ *(b)* $\mathrm{R} = 1.0\mu\mathrm{m}$ *(c)* $\mathrm{R} = 2.0\mu\mathrm{m}$ *respectively. Results are obtained from simulations with a single crystal oriented 0 degree as specimen and 0.2 as the coefficient of friction between the specimen and indenter.* *177*

Figure 7.18. Sketches of (a) sinusoidal indentation and (b) sliding and fretting boundary value problems analysed using discrete dislocation plasticity. The origin of the coordinate system employed is marked as a filled-in circle (•) in (a) and (b). *179*

Figure 7.19. Sketches of (a) a cohesive zone model (b) the softening and non-softening cohesive laws prescribing the relationship between the shear traction and the displacement jump at the nodes belonging to the contact partition. The non-softening relation is adopted in sliding and fretting calculations. *181*

Figure 7.20. Indentation pressure p versus contact length for sinusoidal asperity indentation with amplitude $\Delta = 0.5$ μm *and wavelengths (a)* $\lambda = 20$ μm *and (b)* $\lambda = 10$ μm. *Results are shown for* $h = 10$ μm *and* $h = 2$ μm *films.* *184*

Figure 7.21. (a) shear stress τ *versus sliding displacement* U *curves for* $h = 10$ μm *film for selected values of contact length* a. *(b) average stress stress* τave *versus contact length* a *for two values of film thickness* h. *These results are obtained from sliding simualtions with no prior indentation.* *185*

Figure 7.22. The coefficient of friction μ v*ersus sliding displacement* U *for a* $h = 10$ μm *film. Indentation pressure p is from the sinusoidal asperity indentation with* $\Delta = 0.5$ μm*and wavelength* $\lambda = 20$ μm. *The sliding calculations are carried out for an initially stress and dislocation-free crystal, while the pressure* p *for each* a *is the value needed to achieve this contact length under indentation.* *186*

Figure 7.23. The shear stress τ *versus sliding displacement* U *curves for* $h = 10$ μm *with contact length (a)* $a = 4.0$ μm *and (b)* $a = 10.0$ μm. *Results are obtained from pure sliding simualtions with different loading rates.* *187*

Figure 7.24. Dislocation structure for $h = 10$ μm *film with the contact length* $a = 4.0$ μm *and loading rate (a)* U/a = 1e5s-1, *(b)* U/a = 0.5e5s-1 *(c)* U/a = 0.1e5s-1 *and (d)* U/a = 0.05e5s-1. ..... *188*

Figure 7.25. The dislocation structure in a $h = 10$ μm *film at different applied sliding displacement for pure sliding. The flat contact length* $a = 2.0$ μm *is illustrated by a black filled bar.* *189*

Figure 7.26. Dislocation density evolution in $h = 10$ μm *film at different applied sliding displacement for pure sliding. The flat contact length is* $a = 2.0$ μm*, and results are shown for dislocation gliding on different slip systems.* *190*

Figure 7.27. Shear stress τ *versus sliding displacement* U *curves for a* $h = 10$ μm *film in contact with an asperity (contact size* $a = 4.0$ μm*) for selected values of dislocation source densities,* ρ. *191*

Figure 7.28. The average shear stress τave *versus average source spacing* $davg.$ *curves for a* $h = 10\ \mu m$ *film with contact size* $a = 4.0\ \mu m$ *for selected values of dislocation source densities.* *192*

Figure 7.29. The coefficients of friction μ versus the average source spacing $davg.$*; curves for a* $h = 10\ \mu m$ *film with contact sizes* $a = 4.0\ \mu m$ *and* $a = 8.0\ \mu m$ *for selected values of dislocation source densities.* *193*

Figure 7.30. Dislocation structure in a $h = 10\ \mu m$ *film for* $a = 4.0\ \mu m$. *Results are obtained for films with (a)* $\rho nuc = 9.71\ \mu m\text{-}2$ *and (b)* $\rho nuc = 97.18\ \mu m\text{-}2$ *at the instant when the sliding displacement is* $U = 0.04\ \mu m$ *193*

Figure 7.31. Dislocation structure in a $h = 10\ \mu m$ *film for* $a = 8.0\ \mu m$ *size. Results are obtained for films with (a)* $\rho nuc = 9.71\ \mu m\text{-}2$ *and (b)* $\rho nuc = 97.18\ \mu m\text{-}2$ *at the instant when the sliding displacement* $U = 0.08\ \mu m$ *194*

Figure 7.32. Effect of preceding indentation on frictional response. (a) Shear stress versus displacement response for a $h = 10\ \mu m$ *film. (b) Average friction stress* τave *versus contact size for* $h = 10\ \mu m$ *and* $h = 2\ \mu m$ *films. In these calculations, the films were firstly indented by a sinusidial asperity with amplitude* $\Delta = 0.5\ \mu m$ *and wavelength* $\lambda = 20\ \mu m$, *which produced the pre-existing stress field and dislocation structure that determine the subsequent response during sliding.* *195*

Figure 7.33. Effect of preceding indentation on dislocation structure. Dislocation patterns are obtained at the instant $U = 0.02\ \mu m$ *of simulations (a) pure sliding with contact size* $a = 10 \mu m$ *(b) sliding with a preceding indentation that introduces a contact size* $a \approx 10\ \mu m$. *196*

Figure 7.34. Slip contours obtained in simulations for (a) pure sliding, and (b) sliding with a preceding indentation on a $h = 10\ \mu m$ *film by a sinusidial asperity with amplitude* $\Delta = 0.5\ \mu m$ *and wavelength* $\lambda = 20\ \mu m$ *at the applied sliding distance* $U = 0.02\ \mu m$. *The contact area is* $a = 10\ \mu m$ *indicated as a filled black bar in both cases.* *197*

Figure 7.35. Slip contours obtained in simulations for (a) pure sliding, and (b) sliding with a preceding indentation on $h = 10\ \mu m$ *film by a sinusidial asperity with amplitude* $\Delta = 0.5\ \mu m$ *and wavelength* $\lambda = 20\ \mu m$ *at the applied sliding distance* $U = 0.022 \mu m$. *The contact area is* $a = 2.45\ \mu m$ *indicated as a filled black bar in both cases.* *197*

Figure 7.36 Dislocation structure obtained in simulations for (a) pure sliding, and (b) sliding with a preceding indentation on a $h = 10\ \mu m$ *film by a sinusidial asperity with amplitude* $\Delta = 0.5\ \mu m$ *and wavelength* $\lambda = 20\ \mu m$ *at the applied sliding distance* $U = 0.022\ \mu m$. *The contact area is* $a = 2.45\ \mu m$ *indicated as a filled black bar in both cases.* *198*

Figure 7.37. Shear stress τ *evolution during a fretting process. Results are obtained by cyclic sliding for a* $h = 10\ \mu m$ *film with a stress- and dislocation-free status initially. The contact length is set as* $a = 2.0\ \mu m$. *199*

Figure 7.38. Dislocation structure evolution during the fretting process. Results are obtained for cyclic sliding on a $h = 10\ \mu m$ *film with a stress- and dislocation-free status initially. The contact length is set as* $a = 2.0\ \mu m$ *201*

Figure 7.39. Dislocation density evolution during the fretting process. Results are obtained by cyclic sliding on the $h = 10\ \mu m$ *film with a stress- and dislocation-free status initially. The contact length is set as* $a = 2.0\ \mu m$. *The evolution of dislocations gliding on horizontal and inclined slip systems are separated to discuss their roles during the fretting process*..... *201*

Figure 7.40. Displacements in the Y direction along the contact surface of the specimen during the fretting process without preceding indentation. *202*

Figure 7.41. Dislocation motion in a most favourably oriented grain and the formation of extrusion and intrusion of surface due to dislocation pile-up with certain patterns.202

Figure 7.42. A typical dislocation structure near the contact in fretting process. Results are obtained at the end of 71st cycle. *203*

Figure 7.43 Surface roughness, including arithmetic average Ra *and root mean squared* Rq*, along the contact surface variation during fretting process* *204*

Figure 7.44. Shear stress τ *evolution during the whole fretting process of 100 cycles. Results are obtained at the end of the stroke for each cycle from the simulation performed for a* $h = 10\ \mu m$ *film with a stress- and dislocation-free status initially and various values of contact size.* *205*

Figure 7.45 Total dislocation density evolution during a fretting process. Results are obtained at the end of the stroke for each cycle from simulations of a $\mathrm{h} = 10\ \mu\mathrm{m}$ *film with a stress- and dislocation-free status initially and various values of contact size. 206*

Figure 7.46. Displacement profiles of surfaces at the end of the 100th fretting cycle. Results are obtained from a simulation performed for a $\mathrm{h} = 10\ \mu\mathrm{m}$ *film with a stress- and dislocation-free status initially and various values of contact size. 207*

Figure 7.47. Roughness parameters of contact partition and the whole surface during a fretting process. Results are obtained from simulations on $\mathrm{h} = 10\ \mu\mathrm{m}$ *film with a stress- and dislocation-free status initially and various values of contact sizes..... 208*

Figure 7.48. Displacement profiles of surfaces at the end of each cycle. Results are obtained from simulations performed for a $\mathrm{h} = 10\ \mu\mathrm{m}$ *film preceding indented with contact sizes (a)* $\mathrm{a} = 2.4\mu\mathrm{m}$ *(b)* $\mathrm{a} = 4.1\mu\mathrm{m}$ *(c)* $\mathrm{a} = 9.3\mu\mathrm{m}$ *, respectively..... 210*

Figure 7.49. Surface roughness parameters including arithmetic average Ra *and root mean squared* Rq *along specimen surface during fretting process that starts from a preceding indentation with contact size (a)* $\mathrm{a} = 2.4\mu\mathrm{m}$ *(b)* $\mathrm{a} = 9.3\mu\mathrm{m}$ *repectively.... 211*

Figure 7.50. Shear stress τ *evolution during a fretting process. Results are obtained on* $\mathrm{h} = 10\ \mu\mathrm{m}$ *film cyclically sliding from a preceding indentation with contact size (a)* $\mathrm{a} = 2.4\mu\mathrm{m}$ *(b)* $\mathrm{a} = 4.1\mu\mathrm{m}$ *(c)* $\mathrm{a} = 9.3\mu\mathrm{m}$ *repectively..... 213*

Figure 7.51. the sketch of the concurrent multi-scale coupling method in sliding and fretting problems..... 217

List of Tables

Table 3.1. DDP material parameters used in the tension and indentation problem solved with the proposed coupling method. *44*

Table 3.2. CPFE material parameters used in the tension and indentation problem solved with the proposed coupling method. *44*

Table 4.1. The simulation time cost of the reference specimen under the unxial tension loading modelled by CPFE, discrete dislocation plasticity and Coupling methods respectively. *83*

Table 5.1. General DDP material parameters used in the wedge-shaped indentation problem. *87*

Table 5.2. Values of thickness, nucleation and obstacle density of films in Figure 5.9 ... *96*

Table 5.3. the micro-structure of the indented films plotted in Figure 5.10. ..... *98*

Table 5.4. the dislocation structure of the indented films plotted in Figure 5.11 ..... *99*

Table 5.5. The initial intrinsic hardness Hi *from best-fit calculations for hardness curves in Figure 5.9 of crystals with dislocation structure in Table* *101*

Table 5.6. the best-fit parameter sets using eq. (5.7) of the dependence of $a*$ *on* ρnuc *102*

Table 5.7. The best fit parameter set of the acutal indentation pressure pA *evolution against the acutal indentation depth* δ *for* $h = 10\ \mu m$ *film with different dislocation source nucleation density* *103*

Table 5.8 Best fitting results of experimental data in Figure 5.14 using eq.(5.6). *106*

Table 5.9. parameters used to plot the best fit curves using Eq. (5.15) in Figure 5.24.. *119*

Table 5.10. parameters used for fitting an indentation experiment data *121*

Table 6.1 Coating systems well fitted with Korsunsky's formula 128

Table 6.2. Relative deviation in indentation pressure with different discrete dislocation plasticity film thickness; based on Eq. (6.6). 134

Table 6.3. The normalized dislocation density at the instant $\delta = 0.2\ \mu m$, both of the DDP only and the coupling responses are included. 136

Table 6.4. The fraction of computational time and time saving for the indentation depth from $\delta = 0.05\ \mu m$ to $\delta = 0.10\ \mu m$. Results are shown for various sizes of the discrete dislocation plasticity region and the time consumed of modelling the whole material $300\ \mu m \times 100\ \mu m$ with discrete dislocation plasticity is included for reference. 143

Table 6.5. the substrate hardness values and the corresponding fitting parameters of indentation pressure in Figure 6.14 curves fitted by equation (6.10) in Figure 6.14..... 149

Table 6.6. the substrate hardness values and the corresponding fitting parameters of the indentation pressure curves fitted by using eq.(6.11). The values of fitting parameter a and α are the same as the corresponding discrete dislocation plasticity simulation fitting results. 153

Table 7.1. Parameters of reference CPFE single crystal in sliding and fretting problems 158

Table 7.2. Parameters for realizing microstructure with different average source spacing $davg.$ in $h = 10\ \mu m$ film. The obstacle density is varied with the source density $\rho obs = \rho nuc$ in this set of calculations. 190

Table 7.3. Time consumed for fretting simulations with different contact sizes a. 213

Nomenclature

All symbols are also defined in the text.

Symbol	Description	Units
A/a	Contact area/length	µm
A_N	Actual contact area/length	µm
a^*	Length scale parameter	µm
a_0^*	Intrinsic length scale parameter	µm
B	Drag coefficient along slip planes	$\mathrm{Pa \cdot s}$
b	Burger's vector	nm
$\mathrm{C_{ij}}$	Elastic constant matrix	-
D	Damage parameter	-
d	Grain size	µm
d_{ave}	Average source spacing	nm
E	Young's Modulus	MPa
$\boldsymbol{F}$	Total deformation gradient	-
F	Indentation force	N
$\boldsymbol{F}_e$	Elastic deformation gradient	-
$\boldsymbol{F}_p$	Plastic deformation gradient	-
f	Coefficient of friction	-
G	Shear Modulus	MPa
H	Hardness	MPa
H_i	Initial intrinsic material hardness	MPa
H	Height	µm
H_{film}/H_f	Hardness of coating film	MPa
$H_{substrate}/H_s$	Hardness of substrate	MPa
$\mathrm{H_F}$ $\mathrm{H_R}$ $\mathrm{H_{exp}}$ q	Hardening constitutive parameters	-
$\boldsymbol{h}_{\alpha\beta}$	Hardening modulus matrix	-
h	Film thickness	µm
J	Stress invariants	MPa
$\boldsymbol{L}$	Velocity gradient	-
L	Length	µm
$\mathrm{L_{ann}}$	Annihilation distance	µm
l	Film width	µm
N	Number of fretting cycles	-
$\boldsymbol{n}$	Unit normal vector	-
O	Big O notation; computational complexity	-
$\mathrm{p_A}$	Actual indentation pressure	MPa
$\mathrm{p_N}$	Nominal indentation pressure	MPa
$\mathrm{R^2}$	Coefficient of determination	-

Ra	Arithmetic average of absolute roughness values	nm
Rq	Root mean squared of roughness values	nm
$\boldsymbol{s}$	Unit slip vector	-
T	Traction/Shear	MPa
t	Time	s
t_{nuc}	Nucleation time	ns
Δt	Time increment	ns
U	Sliding distance	µm
w	Width of specimen	µm
Z	Zener's Factor	-
β	Relative indentation depth	-
β_0	Transition fitting parameter	-
Γ	Problem domain boundary	-
Γ	Total slip	-
$\dot{\boldsymbol{\gamma}}$	Shear rate	-
γ	Shear strain	-
γ_s	Damage onset parameter	-
γ_f	Complete damage parameter	-
γ_{acc}	Accumulated plastic strain	-
Δ	Sinusoidal indenter amplitude	µm
δ	Displacement	µm
δ	Applied indentation depth	µm
ε	Normal/engineering strain	-
ε	Exponent fitting parameter	
ε_e	Elastic strain	-
ε_p	Plastic strain	-
ζ	Sliding index	-
θ	Grain orientation	°
λ	Sinusoidal indenter wavelength	µm
ν	Poisson's ratio	-
µ	Coefficient of friction	-
ρ_{obs}	Obstacle density	μm^{-2}
ρ_{nuc}	Nucleation source density	μm^{-2}
ρ	Dislocation density	μm^{-2}
σ	Normal stress	MPa
σ_y	Yield stress	MPa
$\dot{\boldsymbol{\sigma}}$	Cauchy stress rate	$MPa \cdot s^{-1}$
τ	Shear stress	MPa
τ_{ave}	Average shear stress over a sliding range	MPa
τ_c	Critical resolved shear stress	MPa
τ_{obs}	Obstacle strength	MPa
τ_{nuc}	Nucleation source strength	MPa
$\phi^{(i)}$	i^{th} slip system orientation	°

ϕ_1, Φ, ϕ_2	Euler angles	°
Ω	Problem domain	-
Ω	Lattice rotation	radian
ω	Wedge-shaped indenter angle	°

Abbreviation

The following table describes the interpretations of abbreviations and acronyms used throughout the thesis. The number of Chapter on which each one is defined or first used is also given.

Nonstandard acronyms that are used in some places to abbreviate the names of certain terminologies are not in this list.

Abbreviation	Meaning	Chapter
CPFE	Crystal Plasticity Finite Element	1
CP	Crystal Plasticity	1
DD	Discrete Dislocation	1
DDP	Discrete Dislocation Plasticity	1
BCC	Body Centred Cubic	2
FCC	Face Centred Cubic	2
HCP	Hexagonal Close Packed	2
GO	Grain Orientation	2
CRSS	Critical Resolved Shear Stress	3
RVE	Representative Volume Element	3
EBSD	Electron Backscatter Diffraction	3
GUI	Graphic User Interface	3
UMAT	User material subroutine	3
S.D.	Standard Deviation	3
CFTOOL	Curve Fit Toolbox	3
LSD	Low Source Density crystal	4
HSD	High Source Density crystal	4
ISE	Indentation Size Effect	5

SDV	Solution Dependent Variable	5
SGP	Strain Gradient Plasticity	5
GND	Geometry Necessary Dislocation	5
SSG	Statistically Stored Dislocation	5
COF	Coefficient of Friction	7
CZM	Cohesive Zone Model	7
CSE	Contact Size Effect	7

1 Introduction

1.1 Motivation

1.1.1 Multi-scale modelling of materials

The behaviour of materials is extensively observed to be length and/or time scale dependent in experiments, see *e.g.* [1-4]. For instance, crystalline metals or their alloys are significantly hardened when the specimen size shrinks down to the level of several micrometres. Although conventional finite element method is able to explain some features of materials' behaviour at the macroscopic scale, it is still impossible to employ continuum modelling techniques to fully capture a size dependent material behaviour, for instance, Hall-Petch effect and indentation size effect. On the other hand, it is not computationally feasible to apply a sophisticated modelling technique (for instance discrete dislocation plasticity), which focuses on material performance at fine scale, on the whole specimen. Therefore, it is desirable to develop a computational approach that is able to cover multiple length and time scales. It is worth noticing that the terminology "multi-scale" here refers to the resolution at which materials features are captured at different scales and does not necessarily refer to the dimensions of the components under consideration.

Modelling materials from atoms to engineering applications requires spanning a large range of length scales, from $10^{-3}m$ to $10^{-10}m$. These length scales are illustrated using the modelling tools that would be eventually required to perform the stress analysis of a turbine fan in Figure 1.1 [5]. Generally speaking, we desire different levels of definition and accuracy at different scales. For instance, the general stress distribution and the maximum stress position of the fan specimen is simply required at component scale (Figure 1.1 (a)), while the details of stress and strain field needs to be evaluated near nucleating micro-cracks at the micro scale (Figure 1.1 (c)). Corresponding to different length scale, different simulations methods are being applied to capture phenomena that take place at different characteristic length and time scales. For instance, discrete dislocation plasticity has been used in meso-scale simulations; here the Burger's vector is the characteristic length to investigate the plastic behaviour of materials due to dislocations' activity (Figure 1.1 (b)). Different timescales are also associated with the resolution of different phenomena at different length scales and this is reflected in the need to also account for the disparity in timescales when coupling techniques are developed.

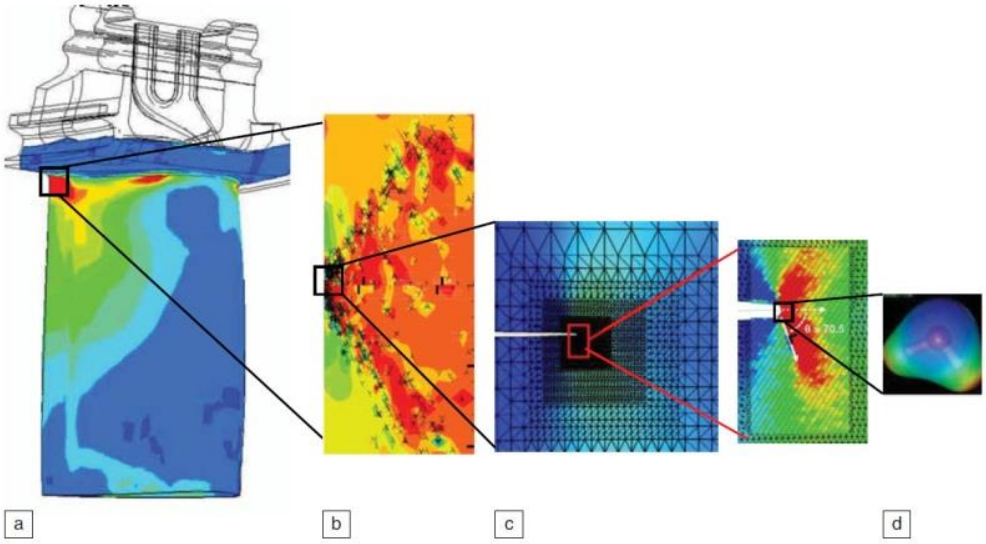


Figure 1.1. Size scales and corresponding modelling methods involved in the study and usage of a turbine fan analysis. (a) Component scale with finite element method, (b) Meso-scale with discrete dislocation plasticity, (c) Nano-scale with dislocation plasticity and atomistic models and (d) Quantum scale [5]

In order to obtain a balance of the computational expense and accuracy, as a consequence, it is necessary to develop a predictive tool to model material performance covering dislocation length scale (sub-microns meters) and time scales (pico-seconds) to crystal lattice length scales (micron meters) and component service time scales (seconds).

In the following sections, challenges related to size effect in several most common engineering tests are discussed. These tests include uniaxial tension tests, which are commonly employed to obtain material strength, indentation tests, which are typically carried out to obtain hardness and elastic constants of material, and sliding/fretting tests that are conducted to predict working life of components subjected to contact damage.

1.1.2 Size Effect in Uniaxial Tension Tests

Tension tests are commonly used to obtain fundamental material mechanical parameters, e.g. ultimate strength, elastic moduli and Poisson's ratio, etc. However, it has been found experimentally that the hardening behaviour experienced during the loading process when the specimen size is of the order of several micrometres is strongly affected by the grain size and the material microstructure. Also, the well-known Hall-Petch effect, namely the increase in yield stress associated with the presence of smaller grains in specimens, can only be explained by the means of theories developed to capture the physics at the microscopic level.

The development of a multi-scale coupling tool and its application to solve uniaxial tension problems with the hope will enable to investigate the material performance at a micro-scale and its links with the perceived macroscopic response. Also, the uniaxial tension simulations will be used as a starting point to validate the newly-developed multi-scale coupling methodology.

1.1.3 Indentation Size Effect and Hardness Evolution

Indentation tests are extensively used in order to obtain the hardness and also to infer other mechanical properties of materials. When the contact area becomes sufficiently small, the hardness of materials is not constant but increases with the decreasing contact size instead; this is the well-known indentation size effect.

The indentation size effect motivates the development of a plasticity theory which is capable of capturing the physics of the problem at a characteristic length scale in the microscopic range. Besides, studying the performance of a coated system requires a multi-scale coupling approach; a variety of processes involving different length scales need to be captured for example to shed light on the mechanical behaviour of thin coating films bonded to bulk substrates when such systems are subjected to indentation.

1.1.4 Size Effects in Sliding and Crack Initiation in Contact Fatigue

Sliding and cyclic sliding (*e.g.* fretting) phenomena are frequently observed in natural and engineering processes, and they are considered as an important source of damage and micro-crack initiation near the contact surface; this often leads to the catastrophic failure of parts due to fatigue. Classical approaches tend to link the shear force (and shear stresses) directly to the normal force only via Coulomb's law. However, experiments have shown that the shear stress and contact behaviour indeed depends on the contact size when this approaches to the grain size.

On the other hand, the development of crack initiation criteria for predictive modelling approaches in contact fatigue are generally based on macroscopic plasticity and phenomenological laws derived using empirical or experimental data. A more physically-grounded approach is required to relate the crack initiation mechanisms to the intrinsic material behaviour.

1.2 Objectives

The general aim of this project is to develop a general multi-scale modelling framework between discrete dislocation dynamics plasticity (DDP) and crystal

plasticity finite element (CPFE) in order to simulate the plasticity of materials occurring at different length/time scales. The proposed coupling approach is first verified using benchmark problem (uniaxial tension case), and then it is applied to problems, such as indentation and sliding, where size effect and the response of the material at different scales plays a significant role in order to investigate the size relevant issues and shed light on the physics governing the behaviour of the materials under investigation.

1.2.1 A General Multi-scale Modelling Framework

The first aim of this work is to develop a general multi-scale modelling framework between DDP and CPFE by using a sub-model scheme. The multi-scale modelling framework should be able to cover different scales of DDP and CPFE, capture the material deformation details via dislocation activity in the sensitive region, and improve the computational efficiency compared to modelling the whole region with DDP. The arrangement of sub-regions and corresponding microstructure should be flexible, and the external boundary conditions should be applied according to different engineering problems.

1.2.2 Multi-scale Coupling Framework Applied to Uniaxial Tension

The proposed multi-scale coupling framework is first applied to solve the uni-axial tension problem. The polycrystalline specimen is modelled using the sub-region multi-scale approach, and a uni-axial displacement is imposed on one boundary of the specimen while the other boundary is fixed. The traction and displacement compatibility must be satisfied along the nodes at the coupling boundary between CPFE and DDP sub-regions.

The uniaxial tension case is used as a benchmark problem to provide the validation of the proposed coupling scheme. Also, the in-depth study of the tension problem enables to shed some light on the performance of polycrystalline materials at different scales using DDP, CPFE and the coupling approach, respectively.

1.2.3 Multi-scale Coupling Framework Applied to Indentation Problems and Coated Systems

The proposed multi-scale coupling framework is then applied to solve the wedge-shaped indentation problem. The polycrystalline specimen is modelled using the sub-region multi-scale approach, and a displacement is imposed on the indenter and the bottom boundary is fixed. Analogous to its application to tension problem, the traction

and displacement compatibility must be satisfied along the nodes at the coupling boundary between CPFE and DDP sub-regions.

The indentation case aims to further verify the effectiveness of the proposed coupling scheme, and investigate the comprehensive polycrystal material performance under a normal pressure load. Also, the in-depth study of the tension problem enables to shed some light on the indentation pressure variation of polycrystalline materials at different scales using DDP, CPFE and the coupling approach, respectively

1.2.4 Apply Multi-scale Coupling Framework in Sliding and Fretting

Finally sliding and fretting problems are considered. The polycrystalline specimen is modelled using DDP and CPFE at different scales, respectively, and a uniform displacement rate is imposed on the sliding asperity and the bottom boundary is fixed.

The sliding and fretting cases aim to investigate polycrystalline material performance under a shear pressure loading at different scales. Also, the calculation results obtained from DDP scale are shown to be able to provide damage parameters for CPFE calculations. Besides, the mechanisms responsible for crack initiation of a polycrystalline film under a sliding or/and fretting loading is investigated by studying the dislocation activities in sensitive regions. Size effects in sliding and fretting problems are also to be investigated.

1.3 Approaches and Tools

The majority of the work presented in this thesis is obtained by the means of numerical simulations. The material performance modelling with different approaches is illustrated by various curves and contours post processed using different software. In particular, stress-strain response curves and the stress contours are used in tension problem, indentation pressures and the stress contours are used in indention problem, and the shear stresses and the corresponding slip contours are used in sliding and fretting problem. Dislocation structures are provided in relevant simulations to show the dislocation activity.

1.3.1 Commercial Software Package and Subroutines

Crystal plasticity finite element employs user defined material subroutine (UMAT) in the commercial finite element method (FEM) software package ABAQUS. The CPFE material response is embedded in a FORTRAN source code. Version 6.9.1 and 6.12 of ABAQUS are both used to create the finite element models and extract the results of the CPFE part of the simulations performed by the author.

Discrete dislocation plasticity employs independent executable files directly compiled from FORTRAN source codes. FORTRAN 77 and 95 standards are both involved to adapt to different codes. GFORTRAN is used as the FORTRAN compiler.

EXCEL, MATLAB and TECPLOT software are used to illustrate the results.

1.3.2 Simulation Environment

The majority of the simulations are conducted in the cluster of Imperial College London. The cluster is based on Linux operation system and equipped with a Quad-Core AMD Opteron(tm) Processor 8384 2.7 GHz processor and 2GB RAM. Simulations are generally performed using one single CPU.

Some of the simulations are conducted in a PC that is equipped with an Intel i5 processor 2.1 GHz processor and 8GB RAM.

1.4 Thesis Outline

This thesis is divided into the following chapters:

Chapter 1 – Introduction: briefly introduces the motivations, objectives and research methodologies developed and used for the project.

Chapter 2 - Literature Review: Mechanical Behaviour and Modelling of Materials: reviews important materials' characteristics linked to plastic behaviour, especially focusing on features relevant to the microstructure of materials. The testing methods and modelling techniques adopted to study material response under loading and microstructural features are reviewed.

Chapter 3 - A General Approach to Study Plasticity by Coupling Crystal Plasticity Finite Element and Discrete Dislocation Plasticity: describes the proposed multi-scale coupling approach between discrete dislocation plasticity and crystal plasticity finite element method developed during my doctoral studies. The fundamental mechanisms, boundary conditions passing between different sub-regions, the iterative scheme, convergence issues and validation through simple test cases are discussed in details.

Chapter 4 – Application of the Multi-scale Modelling Approach: Uniaxial Tension Problem: discusses the application of the proposed multi-scale coupling approach to a uni-axial tension problem. Benchmark simulations are conducted to verify the effectiveness of the proposed coupling approach; this reveals the effect that coupling has on sub-region modelled using DDP and CPFE. Calculations are also performed using DDP and CPFE in isolation to investigate parameters' influence in the two frameworks.

Chapter 5 – Indentation Problem: Resolving Different Scales: discusses a planar indentation problem solved using DDP and CPFE at different scales. Indentation size effect has been captured and further quantitatively described with a newly proposed formula using the results obtained using DDP, while the transition of the material response in terms of indentation pressure between a coating-dominated and a substrate-dominated region is observed and quantitatively predicted using CPFE. These calculations provide a further application of our proposed multi-scale modelling for coated systems, highlighting the capabilities of the proposed approach to span a very large range of length scales and loading conditions. Besides, parametric study are carried out to investigate the influence of microstructure on indentation pressure and material hardness.

Chapter 6 – Application of the Proposed Multi-Scale Coupling Method to Indentation: discusses the application of the proposed multi-scale coupling approach to a wedge-shaped indentation problem. Calculations are conducted using the coupling approach introduced in Chapter 3, but the sub-modelling strategy and the microstructures studied are different. Also, the application of the coupling approach to coated materials quantitatively predicts the hardness evolution of coating systems during indentation process over a wide ange of length scales. Besides, this application further verifies the effectiveness and the robustness of the proposed multi-scale modelling techniques.

Chapter 7 – Nano-Sliding and Fretting Problems: describes the application DDP and CPFE to study sliding and fretting problems. Various simulations are carried out for sliding problems using DDP and CPFE, respectively, and dislocation activities of DDP simulation results are shown to be able to shed light on damage initiation and to potentially provide damage parameters for CPFE damage calculations at the macroscopic scale. Calculations are also carried out with DDP and CPFE methods to investigate parameters' influence in the two frameworks. The effects of contact size and loading rate for sliding and fretting problems have been revealed using DDP calculations.

Chapter 8 – Conclusion: summarizes the main results, discusses the research findings, and draws conclusions from the work presented in the thesis. After presenting the main research contributions of this thesis, it discusses the current limitations of the proposed techniques and suggests avenues to be explored for future work.

2 Literature Review: Mechanical Behaviour and Modelling of Materials

In this chapter, a literature review of the main features required to characterize the mechanical behaviour of materials and the corresponding modelling techniques is provided. In particular, the performance and modelling of polycrystalline materials undergoing plastic deformations is key to this project and will be the focus of this chapter. Macroscopic mechanical behaviour of materials, including tensile strength, plasticity and hardening, etc., are addressed and linked to their microstructure at the microscopic scale. Numerical modelling techniques (including crystal plasticity finite element and discrete dislocation plasticity) at different scales therefore are reviewed to explain and further understand the mechanical behaviour of materials and their dependence on microstructure. Besides stress-strain relationship and mechanical behaviour under conventional static loading, fatigue and damage are also reviewed to illustrate the significance of their mechanisms and modelling techniques on predicting the life of mechanical components and systems.

2.1 Introduction

The design of machines and their parts must achieve required levels of performance, and guarantee that they meet both safety and reliability requirements during the desired life time. In order to ensure the performance, safety and durability of a system at the same time, it is important to limit the deformation of certain sensitive components. Besides, the initiation and propagation of cracks are also taken into serious consideration in order to avoid catastrophic structural failures. The most fundamental criterion in mechanical engineering design corresponds to ensure that the maximum stress in a component does not exceed the strength of the used material. This corresponds to the stress level that leads to static or fatigue failure of materials depending on the particular application under investigation.

Most failures of material are attributed to excessive deformation. Therefore, the deformation of a certain part due to external loads is obtained by testing or simulations so that the performance and safety of components and the whole structure can be evaluated. Macroscopic deformations are commonly evaluated in terms of accumulative normal and shear strain in an elementary numerical analysis on materials.

Metals and their alloys are materials conventionally applied in practical engineering structures. The mechanical performance of such structures is intrinsically determined by their microstructure, including metallic bonding between atoms and crystal grains in polycrystalline materials. The unique characteristic of microstructure of metals and alloys enables them to be stiff and ductile, but more valuable to fracture and fatigue, compared to non-crystalline solids, such as polymers.

In the following sections, various plasticity mechanisms and relevant modelling techniques at different scales are then discussed in the context of work reported in this thesis. At the end of this chapter, mechanisms of fatigue, with particular interest in contact and fretting fatigue, and failure of crystalline materials are introduced. Finally this chapter summarizes the literature review on the mechanical behaviour of polycrystalline material undergoing plastic deformations and corresponding modelling methods.

2.2 Modelling Material Plastic Deformations Using Frameworks at different scales

Understanding deformation and stresses of materials when they are subjected to external loads is the key to capture their behaviour. In this section, the mechanisms and modelling techniques to study deformation and stresses in various regimes and length scales are reviewed. In particular, various plasticity models are reviewed. This section will also provide a brief summary of crystal plasticity finite element (CPFE) and discrete dislocation plasticity (DDP) techniques that serve for material modelling at two different scales. Their description is functional to the description of the coupling philosophy of our material modelling approach that will be discussed in Chapter 3, and its application for the prediction of material response under different scenarios discussed in Chapters 4-7.

2.2.1 Macroscale plasticity

Plasticity characterizes materials when they undergo excessive macroscopic deformation after yielding. Performance of materials is strongly determined by their plasticity flow, especially where there is evident stress concentration locally. Examples of processes in which stress concentrations are linked to local plastic flow will be addressed in indentation and sliding simulations performed in Chapters 4-7.

The macroscopic theory of plasticity is based on the experimental observations of ductile materials. Figure 2.1 shows a typical stress strain response curve of a ductile material in a uniaxial tension test. The theory assumes that the material is homogenous and isotropic and has the same yield stress in tension and compression. The influence of anisotropy will be discussed in the following section introducing crystal grain anisotropy.

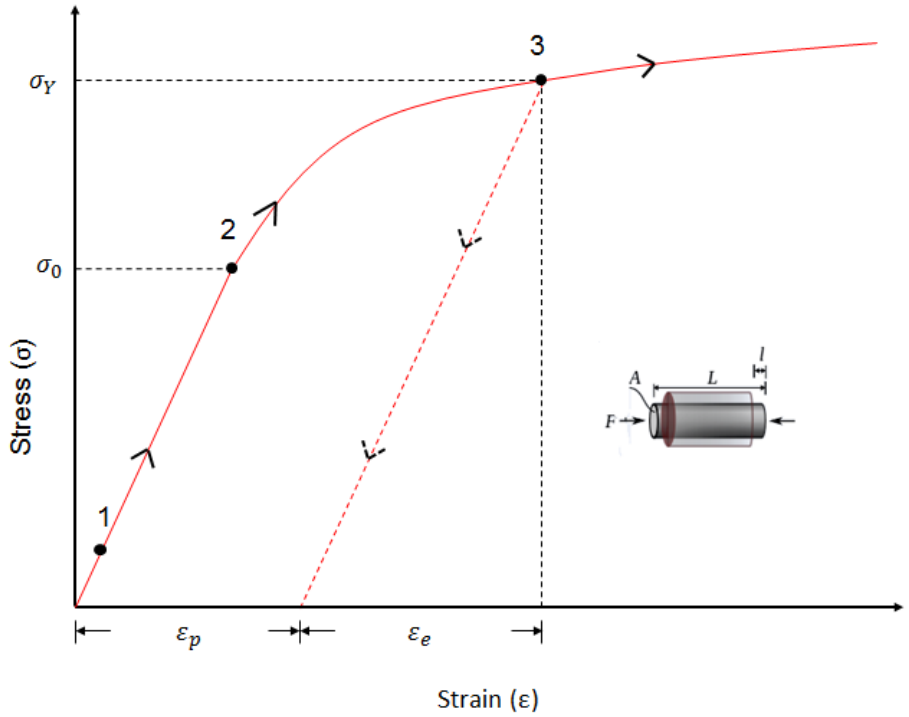


Figure 2.1. Stress-strain curve showing typical plastic behaviour of materials in uniaxial tension test

When the stress level exceeds the yield point of the material under investigation (σ_0 in Figure 2.1), the material behaviour enters the plastic realm. Plasticity describes ductile materials undergoing an irreversible deformation process, *i.e.* the material has a macroscopic permanent deformation (ε_p in Figure 2.1) after complete unloading.

In engineering design and analysis, the equation that describes the relationship between strain and stress (constitutive law) are often required. After the initial linear elastic response, the plasticity theory needs to cover the following aspects:

- The yield criteria: to define specific multi-axis stress levels that will initiate the plastic response, *i.e.*to define the initial yield surface
- The flow rule: to formulate the evolution of plastic stress as a function of the applied strain
- The hardening rule: to define the evolution of the yield surface

2.2.2 Strain gradient plasticity

Size effects are widely observed in experiments aimed at characterizing materials' behaviour, including the famous Hall-Petch effect [6], the indentation size effect [7-9] and the torsion of thin wires [10]. But the conventional plasticity or crystal plasticity without a length scale is not able to explain these size effects. Fleck and Hutchinson summarized the previous work on the higher order continuum elasticity [11, 12] and developed strain gradient plasticity (SGP) based on the dislocation principle that the plastic flow strength of a material is not only determined by strain itself but also affected by the strain gradient. From the mechanism of dislocation storage, the strain

and strain gradient are associated with statistically stored dislocations (SSD) and geometry necessary dislocations (GND).

The strain gradient plasticity framework proposed by Fleck and Hutchinson has been widely applied on various simulations aiming to explain length scale involvement, including the strength of polycrystalline materials [13] and composites [14], shear bonds [15] crack propagation [16], micro- and nano-indentation [17-19] and grain boundary effects in polycrystals [20].

Although the strain gradient plasticity is able to explain and predict some size effects in micro length scale, it cannot solve the size effect issue in problems where strain gradients are absent, for instance, the uniaxial tension problem size effect [1]. The drawback is attributed to the absence of dislocation activities in strain gradient plasticity frame work. The density of dislocations is indeed an important feature, but cannot fully capture the nature of dislocation activity in a crystalline material with itself only.

2.2.3 Crystal plasticity

Most crystalline metals and their alloys undergo plastic behaviour that is strongly dependent on their crystal structure. Hence, it is essential to investigate the influence of microstructure on material performance in experiments. Experimental results motivate researchers to develop crystal plasticity theory and models to explain and predict their performance. The numerical crystal plasticity model will be discussed in Chapter 3 and further applied in simulations under different types of loading in Chapters 4-7.

2.2.3.1 Crystalline anisotropy

Elastic and plastic deformations of crystalline aggregates depend strongly on the direction of loading with respect to the crystal structure, *i.e.* crystalline materials are mechanically anisotropic. The elastic anisotropy is due to the anisotropy of elastic tensor while plastic anisotropy depends on the detailed orientation of the crystallographic slip systems and deformation mechanisms. This implies that most of mechanical behaviours (shape change, crystallographic texture, strength, strain hardening, deformation-induced surface roughening and damage) are determined by the crystal orientation.

The uniaxial stress-strain curve, which is the most important mechanical measure in structural materials design, can be used to illustrate the anisotropy of crystalline material. When the material is subjected to a macroscopic strain, the stress responses along different directions are different. Thus, the partition of the new subsequent yield surface shifts irregularly. An example of the shift of yield surface of an anisotropy of crystalline material can be seen in Figure 2.2. Being strained by a macroscopic strain, the magnitude change of three components shows discrepancy due to the anisotropy of plastic hardening. Thus the new yield surface shape is strongly determined by the microstructure of materials

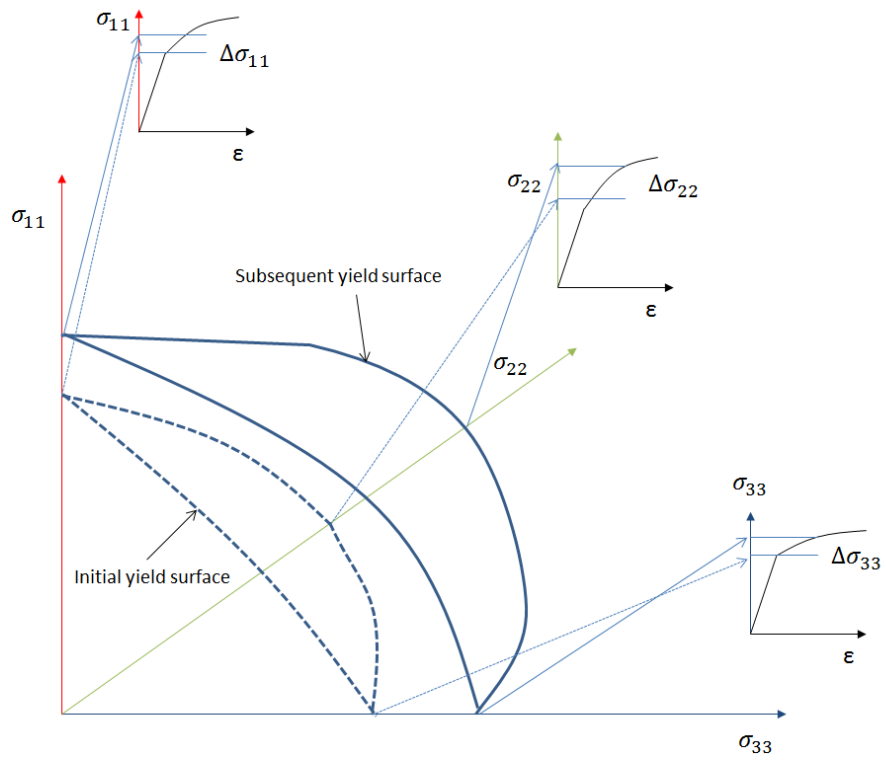


Figure 2.2. Flow stress and strain hardening of anisotropic crystalline materials

A consequence of this phenomenon implies that the crystallographic texture (grain orientation (GO) distribution) of a specimen in microscope inherently determines the plasticity mechanisms during its deformation process. Texture and its further evolution during deformation is hence able to applied to represent the anisotropy of a polycrystal by integrating individual behaviour of a single grain and their interactions at grain boundaries orientation-dependent boundary. As an external boundary condition, plastic shear results in changes both in shape (symmetric components of its stiffness matrix) and orientation (skew-symmetric components of its stiffness matrix). Therefore, this consideration leads researchers to develop computational approaches for simulating macroscopic plasticity of crystalline materials by incorporating both of the crystallographic and anisotropic characteristics and microstructure influence (i.e. grain orientation and distribution) under boundary conditions [21].

2.2.3.2 Early development

Early efforts, including works in [22-26] were tried to capture the anisotropy of crystalline materials during plastic deformation. However, those approaches neither explicitly considered the mutual interaction between grains in polycrystals nor managing to tackle with complicated external boundary conditions. In fact, those approaches dealt with interactions within polycrystalline structure by simplifying the strain or stress within the grain using the homogenised response. Therefore, they are not able to be fully applied to a practical crystal plasticity calculation.

This is until the advent of the finite element method [27, 28] and the development of *ad hoc* numerical algorithms [29] for crystal plasticity within this framework that

enabled more complex problems to be solved. That is, the birth of Crystal plasticity finite element (CPFE) method

2.2.3.3 Crystal plasticity finite element method

Crystal plasticity finite element (CPFE) is based on the on the variational solution of the equilibrium of the forces and the compatibility of the displacements using a weak form of the principle of virtual work in a given element while the investigated region is discretized into such elements. CPFE considers the velocity gradient in a dyadic form, and it indicates that the both shape changes (symmetric part) and lattice rotations skew-symmetric part) are taken into consideration.

Almost all CPFE methods are originated from the decomposing of total deformation gradient at a finite strain level. The decomposing of deformation gradient is sketched in Figure 2.3 [30] and mathematically expressed in eq.(2.1).

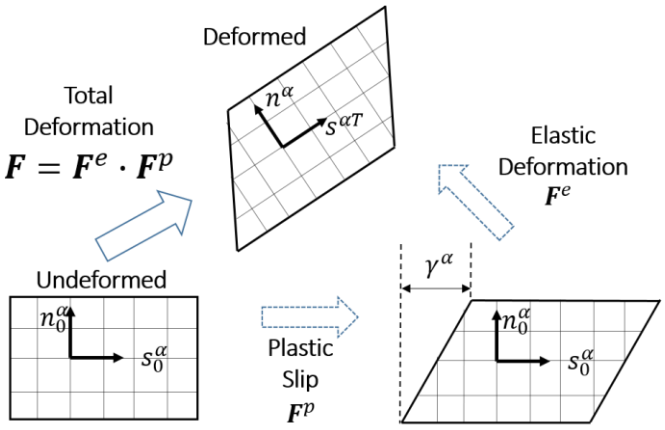


Figure 2.3. a schematic representation of the decomposition of total deformation gradient F. $m^\alpha$is the slip direction and n^α is the slip plane normal of slip system α.

$$\mathbf{F} = \mathbf{F}_\mathrm{e}\mathbf{F}_\mathrm{p} \tag{2.1}$$

In the equation above, $\boldsymbol{F}_e$ is the elastic part of the deformation gradient that describes both the elastic distortion and the rigid-body rotation. $\boldsymbol{F}_p$ is the plastic part of the total deformation that is due to crystallographic slip.

Furthermore, CPFE method decomposes the deformation kinematics of a crystal plasticity formulation where the velocity gradient is written in dyadic form. This essential step, expressed in eq. (2.2) reflects the tensorial crystallographic nature of the underlying defects that lead to shear and consequently, to both shape changes (symmetric part) and lattice rotations (skew-symmetric part).

$$\tilde{\mathbf{L}}_\mathrm{p} = \sum_{\alpha=1}^{\mathrm{N}} \dot{\gamma}^\alpha \mathbf{m}^\alpha \otimes \mathbf{n}^\alpha \tag{2.2}$$

Where the magnitude of the shear rates $\dot{\gamma}^\alpha$ is determined by the constitutive models applied in different CPFE models.

By introducing the decomposing of velocity gradient, some extensive knowledge of single crystal behaviour and experimental results (*e.g.* dislocation density) can be incorporated to CPFE method. Besides, this general variational CPFE work is capable of flexibly incorporating up-to-date understanding of physical-based deformation process, *e.g.* the work of Curtin[31], Arenlis[32], Cetinkaya[33] and Vitek[34].

The most significant feature of crystal plasticity finite element approaches is believed as their ability to solve mechanical problems in crystal length scale under complicated internal and/or external boundary conditions. This feature enables researchers to study the inter- and intra-grain micromechanical interactions observed in experiments [35]. It is also beneficial to investigate the abrupt mechanical transitions at interfaces [36].

2.2.3.4 CPFE application and development

The very first CPFE simulation carried out by Peirce, Asaro and Needleman was dated back to 1982 [37]. By increasing the number of slip systems up to 12 in a FCC crystal, Becker led a series of more practical CPFE calculations on both a single crystal [38] and polycrystal [39] of aluminium in 1991.

Since then, much efforts have recently been placed on the development of crystal plasticity models and constitutive laws, e.g. [40-42], particularly for FCC metals. With the rapid development of computational capacity and efficiency, both two dimensional and three dimensional approaches of CPFE were developed based on phenomenological constitutive equations, including the work of Pierce, Asaro, Becker, Zhao, etc. in [43-47]. The microstructure textures were provided either by explicitly grain information [48, 49] or by a grain orientation distribution function (ODF) [50-52].

Most of these approaches considered dislocation slip as the only deformation mechanism that indicates those CPFE techniques based on phenomenological constitutive equations are insufficient to deal with small-scale deformation or new types of materials that with apparent twinning related plasticity, *e.g.* TWIP (twinning-induced plasticity) and TRIP (transformation-induced plasticity) steels. The twinning and transformation-induced plasticity were also solved by an extended CPFE method [53, 54].The most recent CPFE constitutive models also enable grain boundary mechanics [55, 56] or damage initiation [57] to be incorporated.

The microstructural deformation and its evolution of investigated materials are strongly dependent on the constitutive model used in CPFE formulations. There are generally two types of constitutive models that are most commonly used in current CPFE applications, namely phenomenological models and physics-based models.

Phenomenological constitutive models simplifies the plasticity onset as that a critical resolved shear stress needs to be achieved at a slip system. Rate-independent phenomenological constitutive formulations were adopted in Dini and co-workers' work [58-62] that is based on the Hill and Rice's formulations [63]. These works employ a constitutive hardening law that empirically captures the micromechanical

interaction among different slip systems. Different forms of hardening laws were developed, e.g. in Becker's work [38, 64] and Kocks' work [65, 66]. However, these works are limited due to their critical drawback that the crystallographic deformation is only determined by the critical resolved shear stress without addressing the details of defects, *e.g.* dislocations and grain boundary, of crystal materials.

Physics-based constitutive models, in contrast, explicitly describe the microstructural deformation by terms of internal defects. As dislocation density is considered as the most significant microstructural state variable, many works, e.g. [32, 56, 67-70] have introduced it to calculate the stress status. When the size scale decreases to a smaller value than grain size, some well-known size effects in nano-indentation [71-74], micro-pillar compression [75], micro-bending[76], etc. are experimentally observed. In order to explain and further understand the localized plasticity, meso-scale size length scales have been integrated into CPFE frame work by using phenomenological strain gradient plasticity (SGP) [10, 18, 77]. As strain gradient plasticity argues that the strain gradient highly localizes deformation within materials due to the existence of geometry necessary dislocations (GNDs), recent physics-based models, e.g. Dunne and co-workers' work [78-81] have integrated the density of GNDs based on the model proposed by Nye[82].

Damage initiation and evolution is involved in CPFE models to evaluate the microstructural fatigue of materials. Plastic stain and strain energy are commonly state variables for damage. Dunne and co-workers' work [80] employs accumulative plastic strain of a CPFE analysis on Ni and Ti alloys in low-cycle fatigue studies. Fatigue fretting simulations have been conducted using CPFE models [83-86]. These simulations aim to predict locations of the fatigue micro-crack initiation. Results are well consistent with experimental observation reported in [80].

In general, CPFE formulations are able to resolve the detailed deformation, including slip and rotation, of materials at grain size level. Numerical results solved using CPFE method can be further improved by introducing length and/or time scale parameters, as shown in the work presented in Ref. [81]. CPFE simulations can be applied to a plethora of relevant engineering problems, including tension [87], indentation and cyclic loading [58], creep [88, 89], recrystallization [90] ,etc.

2.2.4 Discrete dislocation plasticity

The observation of dislocation presence and activity in crystalline metals are dated back to 1930's, and the theory of dislocations have been adopted to explain and predict material performance, especially the plasticity, since then. The following sections will review the development of discrete dislocation plasticity and current applications. Our discrete dislocation plasticity model will be illustrated in Chapter 3, and further applied in simulations under different types of loading in Chapter 4-7.

2.2.4.1 Early observations of dislocations

In 1934, several scientists, almost simultaneously, attributed the plastic deformation to the existence and motion of dislocations. Dislocations are crystalline defects around where some atoms are misaligned with respect to the perfect crystalline lattice. There are two types of dislocations, catalogued by the different directions, edge and screw dislocations. If the local stress is adequate to overcome the lattice resistance to the movement of the dislocations, they will glide at a specified velocity on a certain slip plane, shown in Figure 2.4.

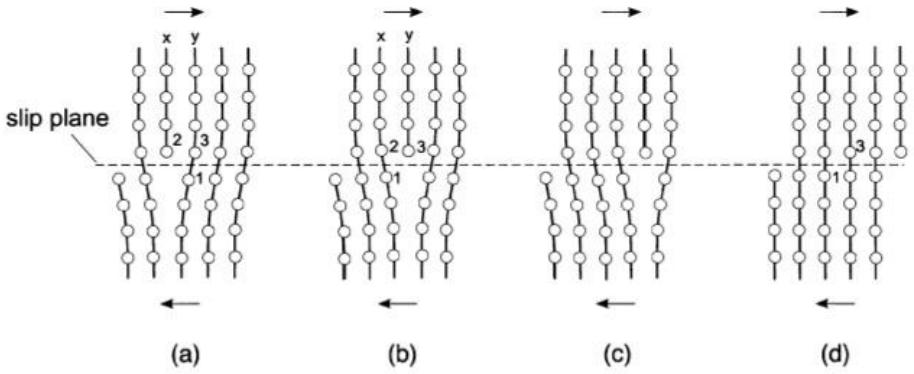


Figure 2.4. dislocation motion on a slip plane, taken from [91]

The plastic flow is considered as the collective motion of large amount of dislocations in materials. The motion of dislocations results in the permanent change of material shape, i.e. the above mentioned non-reversible deformation. In addition, the interaction between dislocations with each other as well as the interactions between dislocations and obstacles pins the motion of dislocations, which causes the pile-up of dislocations and thus an increase of stress required to produce plastic deformation, i.e. the strain hardening

2.2.4.2 Algorithm development

Although the concept that the performance of ductile metals at a micro- or sub-micron scale is determined by the discreteness of dislocations has been established for a long time, the concrete attempts to develop a practical discrete dislocation plasticity algorithm are implemented only recent years.

The early efforts for developing discrete dislocation plasticity models by Brown [92], Bacon [93] and Foreman [94] were dated back to mid-1960s. These authors studied the deformation of an edge dislocation under an applied stress. The numerical computational tool for studying collective motion of dislocations was firstly developed by Amadeo and Ghoniem [95] and Canova and Kubin [96].

With the advances in computational power and the optimization of the dislocation theory, the computational method of dislocation dynamics is capable of capturing the details of dislocation activity in a reasonable simulation time. While early-stage scaling arguments on the dislocation appeared in multi-scale modelling [97] several decades ago, a classical two dimensional framework for solving the boundary value problem

where the plastic flow is attributed to the collective motion of discrete dislocations has been developed by Lubarda et al. [98], and van der Giessen and Needleman [99].

For three dimensional discrete dislocation plasticity framework, the first numerical simulations was developed by Kubin [96]. There are generally two approaches modelling the three-dimensional dislocation dynamics, categorized by the method on line discretization and representation of a curved dislocation segment [100]. The first approach discretizes dislocation lines into edge-screw [96] or edge-mixed-screw [101, 102]. The second approach considers dislocation lines as smooth flexible curves, such as splines [103-105] and circular arcs [106, 107]. All major works were developed in isotropic continuum solid. However, the elastic anisotropy was studied by Rhee[108] and it has been included into the code "MICRO3D".

2.2.4.3 Applications review

The discrete dislocation plasticity algorithms aforementioned need to be extended to solve a boundary value problem. Most of the solutions presented in the literature are conducted using the superposition method proposed by Van der Giessen and Needleman[99].

This framework was applied to solve a variety of problems, including the uni-directional tension problem on single crystal and polycrystalline specimen [1], the plastic zone size of uniaxial compression and tension problem, the analysis of bending plasticity [109], the investigation of the relationship between the strength and the grain size of polycrystalline materials [110] and a series of indentation problems [2, 111].

The indentation size effect has been studied in detail using discrete dislocation plasticity methods. Some literatures [111-113] reported a size effect in nano-indentation by a sinusoidal-and wedge-shaped indenter on crystals with a low density of sources. Furthermore, the source density effect was investigated in [2, 114]. Different definitions of contact area have been found to strongly influence the corresponding hardness values due to the asperity induced by the exiting dislocations [115]. The effect of indenter shape was simulated in the work presented in Refs. [115, 116]. The hardness curve was found to strongly depend on the penetration depth by wedge-shaped indenter, while the typical size effect was not apparently discovered in the simulations of cylindrical indenter but the hardness variation was associated with the indenter radius instead. Those findings have been further validated by experimental data [117]. The number and the orientation of pre-defined slip planes were studied in [118]. The damage induced by the indentation process was computed using discrete dislocation plasticity, and the plastic flow may occur before the theoretical strength has been achieved [119].

In general, the DDP method is able to resolve the highly localized stress and strain field within the investigated specimens. Compared to strain gradient plasticity, one of the major advantages of DDP lies in its ability to capture the size effect of materials when the strain gradient is absent, for instance, in a uniaxial tension simulations [1].

Dislocation dynamics simulations can also be used to solve a variety of engineering applications, including micro-bending[120], nano-indentation[2] and nano-sliding[4], etc.

2.2.5 Multi-scale plasticity and its modelling

In this section, a review of the state-on-art of multi-scale modelling is summarized, which follows a brief introduction of its significance. Focus is placed on the existing coupling methods of scales between crystal plasticity and discrete dislocation plasticity, which have motivated me to develop a new coupling approach. Our coupling philosophy will be illustrated and discussed in Chapter 3, and its further application in different types of problems will be shown in Chapters 4, 6 and 7. It is again worth noticing that "multi-scale modelling" in this thesis refers to the resolution at which materials features are captured at different scales, rather than specimen dimensions.

There are a number of problems in mechanics of materials where the physical phenomenon occurring and developing at different length and/or time scale is attributed to understanding the detailed material behaviour in different scales. One of the typical examples is the deformation and failure of ductile polycrystalline materials. In that particular problem, the interaction mechanisms involving crystal point (vacancies and impurities), lines (dislocations), plane (grain boundaries, interface and cracks) and volume (precipitates and twins) determines the strength and deformability of ductile polycrystalline materials. Particularly, the role of dislocations' nucleation, motion, pinning, interaction and annihilation on the plastic onset and hardening history has been assured via both experimental and theoretical investigations. As a consequence, it is necessary to develop a predictive tool to model material performance covering atomic length (Angstrom) and time scales (pico-seconds) to crystal length scales (microns) and component service time scales (seconds). Figure 2.5 illustrates the material modelling methods with length scales ranging from automatic scale to macroscale.

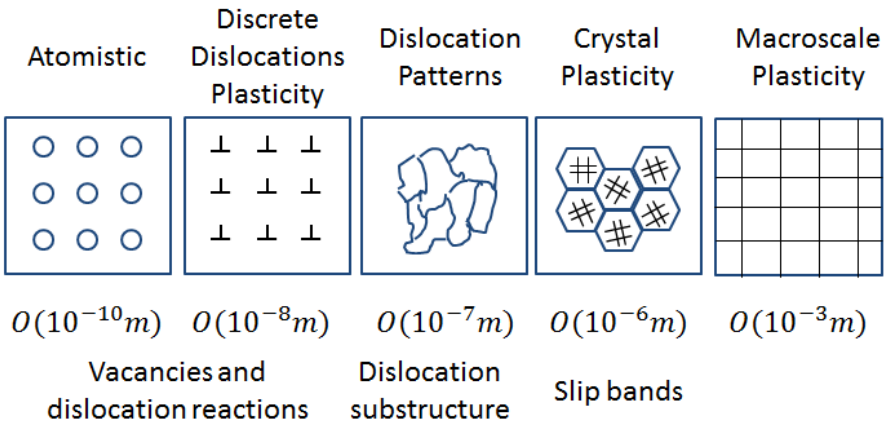


Figure 2.5. the hierarchy of length scales in structure material plasticity ranging from atoms to macroscale. The corresponding modelling methods are also reported for each scale.

Multi-scale modelling generally employs either unidirectional (sub-modelling / hierarchical modelling) or bidirectional (concurrent modelling) modelling strategies, categorized by the methodology used for information passing between scales. The former method uni-directionally passes information from a lower scale to a larger scale. For instance, a hierarchical modelling between atomistic and continuum scales obtains elastic constants, thermal expansion coefficients and other properties of defect-free crystals from atomistic models and then provides continuum scale models with these properties as constitutive material parameters [121]. Continuum models of fracture mechanics relevant to crack initiation and propagation are benefited of receiving information on material separation, which is provided by calculations [122, 123] on atomistic and quantum scale. For multi-scale modelling between dislocation (*i.e.* meso-) and lower scales, information on Burgers' vector, Peierls stress, strength of Frank-Read dislocation sources and dislocation mobility are taken from atomistic studies on isolated defects to discrete dislocation analysis as input [99, 124-126]. In general, hierarchical modelling techniques benefits from simplicity of implementation and computational efficacy as the finer scale model does not enquiry any feedback information from the coarser one.

However, a hierarchical modelling approach is limited in application as the finer scale model is only treated as a "parameters provider" and highly localized on particular zones. For instance, the hierarchical coupling from atomistic to dislocation scale focuses on a simple defect geometry only so that certain complex meso-scale phenomenon cannot possibly captured [31]. Therefore, another coupling approach that mutually conveys material and field information between disparate models in a single analysis has been proposed and developed.

There is now a wide range of concurrent coupling methods that have been established over recent decades, for example coupling electronic structure to atomistic modelling ([127]), atomistic to discrete dislocation dynamics [128], atomistic to continuum [129], etc. A natural coupling for capturing localised size effect behaviour large polycrystal boundary value problems is concurrent coupling of discrete dislocation plasticity (DDP) to the crystal plasticity finite element (CPFE) method, a continuum method that accounts for crystal structure and homogenises the effect of crystallographic slip. In this thesis, the multi-scale concurrent coupling between scales of dislocations (i.e. meso-) and crystal plasticity (macro-) will be focused in particular.

A two-dimensional method for concurrent coupling of DDP to CPFE in a single crystal was developed in [130]. The coupling boundary between the DDP and CPFE regions was treated as transparent to dislocations, and the compatibility of tractions and displacement was ensured in an average sense. Tension and mode I crack growth problems were analysed; in the latter, computation time was reduced by up to a factor of 14 with only a minor reduction in accuracy. 3D DD was coupled to strain gradient crystal plasticity via the solution of separate models with bi-directional information passing in [131]. The so-called Multi-scale Dislocation Dynamics Plasticity (MDDP) approach was also used in [132] to investigate micro-pillar compression, and in [133]

to study spherical nano-indentation. Micro-pillar compression was also investigated in [134] using a hybrid DD/FEM coupling method.

We have developed a new coupling strategy whose philosophy will be generally illustrated and discussed in Chapter 3, and its further application in different types of engineering problems will be shown in Chapter 4, 6 and 7.

2.3 Mechanical Behaviour of Materials under Different Working Conditions

The detailed behaviour of crystalline materials needs to be investigated by performing typical engineering tests on corresponding specimens. In the following sections, several engineering tests and their simulations are introduced. Furthermore, an overview of the modelling methods and of the results of tests performed at different scales is provided.

2.3.1 Uni-axial Tension

Tension tests, in which specimens are subjected to controlled tensile loading condition, have been extensively used in material science and technology. Uniaxial tension tests are routinely employed to obtain fundamental material properties, including Young's modulus, Poisson's ratio, yield stress/strength, hardening parameters. The results of a uniaxial tension test commonly provide necessary material information for material selection in mechanical design and risk assessment of parts under different types of loading.

Given the use of uniaxial tension tests as a standard for the determination of macroscopic material properties, the elasto-plastic response of materials under uniaxial tension has been extensively studied. Simulations in which the microstructure of specimens is, more or less explicitly, considered have been conducted. In particular, a large amount of investigations (see *e.g.* [135-138]) have been carried out using crystal plasticity finite element (CPFE) to study the role of grains and grain structure in determining the specimen performance. At an even smaller scale, discrete dislocation plasticity (DDP) has also been adopted to explicitly describe the activity of dislocations including nucleation, moving, pinning and annihilation, etc, in the elongated specimen. Thus, DDP simulations [1, 110, 139] were carried out to study the size effect and grain boundary effect in tension test. Thanks to its simplicity and the widespread use of the uniaxial tension problem for simulations benchmarks, it has been chosen as an effective validation tool for the new modelling method. A multi-scale model of the uniaxial tension specimen was developed in [130] to illustrate the validity of the coupling approach. However, that approach only allows the field information passing from discrete region to continuum region. A natural method for capturing localised size effect behaviour in large polycrystal boundary value problems is concurrent coupling of discrete dislocation plasticity (DDP) to the crystal plasticity finite element (CPFE) method, a continuum method that accounts for the crystal structure and homogenies the effect of crystallographic slip. Thus, a concurrent multi-

scale coupling approach is required to apply on the uniaxial tension problem. The application of the newly proposed coupling method between DDP and CPFE will be applied in the uni-axial tension problem in Chapter 4.

2.3.2 Indentation

Small-scale indentation is being increasingly used to measure yield stress and Young's modulus for films and small volumes of material. Researchers have been investigating the microstructure effect on the indentation response of materials using crystal plasticity method. Meso-scale simulations [72, 73, 75, 76, 140, 141] were conducted using crystal plasticity formulations in order to reproduce the instrumented indentation applied load versus penetration depth curves discovered in experiments [142, 143]. In the meanwhile, local crystalline rotations underneath spherical and sharp indenter tips were captured in simulations [73] and [140, 144] respectively, by employing the anisotropy in crystal plasticity method.

However, it has been established experimentally that continuum relationships for hardness applicable to large scale conical (or pyramidal) and spherical indentation [145, 146] fail when indentation depths are sufficiently small (nano/micro); the observation is that sufficiently smaller indentation depths correspond to larger indentation pressures [7, 8, 117, 147, 148]. Furthermore, the effect of the substrate material on the response becomes important at larger indentation depths, which can be characterized by empirical relationships [149, 150]. At present no empirical relationship exists that is effective over the full range of indentation depths encountered in typical experiments.

Among the early models of the indentation size effect, the authors of Ref. [18] developed an analytical formula that predicted size-dependent hardness based on geometrically necessary dislocations and strain gradient theory. Some further work based on strain gradients was conducted in [17, 151-153], in order to study the relationship between the indentation size effect and the material length scale parameters. Using a different approach, Guo et al. [154] developed the Taylor-based nonlocal theory (TNT) of plasticity based on general non-local plasticity theory [155].

However, continuum methods require fitting a length scale parameter to experimental data, *e.g.* the formula developed by Nix and Gao works well but only captures the experimental behaviour [156] after suitably fitting a length scale parameter in the model to the data. On the other hand, the length scales in discrete dislocation plasticity, which captures dislocation mediated size effects naturally, are measurable and have clear origins in the microstructure. The indentation size effect has been studied in detail using discrete dislocation plasticity methods. The work reported in references [111-113] primarily focused on size effects in nano-indentation by sinusoidal and wedge-shaped indenters on crystals characterised by a low density of sources. The work was devoted to the investigation of the effect of microstructure, including nucleation source density, and number and the orientation of pre-defined slip planes, on the indentation pressure [2, 114, 118]. Furthermore, the effect of

indenter shape on the indentation pressure was studied using numerical simulations [115, 116], which have also been successfully corroborated by experimental data [117]. The damage due to dislocation activity in indentation processes was simulated in [119], which aimed to provide the link between the dislocation structure and the macroscopic fatigue phenomenon. Recently, Nicola and co-workers [157-160] conducted discrete dislocation plasticity simulations of the flattening of surface roughness obtained by nano-imprinting thin single crystal films. In all the aforementioned studies, the dislocation activity is studied in simplified configurations, namely where the film is adhering to a rigid substrate, and these studies cannot be easily extended to scenarios in which the crystal films are adhering to or resting on polycrystalline substrates characterised by similar elastic/plastic response. This issue will be tackled in Chapter 6 using the newly developed CPFE/DDP coupling technique.

Saha and Nix have performed a large number of nano-indentation experiments and simulations [149, 161-164] since 2001, focusing on the substrate effect on the coating system. In their experiments, various films were deposited on different substrates and then indented using a diamond tip. Based on those experimental data, they developed a numerical model with mechanism-based strain plasticity (MSG) to deduct the intrinsic hardness and elastic modulus of the composite material. The model managed to explain the hardness transition when the ratio between the indentation depth and the film thickness increased to a certain value. However, the model was not able to predict the hardness decreasing with increasing indentation depth/thickness ratio when the indentation depth was small, i.e. the indentation size effect, due to the absence of explicit dislocation description.

Discrete dislocation dynamics is able to bridge the gap between the micro- or nano-indentation and the size-independent scales. Although the results extracted from a three-dimensional simulation [165] were well consistent with the experimental data, the indentation penetration depth was confined up to $50\ \mu m$ due to the complexity of three-dimensional modeling of dislocations. A recent multi-asperity contact simulation by the discrete dislocation plasticity provided a pioneering trial that simulates the similar practical engineering contact process [166]. Although the perfect periodical modelling of the indenters is not able to provide an actual description of the surface roughness, more efforts including modifying the space between the indenters and the specimen and randomizing the shape of the indenters can be done to closer simulate engineering problems. The application of the newly proposed coupling method between DDP and CPFE will be applied in the indentation problem in Chapter 5 and 6.

2.3.3 Sliding

The resistance of two mating surfaces to sliding is a characteristic of the frictional response of the materials in contact. The presence of roughness due to asperities of practical engineering surfaces causes that actual contact area usually occupies only a small fraction of nominal contact area. A physical model proposed by Bowden and

Tabor [167] described the behaviour of frictional sliding on an unlubricated (dry contact) solid surface. Bowden and Tabor [167] catalogued sliding resistance into two types: the "adhesion" effect acting on contact interface between asperities and the "ploughing" effect representing the micro plastic deformation of contact surface.

The classical Amontons–Coulomb description of friction states that shear forces along an interface is proportional to the normal force, with a proportionality constant being the coefficient of friction μ. In a more general context it is the evolution of a sliding force and its dependence on the normal force that characterizes frictional sliding. In their classical work Bowden and Tabor [5] wrote frictional force as:

$$F_f = \tau_f A_t \tag{2.3}$$

where τ_f is contact shear stress and A_t is true area of contact. The main contribution to normal force dependence arises from its effect on the true area of contact, both through the number of asperities in contact and the evolution of asperity shapes, although there can also be an effect of normal force for a single asperity.

Frictional sliding is a complicated process, generally involving large deformation of asperities having a wide range of size scales. The asperity contact, including normal and tangential behaviour, has been investigated using classical plasticity theory and single asperity interacting theory (see *e.g.* [168-174]). However, the lack of a characteristic length scale prevents models based on conventional plasticity from capturing the size effect often observed in tangential behaviour [4], especially when the asperity and contact size approaches the dislocation spacing. Experiments have also shown that friction is both time-and slip distance-dependent (*e.g.* Dieterich [175], Ruina [176], Prakash and Clifton [177], Gearing et al [178]). Pioneering work was reported in 1981 by Kuhlamnn Wilsdorf [179], showing that the specimen plastic response would be size dependent if the single asperity size is of the same order of magnitude as the dislocation spacing. The large plastic strain and strain gradients caused by the stress concentration experienced by the material during a sliding process inherently drive the highly localization of dislocation activity and the generation of complicated dislocation patterns [180, 181]. Therefore, the discrete dislocation plasticity has been adopted to investigate the complexity of micro-sliding processes. Discrete dislocation plasticity was first used to study the micron-sliding size effect when the contact size is too small to apply conventional plasticity by Polonsky and Keer [182, 183]. Their work mainly showed that the asperity is able to undertake significantly higher stress than that predicted by continuum plasticity when its size reduces to the scale of dislocation spacing. Those calculations still under-estimate the frictional forces that were observed in experiments, although the enhanced ploughing force term had been taken into consideration. This deduction indicates that the adhesion force term contributes more to the total friction forces.

Computational techniques involved with characteristic length scale have been extensively employed to quantitatively analyse the dependence of the frictional force

on the contact size. Bhushan and Nosonovsky [184] adopted a strain gradient plasticity (SGP) model and demonstrated that there are three zones of frictional stress τ_f dependence on the contact area. For small contact areas, frictional stresses τ_f are found to be identical to the shear strength of the specimen while for sufficient large contact areas, limiting shear stresses are determined by the Peierls stress (that introduces a driving force for a dipole of dislocations to move). Between the two zones, frictional stresses are governed by the contact size, and this was linked to the plastic flow extending along the interface. Hurtado and Kim [185, 186] conducted a discrete dislocation plasticity analysis on the micro-sliding problem with the assumption that dislocation are only nucleated along the contact surface, and a similar three-regime variation of the shear stress based on the contact size was obtained. For the transition regime, a model that was developed by Rice and Thomson [187] predicted that $\tau_f \propto a$ for a given contact radius a. Deshpande et al. [4] applied different cohesive shear traction formulas along the contact area to study the effect of different constitutive laws describing interfacial strength; results show that both softening and non-softening cohesive constitutive equations generate similar trends in terms of frictional forces. The normal load has strong influence on the frictional forces when the contact size is sufficiently large, while frictional forces are not strongly affected when the contact size is small. Based on the non-softening cohesive constitutive equation, Balint et al. [3] investigated the asperity shape effect and film thickness effect on the frictional stress. Indentation performed before the application of shear forces is reported to have negligible effect on the friction stress and thus the friction coefficient, although the stress field and dislocation structure show completely different patterns. Molecular dynamics have also been adopted by Landman [188] and Gerde and Marde [189] to shed light on frictional interactions covering even lower length and time scales. The sliding problem will be simulated using methods at different scales in Chapter 7.

2.3.4 Fretting

Besides the failure due to excessive deformation caused by the application of excessive load during individual events, the repeatedly weakening of engineering materials during a cyclic loading condition, *i.e.* fatigue damage, has become a significant failure factor [190]. Plain damage of materials are due to irrecoverable deformation, and the accumulation of damage further weakens the material performance during a cyclic loading process. In particular, fatigue applied in a contact problem leads to contact or fretting fatigue that are believed to be some of the major reasons for micro-crack initiation and thus failure of specimens subjected to contact loading. This section will briefly address the experimental and numerical approaches developed to study both plain and fretting fatigue.

In Chapter 7 of this thesis, mechanisms on micro-crack initiation under fretting loading are investigated at crystal plasticity and discrete dislocation plasticity scales, respectively. Furthermore, a new micro-crack initiation criterion has been proposed based on discrete dislocation analysis.

2.3.4.1 Plain fatigue and damage

Machine components are frequently subjected to cyclic applied loading, especially for crank arms, shafts and bears. The resulting cyclic stresses can lead to localized and progressive damage to materials even though the nominal stress level is far lower from the material ultimate strength. This type of microscopic damage accumulates during the continued loading cycles, and leads to microscopic cracks that would result in the final macroscopic failure of the component. Mechanical failures of components due to fatigue have been an important standard of engineering design and analysis for more than one century. For the time being, scientists and engineers are able to computational tools to predict the reliable working life for components to avoid the abrupt fracture due to fatigue.

Presently, there are three major approaches to analysing and predicting the fatigue status of materials, catalogued by the variables involved. The conventional stress-based approach was developed from direct transformation of ultimate or yield stress of materials, and nominal (global) stresses in the affected sensitive zone were analysed. The second approach, namely strain-based approach, considers the localized plastic deformation and stress levels. The third approach focusing on the crack growth period and using extensive knowledge of fracture mechanics is called as fracture mechanics approach.

Fatigue mechanism is directly linked to localized and microscopic plasticity in sensitive regions of components during cyclic straining [191]. Thus it is necessary to investigate the effect of microstructure of materials in terms of micro-crack initiation and propagation. For instance, some literature pointed that the crack initiation were related to persistent slip bands by the intrusion–extrusion mechanism [192, 193].

2.3.4.2 Fretting fatigue

Besides plain fatigue phenomena, a particular type of damage encountered in engineering materials is fretting fatigue, that is caused by a cyclic contact loading and is an important process for micro-crack initiation and propagation[194, 195], and thus may be responsible for the weakening of materials.

The term fretting herein refers to wear damage of contact surface due to relatively cyclic sliding with micro scale magnitude, although the amplitude of the relative sliding can be as low as 3 to 4 nanometres. Fretting was believed to be associated with reducing the life of components [196, 197] in the early stage of last century, and so that the term ‘fretting fatigue’ becomes common when micro-slip between contact surfaces decreases components life [194].Since the sliding volume is at the same length scale as microstructural feature, the role of microstructure is quite significant for the analysis and prediction of fretting fatigue. Therefore, efforts have been made on both of experiments and computations in order to understand the microstructure influence on fretting fatigue.

Micro-sliding and its subsequent cyclic process, fretting, are considered as a major contribution to micro-crack initiation and propagation originating from surface or/and

subsurface [198, 199]. Being distinguished from a plain fatigue problem, which has been extensively studied using both crystal plasticity [58, 81, 200] and dislocation dynamics [201, 202], fretting fatigue is characterised by its highly localized stress/strain concentration, and thus the microstructure and length scale sensitivity.

There have been many experiments and simulations investigating fretting fatigue crack propagation problems; some of the most recent studies used crystal plasticity [203, 204] with the hope of shedding some light on the role played by the microstructure. After the pioneering study of the general mechanism of fretting fatigue by D.A. Hills, D. Nowell and other researchers in the 1990s, *e.g.* [199, 205-212], more focus has been placed on the mechanisms that govern fretting fatigue at the micro-scale, e.g. Dini and Hill's work[194, 213, 214]. Goh et.al [215-218] investigated the plastic deformation (especially plastic ratcheting) along the contact surface and in the bulk of the material using crystal plasticity, with particular application to Ti–6Al–4V alloys. The simulations revealed the influence of grain size and orientation on the cyclic and ratcheting plastic deformation, which cannot be predicted using standard continuum (*e.g.* J_2) plasticity. Zhang et.at [200, 204, 219] studied effects of the crystallographic texture, grain size, and grain size distribution on the fretting fatigue resistance of alpha phase Ti–6Al–4V alloys.

Discrete dislocation dynamics have been recently used to investigate the crack propagation problem. Deshpande et al. [220] first introduced discrete dislocation dynamics to predicting the near crack stress field and crack propagation. After this pioneering work, many researchers worked on the stress field near the crack tip (*e.g.* [221, 222]), crack-dislocations interactions (*e.g.* [223]), the material resistance to the crack growth (*e.g.* [224]) and the orientation and trajectories of growing cracks (*e.g.* [225]).

However, very few simulations have been carried out with the aim to predict fatigue crack initiation, especially at the scale of discrete dislocation dynamics. Most of damage initiation and damage evolution criterions in crystal plasticity are based on empirical stress/strain-based parameters. Discrete dislocation dynamics is technically able to provide more physically-based information on crack nucleation. In fact, the pattern of dislocations near a contact edge reported in [3, 4] has shown that there might exist an intrinsic relationship between dislocation structure and fretting fatigue crack nucleation.

Results from fretting fatigue experiments show some unique features compared to plain fatigue. Firstly, the localization of stress concentration and strain gradients are commonly found near the end point of sliding stroke. This indicates that those locations are likely to generate micro cracks. Secondly, the response of materials being fretted exhibit a highly non-linear performance even though the external applied load is proportional. Finally, cracks that have been nucleated would be subjected to a variable stress R-ratio (*i.e.* the ratio of minimum stress to maximum stress in one cycle of loading in a fatigue test) when they propagate far away from the contact.

Simulations on fretting fatigue need to represent and explain these features based on detailed microstructure. A large amount of simulations have been carried out on the Ti–6Al–4V alloy using two-dimensional crystal plasticity finite element model; they showed the impact of microstructure on the fretting process [216, 218]. The anisotropy of yielding among grains results in the highly intensive shear stress concentration and strain gradient, and the accumulated plastic strain accumulation is mainly attributed to plastic ratcheting [219]. The applications of three-dimensional crystal plasticity models are able to fully represent the actual microstructures [200, 226] (including three-dimensional grain orientations and realistic texture).

However, the critical problem that emerges during a fretting process, *i.e.* micro-crack initiation, has not been fully understood and simulated [227, 228]. Due to the absence of a length scale, conventional plasticity models are not able to capture the initiation of a micro-crack. Moreover, the length scale of crystal plasticity models is also larger than a micro-crack. In principle, discrete dislocation plasticity framework should be capable of capturing this crack initiation feature as its characteristic length, Burger's vector, is close to a micro-crack [229, 230]. Therefore, a discrete dislocation plasticity approach is developed in Chapter 7 to investigate the micro-crack initiation in planar fretting problems. Furthermore, efforts are also made to link dislocation pattern and density at dislocation scale to macroscopic damage parameters in CPFE approach in order to quantitatively predict the number of cycles required to initiate a crack.

2.4 Summary

In this chapter, the major mechanisms and corresponding modelling techniques of engineering material behaviours are reviewed for different deformation regimes and various scales. At the beginning, the crystalline material and its interior defects are briefly introduced. Following the characteristics of crystalline defects, the deformation and modelling methods of crystalline materials are addressed in details. In particular, focus is placed on the mechanism and applications of crystal plasticity finite element (CPFE) and discrete dislocation plasticity (DDP). These sections serve as a general introduction to the formulations employed in this project, which will be described and discussed in Chapter 3. The significance of multi-scale modelling has then been discussed to provide example of state-of-the-art strategies currently available and provide background information for the coupling strategy that will be introduced in Chapter 3 and whose application to relevant problems will be illustrated in Chapters 4, 6 and 7. At the end of this chapter, experiments and mechanisms for damage and fatigue of materials due to the accumulation deformation during cyclic loading are reviewed for both plain and contact fatigue, with particular emphasis placed on fretting. This is linked to the simulations and development of micro-crack initiation in fretting that will be addressed in Chapter 7.

Overall, this chapter provides an overview of mechanisms and current modelling approaches employed at different scales for the simulation of materials when they

undergo plastic deformation and damage, which will be the focus of the investigations presented in the thesis.

3 A General Approach to Study Plasticity by Coupling Crystal Plasticity Finite Element and Discrete Dislocation Plasticity

At the beginning of this chapter, the significance of developing and applying a multi-scale material modelling technique is addressed. After describing the details of the implementation of the crystal plasticity finite element (CPFE) and the discrete dislocation plasticity (DDP) codes used in this thesis, the proposed coupling philosophy is illustrated which aims to improve the current coupling models mentioned in Chapter 2. Details of the general strategy developed by the author are provided together with the physical interpretation of this newly proposed approach. Further applications of the newly propose coupling approach in various boundary problem are discussed in Chapter 4, 6 and 7.

3.1 Introduction

Most well-known material size effects require discrete resolution of defects in crystal lattice to be captured by modelling methods. For example, grain size (Hall-Petch) and specimen size (micro-pillar and micro-film) strengthening cannot be captured by conventional crystal plasticity theories [5]; however, these effects arise naturally from discrete dislocation dynamics methods that capture the interactions between dislocations and interfaces [231]. However, large-scale boundary value problems remain computationally intractable for dislocation dynamics in terms of both spatial and/or temporal scales. Embellishment of continuum methods with physically-based information from smaller scales, as in strain gradient plasticity theories [77] and geometrically-necessary dislocation based crystal plasticity formulations [232] is one way of approaching the problem; however, the mechanisms causing size effects are to some extent prescribed when taking that approach. Adopting multi-scale approaches to couple simulations at different scales can alleviate the computational burden by using a higher resolution method only in an area of interest, where it is required.

Multi-scale modelling generally employs either unidirectional (hierarchy modelling) or bidirectional (concurrent modelling) information passing. The detailed features of them have been discussed in Chapter 2. A natural method for capturing localised size effect behaviour in large polycrystal boundary value problems is concurrent coupling of discrete dislocation plasticity (DDP) to the crystal plasticity finite element (CPFE) method, a continuum method that accounts for the crystal structure and homogenises the effect of crystallographic slip.

A planar method for concurrent coupling of DDP to CPFE in a single crystal was developed in [130]. The coupling boundary between the DDP and CPFE regions was treated as transparent to dislocations, and the compatibility of tractions and

displacement was ensured in an average sense. Tension and mode I crack growth problems were analysed; in the latter, computation time was reduced by up to a factor of 14 with only a minor reduction in accuracy. 3D DDP was coupled to strain gradient crystal plasticity via the solution of separate models with bi-directional information passing in Ref. [131]. The so-called Multi-scale Dislocation Dynamics Plasticity (MDDP) approach was also used in [132] to investigate micro-pillar compression, and in [133] to study spherical nano-indentation. Micro-pillar compression was also investigated in [134] using a hybrid DDP/FEM coupling method.

In this chapter we present a new methodology for concurrent coupling of planar discrete dislocation plasticity to crystal plasticity; the method is useful for *e.g.* the purpose of extending a well-established relationship between hardness and indentation depth for a thin film on a substrate to include the indentation size effect regime, for a wide range of coating and substrate materials. In the proposed method, compatibility of displacements and tractions is ensured at the coupling boundary through an iterative boundary condition passing scheme; this is achieved at each node in the coupling boundary rather than in an average sense as done in previous studies [130]. After an introduction of formulations of CPFE and DDP adopted in this project, details of the newly proposed coupling method are reported.

3.2 Crystal Plasticity Finite Element

In this section, the computational framework of the crystal plasticity finite element (CPFE) formulations employed in this project is introduced. The formulations are adapted from the foundation deformation of crystalline materials that is reviewed in Chapter 2 at meso-scale. This CPFE framework is independently used in the project to solve planar uniaxial tension problem (Chapter 4), indention problem (Chapter 5-6), sliding and fretting problems (Chapter 7). Besides, it also contributes to calculations of the CPFE sub-region in the proposed coupling method that solves the problems mentioned above.

3.2.1 Mechanisms

The CPFE implementation adopted in this project is a rate-independent formulation described in [85], which is based on the prior work of Asaro [41] and Anand & Kothari [40]. Further developments have been incorporated by various authors to include a full elastic anisotropy description and different crystalline structures, and to study energy dissipation at the meso-scale and localized plasticity and residual stresses (e.g. [58, 60, 61]).

CPFE calculation is able to obtain important features of the micromechanics of crystalline plasticity with some appropriate assumptions. For some particular problems, polycrystal plasticity theory is applied to describe and calculate the macroscopic stress state. For this project, rate and temperature effects are not taken into consideration. Thus a time-independent plasticity model is adopted. The detailed function employed here is based on the work presented in Ref. [85].

The formulation is based on the standard two-term multiplicative decomposition of the deformation gradient into the elastic and plastic parts, where plastic slip occurs on individual slip systems when the resolved shear stress on the slip system exceeds the current critical resolved shear stress, τ_c.

3.2.2 CPFE formulation

When a load is applied, the total deformation and rotation of a crystal is given by the deformation gradient $\boldsymbol{F}$, which can be resolved in terms of elastic and plastic parts[41]:

$$\boldsymbol{F} = \boldsymbol{F}^{\mathrm{e}}\boldsymbol{F}^{\mathrm{p}} \tag{3.1}$$

The velocity gradient $\boldsymbol{L}$ is given by:

$$\boldsymbol{L} = \dot{\boldsymbol{F}}\boldsymbol{F}^{-1} = \dot{\boldsymbol{F}}^{\boldsymbol{e}}(\boldsymbol{F}^{\mathrm{e}})^{-1} + \boldsymbol{F}^{\mathrm{e}}\dot{\boldsymbol{F}}^{\boldsymbol{p}}(\boldsymbol{F}^{\mathrm{p}})^{-1}(\boldsymbol{F}^{\mathrm{e}})^{-1} \tag{3.2}$$

Also, the gradient $\boldsymbol{L}$ is decomposed into the deformation rate and the spin tensor:

$$\boldsymbol{L} = \boldsymbol{D} + \boldsymbol{W} \tag{3.3}$$

The formulation is based on standard two-term multiplicative decomposition of the deformation gradient into elastic and plastic parts, where plastic slip occurs on individual slip systems when the resolved shear stress on a slip system exceeds the current critical resolved shear stress (CRSS), τ_c. The rate of change of resolved shear stress on α^{th} slip system is taken to evolve as [85]:

$$\dot{\boldsymbol{\tau}}^{\alpha} = \sum_{\beta=1}^{N} \boldsymbol{h}_{\alpha\beta}\dot{\boldsymbol{\gamma}}^{\beta}$$

$$= \boldsymbol{P}^{\alpha}\!:\left(\boldsymbol{C}\!:\boldsymbol{D} - \boldsymbol{C}\!:\sum_{\alpha=1}^{N}\boldsymbol{P}^{\alpha}\,\dot{\boldsymbol{\gamma}}^{\alpha} - \sigma\ \mathrm{tr}(D)\right) + \boldsymbol{\beta}^{\alpha}\!:(\boldsymbol{D} - \sum_{\alpha=1}^{N}\boldsymbol{P}^{\alpha}\,\dot{\boldsymbol{\gamma}}^{\alpha}) \tag{3.4}$$

where $\boldsymbol{h}_{\alpha\beta}$ is the hardening modulus matrix, $\dot{\boldsymbol{\gamma}}^{\beta}$ is shearing rate $\dot{\boldsymbol{\gamma}}$ on the $\boldsymbol{\beta}^{th}$ active slip system, and $\boldsymbol{P}^{\alpha}$ is given by:

$$\boldsymbol{P}^{\alpha} = \frac{1}{2}(\boldsymbol{s}^{\alpha}\boldsymbol{n}^{\alpha T} + \boldsymbol{n}^{\alpha}\boldsymbol{s}^{\alpha T}) \tag{3.5}$$

where s^{α} and n^{α} are the slip direction and slip plane normal of the αth active slip system, respectively.

$\boldsymbol{C}$ is the fourth order tensor of elastic constants and $\boldsymbol{D}$ is the second order deformation rate tensor calculated from velocity gradient $\boldsymbol{L}$:

$$\boldsymbol{D} = \frac{1}{2}(\boldsymbol{L} + \boldsymbol{L}^{T}) \tag{3.6}$$

And $\boldsymbol{\sigma}$ is the Cauchy stress and $\boldsymbol{\beta}^{\alpha}$ as the skew part of velocity gradient is computed as:

$$\boldsymbol{\beta}^{\alpha} = \boldsymbol{\Omega}^{\alpha}\sigma - \sigma\boldsymbol{\Omega}^{\alpha} \tag{3.7}$$

With $\boldsymbol{\Omega}^{\alpha}$ as the spin tensor at the αth slip system, given by:

$$\boldsymbol{\Omega}^{\alpha} = \frac{1}{2}(\boldsymbol{s}^{\alpha}\boldsymbol{n}^{\alpha T} - \boldsymbol{n}^{\alpha}\boldsymbol{s}^{\alpha T}) \tag{3.8}$$

The matrix of hardening moduli is defined as:

$$\boldsymbol{h}_{\alpha\beta} = (q + (1-q)\boldsymbol{\delta}_{\alpha\beta})h \tag{3.9}$$

With *q* representing the latent hardening parameter with the common value range $1 < q < 1.4$, and the self-hardening function, *h*, is defined as:

$$h = H_F(1 + (H_R - 1)e^{-H_{exp}P}) \tag{3.10}$$

where H_F, H_R, and H_{exp} are constitutive variables used to capture the initial and final hardening modulus and *P* is the accumulated plastic strain within the grain. An example of how these parameters can be selected to match the experimental stress-strain response is reported in [58]. In this project, the CPFE material parameters (including critical resolved shear stress and hardening) are obtained by matching the plastic behaviour of materials modelling by DDP in the uniaxial tension case (reported in section 3.4.2).

Rearranging equation (3.4) into a set of general linear equations, the unknown parameter $\dot{\gamma}^{\alpha}$ can be found using a singular-value decomposition to avoid potential issues related to matrix inversion [233-235], as discussed in [130]. This enables CPFE model to update stresses and strains throughout a simulation and capture the evolution of accumulated plastic deformations along slip systems. After obtaining the value of $\dot{\gamma}^{\alpha}$ at each slip plane, the Cauchy stress rate $\dot{\sigma}$ is given by the following equation (3.11) at a node

$$\dot{\boldsymbol{\sigma}} = \boldsymbol{C}:\boldsymbol{D} - \boldsymbol{\sigma}tr(D) - \boldsymbol{\Omega}\sigma + \sigma\boldsymbol{\Omega} - \sum_{\alpha=1}^{n}(\boldsymbol{C}:\boldsymbol{P}^{\alpha} + \boldsymbol{\beta}^{\alpha})\dot{\boldsymbol{\gamma}}^{\alpha} \tag{3.11}$$

Therefore, stresses can be calculated at every node in the crystal and at each time step. All of the parameters used to describe the constitutive law (critical resolved shear stress and hardening constitutive parameters) in the equations above, which are material properties physically linked to the evolutions of dislocations within the material, are usually obtained by matching the macro-scale tensile stress-strain response with experimental results or dislocation dynamics simulations. In this project, dislocations dynamics simulations will be used to calibrate these parameters.

The CPFE formulation discussed above is versatile and allows simulating both two-dimensional and three-dimensional real polycrystalline structures obtained using e.g. EBSD or randomly distributed grains or statistically equivalent grain structures modelled using Voronoi tessellations [60, 236].

3.2.3 Implementation

3.2.3.1 Microstructure initialization

An ABAQUS UMAT (user-defined material) subroutine integrated with CPFE algorithms has been employed and further adapted in this project. Prior to calculate the necessary relevant crystal plasticity status variables, an input file (named the "seeds" file) is read to define the parameters needed to describe the material elastic and plastic behaviour at grain level, and the polycrystalline microstructure of the system in terms of grain centre positions and orientations of crystals. A typical seeds file structure for a 2D simulation is shown in Figure 3.1. The integer number in the first row is the number of grains, which might be adapted to study different polycrystalline or single crystal structures. The second block contains information about the geometry and orientation of each crystal. In particular, in each individual line, the first two columns stands for the X and Y coordinate values of grain centre. The following three columns stands for the specific grain orientation, in terms of Euler angles[237]. In details, the third (ϕ_1) column value rotates the crystal about the North Pole, and the fourth (Φ) columns rotate the crystal out of the plane about the [100] axis. Therefore, the third and fourth columns provide the position of the [001] crystal with respect to the specimen axes. The fifth column rotates the crystal about [001] axis. In this project, lengths are in millimetre while angles are measured in radians, and the structure corresponds to a 20 randomly seeded and oriented grains. The last block of the input file defines material properties, including Young's modulus, Poisson's ratio, elastic anisotropy index (Zener's factor) critical shear stress, and hardening parameters etc.

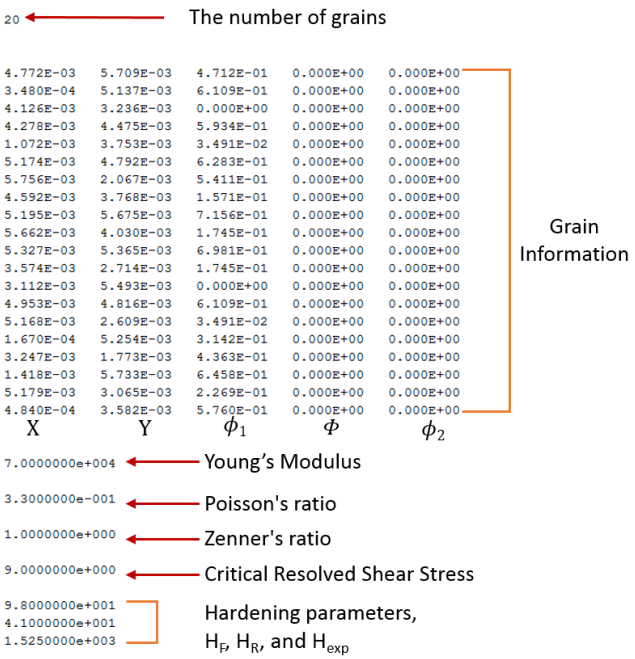


Figure 3.1. The structure of a typical seeds file employed in crystal plasticity finite element method

Based on the microstructure information provided in seeds file, the CPFE code generates the corresponding polycrystalline microstructure of a specimen made up of grains with different orientations. The positions of seeds are taken as the centre of grains, and grain boundaries are generated by making the grain grow from the seeds with an identical rate until the boundaries of adjacent grains meet each other, according to the standard generation of a Voronoi tessellation procedure [238]. In experiments, electron backscatter diffraction (EBSD) [239, 240] measurements are widely used, e.g. in Dunne's work [87], to obtain the grain microstructure image.

The microstructure of a polycrystalline rectangular specimen consisting 20 grains is illustrated in Figure 3.2. It can be observed that the grain (*i.e.* Voronoi cells) generation follows the Voronoi tessellation [60, 236], *i.e.* points along the grain boundary are equidistant to the centre of adjacent grains.

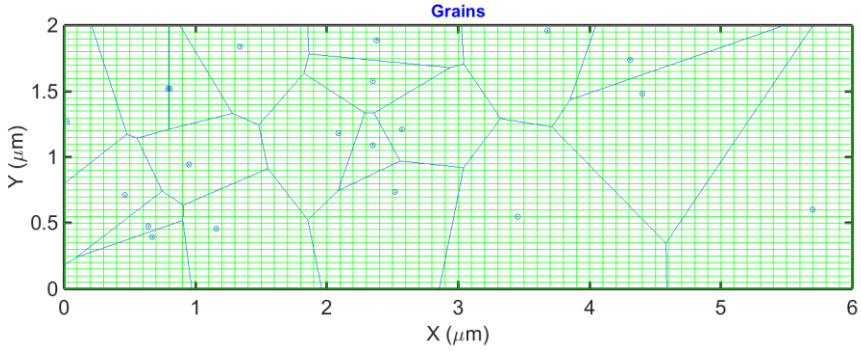


Figure 3.2. The Voronoi tessellations microstructure and finite element mesh of a rectangular specimen with dimension $6 \times 2\mu m$ modelled with CPFE

3.2.3.2 Mesh configuration and material properties assignment

In the finite element model, the representative volume element (RVE) of polycrystalline FCC aluminium material is represented by cube-shaped unit volume. For a planar problem, this unit volume degrades to a 2D area that is discretised into four-noded plain strain elements (CPE4 in ABAQUS mesh library) mesh with crystal lattice orientation assigned at each Gaussian point. Thus, each grain is assigned material properties in the seeds file.

Plain element type is used here in for reducing the computational expense. Besides, plane stress elements are not used as we need calculate the macro-level stress from the finite element representation of the microstructure [85].

The relationship between grain numbers and Gaussian point numbers has been discussed in works of Barbe et al. [241, 242]and Diard et al. [243]. CPE4 element type satisfies the required minimum number of Gaussian points

3.2.3.3 Work flow

After initializing relevant parameters, the stress information is calculated using a conventional finite element discretization and the algorithms available to the user to determine stresses and strain within the structure given the applied boundary

conditions via the general purpose ABAQUS solver. Instead of operating in graphic user interface (GUI) of ABAQUS, it is more convenient and efficient to use an input (.INP) file, which is more suitable for cluster computation. The *.INP file contains all necessary information, including geometry, mesh, boundary and loading conditions, etc. For a certain loading increment, the resolved shear stress is firstly calculated at each slip plane of grains, and plasticity flow would initiate if the calculated shear stress value exceeds the critical value. Once the plasticity has initiated, the hardening law is introduced to define the hardening matrix. Therefore, the shear strain rate and thus the stress rate at each slip plane can be solved using eq.(3.4) and (3.11) subsequently. For the current increment, stress and intermediate state variables are updated and passed back to ABAQUS. Thus, the whole calculation can advance with an updated boundary condition. Figure 3.3 illustrate the general work flow of a typical CPFE code that is applied in this project.

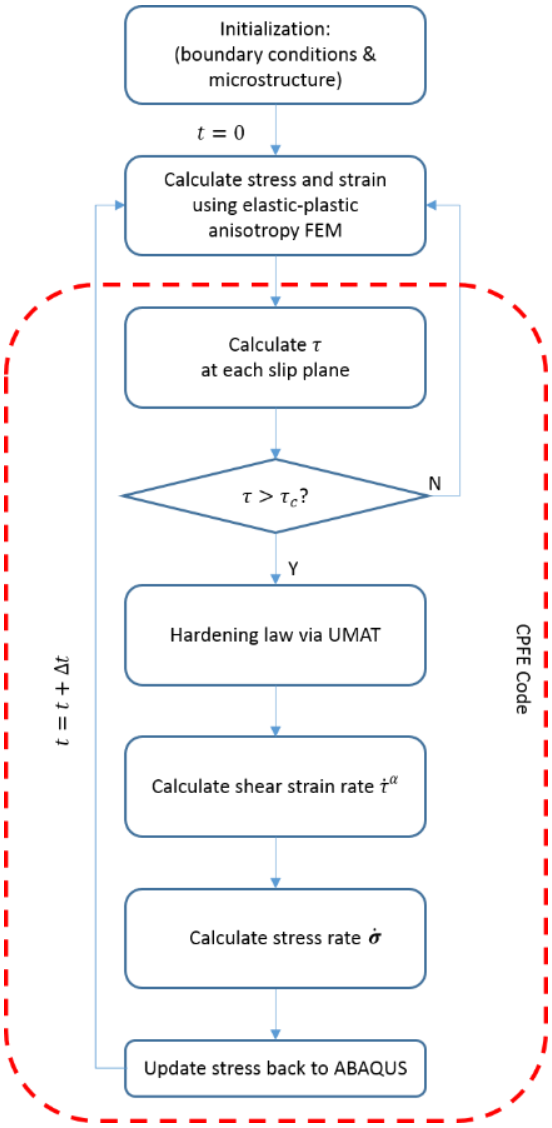


Figure 3.3. The general flow chart of the CPFE code employed in this project

It is more reliable and efficient to use clusters of Imperial College London to process CPFE calculations. Clusters are employed to call the package ABAQUS with an .INP file and the source code of crystal plasticity finite element subroutine described above. ABAQUS outputs the results of the simulations performed according to the inputs provided into a database file (*.odb) and a data file (*.fil), the latter of which is read internally by the subroutine to calculate and write boundary conditions into a user-defined data file. This data file provides the DDP sub-region or coupling boundary with time-step information for the coupling, boundary conditions, iteration error etc. Also, the CPFE subroutine can receive concentrated nodal force and/or displacement as boundary condition by modifying *.INP file and a DISP subroutine that specifies or redefines the magnitudes of associated boundary conditions, respectively.

3.2.4 Adaption and improvements of the CPFE routines

The CPFE code used in this project is adapted from an original FORTRAN code (UMAT) developed by Dr. Dini and Professor Dunne. Its robustness and efficiency is improved in this project. Of more significance, adaptions that enables CPFE model to receive and output flexible boundary conditions automatically are made on the original code. In the application to the uniaxial tension problem (see Chapter 4), for instance, the CPFE is adapted to allow the part of the structure model using crystal plasticity to receive external nodal displacement boundary condition and output nodal traction boundary conditions. Thus, boundary conditions can be exchanged via nodes along the interface between CPFE and DDP sub-models. Similarly, adaptions are also made to enable the CPFE codes to be used for coupled indentation and sliding problems in later chapters.

3.3 Discrete Dislocation Plasticity

In this section, the computational framework of discrete dislocation plasticity (DDP) formulations employed in this project is introduced. The formulations are adapted from dislocation theory and superposition method that are reviewed in Chapter 2 at discrete dislocation scale. This DDP framework is independently used in the project to solve planar uniaxial tension problem (Chapter 4), indention problem (Chapter 5), sliding and fretting problems (Chapter 7). Besides, it also contributes to calculations of the DDP sub-region in the proposed coupling method that solves the problems mentioned above.

3.3.1 Mechanisms

In discrete dislocation plasticity, the plastic flow in crystalline materials is a result of continuous collective motion of existing dislocations. In order to realize a small strain simulation with the theory of discrete dislocation plasticity, the plane strain, isotropic, quasi-static discrete dislocation plasticity formulation of Van der Giessen and Needleman [99] is used here. An FCC crystal structure is assumed, with the plane of the simulation taken perpendicular to the $[\overline{101}]$ crystal direction to satisfy the plane strain constraint, $\varepsilon_{33} = \varepsilon_{13} = \varepsilon_{23} = 0$. Slip planes are lines in the planar formulation, defined by the intersection of the slip planes with the plane of the simulation, and

dislocations are confined to glide along those lines. The material is assumed to be initially dislocation-free; all dislocations originate from Frank-Read sources. The plane of the simulation is that which intersects the pure edge segments of the incipient loop originating from a Frank-Read source, and the screw parts of the loop are effectively pinned by the plane strain condition, as depicted in Figure 3.4. In 2D, the trapped dislocation line of the Frank-Read source is perpendicular to the simulation plane, hence is a point, and the dislocation loop originating from the source is a dipole of straight line edge dislocations with Burgers vector *b*. The applied loading is such that the glide component of the Peach-Koehler force is large on the edge segments of the dislocation loop, and is relatively small on the screw segments, hence the latter are effectively pinned and the loop expands via the edge segments.

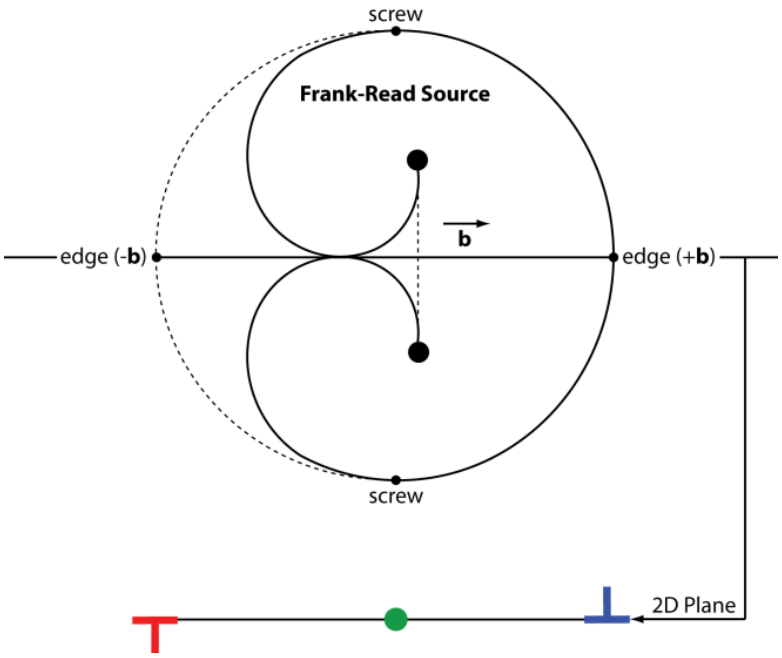


Figure 3.4. An edge dislocation dipole nucleated from a Frank-Read source in the plane of the simulation.

3.3.2 Formulations

Boundary conditions are satisfied using the superposition principle first employed by Lubarda et al. [98], and van der Giessen and Needleman [99] (see Figure 3.5). Displacement, stress and strain are decomposed (see equation (3.12) into the infinite medium dislocation fields ($\tilde{}$) and a correction ($\hat{}$) that ensures the boundary conditions are satisfied; the former is obtained via the superposition of known analytical fields and the latter is obtained via a finite element solution of a problem where singularities are absent and the effect of the dislocations is mediated by the corrected tractions (*T*) and displacements (*u*) boundary conditions.

$$u = \tilde{u} + \hat{u}$$

$$\sigma = \tilde{\sigma} + \hat{\sigma} \qquad (3.12)$$

$\varepsilon = \tilde{\varepsilon} + \hat{\varepsilon}$

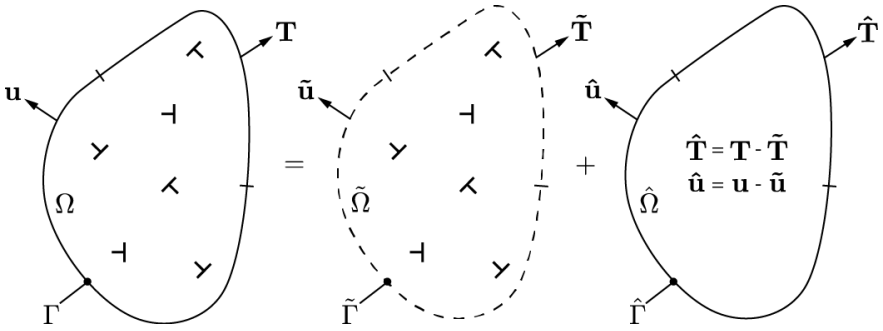


Figure 3.5. The linear superposition scheme

The system to be studied is usually taken as dislocation free initially. Point Frank-Read sources are randomly distributed on the slip planes (lines) to a certain density. Source strengths τ_{nuc} are taken from a normal distribution with specified mean and standard deviation; the latter captures the effect of the statistical distribution of trapped dislocation line lengths in the material. All sources nucleate dipoles with Burgers vector b at the equilibrium spacing. This occurs when the nucleation stress τ_{nuc} is reached and maintained for the nucleation time t_{nuc}; the latter is the time taken for the loop to reach its unstable configuration (see *e.g.* Benzerga [244]). This in general depends on the applied stress, but is relatively insensitive to it at low stresses. Annihilation of a pair of dislocations of opposite sign on the same slip plane occurs when the distance between them is less than the critical annihilation distance. Obstacles are modelled as points that pin dislocations that attempt to glide over them. An obstacle releases a pinned dislocation when the Peach-Koehler force on the obstacle exceeds $\tau_{obs}b$, where τ_{obs} is the obstacle strength.

3.3.3 Implementation

3.3.3.1 Microstructure initialization

Solvers and algorithms developed to apply discrete dislocation plasticity method to different problems are generally divided into two executable files. One of them, usually with the name “gen”, is used to generate the initial dislocation and nucleation structure, “disl.in” file, for the system to be investigated. The other executable file, which is capable of taking displacement and/or traction as boundary condition, is employed to perform the calculations and advance the simulations given the applied loading and boundary conditions and with other relevant supporting files as input information. Three important supporting files used for the uniaxial tension case discussed in Chapter 4 are introduced briefly in the following paragraphs.

The “IN” file offers geometry information, the number of crystals, the number of elements and nodes, Young’s modulus and Poisson’s ratio, Burger’s vector, strength of the dislocation Frank-Read source, nucleation time, mean value and stand deviation of the obstacle strength and output control variables in DDP computation including time increment step and the total number of steps. Both of main and generating subroutines read IN file. The structure of an IN file used for the tension problem is

shown with annotations to describe what the individual inputs do on the right hand side in Figure 3.6.

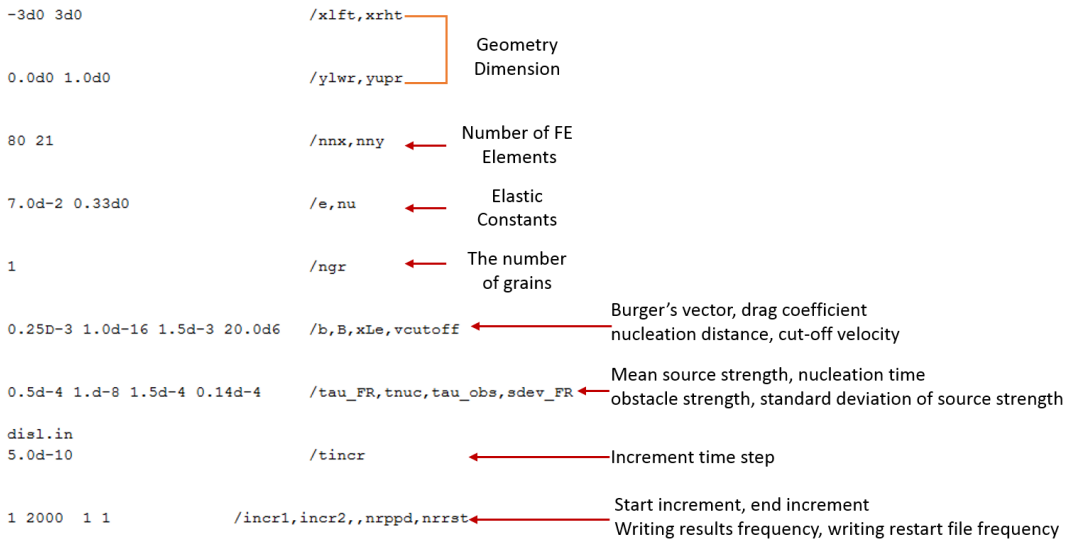


Figure 3.6. A tension IN file structure with explanation

The "DISL" file is generated by running the generation executable file (gen) after users entering several relevant parameters about dislocations, which includes the density of sources and obstacles, the slip system information, etc. There is detailed information about the number of dislocations, dislocation positions and slip planes in DISL file. A typical DISL file used for the uniaxial tension case is shown in Figure 3.7.

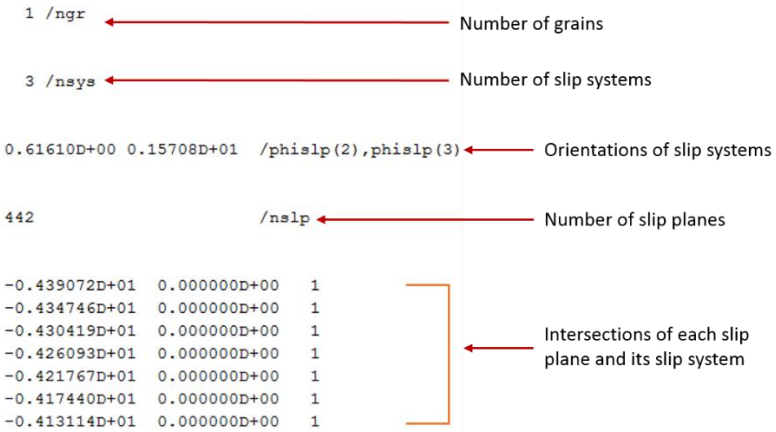


Figure 3.7. Part of a DISL file structure used for generating dislocation information for the DDP specimen adopted for the uniaxial tension problem

The "BCIN" file provides the DDP main subroutine with necessary boundary conditions and solution information. The first flag integer indicates the boundary condition type, 0 for displacement or 1 for traction type. Both of the second and third flag appearing in the second and third row of the BCIN file respectively are enabled only in the coupling procedure; they refer to the number of iterations during current loading step and the number of boundary condition increment, respectively. The fourth integer refers to the number of nodes on the boundary which receives boundary conditions

from CPFE domain or user predefined field. The last block of the BCIN file writes traction or displacement values, depending on the value of the first integer as explained above, of each node on the boundary identified by the user. A typical BCIN file used for the uniaxial tension case is shown in Figure 3.8.

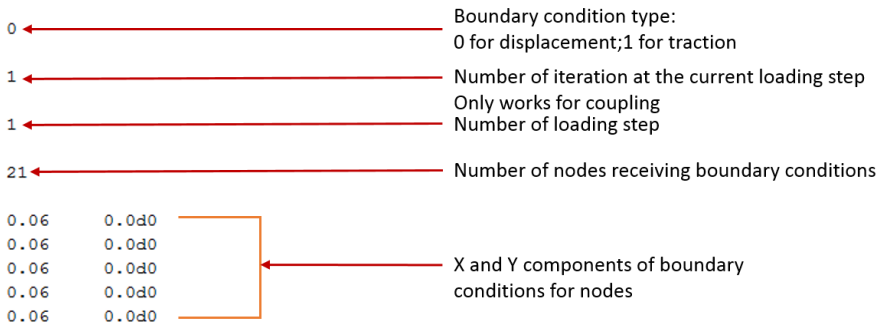


Figure 3.8. The structure of a BCIN file used for the tension coupling problem

The results of the DDP main subroutine is written in a data file, namely the 'PPD' file. There is normally information of strain, tensile stress, dislocation density, plastic strain and plastic stress recorded throughout the simulation. Intermediate results are written in data files, namely 'rst', which enable users to restart a discrete dislocation simulation and to post-process intermediate results.

3.3.3.2 Mesh configuration

The geometry for all DDP problems investigated in this PhD project is confined as rectangle with different dimensions. Thus it is feasible to discretize the problem domain with a structured mesh in order to minimize the half-band-width and thus computational expense in FEM calculations (*i.e.* the smooth field solution). This mesh feature also enables positioning of dislocations to be more efficiency. Regarding the mesh size, the number of element along X and Y directions are predefined in IN file (see Figure 3.6 for details). A uniform mesh size is adopted in non-localized problems, e.g. uniaxial tension problem; a biased mesh is adopted along both X and Y direction in localized problems including nano-indentation, nano-sliding and fretting problems. The biased structured mesh generation is based on the geometric progression algorithm with a certain biased ratio. Details can be found in Chapter 5 and Chapter 7. The biased mesh with finer mesh near the indenter tip or contact edges is able to achieve a higher dislocation resolution at the sensitive region. A bi-linear four-noded plain strain element type is commonly used in all DDP codes. Besides, all nodes are able to take displacement and/or traction as their boundary conditions.

3.3.3.3 Workflow

After the initialization of microstructure and reading boundary conditions, a DDP code starts to solve the smooth fields using a conventional finite element method. It calculates stress along each slip system to evaluate whether the dislocation dipole nucleation criterion has been satisfied. Afterwards, the calculations related individual dislocation states, including annihilation, pinning, release and generation, are carried out; which are followed this is followed by dislocations' velocity update. Time is

advanced after the smooth and discrete fields are superimposed. Figure 3.9 illustrates the general work flow of a DDP code that is applied in this project.

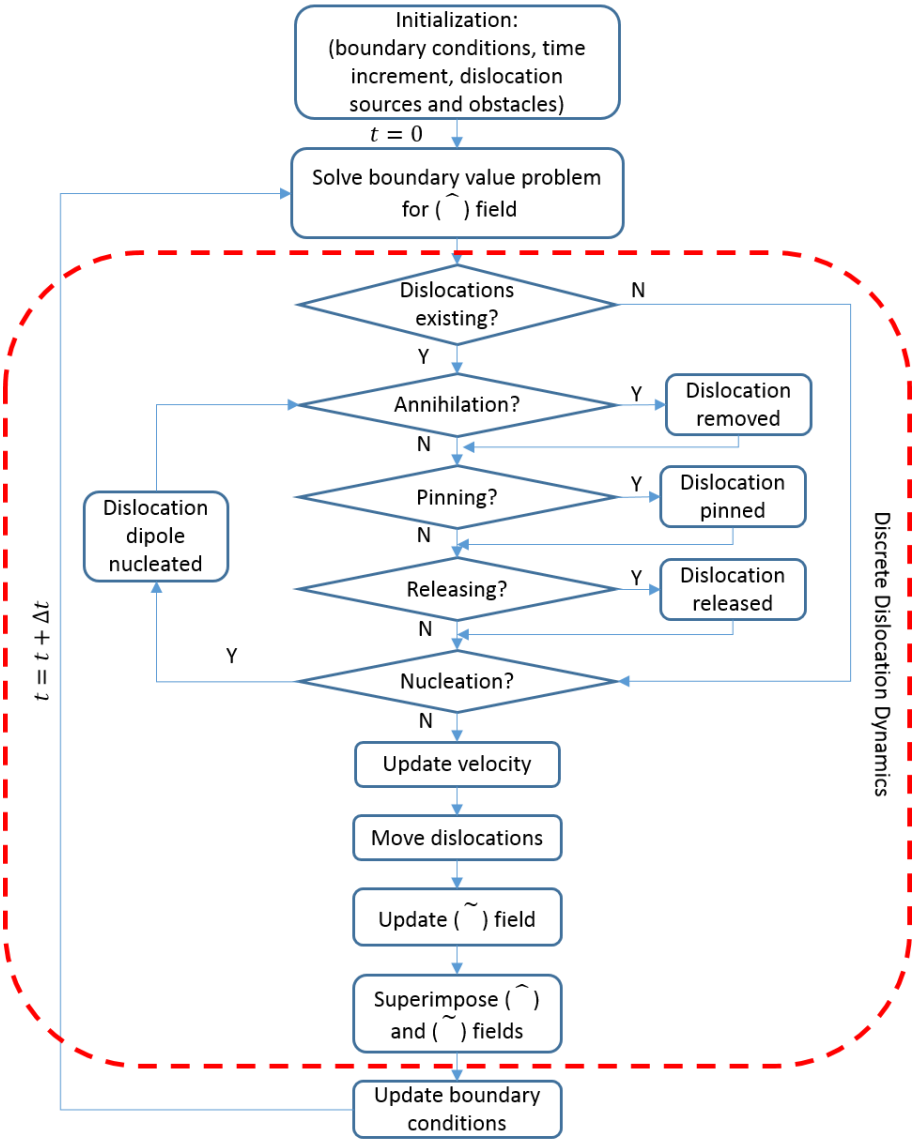


Figure 3.9. The general flow chart of the DDP code employed in this project

3.3.4 Adaption and improvements of the DDP code

The DDP codes used in this project are commonly adapted from FORTRAN codes originally developed by Dr. Balint. The robustness and efficiency of the routines is improved in this project. Of more significance, adaptions that enables DDP models to receive and output boundary conditions automatically are made to improve the flexibility of the original codes when exchanging information with the CPFE (see Section 4). In the application on uniaxial tension problem, for instance, while the CPFE region is adapted to receive external nodal traction boundary condition and output nodal displacement boundary conditions, the DDP code is also adapted to exchange information via the nodes along the interface between DDP and CPFE regions. In particular, the adapted DDP code is able not only to take nodal traction boundary

conditions that is calculated and passed from CPFE subroutine, but also to output displacement boundary conditions (i.e. the superimposed displacement field) at nodes so that CPFE subroutine can read and apply them via DISP subroutine. The boundary condition exchange process in uniaxial tension problem is illustrated in Figure 3.10.

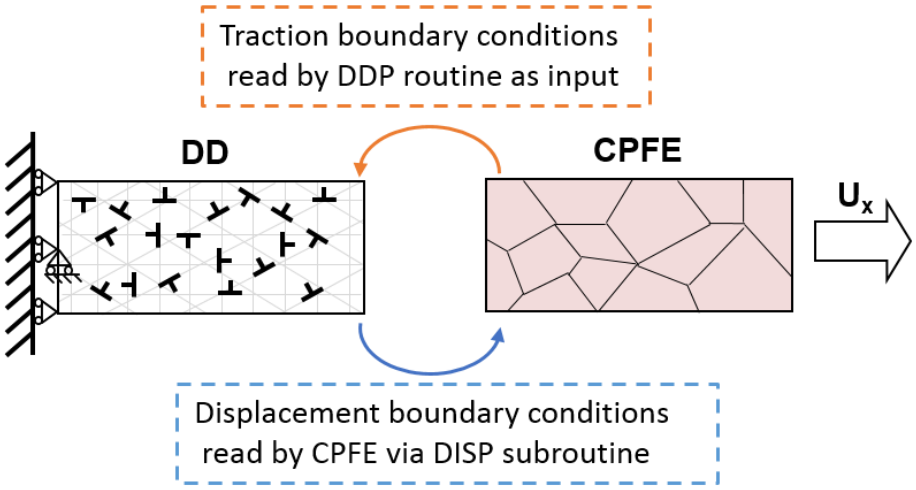


Figure 3.10. the boundary conditions passing process between CPFE and DDP domains in uniaxial tension problem

Similarly, adaptions are also made to the DDP codes applied to indentation and sliding problems. A new calculation framework for simulating fretting process on thin films is developed based on the previous work on sliding [245-247]. This new framework is used in Chapter 7 to predict the shear performance of thin films under fretting load and thus potentially predict the onset of micro-crack initiation.

3.4 General Coupling Philosophy

The introduction in previous sections provide CPFE and DDP formulations that are applied in their own regions and scales. In this section, the philosophy of our newly proposed coupling is introduced in a general way. The development of this new coupling approach aims to improve the current coupling methods reviewed in Chapter 2. Key issues of the new coupling method will be discussed in the later part of this section. The newly proposed coupling approach will be applied in various boundary value problems, including uniaxial tension problem (Chapter 4), wedge-shaped indentation problem (Chapter 6) and nano-sliding/fretting problem (Chapter 7). In these applications, the coupling work flow and issues will be addressed specifically.

3.4.1 Problem definition

The method is based on a concurrent coupling of a sub-model of DDP inside a CPFE region (see Figure 3.11). The fine scale area of interest is the DDP region (Ω_{DD}), while the remainder is modelled using a CPFE description (Ω_{CPFE}). The aim of the proposed coupling strategy is to achieve compatibility of stresses and displacements at a local

level (*i.e.* at each node) between the two regions instead of exchanging average information along their mutual boundaries.

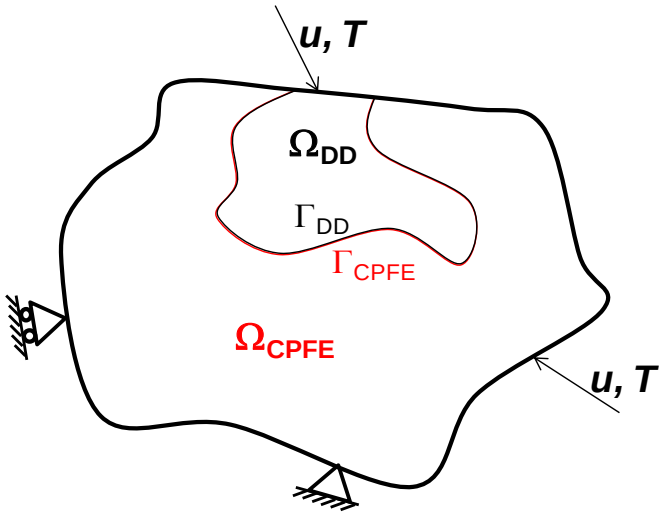


Figure 3.11. Schematic of the domain-decomposition strategy used for the DDP-CPFE coupling

3.4.2 Material calibration

The first requirement before coupling is to match the material behaviour. It is necessary to match both the elastic and plastic response of the two regions by modulating the CPFE inputs to match the stress-strain curve obtained using DDP in uniaxial tension; the latter is taken to be the actual material response, since it is derived from a fuller physical description of the material behaviour rather than phenomenological input. It should be noted here that the DPP inputs can also be adjusted to match experimental results as done in Balint's works [110, 120].

Figure 3.12 shows the comparison between the two stress-strain responses after the CPFE calibration was performed. The best match CPFE stress-strain curve is achieved using a least square fit. The parameters used in the dislocation simulations are summarized in Table 3.1. They are also used in the indentation problem in Chapters 5 and 6. The best match between the two descriptions was achieved using the CPFE parameters tabulated in Table 3.2.

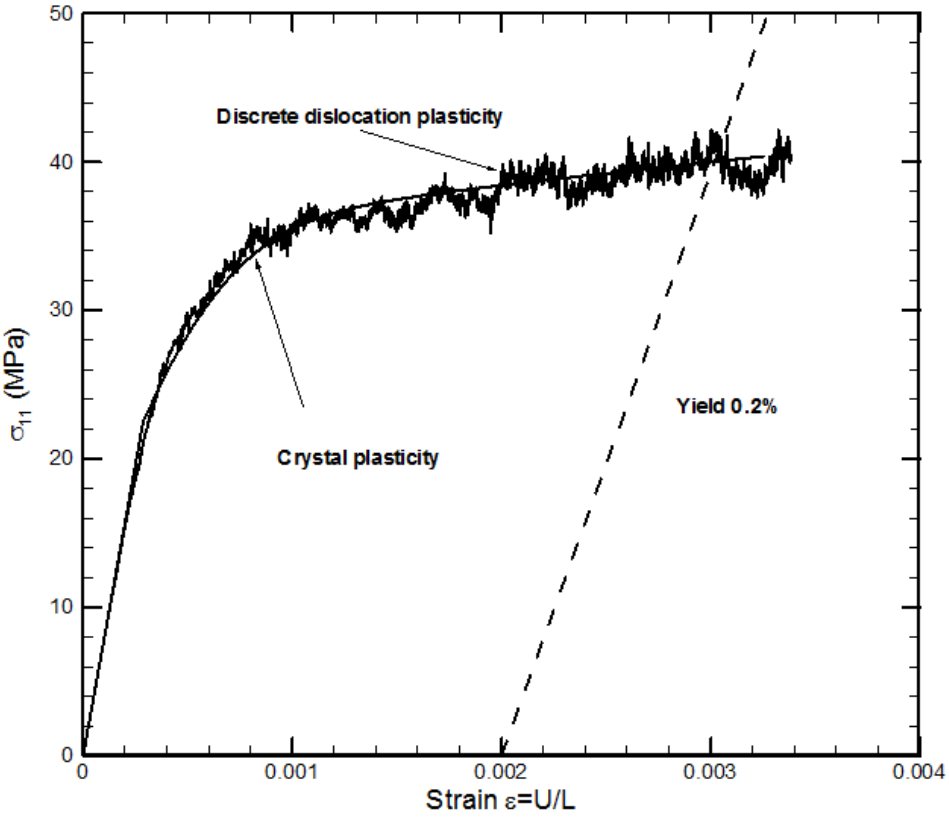


Figure 3.12. Macroscopic stress–strain responses predicted by DDP and CPFE for the Al crystal after calibration of the CPFE constitutive parameters to produce the best match between the two simulations.

Table 3.1. DDP material parameters used in the tension and indentation problem solved with the proposed coupling method.

Parameter Name	Symbol	Unit	Value
Young's Modules	E	GPa	70
Poisson's Ratio	υ	-	0.33
Burger's Vector	b	nm	0.25
Slip Plane Spacing	-	|b|	100
Slip Systems	$\phi^{(\alpha)}$	Degree	$\pm 54.7, 0$
Annihilation Distance	L_e	|b|	6
Source Strength Mean	$\bar{\tau}_{nuc}$	MPa	50
Source Strength S.D.	$\sigma_{\tau_{nuc}}$	MPa	10
Nucleation Time	t_{nuc}	ns	10
Nucleation Dipole Spacing	L_{nuc}	nm	15
Source Density	ρ_{nuc}	μm^{-2}	42
Obstacle Density	ρ_{obs}	μm^{-2}	42
Obstacle Strength	τ_{obs}	MPa	150

Table 3.2. CPFE material parameters used in the tension and indentation problem solved with the proposed coupling method.

Parameter Name	Symbol	Unit	Value
Young's Modules	E	GPa	70
Poisson Ratio	υ	-	0.33
Grain Orientation	ϕ	Degrees	0
Critical resolved shear stress	τ_c	MPa	9
Zener's Factor	Z	-	1
	H_F	-	98
	H_R	-	45
	H_{exp}	-	1525
	q	-	1.01

3.4.3 Mesh configuration

Mesh is initially generated in the sensitive sub-region (*i.e.* DDP sub-region in this project) in order to ensure that adequate resolution of fields is able to obtain. The mesh configuration along the coupling boundary is set as identical for both sub-regions which helps and boundary conditions passing (see 3.4.7) via boundary nodes and thus achieve the "nodal compatibility" of stress and strain fields. Therefore, the mesh of CPFE sub-region is generated according to the counterpart of DDP sub-region. For instance, in the indentation problem, a biased mesh is firstly generated in the DDP sub-region. According to the nodes and elements along the coupling boundary of DDP sub-region, mesh seeds are assigned on the coupling boundary of CPFE region so that ABAQUS discretizes the CPFE sub-region accordingly. In order to decrease the computational time expense, a biased mesh is also adopted in the zone far away from the coupling boundary of CPFE sub-region.

3.4.4 External boundary conditions

External boundary conditions are applied based on the specific problems, and the loading rate is determined by the coupling step. As both DDP and CPFE models are able to receive boundary conditions in terms of displacements and tractions, external boundary conditions (u, T) shown in Figure 3.11 can be provided to either the DDP or CPFE sub-region. However, the sensitive sub-region of a crystalline specimen is usually modelled with DDP description in order to obtain a higher resolution there. Thus the DDP sub-region is usually taken as the sub-region receiving the external boundary conditions (see *e.g.* indentation and fretting problems described in Chapters 5-7). The time-scale of the coupling procedure is also therefore dominated by the DDP subroutine. The type of external boundary conditions can be either displacement or tractions and they are applied to specific nodes, which is based on the DDP subroutine input requirement.

3.4.5 Sub-regions modelling

According to the description of the protocol described in the previous section, the DDP sub-region usually coincides with the areas in the specimens affected by the highest

strain or stress gradients. Unless otherwise specified, the DDP region is made up of one single crystal with enclosing grain boundary, although the DDP algorithm is suitable of modelling polycrystalline material. The microstructure of DDP sub-region can be based on either FCC or BCC by varying the orientation of its slip systems (e.g. the orientation angles are changed in *DISL file in implementation)according to Rice's work[248]. In implementation, the orientated angles in the third line of the disl.in file are varied accordingly. The surrounding bulk sub-region is correspondingly modelled using the CPFE description. The material properties of CPFE sub-region are obtained from the calibration process, and a polycrystalline microstructure can be applied on the CPFE sub-region as mentioned in Section 3.2.3.1.

3.4.6 Interface coupling

The key feature of the proposed coupling strategy is the passing of boundary conditions between two sub-regions via the coupling interface. The two sub-regions, Ω_{DD} and Ω_{CPFE} in Figure 3.11, communicate via the coupling boundaries, Γ_{DD} and Γ_{CPFE}; in particular, displacements and stresses are passed at nodal points, which are shared by the two finite element descriptions used for the corrective field ($\widehat{\ }$) in the DDP simulation and the CPFE description, in a forward-iterative manner. At every loading step, which is defined by updating external applied loads and/or displacements, *T* and *u* respectively, along the external boundaries of the two domains, Ω_{DD} and Ω_{CPFE}, one field variable (either stress or displacement) is passed between the two coupling boundaries Γ_{DD} and Γ_{CPFE} until the other field variable converges between two consecutive iterations to within an error. In order for the sets of stresses and displacements passed between the interfaces to converge, it is sometimes needed to use a "buffer" at the common boundary. This buffer region enables the dislocation fields to be relaxed slightly in the proximity of the coupling boundary and improves convergence; this is similar to other averaging and interpolation schemes proposed in the literature [128, 130].

A coupling strategy at the boundary that separates sub-regions with different material length scales is required not only to smooth the transition between the different descriptions but also to impose rules for the transfer of dislocations across the coupling domain. Curtin et al. developed a technique to deal with the passage of dislocations between the two regions [130]. Although their technique could be employed here, in this thesis the interface between the DD and CPFE regions is chosen to coincide with an interface or grain boundary, *i.e.* dislocations are pinned at the interface and do not pass through it.

3.4.7 Boundary conditions passing

In principal, based on the fact that both DDP and CPFE sub-regions are capable of receiving tractions or displacements as their boundary conditions, it is feasible to set boundary conditions passing between two sub-regions at nodes along the coupling boundary. This nodal-based coupling naturally ensures that the compatibility of stress

and displacement fields between two sub-regions at each single node rather than in a averaged sense, as Curtin's work [130].

However, the type of boundary conditions passing is determined by calculation of the sensitive sub-region (*i.e.* DDP sub-region). For instance, DDP sub-region in nano-indentation problem receives displacement boundary condition from indenter. Thus, it is reasonable to request DDP sub-region to output tractions (or concentrated forces) to CPFE sub-region as boundary conditions. Besides, the convergence issue also limits the choice of type of boundary conditions passing. For example, in the uniaxial tension problem, the traction transferred from CPFE to DDP sub-region as latter's boundary condition as this choice ensures and helps the convergence of this particular problem. Please see the Section 3.4.9 for full details.

3.4.8 Iterative scheme

An iterative scheme is conducted to achieve the compatibility of tractions and displacements of each node along the coupling boundary. An independent subroutine examines whether the iterative scheme has converged, based on the imposed target and the specific criteria identified for the problem under investigation, after a new boundary condition is updated in one sub-region. If the convergence has been achieved, the iterative scheme exits and the coupling script abandons the internal loop; if not, the iterative scheme continues to pass the updated boundary conditions between the two sub-regions. It should be noted that there is no relaxation algorithm within the iterative scheme. Also, the external boundary condition type determines the target parameters that are passed from one sub-region to the other sub-region.

3.4.9 Convergence issue

The compatibility of tractions or displacements cannot always be satisfied at each individual node along the coupling boundary, for both physical (i.e. dislocation singularity) and mathematical reasons. In order to improve the convergence efficiency, several measurements are taken.

Firstly, an acceptable tolerance between the current iteration step and previous one needs being set in order to help the convergence. For example, this tolerance value is set as 2% in uniaxial tension problem. This measurement aims to exclude the numerical errors that could cause troubles in achieving convergence.

Secondly, a moving average algorithm [249] is applied to the boundary conditions passing from the discrete sub-region when compared to the continuum sub-region. This measurement aims to smooth possible peaks of stress and thus tractions/concentred nodal force close to discrete dislocations that could result in calculation difficulties in CPFE sub-domain.

Thirdly, In order for the sets of stresses and displacements passed between the interfaces to converge, it is sometimes needed to use a "buffer" at the common boundary. This buffer region enables the dislocation fields to be relaxed slightly in

the proximity of the coupling boundary and improves convergence; this is similar to other averaging and interpolation schemes proposed in the literature [128, 130].

Fourthly, the choice of boundary condition type passing between sub-regions also affects the convergence. Numerically, the boundary condition iteration should follow a convergent form. Therefore, a final convergence is promisingly to be achieved. For instance, in the uniaxial tension problem, the hardening law physically decreases the gradient of stress over strain response. Thus, displacement (macroscopic response of strain in elementary response) is chosen to be passed from CPFE sub-region to DDP sub-region to help the convergence. In contrast, there are examples (please see the content of Chapter 4) that show the divergence or oscillation situation between two unstable iterations when an inappropriate boundary condition type is passed.

3.4.10Implementation

The whole coupling procedure is controlled by a BASH script, which is able to call various procedures, to read and write associated files and thus to conduct calculations. The script is conducted with the aid of clusters of Mechanical Engineering, Imperial College London.

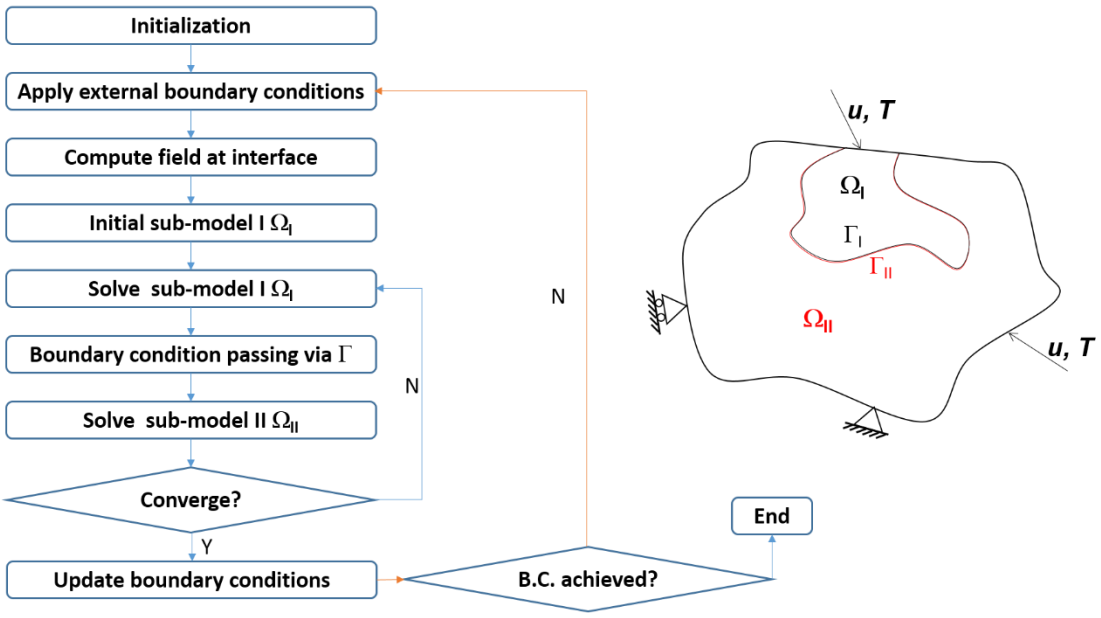


Figure 3.13. the general flow chart of newly proposed multi-scale modelling approach

Applying the newly proposed multi-scale coupling method on a general boundary value problem, the work flow of the coupling process is illustrated in Figure 3.13. After initializing relevant parameters, the external boundary conditions are applied on sub-model Ω_I. With a start-up model, Ω_I is solved and outputs field solution at interface Γ. Sub-model Ω_{II} receives this field solution and thus is solved to generate a new field solution. The convergence (i.e. compatibility of both displacement and traction) of this inner loading step is checked by comparing field solutions at interface. If the convergence is not achieved, the coupling process iterates from solving sub-model Ω_I. Otherwise, the coupling process updates the external

boundary conditions so that a new loading step is initialized as an outer loop. The whole coupling process will terminate until the external boundary condition achieve the user-defined value.

3.5 Summary

In order to link macroscopic crystal plasticity and discrete dislocations formulations, a multi-scale coupling approach between discrete dislocation plasticity (DDP) and crystal plasticity finite element (CPFE) has been devised in this chapter after briefly introducing the physical foundations, modelling formulations and implementation strategies for both methods. The formulations of CPFE and DDP methods are developed from the concepts reviewed in Chapter 2. The foundation of the proposed multi-scale modelling approach is illustrated for a general boundary value problem. Several main aspects of this multi-scale modelling coupling approach, including coupling boundary modelling, sub-region modelling, boundary conditions passing etc. have been discussed in details. Several applications of the proposed coupling approach will be carried out to assess the validity and applicability of the proposed technique to typical engineering problems, including the uniaxial tension problem (Chapter 4), the wedge-shaped indentation problem (Chapter 6) and nano-sliding/fretting problems (Chapter 7).

It is envisaged that this new multi-scale coupling approach will lead to new insight in the mechanisms responsible for damage initiation and governing plasticity and fatigue. It will also prompt the development of other multi-scale modelling methods.

4 Application of the Coupled Modelling Approach: Uniaxial Tension Problem

In this chapter, the proposed multi-scale modelling approach introduced in Chapter 3 is applied to the uniaxial tension problem. Before exploring the capabilities of the proposed coupling methodology, the solutions of the planar uniaxial tension problem that could be obtained using either crystal plasticity finite element (CPFE) or discrete dislocation plasticity (DDP) are presented. Parametric studies are conducted using both methods to investigate the influence of microstructure and dislocation activity (using the two different levels of "magnification" provided by CPFE and DDP respectively) on material performance. This reflects the microstructure influence on the material performance under uniaxial tension loading that is generally reviewed in Chapter 2. The application of the proposed multi-scale modelling approach to the uniaxial problem is then used to verify its validity and effectiveness by showing stress-strain response, stress field, evolution of the dislocation structure, etc.

4.1 Introduction

A literature review on the mechanical behaviour and its modelling of materials under uni-axial tension test has been provided in Section 2.3.1. In this chapter, simulations of standard uniaxial tension problem are conducted using crystal plasticity finite element and discrete dislocation plasticity respectively. Results are discussed with focus on the role of microstructure and size effect on the response of the specimen. Afterwards, the proposed multi-scale coupling approach is applied to the uniaxial tension problem using the coupling strategy shown in Figure 4.19. The coupling effect is illustrated in terms of stress strain response curves and dislocation density evolution.

4.2 Tension Problem Solving with Crystal Plasticity Finite Element

In this section, the uniaxial tension problem is solved by applying the CPFE description that is introduced in Chapter 3 into specimens. Parametric studies are conducted to the influence of microstructural and hardening parameters on the macroscopic material response. This study provides not only a practical understanding of CPFE formulations but also a foundation for the upcoming coupling calculations.

4.2.1 Methodology

The microstructure of a polycrystalline specimen in crystal plasticity finite element (CPFE) consists the following aspects.

First, CPFE models geometry information of grain information by specifying the number and spatial coordinates of several grain seed. It populates the sub-model of crystals using the Voronoi construction [60]. Random numbers are selected for those coordinates if there are no specific lay out of grains.

Second, CPFE models crystal orientation by a rotation matrix. In the theory of crystal plasticity finite element, it believes the fact that slip takes place only in certain crystallographic planes and directions, so for each crystal, crystal orientation with respect to the global coordinate axis x_1, x_2 must be specified using Euler angle convention. For a three dimensional frame work, the detailed mathematical representation of Euler angles rotation is shown in Appendix I. As the uniaxial tension case is a two-dimensional problem, grains are only allowed to rotate along the local z axis. Thus, for a rotation from a local coordinate x, y, z to a global x_1, x_2, x_3 is equivalent to that a positive rotation (Φ_2) of axes around the local rotated z axis, aligning the remaining axes, shown below:

$$Z_1 = \begin{pmatrix} \cos\phi_1 & \sin\phi_1 & 0 \\ -\sin\phi_1 & \cos\phi_1 & 0 \\ 0 & 0 & 1 \end{pmatrix} \tag{4.1}$$

The elastic constant matrix of a grain is defined locally so that the material matrix of each grain must be transformed to the global matrix in CPFE calculations

Thirdly, CPFE models the elasticity of materials using traditional elastic properties: Young's modulus E and Poisson's ratio ν

Fourthly, CPFE models the anisotropy of crystals using Zener's anisotropy factor, which is defined as:

$$\mathrm{z} = \frac{\mathrm{C}_{44}}{\frac{1}{2}(\mathrm{C}_{11} - \mathrm{C}_{22})} \tag{4.2}$$

where C_{11}, C_{12}, C_{44} are the non-zero elastic constants of the elastic constant tensor of a cubic crystal in matrix Voigt's notation. If $\mathrm{z} > 1$, the material is anisotropic; if $\mathrm{z} = 1$, the material is isotropic.

Fifthly, CPFE herein models plastic properties using a rate-independent formula. When the resolved shear stress level along a certain slip plane reaches a critical value (called as the critical resolved shear stressτ_{CRSS}), plastic flow will commence. Hence, τ_{CRSS} must be defined. Once slip begins, the phenomenological crystal plasticity model imposes a hardening law, defining how plastic stress varies with the increasing plastic strain. This phenomenological hardening law presumes that all hardening due to dislocation activity is assembled to a general formula, which herein is shown below:

$$\frac{\partial\sigma}{\partial\varepsilon} \equiv \mathrm{H} = \mathrm{H_F}[1 + (\mathrm{H_R} - 1) \times 10^{-\mathrm{H_{exp}}\gamma_{acc}}] \tag{4.3}$$

where ε is the strain, γ_{acc} is the accumulated plastic strain of all slip systems $\mathrm{H_F}, \mathrm{H_R}$ and $\mathrm{H_{exp}}$are predefined empirical hardening parameters. Their effects are studied by using stress strain response curves afterwards.

4.2.2 Problem definition

The parametric study on crystal plasticity finite element model is implemented on a dimension-fixed FCC aluminum rectangular bar (shown in Figure 4.1). The specimen with geometry dimension $2L \times H = 12\ \mu m \times 2\mu m$ is divided into symmetrical two parts. The left part, which for the development stage replaces the part of the specimen that will be modelled using DDP, is modelled as perfect elastic-plastic material, while the right part is modelled as crystal plasticity finite element continuum.

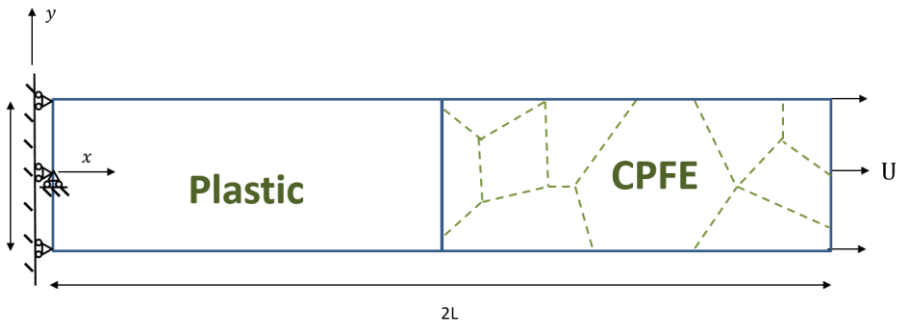


Figure 4.1. Sketch of the uniaxial tension boundary value problem analysed .The left region is modelled as elastic-plastic continuum material while the right region is modelled as CPFE.

The elastic plastic response of the left part material is shown in Figure 4.2. The plastic response is obtained from a fitting of the CPFE crystal with 0 degree orientation. Since in the following coupling section, the left half part is modelled using DDP, we herein replace it with an elastic-plastic continuum to investigate the CPFE response. Besides, this configuration allows to visually compare the difference of performance between an elasto-plastic continuum and a CPFE crystal in a single frame.

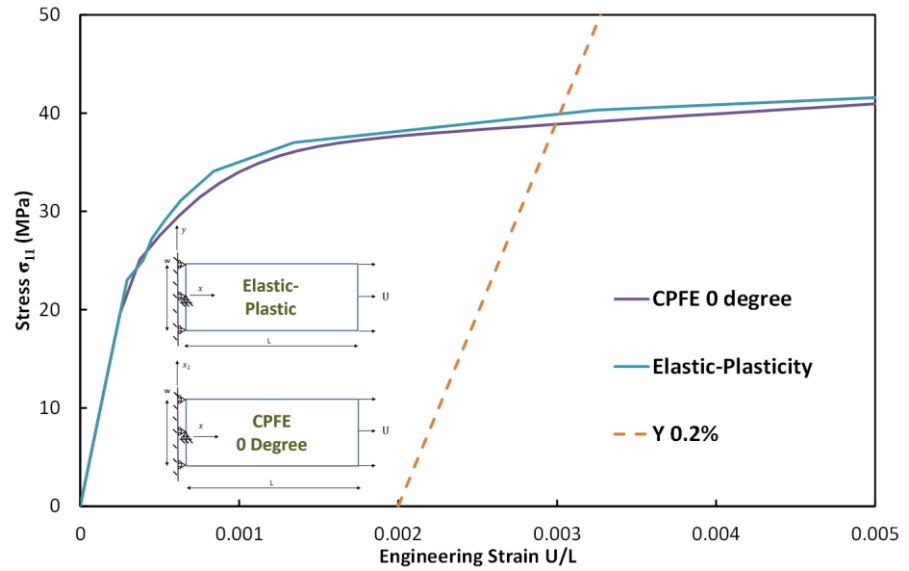


Figure 4.2. Stress strain response curve of the elastic-plastic material. This curve is fitted from the 0 degree CPFE crystal whose stress strain response curve is also included for reference.

The finite element model discretises each part of the specimen into quadrilateral plane strain elements in a regular 80×20 mesh. We use a reduced integration 4-noded bi-linear (CPE4 element type in ABQUS 6.10) element in the mesh. All nodes along the left boundary are fixed and cannot displace along the X direction, while the middle node is fixed in both X and Y directions. The right boundary is subjected to a positive horizontal displacement boundary condition with the magnitude of strain rate: $\dot{U}/L = 0.05\ s^{-1}$ with the aim of achieving an engineering strain up to 1%. Boundary conditions for CPFE parametric study are summarized as following:

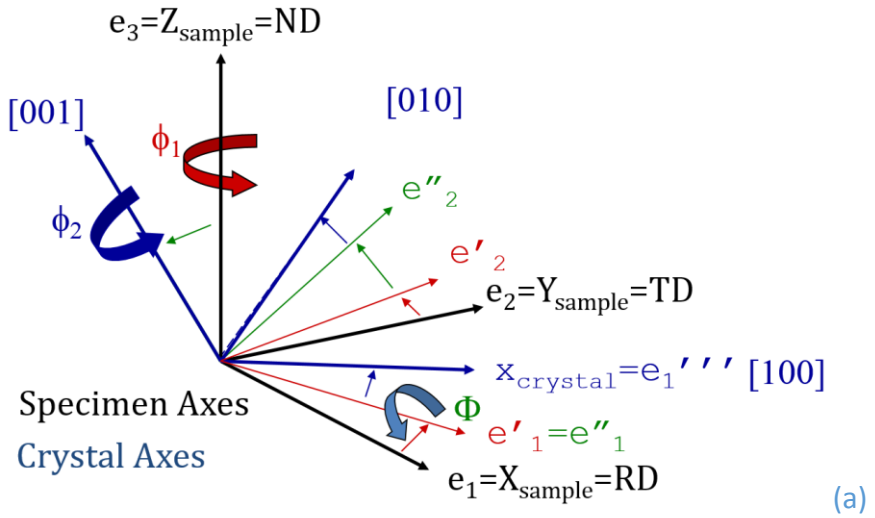
$$\dot{x} = 0 \ \ at \ \ x = 0$$
$$\dot{y} = 0 \ \ at \ \ x = 0, y = w/2 \qquad (4.4)$$
$$\dot{x} = \dot{U} \ \ at \ \ x = 2L$$

The fixed values of Young's modulus E and Poisson's ratio ν of FCC aluminium are set as $70MPa$ and 0.33 respectively. The CPFE formulation is applied into a UMAT code of ABAQUS user-defined subroutine, and thus the uniaxial tension CPFE problem is solved using ABAQUS completely. The stress field and overall macroscopic stress strain curve are exacted from ABAQUS ODB output processing file to illustrate results.

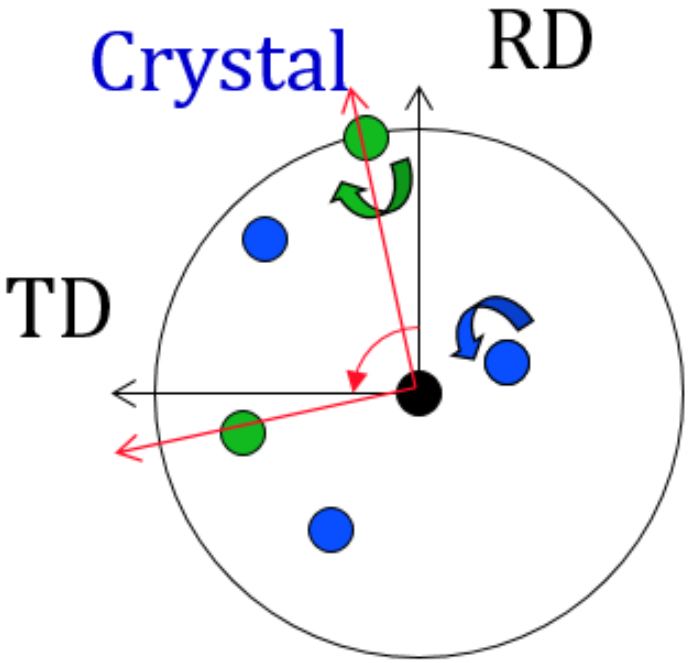
The number of grains assigned in the CPFE part is varied to study the different response given by single crystals and polycrystalline (poly-grain) materials. The anisotropic Zener's factor, Z, is also varied together with the grain orientation (from 0 to 45 degrees) to study the effects produced by elastic anisotropy.

4.2.3 Results and discussion

The crystal orientations and the critical shear stress (τ_{crss}) are taken as key parameters to study their influence on the stress-strain response curve. In studying the effect of crystal rotation angles, Euler angle notations are employed to describe the crystal rotation. In a full three dimensional framework, there are three rotation angles ϕ_1, Φ and ϕ_2 for rotating crystals that can be seen in Figure 4.3. However, only the angle rotating about the Z axis (i.e. ϕ_1) takes their effect in a planar crystal plasticity description. The angle ϕ_1 thus describes the rotations of slip system orientation of a crystal with respect to the specimen axes. Besides, the single crystals can rotate about the Z axis with magnitude ranging from 0 to 45 degree due to the symmetry of rotation that characterizes the crystal. A specimen composed of a mixture of random angles of single grains, which represents a typical polycrystalline material, is also taken into consideration.



(a)



(b)

Figure 4.3. Crystal rotation with Euler angles notation ϕ_1, Φ and ϕ_2 (a) the three-dimensional perspective (b) the view along the Z direction showing the two-dimensional rotation situation.

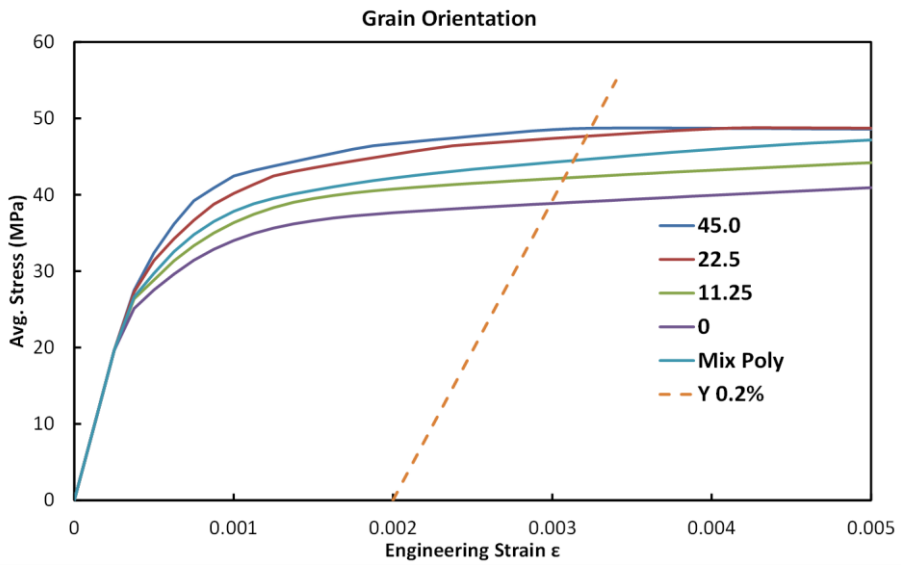


Figure 4.4. The stress strain response curves of four uniform values grain orientations of a single crystal specimen modelling (see Figure 4.1) with crystal plasticity finite element. The result of the response of single crystal specimen and a polycrystalline sample characterised by a micro structure with 20 random distributed grain orientations are shown. A 0.2% strain yield line is also included for reference.

The grain orientations effect is illustrated in terms of stress-strain response in Figure 4.4. Different single crystal orientations are specified by a rotation angle about the Z axis in the specimen. The angles range from 0 degree to 45 degree due to the symmetry property of the specimen. The orientation angles are assigned four typical values, 0, 11.5, 22.5 and 45 degree respectively. Also, a polycrystalline material response is studied by assigning a random mixture rotation angles of ϕ_1 to the specimen that is shown with the label "Mix Poly". Besides, a 0.2% strain yield line is included for reference with the label "Y 0.2%". The stress stain response curves are generated to study the orientation effect of single crystals and polycrystalline materials. All the curves reveal a strong plastically hardening behaviour, which follows a linear elastic response. All of the curves share the same threshold for the transition between elastic and plastic behaviour, which indicates that the orientation angles cannot influence the elastic performance of a polycrystalline material when the anisotropic factor $Z = 1$. However, as expected, there appears to be a strong relationship between the rotation angles and the response curves in the plastic regime. With the increase of angles up to 45 degree, the curves show increased hardening, *i.e.* larger stresses under the same level of strain is reached when the applied strain is increased. For instance, the 0.2% yield stress achieves as much as $47\ MPa$ in the grains with $\phi_1 = 45°$ degree rotation while the value of $\phi_1 = 0°$ crystal is only about$35\ MPa$. Recalling the Schmid's law (see Appendix II), the product of $\cos\phi_1$ and $\sin\phi_1$yields its maximum when $\phi_1 = 45°$, which makes slip planes $\{111\}$ with $\phi_1 = 45°$ in the crystal achieving the hardest resistance. A detailed mathematical analysis of crystal rotation angles' effect on the material hardening can be found in Appendix I. However, the flow stress of materials with 45 and 22.5 degree converge

to a similar value, around $50\ MPa$. This indicates that the crystal orientation affects less when the engineering strain approaches to a large value.

A specimen with a mixture of grains with random orientation angles (using Gaussian distribution) is also included in this parametric study to represent a polycrystalline sample. Its stress-strain response curve falls between the extreme values of crystals with 0 and 45 degree, but more close to the response of 45 degree. This phenomenon is rationalized that the adjacent grains mutually constrain deformation and thus more stress is required to initiate slip. This calculation is able to represent the performance of a typical polycrystalline material.

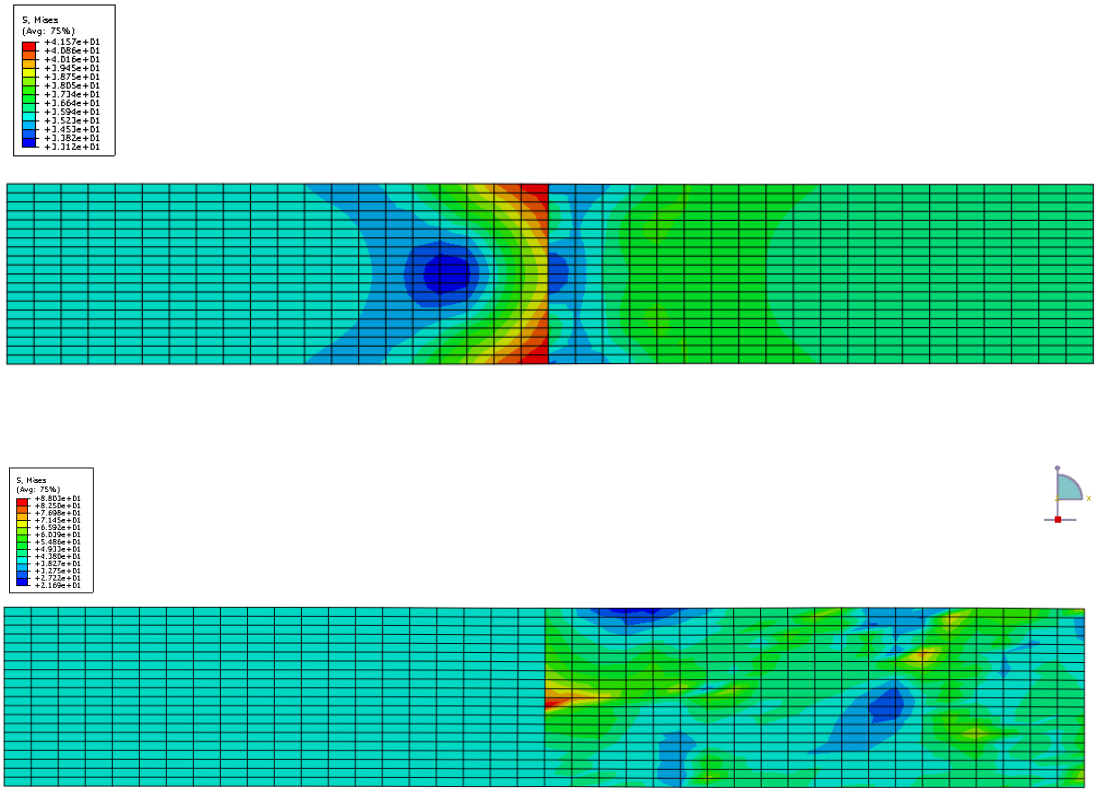


Figure 4.5. the Von Mises stress field generated by a 20-grain (a) 0 degree single crystal (b) polycrystalline structure with random orientations

The Von Mises stress fields at the same strain level $\varepsilon = 0.5\%$ for a single cystal and a polycrystalline simulations are depicted in Figure 4.5. The homogeneity difference between two stress fields reveals the micro structure effect on the material performance. The direction of slip planes varies within a polycrystalline material, so grains interact and compromise with neighbourhoods to ensure deformation compatibility of the whole material. This thus ruins the homogeneity and isotropy behaviour of materials composed with a single crystal and therefore its stress field as well.

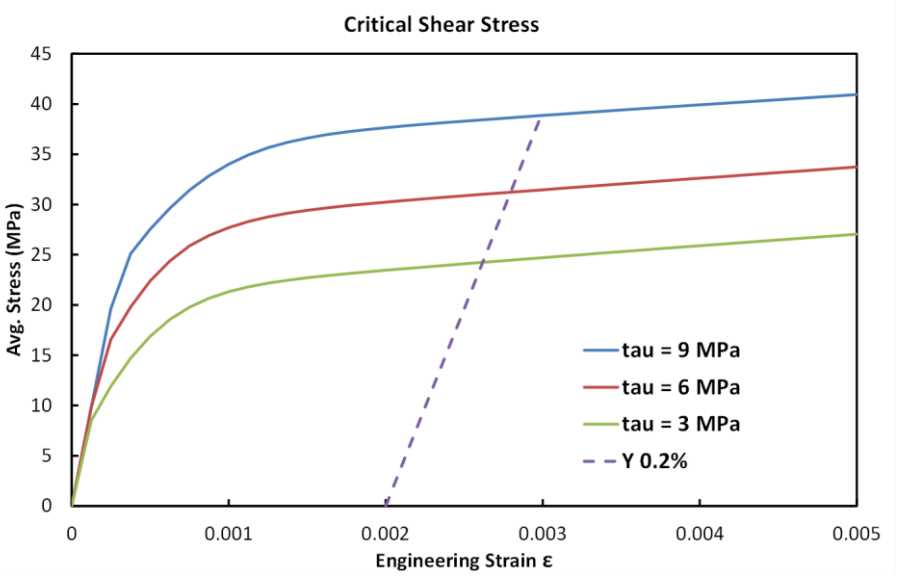


Figure 4.6. The stress strain response curves of three values different critical shear stress of a single crystal specimen modelling (see Figure 4.1) with crystal plasticity finite element. A 0.2% strain yield line is also included for reference

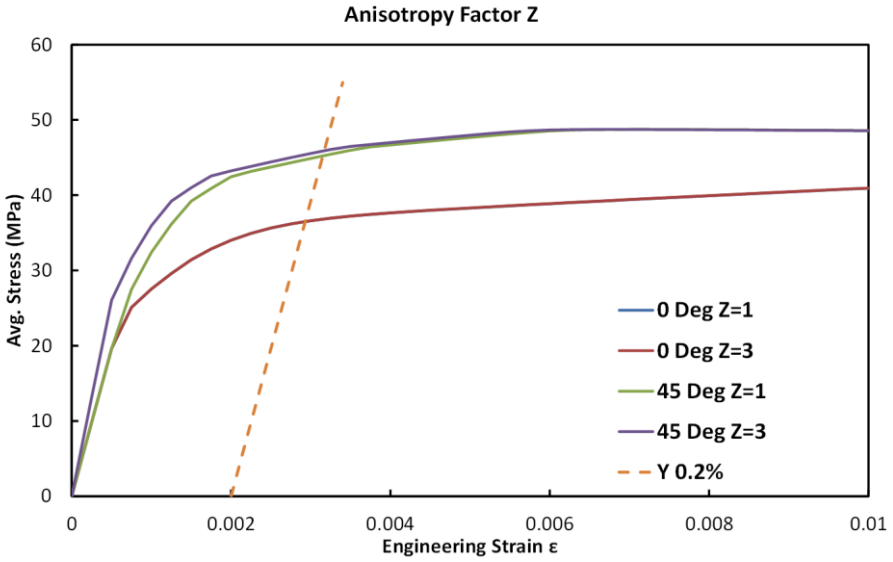


Figure 4.7. The stress strain response curves of different values Z of single crystals and specimen modelling with crystal plasticity finite element. Both grains are characterised by 9 MPa as its critical resolved shear stress, but 0 and 45 degree orientation are taken into consideration. A 0.2% strain yield line is also included for reference.

The effect of elastic anisotropy is captured by varying the Zener's factor Z. This is shown in Figure 4.7, which displays the stress strain response curve obtained for two extreme values of the Zener's factor. For a single crystal oriented with the crystal lattice un-rotated with respect to the global axes (0 degrees), the stress curves show identical response with different values of Z. However, the value of Zener's Factor Z has a noticeable influence when the grain orientation inclines to 45 degree. In particular, a large value of anisotropic Z leads to a stronger elastic and initial plastic

response of materials due to a larger transversal elastic constant C_{44}. The Zener's Factor Z has ignorable influence in the major plastic hardening part.

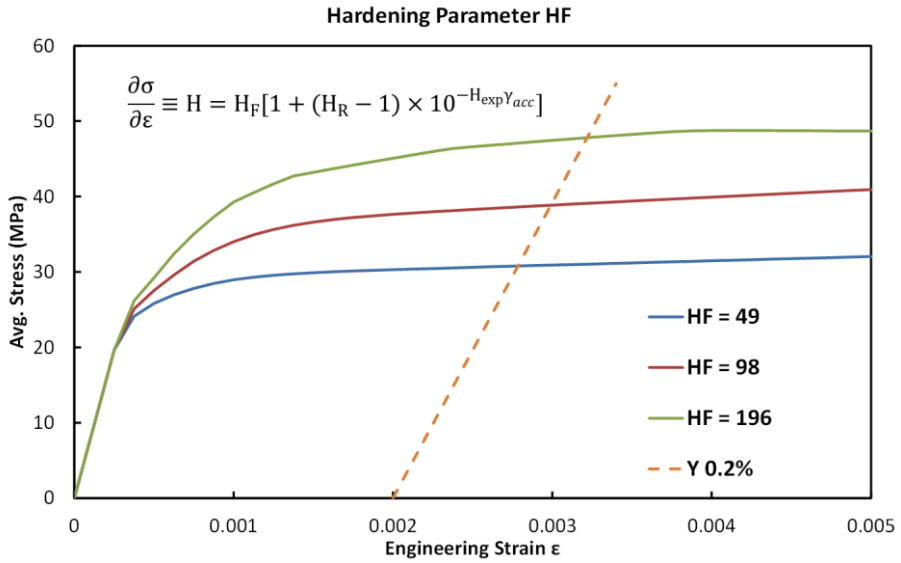


Figure 4.8. The stress strain response curves of three different values H_F of a single crystal specimen modelling with crystal plasticity finite element. The grain is with 9MPa as its critical resolved shear stress and 0 degree orientation. A 0.2% strain yield line is also included for reference.

The tensile stress σ versus applied strain U/L responses of the crystal plasticity finite element specimen with different values of hardening parameter H_F are shown in Figure 4.8. Parameter H_F shows no influence on the elastic response and the onset point of plastic flow. The main influence of the hardening parameter H_F on the material plastic performance is on the slope of the hardening part of stress strain curve. A larger H_F enables the corresponding polycrystalline material to exhibit a much stronger plastic response. For example, the curve $H_F = 196$ achieves 42 MPa under 0.2% engineering strain, much larger than the counterpart value with $H_F = 49$, only about 28 MPa subjected to the same strain level. In particular, H_F strongly affects the initial hardening slope near the onset of plastic flow while the final slope (when the accumulated plastic strain is large enough) is less dependent on H_F. This can also be verified from mathematical aspect in the hardening formula. A material with $H_F = 0$ would exhibit a perfect-elastic like behaviour.

Hardening parameters, H_F, H_R and H_{exp}, in eq.(4.3) are also varied simulations with a 0 degree orientation grain to study their influence on the hardening behaviour of in the single crystal material. Please see the Appendix III for more details.

Although the CPFE formulations employed in this project are rate-independent, a step configuration with sufficient long time step is still required in ABAQUS. This configuration is set to make sure that the stress strain response curve obtained from crystals modelled with CPFE formula is rate-independent. Details can be found in Appendix IV.

4.2.4 Summary

In this section, simulations of uniaxial tension on a rectangular film specimen that is modelled with a rate-independent crystal plasticity finite element formula have been carried out. These simulations help understand the crystal deformation mentioned in Chapter 2 and the CPFE formulations mentioned in Chapter 3. The mechanical behaviour of specimens during uniaxial tension loading condition has been investigated with the focus on their microstructure, including the grain orientation, grain distribution and anisotropy etc. Also, the sub-region of CPFE is able to output corresponding boundary conditions to the adjacent plastic sub-region, which indicates CPFE sub-region is ready to work for the prospective coupling method.

4.3 Tension Problem Solving with Discrete Dislocation plasticity

The discrete dislocation plasticity philosophy has been briefly introduced in Chapter 3. In the uniaxial tension case, we employ the superimpose approach to solve displacement and stress field. The application of DDP method in the uniaxial tension helps understand dislocation theory and formulations that is mentioned in Chapter 2 and 3 by performing parametric studies on variables that are relevant to dislocation structure. Besides, numerical results of DDP calculations provide comparison data, e.g. stress-strain response curves and dislocation density evolution curves to the upcoming coupling methodology.

4.3.1 Methodology

The implementation details of DDP formulations used in the uniaxial tension problem is stated as flowing.

Usually, at the beginning of a simulation, the material is initially taken as a dislocation and stress free continuum, but dislocation dipoles with Burger's vector $\pm\mathrm{b}$ $|\mathrm{b}| = 0.25\mathrm{nm}$ can be generated from various dislocation sources (in order to mimic Frank-Read sources), which are pre-existent and randomly distributed on slip planes in the material. Nucleation criterion is stated as that the magnitude of the resolved shear stress at the source exceeds a critical value τ_{nuc} during a time period t_{nuc}. The signs of dislocations are determined by the sign of the resolved shear stress causing the nucleation while the distance between the two dislocations at nucleation, L_{nuc}, is taken such that the attractive stress that the dislocations exert on each other is equilibrated by a shear stress of magnitude τ_{nuc}. Once nucleated, the dislocations glide apart with a velocity based on the Peach-Koehler force and the drag coefficient along the predefined slip planes. The Peach-Koehler force is given by

$$f^{(I)} = m_i^{(I)} \left[\hat{\sigma}_{ij} + \sum_{J \neq I} \hat{\sigma}_{ij}^{(J)} + \sum_{ij}^{(I)} \right] b_j^{(I)} \tag{4.1}$$

where $m_i^{(I)}$ is the unit normal of the slip system on which the dislocation with Burgers vector $b_j^{(I)}$ and $\sum_{ij}^{(I)}$ is the image field on dislocation I due to the traction-free surface. The glide velocity is the ratio of the Peach-Koehler force and a drag coefficient, given by:

$$V^{(I)} = \frac{f^{(I)}}{B} \tag{4.2}$$

where B is the drag coefficient with the value $B = 10^{-4}Pa$. A cut off glide velocity is set as $v_{cut-off} = 20m/s$ which is with the same value as in [1, 250]. The introduction of cut off velocity aims to improve the simulation efficiency although it could bring side effect to the simulation results e.g. shown in [251]. Annihilation of a pair of dislocations with opposite signs on the same slip plane occurs when the distance between them within a material-dependent critical annihilation distance L_e. In this project, apart from otherwise specified, L_e is set as $6b$. Dislocation sources are randomly distributed on slip planes that are spaced $100\mathrm{b}$ apart, with a density ρ_{nuc} in the specimen. Each source is randomly assigned nucleation strength τ_{nuc} generated from a Gaussian distribution with average $\bar{\tau}_{nuc} = 50\mathrm{MPa}$ and standard deviation $1\ MPa$. The nucleation time is set as $t_{nuc} = 10\ \mathrm{ns}$ for all sources. The obstacles are randomly distributed in each grain with a density ρ_{obs}. Obstacles for dislocation motion are modelled as points populated along a slip. Obstacles with a certain uniform assigned strength τ_{obs} are able to pin dislocations that are about to glide through those sites. Dislocations are released from an obstacle if the applied Peach-Koehler force on the obstacle exceeds $\tau_{obs}b$.

Two sets of source and obstacle densities in specimen are considered: a low source density grain (LSD) case with $\rho_{nuc} = \rho_{obs} = 56\mu m^{-2}$ and a high source density (HSD) case with $\rho_{nuc} = 200\mu m^{-2}$, $\rho_{obs} = 100\mu m^{-2}$. LSD grain represents a typically low-defect specimen while there are lots of potential nucleation sites in HSD grain.

Except for the comparison between grain types, each grain in the polycrystalline specimens has slip systems at $\phi^{(\alpha)}\ (\alpha = 1, 2\ 3) = \pm 54.7°$ and $0°$ which corresponds to the set of orientations termed FCC-like in[248].

A small time increment $\Delta t = 0.5\ ns$ is adopted in order to resolve the dislocation activities. A rather high loading rate $\dot{\mathrm{U}}/\mathrm{L} = 2000\ \mathrm{s}^{-1}$ is prescribed to obtain an engineering strain of 0.01 in 10 000 time steps. The specimen width varies from $w = 0.5\ \mu m$ to $w = 4.0\ \mu m$. For one set of simulations, the specimen aspect ratio is fixed at $L/w = 1.5$ in order to compare simulation and experimental results [252]. For the other set of simulations, aimed at studying the response of samples whose size is similar to the part of the specimen described using DDP in the coupled simulations, the specimen length is fixed at $L = 6\ \mu m$.

4.3.2 Problem definition

We aim to study the single crystal response modelling with discrete dislocation plasticity, including the size effect, under a two-dimensional uniaxial tension problem. This study also provides a primary foundation and understanding of the sub-region modelled by DDP in the following coupling calculations.

We adopt the small strain formulations of Dislocation Dynamics in [139] where a more complete description is given. Plain strain conditions are assumed and most calculations are carried out for specimens with dimensions $\mathrm{L} \times \mathrm{w} = 6 \times 2\ \mu\mathrm{m}$ with the tensile axis aligned with the x direction, see 4.9. Also, as sketched in Figure 4.9, in polycrystalline materials the grains are of size $\beta\mathrm{d} \times \mathrm{d}$, where $\beta = \mathrm{L}/\mathrm{w}$.

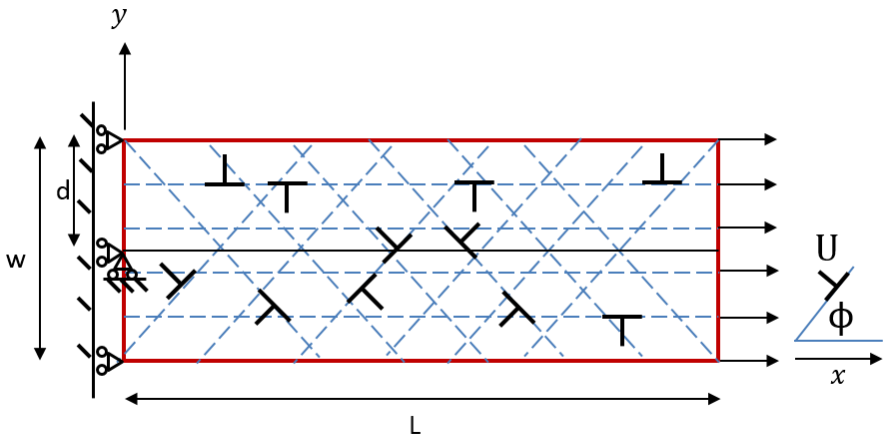


Figure 4.9. Sketch of the uniaxial tension boundary value problem analysed using Dislocation Dynamics. Both BCC-like single and polycrystalline specimens are considered.

The finite element model discretises each part of the specimen into quadrilateral plane strain elements in a regular 80×20 mesh. We use a reduced integration 4-noded bi-linear element in the mesh. All nodes along the left boundary are fixed on the X direction, while the middle node is fixed on both X and Y directions .Boundary conditions for DD parametric study are summarized as following:

$$\dot{x} = 0 \ \ at \ \ x = 0$$

$$\dot{y} = 0 \ \ at \ \ x = 0, y = w/2 \tag{4.3}$$

$$\dot{x} = \dot{U} \ \ at \ \ x = L$$

The traction on the boundary with an outward normal vector $\mathrm{n_j}$ is calculated as:

$$\mathrm{T_i} = \sigma_{\mathrm{ij}} \mathrm{n_j} \tag{4.4}$$

The applied stress σ is computed as:

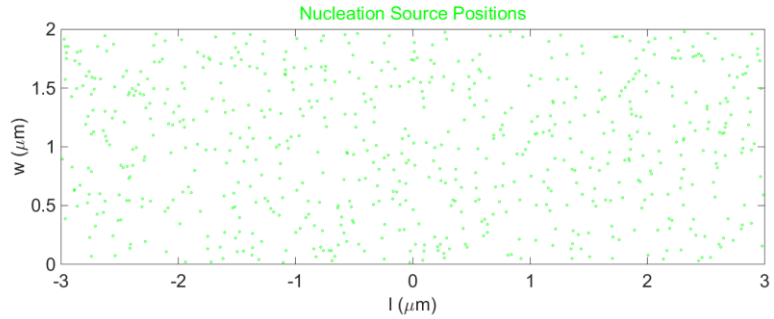
$$\sigma = -\frac{1}{w}\int_0^w T_x(0, y)dy \tag{4.5}$$

Which yields the overall macroscopic stress versus strain $\varepsilon = U/L$ response of specimens.

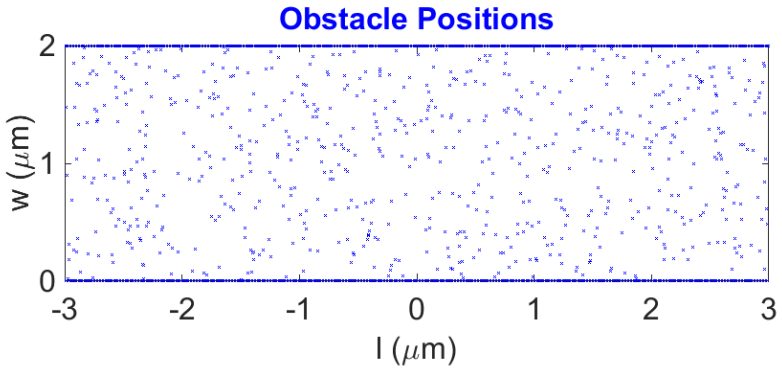
The specimens consist of elastically isotropic rectangular grains with a fixed value of Young's modulus E and Poisson's ratio ν as 70MPa and 0.33 respectively, and with three potentially active slip systems at angles $\phi^{(\alpha)}$ $(\alpha = 1, 2\ 3)$ with respect to the x_1 tensile-axis. The detailed value of $\phi^{(\alpha)}$ depends on the grain type.

4.3.3 Results

The positions of dislocation nucleation sources sites and the obstacles in the LSD specimen ($\rho_{nuc} = \rho_{obs} = 56\mu m^{-2}$) are plotted in Figure 4.10(a) and (b) respectively. From that figure, it is seen that both distribution of dislocation nucleation source sites and obstacles are random. Moreover, dislocation sources and obstacles are assigned along the predefined slip planes with orientations: $\phi^{(\alpha)}$ $(\alpha = 1, 2\ 3) = \pm 54.7°$ and $0°$ with respect to the X axis. It is also noting that there are no obstacles generated along any boundary of DD specimen which indicates that all boundaries are modelled as free surface. Thus dislocations are allowed to pass them and leave a displacement step when they are about to leave the crystal.



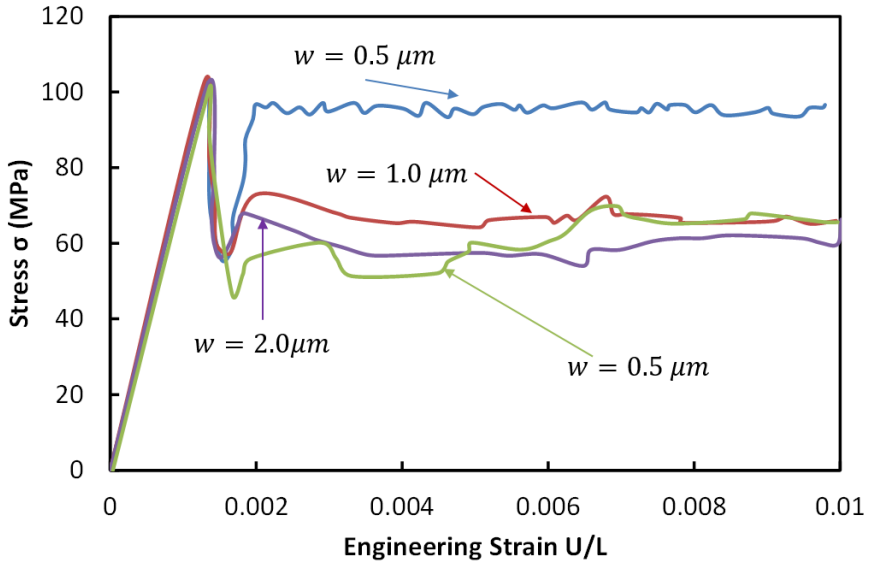
(a)



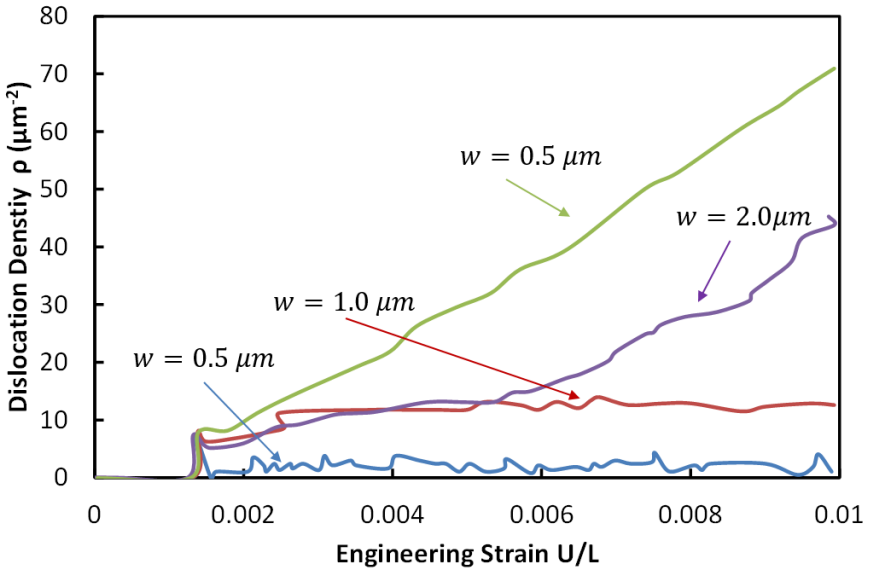
(b)

Figure 4.10. The distribution of (a) dislocation nucleation source sites and (b) obstacles predefined in the single LSD crystal specimen ($\rho_{nuc} = \rho_{obs} = 56\mu m^{-2}$) used in the DD uni-axial tension problem

The overall stress, σ , versus applied strain, U/L, responses of four specimens with the fixed aspect ratio but different sizes of LSD single crystals are shown in Figure 4.11(a). In all calculations in Figure 4.11(a), the first dislocation activity occurs at $\sigma = 100\text{MPa}$ consistent with the resolved shear stress on the current slip systems achieving the nucleation stress $\bar{\tau}_{nuc} = 50\text{MPa}$. After the yielding, for all specimens, there is a sharp drop (due to the sudden burst of dislocation nucleation) in the stress followed by an ideally plastic response. For the specimen with width$w = 0.5\mu m$, the stress level fluctuates around$\sigma = 95\text{MPa}$, which is consistent with the stable periodical fluctuation of the corresponding dislocation density in the specimen, see Figure 4.11 (b). In Figure 4.11 (b), the dislocations density ρ_{dis} (defined as number of dislocations per unit area in the specimen of size) is plotted against the applied strain. For small sizes specimen ($w = 0.5\mu m$ and $w = 1.0\mu m$), dislocation densities level off at a certain value that reveals that the number of dislocations exiting and nucleation are the same, and ρ_{dis} scales with the specimen size. For larger size specimen, dislocations density ρ_{dis} continues to increase with strain up to the maximum value here.



(a)



(b)

Figure 4.11. Uniaxial tensile response curves of the LSD ($\rho_{nuc} = \rho_{obs} = 56\mu m^{-2}$) single crystals. (a) Overall stress, σ, versus strain, U/L, and (b) evolution of the dislocation density with strain. Curves are shown for different values of the specimen size w with a fixed aspect ratio$L/w = 1.5$.

The overall stress, σ , versus applied strain, U/L, responses of four specimen with the fixed aspect ratio but different sizes of LSD single crystals are shown in Figure 4.12(a). In all calculations in Figure 4.12 (a), the first dislocation activity occurs at $\sigma = 75\text{MPa}$ consistent with the resolved shear stress on the current slip systems achieving the nucleation stress $\bar{\tau}_{nuc} = 50\text{MPa}$. Notice that the initial nucleation stress is lower than the case in Figure 4.12(a) as the slip system orientation is more preferable. After the yielding, for all specimens, there is a sharp drop (due to the sudden burst of dislocation nucleation) in the stress followed by an ideally plastic response. Unlike the result of simulation set with a fixed aspect ratio, the width does not show an apparent and uniform effect on the crystal response. For the specimen with width $w = 0.5\mu m$ and $w = 4.0\mu m$ the stress level fluctuates around $\sigma = 65\text{MPa}$ as an elastic perfect plastic response. For the specimen with width $w = 1.0\mu m$ and $2.0\mu m$, the stress level continues to increase after the yielding and shows an noticeable hardening performance. From the dislocations evolution figure, the relationship between the plastic behaviour and dislocation density is revealed clearly. The plastic stress level of single crystal is largely relieved by the activities of dislocations. In particular, a large value of dislocation density leads to a lower stress response of materials. This trend is different from the simulation set with a fixed aspect ratio.

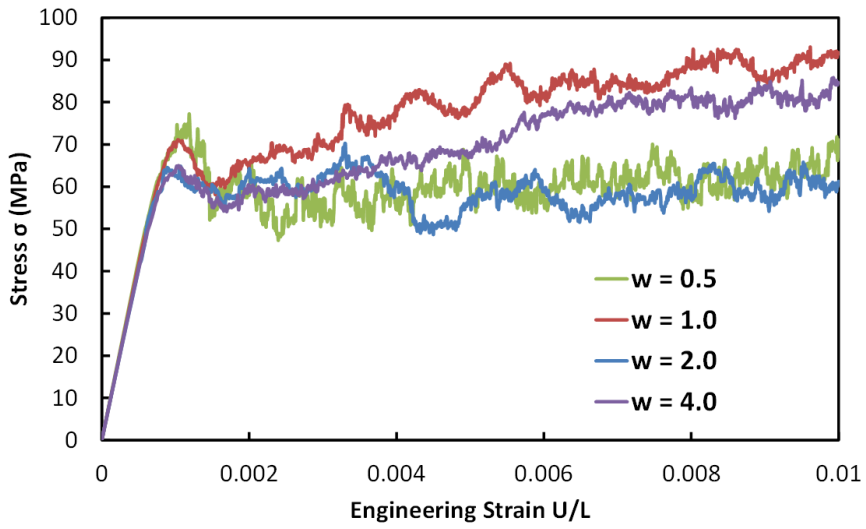
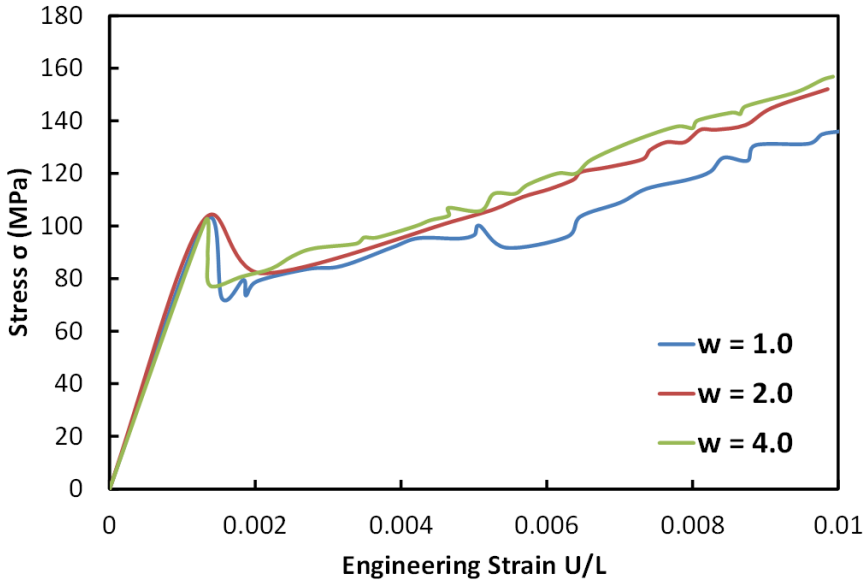
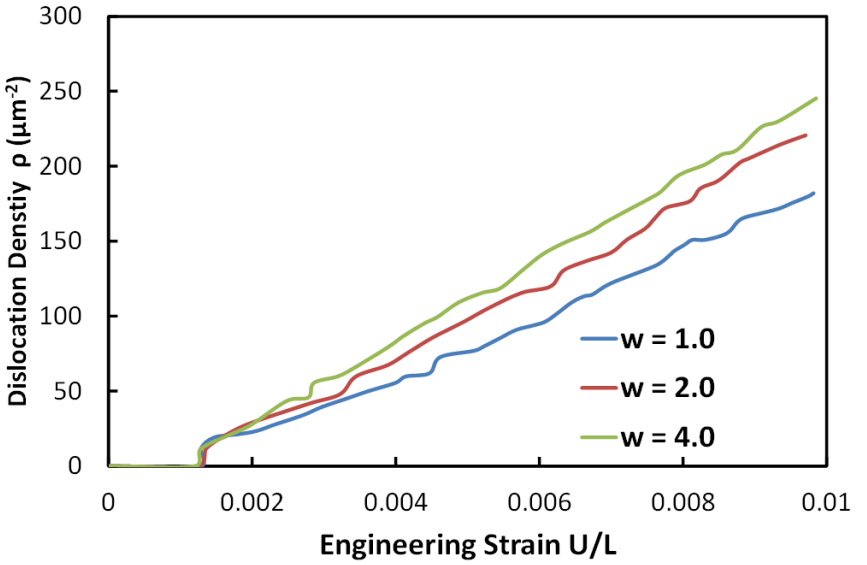


Figure 4.12. Uniaxial tensile response curves of the LSD ($\rho_{nuc} = \rho_{obs} = 56\mu m^{-2}$) single FCC crystals. (a) Overall stress,σ, versus strain, U/L, and (b) evolution of the dislocation density with strain. Curves are shown for different values of the specimen size w with a fixed length $L = 6\mu m$.

The overall stress strain response and the evolution of the dislocation density in the polycrystalline specimens are plotted in Figure 4.13(a) and (b), respectively, for three selected specimen sizes. The initial drop after the initial dislocation nucleation is not that sudden and the magnitude also decreases compared to the response of single crystal specimens. Besides, the post-yield response of polycrystalline specimens, including the stress level and dislocation density is much less dependent on the specimen size. The applied stress and the dislocation density only slightly higher in the $w = 4.0\mu m$ specimen compared with the $w = 1.0\mu m$ specimen.



(a)



(b)

Figure 4.13. Uniaxial tensile response curves of the LSD ($\rho_{nuc} = \rho_{obs} = 56\mu m^{-2}$) single FCC polycrystalline specimens with grain size $d = 0.5\mu m$. (a) Overall stress,σ, versus strain, U/L, and (b) evolution of the dislocation density with strain. Curves are shown for different values of the specimen size w with a ratio $L/w = 1.5$.

The overall stress, σ , versus applied strain, U/L, responses of four specimen with the dimension $L \times w = 6\mu m \times 2\mu m$ but different values of dislocation nucleation source density of LSD single crystals are shown in Figure 4.14. They are all classified as low source density crystals. From the figure, a lower dislocation nucleation source density generally leads to a delayed yield of the specimen, especially apparent in the case of $\rho_{nuc} = 10\mu m^{-2}$. It increased the yield point of the material to around 65MPa while the yield stress of the material with dislocation nucleation source density $\rho_{nuc} = 40\mu m^{-2}$ is only 25MPa. This hardening effect is introduced by the starvation of dislocation nucleation sources in the specimen. The yield of materials is delayed when the stress field exceeds the yield point but there are not enough

nucleation sites. Thus, the material is generally hardened afterwards. Another noticeable point is deducted from the fact that stresses are similar among the response of specimens with $\rho_{nuc} = 20, 30 \ and \ 40 \mu m^{-2}$. Therefore the starvation of dislocation nucleation is largely relived at those levels, which reveals there is a critical value of dislocation nucleation source density between 10 and $20 \ \mu m^{-2}$ dominating the starvation effect.

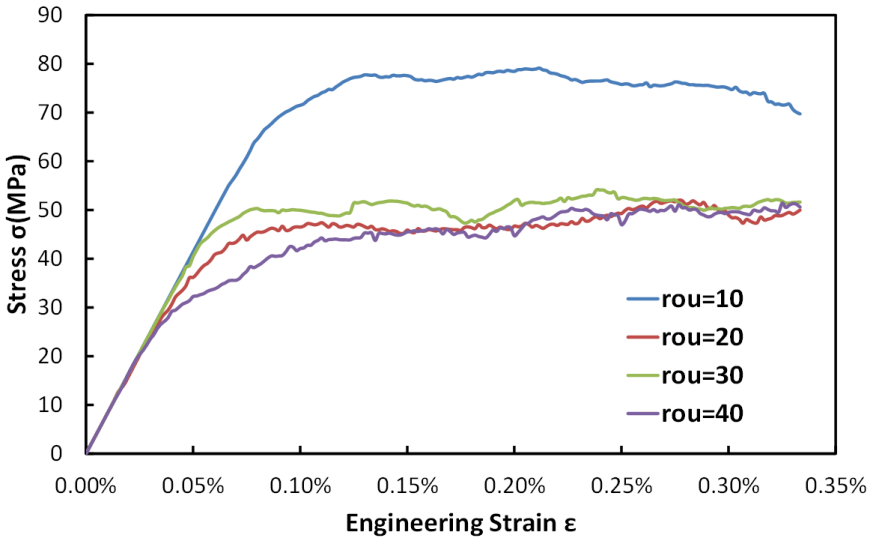
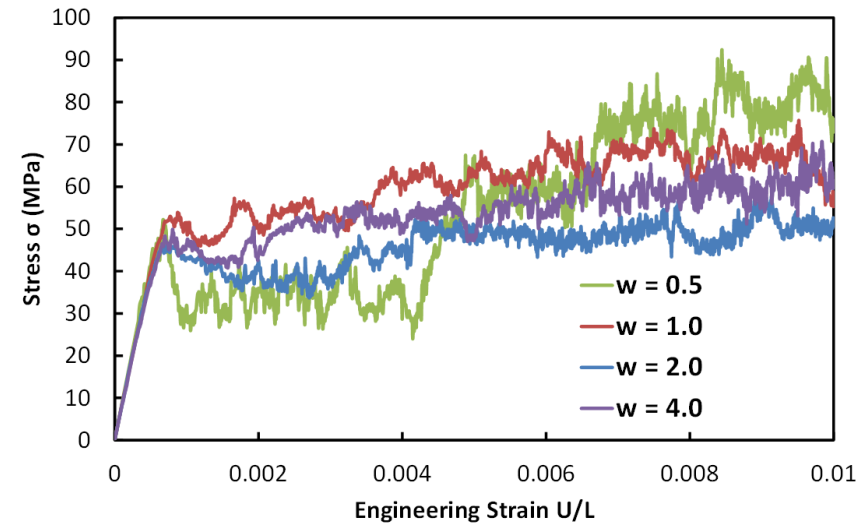
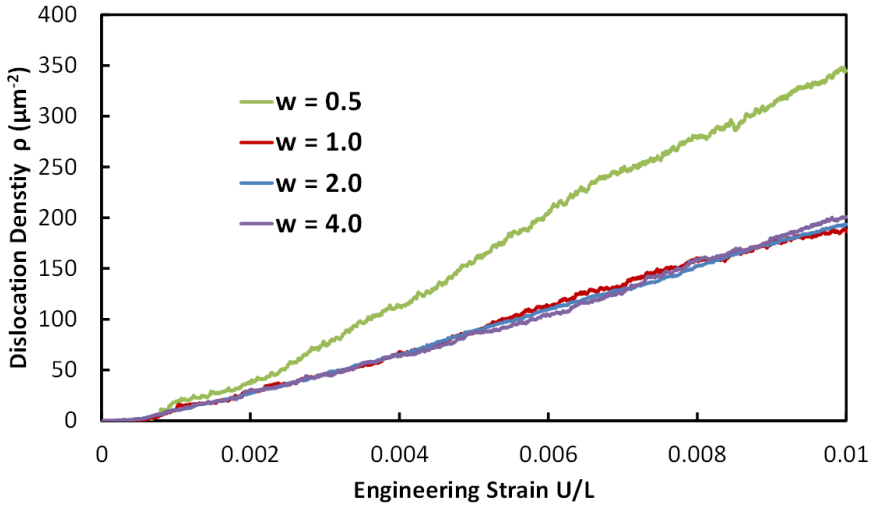


Figure 4.14. Uniaxial tensile stress strain response curves of single FCC crystals with four different values of dislocation nucleation source density. Curves are shown for different values of the same dimension $L \times w = 6\mu m \times 2\mu m$.

The tensile stress–strain responses and dislocation density evolution of the HSD single crystal specimens are reported in Figure 4.15 (a) and (b), respectively, for four selected specimen sizes. For the specimen with a large width $w \geq 1.0\mu m$, the stress strain curves show a perfect plastic response without too much hardening, and their flow strengths are quite similar. Correspondingly, their dislocation density curves are almost overlapped. Thus, the response of single crystals with adequate dislocation nucleation sources is less size dependent. Another noticeable point is the second hardening of the specimen with width $w \geq 0.5\mu m$ taking place at the strain level $\varepsilon = 0.4\%$. With the rapid increase of number of dislocations, dislocations pile up at the boundary of the specimen so that the back effect of these piling up dislocations hardens the crystal, see Figure 4.15. The major difference between responses of the HSD and LSD materials is that both the flow strength and the hardening rate in the HSD materials are reduced from the corresponding values in the LSD.



(a)



(b)

Figure 4.15. Uniaxial tensile response curves of the HSD ($\rho_{nuc} = 200\mu m^{-2}$ $\rho_{obs} = 100\mu m^{-2}$) single FCC crystals. (a) Overall stress,σ, versus strain, U/L, and (b) evolution of the dislocation density with strain. Curves are shown for different values of the specimen size w with a fixed length $L = 6\mu m$.

In Figure 4.14(a) and Figure 4.15(a), regardless of the dislocation nucleation source density, we find there are always a sudden drop of stress due to a dislocation nucleation burst, which follows the first yield of the material. However, the sudden drop has not observed experimentally on either a single crystal [252-254] or a polycrystalline material. In order to solve that problem, the large stress drop can be reduced by enlarging the individual different among nucleation sources, i.e. increasing the predefined value of the standard deviation of the nucleation sources strength. The magnitudes of sudden drop in the single material response are about 40MPa and 15MPa with the standard deviation 1MPa and 14MPa respectively. Alternatively, it is also feasible by setting an initially present dislocation structure to eliminate the drop completely [139].

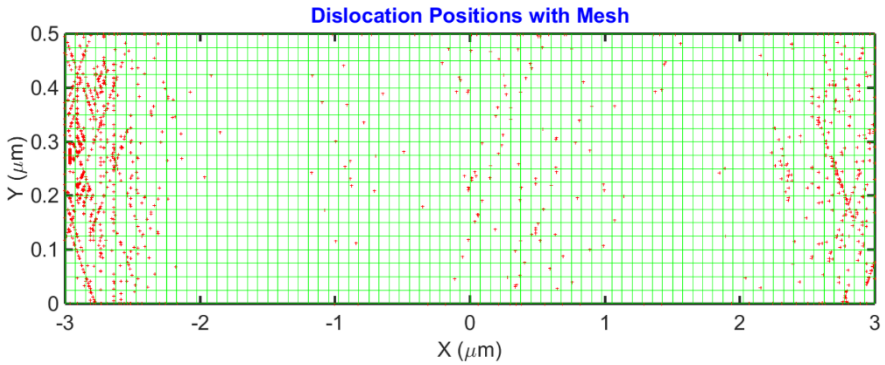
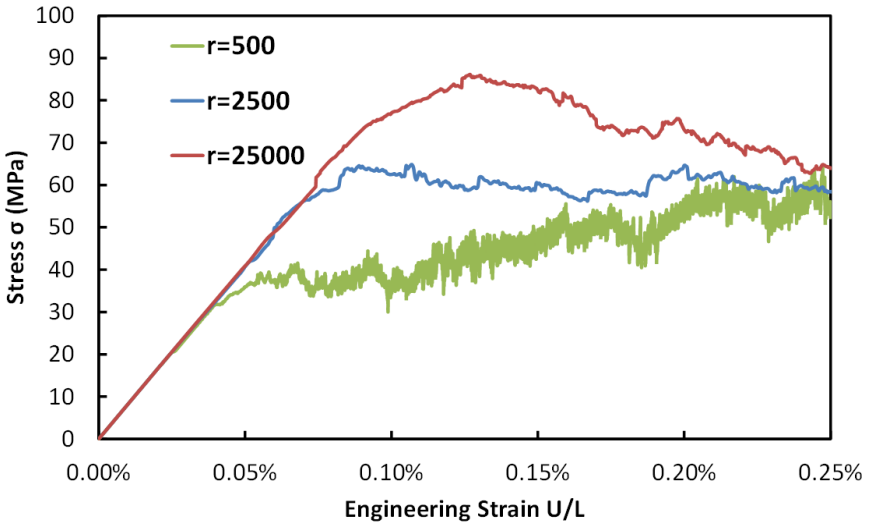
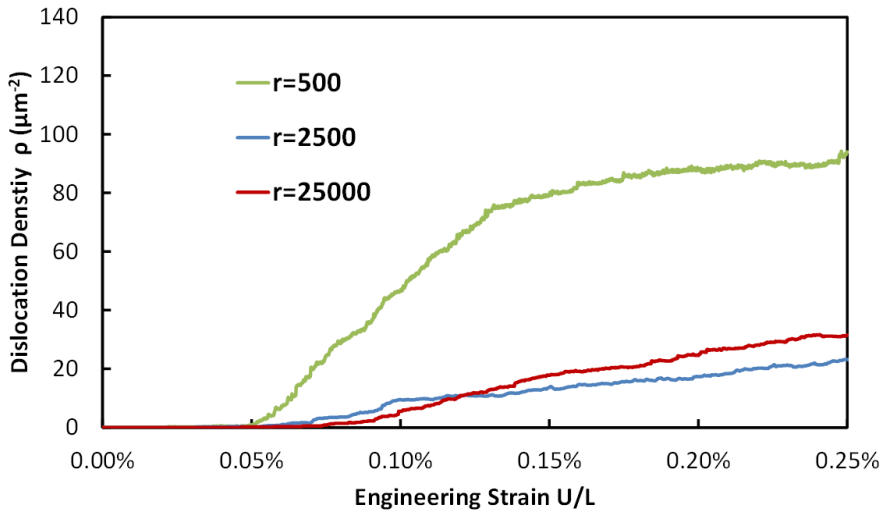


Figure 4.16. the dislocation structure with undeformed FE mesh of the HSD single crystal tension with the engineering strain level$\varepsilon = 1.0\%$. A large amount of dislocations are found pinning (piling up) at left and right boundaries of the crystal.

The tensile stress–strain responses and dislocation density evolution of the LSD single crystal specimens with the same geometry dimension $L \times w = 6\mu m \times 2\mu m$ are reported in Figure 4.17(a) and (b), respectively, for three selected loading rates $\dot{U}/L$ at the right boundary of specimens. As seen in Figure 4.17 (a), the hardening performance of specimens are strongly affected by the loading rate. In particular, a quick loading rate leads to a stronger hardening response of the crystal. For instance, the macroscopic stress level generated by $\dot{U}/L = 25000/s$ is able to achieve up to 86 MPa while the maximum stress value of $\dot{U}/L = 500\ /s$ is found to be only 50 MPa. But the flow stress generated by different loading rate when the strain continues to increase are almost identical as $\sigma_0 = 60$ MPa. The corresponding dislocation density evolution curves in Fig (b) also show that a smaller value of loading rate generally generates larger dislocation density. The loading rate effect is physically related to dislocation activity, especially dislocation nucleation. A slow loading rate benefits dislocations nucleation, and allows dislocation to move fully within a certain increment instead of rushing into an unbalanced status. This quasi-static-like effect thus enables the stress level in the crystal to be relieved.



(a)



(b)

Figure 4.17. Uniaxial tensile response curves of the LSD ($\rho_{nuc} = 56\mu m^{-2}$ $\rho_{obs} = 56\mu m^{-2}$) single FCC crystals. (a) Overall stress,σ, versus strain, U/L, and (b) evolution of the dislocation density with strain. Curves are shown for specimens with a fixed geometry dimension $L \times w = 6\mu m \times 2\mu m$ but subjecting from different loading rates respectively.

4.3.4 Discussion

In the dislocation dynamics calculations, the polycrystalline materials performance show little dependence on the specimen size. By contrast, the flow stress of the single crystal material generally increases with a decreasing specimen size, i.e. the grain size. The relationship between the stress response and the grain size revealed dislocation dynamics calculations is effectively the well-known Hall-Petch effect. The simulation results of [110] prove that the discrete dislocation dynamics is able to predict a Hall-Petch like grain size dependence of the yield strength, as well as other plastic feature including the hardening rate, Hall–Petch exponent and Bauschinger effect dependent on the dislocation nucleation source density.

For single crystal specimens within a certain size range (from $w = 0.5\mu m$ to $w = 4.0\mu m$ herein), there is a strong size effect of the material performance. In particular, the plastic flow strength decreases and the dislocation density increase with increasing specimen size. One argument to the size effect is demonstrated that there are more dislocations nucleation sources larger dislocation sources than small specimens (as the density is independent of the specimen size) and are more likely to have a weak source from statistics prospect. The other proposed mechanism [139]believes that the origin of the size dependence of the tensile flow strength in single crystals is a result of the dislocations exiting the specimen at a rate greater than the nucleation rate of new dislocations dipoles. The size effect of the uni-axial tension is a typical example for illustrating the advantage of dislocation dynamics plasticity compared to the strain gradient plasticity. There is no strain gradient in uni-axial tension analysis so that the strain gradient plasticity computation cannot predict the size effect (i.e. the results are the same as crystal plasticity). However, thanks to the

presence of dislocation activity, dislocation dynamics plasticity is able to present the size effect as shown above.

For polycrystalline specimens with a fixed grain size and a certain size (from $w = 0.5\mu m$ to $w = 4.0\mu m$ herein), that mechanism of size dependence is suppressed in the polycrystalline material as the grain boundaries prevent further dislocation glide. On the other hand, the origin of the size effect is attributed to the applied macroscopically applied strain gradient that is associated with the geometry necessary dislocations, GND (See [10]). This mechanism is also able to explain that decreasing specimen size yields a stronger response at small specimen sizes.

4.4 Comparison between responses of CPFE and DDP descriptions in tension problem

Both stress strain response curves of CPFE and DD calculations can correctly predict the macroscopic material plastic hardening performance under a uniaxial tension load. Moreover, the stress strain curves of DD predictions provide CPFE simulations with necessary information in order to obtain a set of CPFE input parameters (including critical shear stress and empirical hardening parameters) for calibration. However, the detailed response of CPFE and DD illustrates the difference between the mechanisms of two approaches. Firstly, there are some fluctuations (including some random material softening) along the stress strain response curve of DD predication due to some stochastic dislocation activities, including nucleation, annulation and being pinned. The counterpart of CPFE curve exhibits a perfectly smooth hardening behaviour due to a continuum material definition. Secondly, the detailed stress filed of single crystal CPFE simulation (see Figure 4.18 (a)) shows a more homogenous result in contrast to the DD predictions with some apparent stress concentration (see Figure 4.18 (b)) due to the dislocation singularity. Thirdly, as shown in the previous section, DD is able to predict the polycrystalline material performance with explicitly predefining the rigid grain boundary. The Hall-Petch effect is successfully predicted by using DD on polycrystalline specimen with dislocations pinning at grain boundary and thus hardening the material. But CPFE results show no hardening influence of grain boundaries among grains although the inhomogeneity and anisotropy is revealed by using CPFE approach.

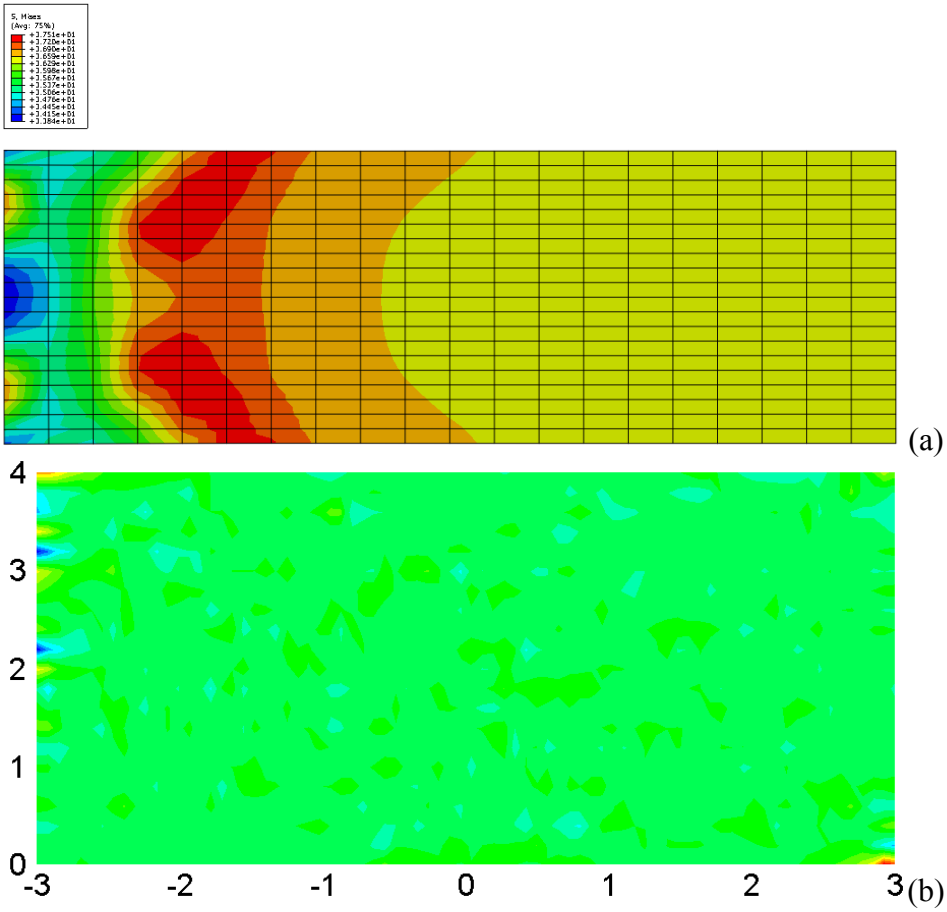


Figure 4.18. The comparison of stress field between CPFE and DDP calculations

Another important difference between the formulations of DDP and CPFE lies in the rate-dependence of the material response. As shown in previous sections, the performance of crystals modelled by DDP shows a strong dependence on the loading rate while the CPFE modelling formulation adopted here implies that the stress is rather rate-independent. DDP has a time scale in its modelling formulations, and dislocation activity is determined by that time scale parameter. However, our CPFE description is a time-independent formulation which lacks of a time scale parameter to show the rate effect. Some researchers use a time-dependent CPFE modelling method, *e.g.* in [130], with an explicitly defined time-scale parameter. The application of rate-dependent CPFE formulation can be easily incorporated in the current modelling framework and will be the subject of future investigations.

4.5 Tension Problem Solving with the coupling approach

After reporting the stress-strain response and dislocation activities of specimens under uniaxial tension loading using CPFE and DDP methods alone, the detailed implementation and results of simulations solved using the proposed multi-scale modelling approach (see Chapter 3) are illustrated in the following sections. It is worth noticing that the terminology “multi-scale” herein specifically refers to the resolution at which materials features are captured at different scales. This definition of “multi-scale” does not mean that the sub-regions (see Chapter 3) modelled using CPFE and

DDP necessarily correspond to different sizes of the domains investigated using the two different resolution.

Numerical results are compared in terms of stress-strain response, stress contour and dislocation density to verify the effectiveness of the multi-scale modelling approach and thus to reveal the coupling effect on the discrete dislocation sub-region.

4.5.1 Coupling methodology

The proposed multi-scale coupling approach between CPFE and DDP methods has been applied in uniaxial tension problem. A sub-region technique is adopted to apply CPFE and DDP description on their own sub-region. In this section, the dimension and boundary conditions of the investigated uniaxial tension problem is defined in details. Following that, the flow chart of multi-scale coupling procedure is illustrated. Finally, the implementation of the coupling procedure is reported at code and file level.

4.5.1.1 Problem definition

A two-dimensional uniaxial tension problem, schematically shown in Figure 4.19, is used as a vehicle to illustrate the implementation of the coupling procedure. The specimen is sub-divided into two rectangular $L \times H = 6\ \mu m \times 2\mu m$ regions, modelled by CPFE and DDP, respectively. The CPFE sub-model is made of a single FCC crystal, represented by the fully 3D FCC slip systems although subject to the plane strain condition, whose axes are oriented at zero degrees with respect to the reference system, i.e. parallel to the x-axis. In the DDP sub-model, also representative of a FCC crystal structure, the slip systems are $\phi^{(\alpha)} = \pm 54.7, 0, \alpha = 1,2,3$. The dislocation structure properties are summarized in Table 1.

A uniform displacement in the x-direction is applied along the right (CPFE) edge of the sample; the other end of the specimen (left edge of the DDP domain) is constrained to not move in the x-direction, and one node is also prevented from moving in the y-direction to prevent translation of the sample. The demonstration consists of 9 coupling steps, achieving $0.054\ \mu m$ final displacement (0.45% strain) on the right boundary.

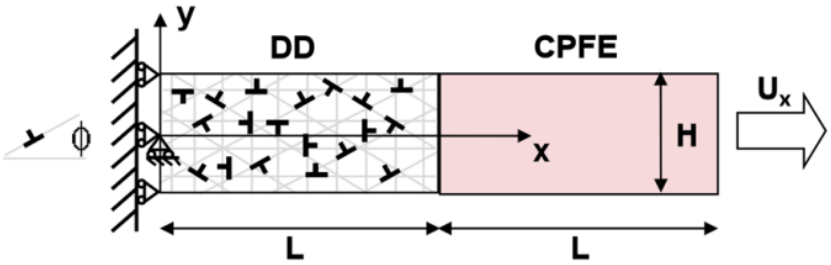


Figure 4.19. The uniaxial tension DD-CPFE coupling example.

4.5.1.2 Coupling strategy for uniaxial tension problem

After the initial calibration of the CPFE model, which is carried out to match the elasto-plastic response of the discrete dislocation model, the DD model is replaced by an equivalent elasto-plastic continuum description to initialise the simulation (the start-

up model; see Figure 4.20). This allows displacing the right hand side boundary by U_x until the onset of plasticity is exceeded, while ensuring continuity at boundary *A* during loading of the specimen; it generates an initial stress profile from the CPFE region to start the coupling, and amounts to an initial guess. The DD model is also separately initialised and set to receive the traction distribution at the interface Γ_{DD} as the boundary condition on its right face. Once the start-up model exceeds yield, the tractions are passed to the DD model.

The response of the DD model to the applied tractions is then computed. The displacements at the boundary between the two domains (the right face of the DD region) are then passed to the crystal plasticity finite element model and applied at Γ_{CPFE}. The resulting tractions at the interface between the two models are again passed to the DD model, and the cycle is repeated until convergence is reached for the level of imposed strain. The above procedure is then repeated at predefined strain targets until the maximum value of imposed displacement,$U_{x,max}$, is reached.

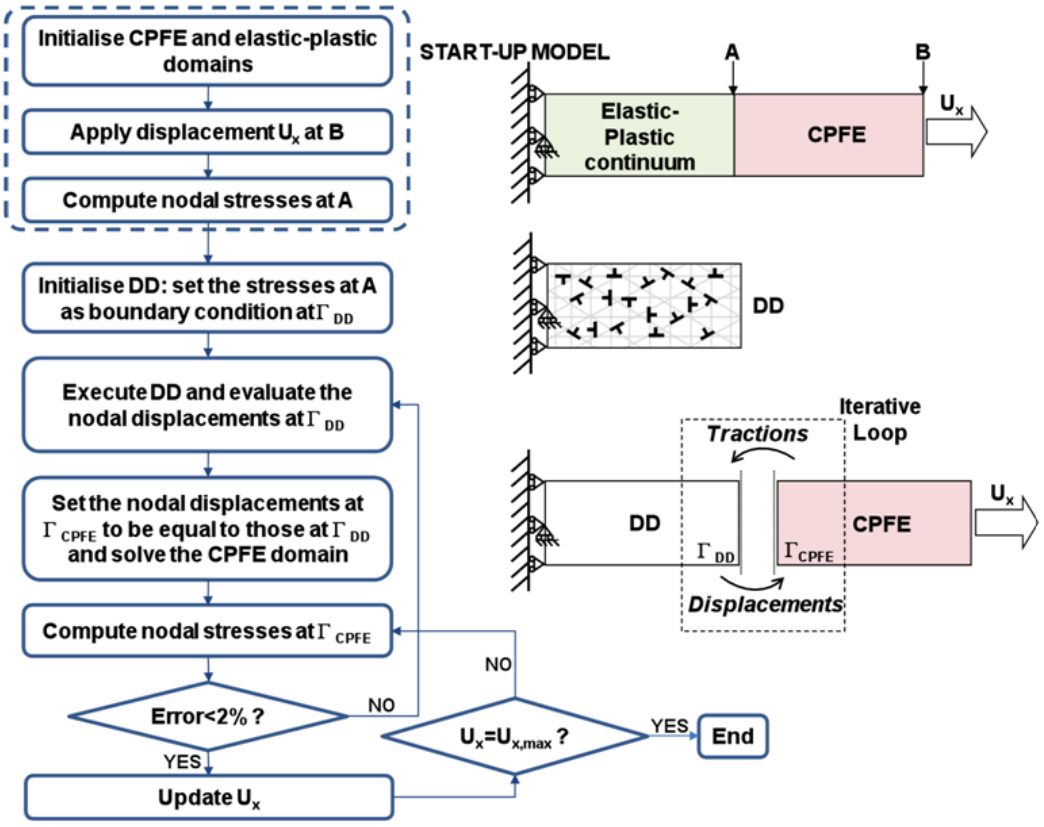


Figure 4.20. The Flow chart of the coupling procedure applied to the uniaxial tension problem.

4.5.1.3 Details of implementation of coupling codes

The whole coupling procedure on tension problem is controlled by a BASH script, which is able to call various procedures and to read and write associated files. The BASH shell script is conducted in UNIX operation system of Imperial clusters.

Before conducting the main body of coupling script, there is still some preparations work to do. The *in* and *disl.in* files are predefined according to detailed geometry and dislocation structure specification for discrete dislocation plasticity executable subroutine, while the seeds file is provided according to the calibration result for CPFE ABAQUS job. Also, the initial boundary condition (that contains 0 as boundary conditions) is given in bcout.dat file for CPFE sub-model left side boundary.

The main BASH script firstly initializes the simulations, including cleaning redundant files and creating new directories. There are two layers of loops in the whole coupling process: an internal loop for the current step convergence (tractions and displacements compatibility) and an external loop for controlling the number of loading steps, i.e. the termination of the coupling procedure. The inner loop starts imposing a new boundary condition (based on the number of loading steps) onto the right boundary of CPFE model with UDISP subroutine (which is an internal ABAQUS subroutine for applying user-defined displacement boundary conditions to models). The main BASH scripts checks whether the CPFE sub-model job has already finished every five seconds by testing whether an intermediate ABAQUS running status file, *.lck still exists in the current folder. If the CPFE job has not yet finished, the coupling procedure has to be waiting for another five seconds and re-check it again. If the result has been generated by ABSQUS successfully, the inner loop then calls the dislocation dynamics executable file to run with a new traction field passing from CPFE sub-model as boundary condition. After the discrete dislocation plasticity subroutine has been conducted (the termination of discrete dislocation plasticity code is automatically ensured by the UNIX command line), the new boundary condition file (bcout.dat) is compared to the old one file (bcout.dat). If the compatibility of tractions (i.e. the difference is less than 5%) has not yet been achieved, the main script returns the beginning of the inner loop. Old traction, displacements and errors files are stored in another folder for collecting the intermediate information when the whole coupling is finished. If the compatibility between CPFE and discrete dislocation plasticity sub-models has not yet been achieved, the main script jumps out of the inner loop and carries on a new external loop for the next coupling loading step. Once the convergence is achieved, there is a status file recording whether the internal loop is finished yet with an integer number to be flagged with a convergence flag.

The external loop starts to update the new displacement boundary conditions for CPFE right boundary when the compatibility criterion is achieved in the internal loop, i.e. the convergent sign is found out in the status file. Afterwards, the external loop script modifies by updating the boundary condition section in the INP file (ABAQUS engineering file) for crystal plasticity finite element job. The increment step of the displacement is predefined by user, and it is defined as $0.003\ \mu m$ equivalent to $\Delta\varepsilon = 0.05\%$ in this project. Thus a new displacement boundary condition applies on the right boundary of crystal plasticity finite element sub-model so that a new internal loop is started. Besides, the external loop is also capable of controlling the number of loading steps in the coupling. In this project, the total number of coupling steps is set

as nine. The main BASH script also does some cleaning and finishing work after the main body of coupling has been finished.

4.5.2 Numerical results

The uniaxial tension case was studied first to test the methodology of the proposed concurrent coupling strategy. A comparison was performed between the response obtained using two coupled solutions: (i) the first approach employs a simple non-iterative and unidirectional coupling, whereby the tractions are passed from the CPFE solver to the DDP region at different times during the monotonic loading of the specimens while the CPFE boundaries are not affected by the evolution of the DDP domain; (ii) the second solution is obtained making use of the proposed fully coupled iterative scheme. Stress-strain curves are plotted to illustrate the differences between the two schemes.

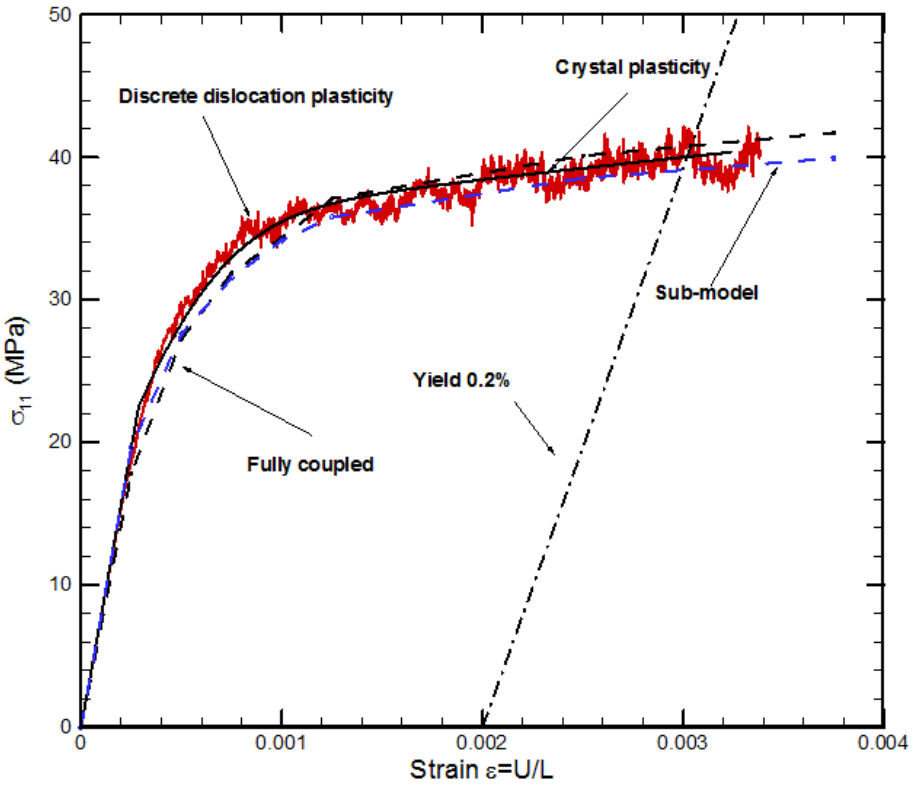


Figure 4.21. Macroscopic stress-strain curves at the right-hand side boundary for the non-iteratively coupled and fully coupled solutions. A comparison with the initial DDP and CPFE individual stress-strain responses is also shown.

Figure 4.21 depicts the macroscopic stress-strain curves for the tensile specimen shown in Figure 4.19, as predicted using the different coupling routes. The response obtained using the DDP and CPFE solutions after the initial calibration is performed are also reported on the plot and serve as references. The dashed blue curve shows the macroscopic stress-strain behaviour calculated in the DDP domain using the unidirectional coupling scheme. Although the traction distributions are correctly matched at the DDP/CPFE boundary, compatibility of displacements is not ensured

using the sub-model approach and there is no feedback from the DDP region to the CPFE; the effect is small in this simple tension calculation, which is shown only to demonstrate the algorithm, but can be significant in other problems (see the next chapter on the indentation case). The dashed black line shows the solution obtained using the iterative coupling strategy proposed by the authors. The solution is deemed convergent when the average values of the traction components at the interface between the two domains do not vary by more than 2%. The fully coupled formulation imposes displacement and traction matching at the interface between the DDP and the CPFE domains, hence produces a more accurate representation of the stress-strain response of the entire specimen than the unidirectional sub-model approach; again, the difference between the methods is considerably more pronounced in more complicated problems, which will be demonstrated later.

Previous coupling work by other co-workers is based on the iteration at a fixed stress level. In this project, the strain field is considered as a new attempt to achieve the convergence. Thus the stress "oscillates" at the same strain level (perpendicular to the X axis, see Figure 4.22).

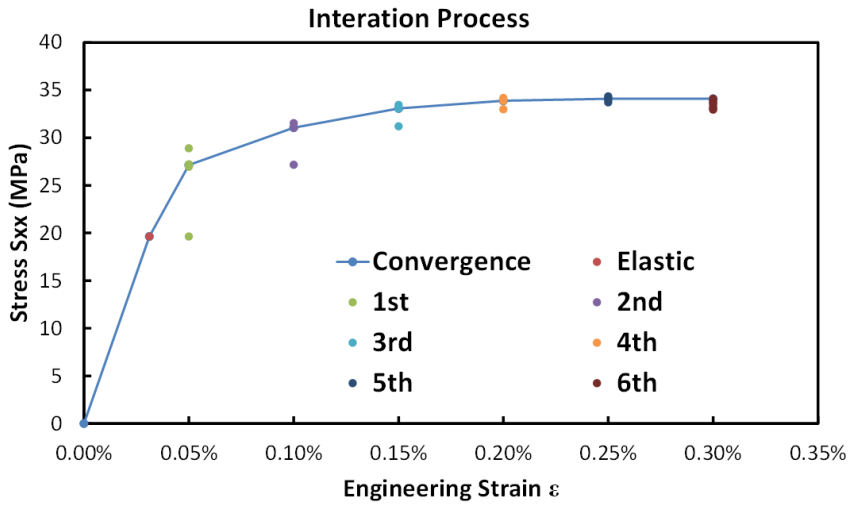


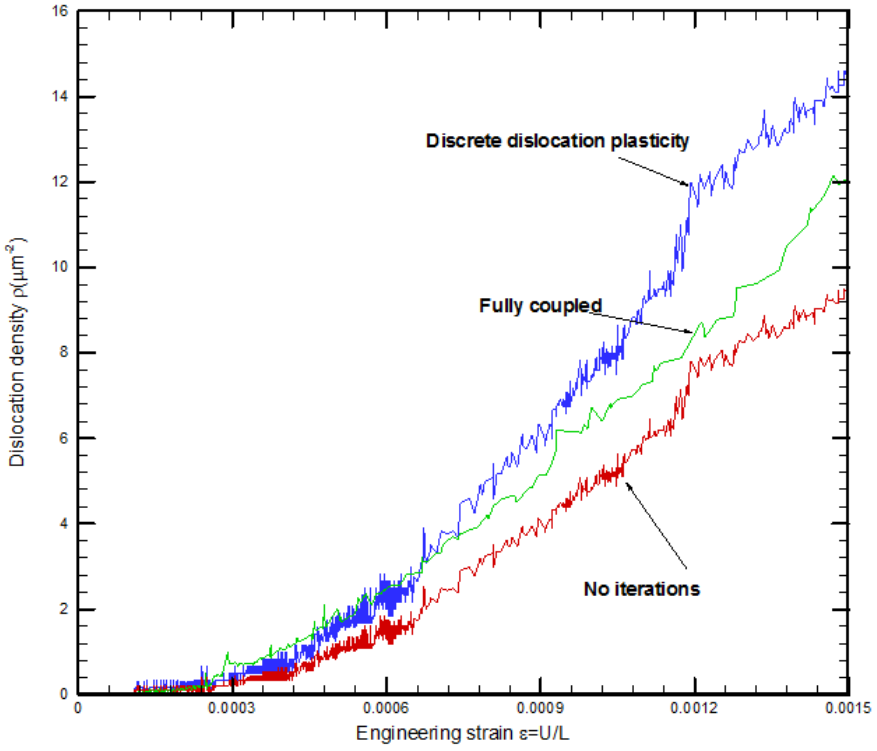
Figure 4.22. The iteration process with iteration points against the final response curve of the uniaxial specimen

Figure 4.22 illustrates the iteration process at some strain levels, compared with the final fully coupled response curve of the uniaxial tension specimen. At the strain level of 0.025% around, the material is still subjected to the elastic tension so that the iteration convergence is achieved at the first computation (only one point shown on the curve) on the crystal plasticity finite element and dislocation dynamics regions. However, after the onset of plastic, the iteration oscillates at a certain strain level (the step size is defined beforehand) until the computation between the crystal plasticity finite element and dislocation dynamics regions converges, i.e. the point almost holds at a fixed point. Besides, it can be discovered that the convergence is more easily achieved at for larger single strain level, and the oscillating magnitude of the iteration becomes smaller with the strain evolution. The reason is revealed by reviewing the

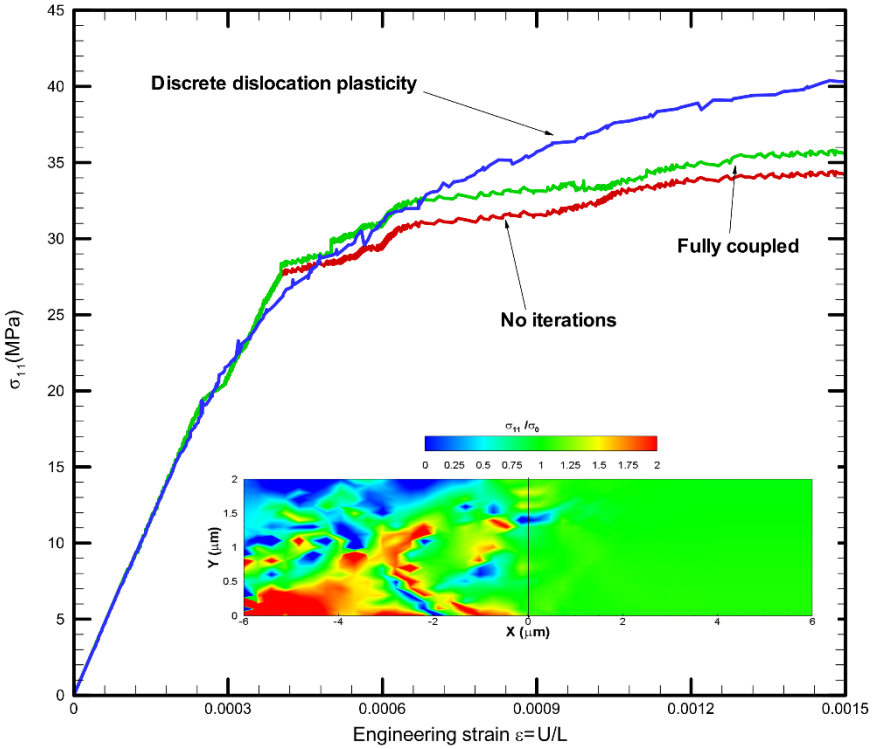
calibration (see Figure 4.21). The increase of stress reduces with increasing engineering strain that indicates the material response approaches a perfect plastic crystal. Figure 43 proves the reliability and effect of the current coupling procedure.

A comparison of the DDP response for the different solution methods at the coupling interface, in terms of the evolution of dislocation density and the macroscopic stress-strain behaviour is reported in Figure 4.23. It can be observed that the implementation of the coupling has an appreciable effect on the dislocation response, even in this simple tension problem, which also varies for the two different coupling schemes. In particular, both a greater decrease in the density of dislocations and relaxation of the stress are observed in the in DDP region, compared to the DD-only calculation.

A contour plot of the σ_{11} component of stress for the entire tensile specimen, is shown in the inset of Figure 4.23 for a strain $\varepsilon = 0.25\%$. This shows both the evolution of dislocation structures in the DDP region and the associated plastic activity and the transition between the DDP and the CPFE domains, with the continuity of stresses across the boundary portrayed.

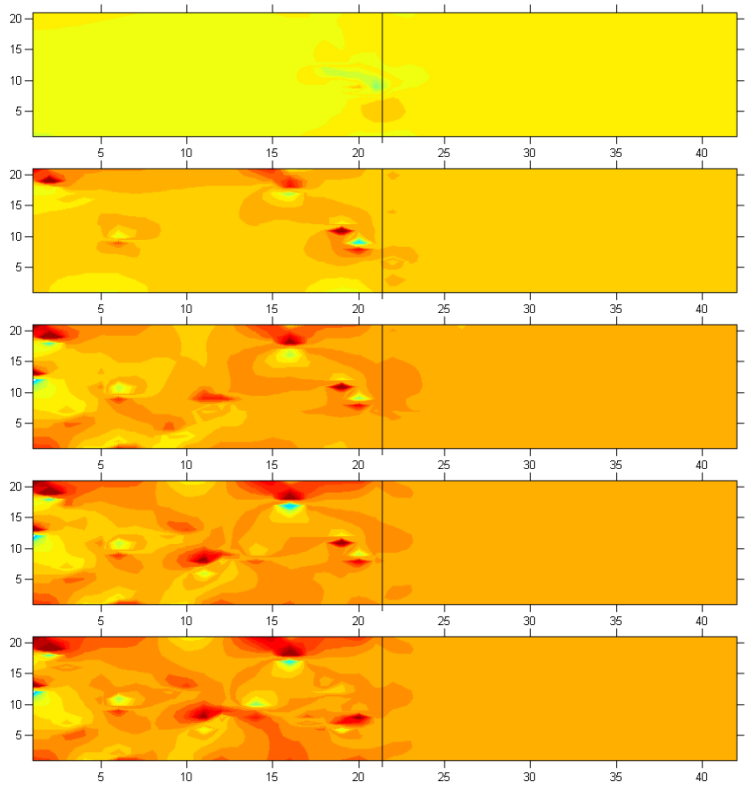


(a)



(b)

Figure 4.23. (a) Dislocation density evolution and (b) stress-strain curves at the coupling boundary for the DDP only solution, the non-iteratively coupled solution and the fully coupled solution.



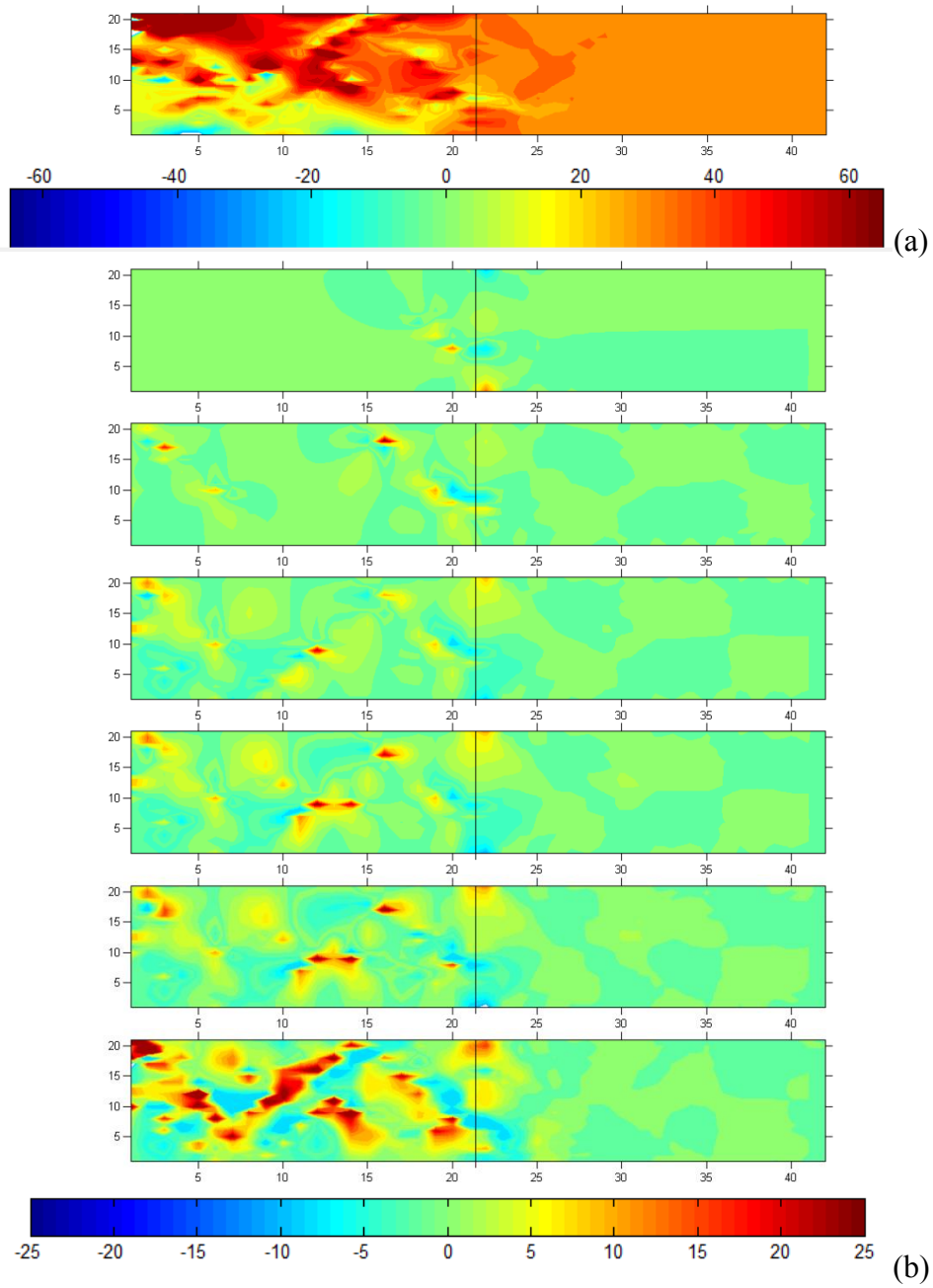
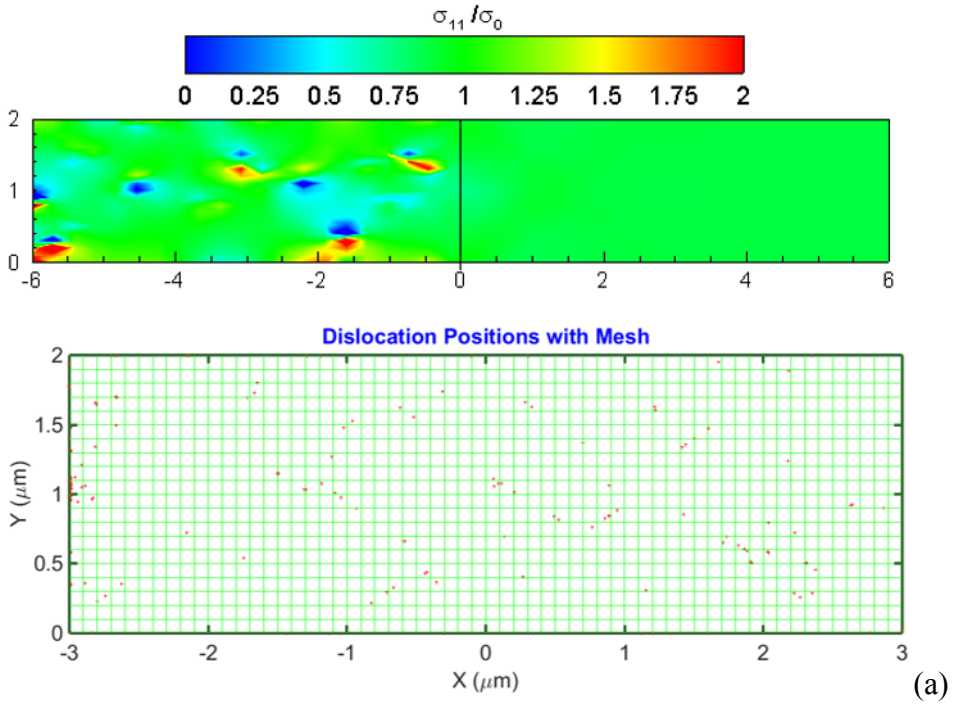


Figure 4.24. the stress field (a) the normal stress S11 (b) the shear stress S12 in the two CPFE and discrete dislocation plasticity crystals at six different coupling steps

Comments: The normal and shear stress field evolution during the coupling process at different strain levels is shown in Figure 4.24. The coordinates are based the number of nodes instead of geometry dimensions. As seen in both normal and shear stress contours, the stress compatibility is indeed obtained at each single node along the coupling boundary between discrete dislocation plasticity and CPFE grains. This improves the effeteness and applicability of the coupling method compared to those methods only aiming at the average along the coupling boundary, although this new proposed needs more efforts to achieve convergence. In the crystal plasticity finite element region, both of the normal and shear stress are nearly homogenous with the value approximately as the macroscopic stress. In the discrete dislocation plasticity

region, the normal stress fluctuates around the macroscopic normal stress. Stress concentration points are found in discrete dislocation plasticity crystals due to dislocation singularity stress field, and some dislocations near the coupling boundary introduce stress concentration into the CPFE region via the boundary conditions passing, especially at corners of coupling boundary. During the tension process, both normal and shear stress are increased and stress concentration becomes more severally especially in the discrete dislocation plasticity regions due to dislocation nucleation. Meanwhile, stress contour comparison between CPFE and discrete dislocation plasticity crystal further shows the advantage of using discrete dislocation plasticity approach. Dislocation activity provides more details of material internal response which enables dislocation dynamics approached to be suitable for some highly sensitive regions of specimens.



(a)

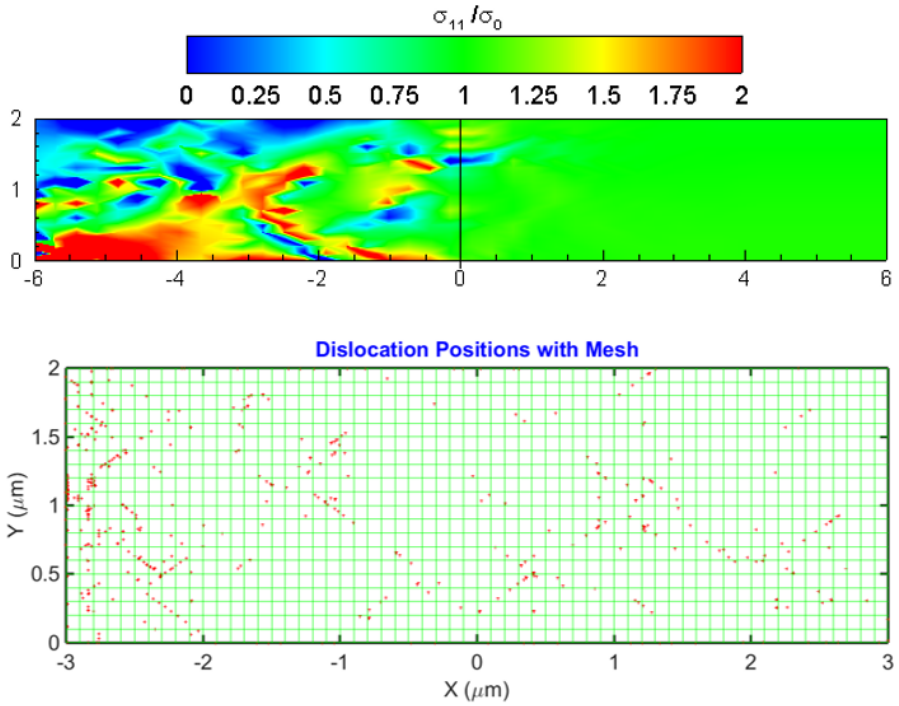


Figure 4.25. The normal stress σ_{11} contour and the corresponding dislocation structure in the discrete dislocation plasticity region of the uniaxial tension problem solved by the proposed coupling approach. Results are shown for the engineering strain level (a) $\varepsilon = 0.125\%$ and (b) $\varepsilon = 0.25\%$.

The stress level and the corresponding dislocations structure at the strain level $\varepsilon = 0.125\%$ and $\varepsilon = 0.25\%$ in the discrete dislocation plasticity region of the uni-axial tension problem are reported in Figure 4.25 (a) and (b) respectively. It is noticing that the there are some dislocations arriving at the coupling boundary at the strain level $\varepsilon = 0.25\%$ and thus resulting in some stress concentration localized a grain boundary between discrete and continuum regions, although this situation was not found when the strain level achieves $\varepsilon = 0.125\%$. This potentially indicates that there would be more severe and localized stress concentration at the coupling boundary when the strain level continues to increase. The stress concentration due to dislocations piling up at the grain boundary could lead to difficulty of convergence.

4.5.3 Computational efficiency

One of the advantages we hope to achieve by using the multi-scale coupling strategy lies in reducing the simulation time and thus improving the efficiency. The application of the proposed coupling strategy on the plain strain analysis under uniaxial tension loading indeed shows this effect. Table 4.1 shows the simulation time for the specimen with the same geometry dimension $2L \times H = 12\ \mu m \times 2\mu m$ under the same uniaxial tension loading conditions $\varepsilon_{max} = 0.3\%$ modelling with CPFE alone, discrete dislocation plasticity alone and the our proposed coupling method. It is clear seen that the coupling method effectively reduces the time cost compared to the simulation with specimen fully modelled as discrete dislocation plasticity description, although the improving effect is not quite apparent. The reason is not only attributed to the simplicity of the uniaxial tension problem but also the sub-model region

assignment. In the current study, the specimen is evenly divided into two regions with the same geometry dimension. In more practical problems, the specimen can be divided into a tiny sensitive region and a large less important region. This could further illustrate the efficiency improving effect by the coupling strategy.

Table 4.1. The simulation time cost of the reference specimen under the unxial tension loading modelled by CPFE, discrete dislocation plasticity and Coupling methods respectively.

Modelling approach	CPFE Alone	DDP Alone	Coupling
Simulation Time t (Hours)	0.6	8.0	5.2

4.6 Discussion

The validity of the proposed coupling approach has been proven via the application of the coupling methodology to the tension case, and the proposed coupling method has some remarkable features:

- Sub-models are solved in different regions in which the effect of different scales needs to be investigated and the coupling is performed at the coupling boundary between sub-models. Therefore, the proposed multi-scale coupling can be readily used to model any key region identified as being the focus of damage initiation within the meso-scale calculations performed using CPFE; employing discrete dislocation plasticity in these regions provides a higher resolution there while limiting the computational expense as DDP is only used to describe a very limited simulation domain.
- The discrete dislocation plasticity sub-model is solved in a separate code while the CPFE sub-model is solved in ABAQUS with user defined material subroutine (UMAT). This confers flexibility to the proposed modelling approach, since different material description can be easily incorporated to describe the material behaviour by simply changing the constitutive laws implemented within the finite element package. This improves the applicability of the model compared to other existing solutions that rely on *ad-hoc* codes developed for the specific purpose.
- Concurrent modelling is employed instead of hierarchical modelling, with the mutual communication between sub-models at different scales as the simulation time advances, and, hence, the applied strain increases.
- Our coupling aims at achieving the compatibility of tractions and displacements at each node along the coupling boundary between two sub-models, instead of using an average convergence scheme.
- Our coupling is able to explicitly describe the coupling boundary as an undeformable grain boundary (*i.e.*by pinning the dislocations at the domain boundary). Therefore, it is suitable to be applied to study any polycrystalline material response, *e.g.* the coupling can be used to study the dislocation activity and plastic response in the proximity of a grain boundary.
- The proposed coupling framework offers great flexibility for solving different boundary value problems. The coupling method presented in this project will provide a foundation for subsequently studying other problems where multi-scale resolution is required.

The stress strain response curve generated by the coupling method falls between the curves of DDP and CPFE method alone. This indicates that the implementation of the coupling has an appreciable effect on the dislocation response, even in this simple tension problem.

Our current coupling method applied in tension case is iterated at a fixed strain level while another trial was conducted using iteration at a fixed traction level. However, the alternative way was not able to obtain a quick convergence, although the final coupling results still fell between the discrete dislocation plasticity and crystal plasticity finite element response. Figure 4.26 illustrates the convergence problem encountered in another coupling where the boundary passing is reversed. The reason is given as the iteration scheme needs a decreasing gradient to achieve convergence. However, the gradient of engineering strain oscillates with a gradual increase of magnitude at the same stress level. The coupling based on the traction would be suitable for a multi-scale simulation of polycrystalline material under tension control. The convergence issue might be solved by matching the boundary conditions passing according to the applied external loads.

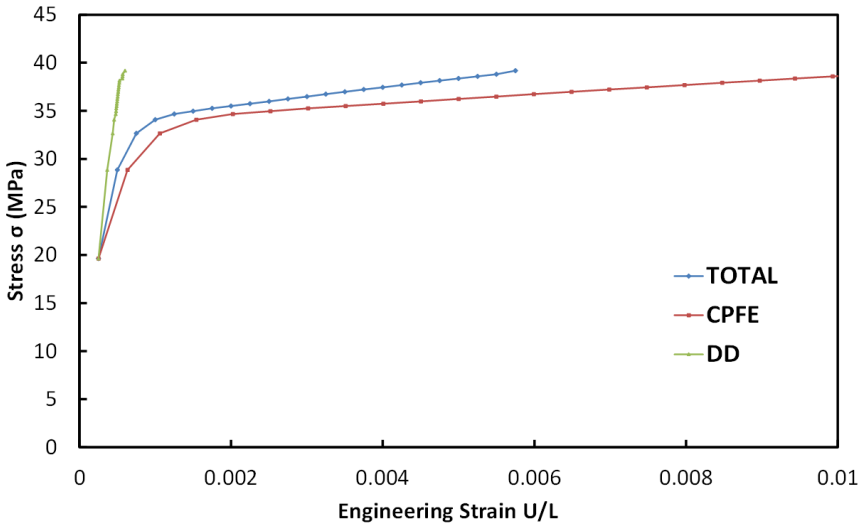


Figure 4.26. The macroscopic stress strain response of the discrete dislocation region, the crystal plasticity region and the coupling region. The results are obtained by another type of boundary condition passing where discrete dislocation region receives displacements and feedbacks tractions to crystal plasticity region.

The methodology implemented in this study produces compatibility at the interface between the two domains due to the fact that discrete dislocations produce singularities and local stress concentration induced by the presence of dislocation cores near the boundaries that cannot be transferred to the crystal plasticity region without causing unphysical behaviour. Furthermore, discrete dislocations are characterised by incompatible deformation gradients while the crystal plasticity formulation is continuous. A further aspect to be considered, as it is directly linked to the impossibility of transferring singular stresses to the continuum crystal plasticity description without generating unphysical stresses and deformations, is the lack of an

explicit representation of the dislocations in the CPFE region. In order to preserve the zero net Burgers vector in the crystal plasticity framework, schemes for capturing and correctly modelling the dislocation flux at the discrete dislocation plasticity/CPFE interface need to be developed [132]. This will be the subject of future investigations.

This multi-scale coupling approach improves the previous coupling work by Curtin [130] by focusing on localized plasticity at the interface instead of achieving compatibility with an average sense. The application of the proposed coupling approach on the uniaxial tension problem proves its fidelity in terms of dislocation structure and stress levels when the size of discrete dislocation plasticity region is sufficiently large.

However, the strain level in the loaded specimen is constrained to very small (less than $\varepsilon = 0.25\%$) in our coupling calculations. It still needs more investigation on the fidelity of proposed coupling results and interface performance when the larger strains/strain gradient, higher dislocation densities and larger strain levels are present. In fact, there are some dislocations having already piled up at the coupling boundary although the number of those dislocations is quite limited (less than 10 in total).

4.7 Summary

A planar uni-axial tension problem has been simulated by applying crystal plasticity finite element (CPFE), discrete dislocation plasticity (DDP) and the proposed multi-scale modelling coupled DDP/CPFE approach, respectively. The formulations of CPFE and DDP employed herein are introduced in Chapter 3, and the coupling calculation acts as a benchmark problem for the newly proposed coupling philosophy also introduced in Chapter 3.

A large number of parametric studies have been conducted in CPFE and DDP calculations to study microstructure influence on material performance, and a comparison between CPFE and DDP results discusses the difference of their material modelling features. These studies help understand the mechanisms and formulations of CPFE and DDP that are introduced in Chapter 2 and Chapter 3.

Application of the proposed multi-scale modelling approach (that is introduced in Chapter 3) on uniaxial problem verifies its validity and effectiveness by investigating the stress-strain response curves obtained using the individual descriptions and the coupled simulations, and coupling effect on dislocation sub-region.

The newly proposed multi-scale modelling approach is successful at capturing the global response of materials under the application of macroscopically uniform deformation. However, this newly proposed multi-scale modelling approach can be and has been further applied on problems where highly localized plasticity occurs in boundary value problems. Chapter 5 and 6 will show another application of this multi-scale approach to a planar indentation problem to illustrate the normal response of materials under localised contact.

5 Indentation Problem: Resolving Different Scales

In this chapter, the planar indentation problem is solved using crystal plasticity finite element (CPFE) and discrete dislocation plasticity (DDP) to resolve the material behaviour at either individual crystal (micro) or dislocation (nano) scales, respectively. The fundamental theory and formulations are introduced in Chapter 2 and 3 respectively. Parametric studies at both scales are conducted to assess the influence of different assumptions made about the crystal and defect structures on the material performance under indentation. These studies provide an understanding the performance specimens modelled using CPFE and DDP under localized boundary condition, which is an extended study from the uniaxial tension studies in Chapter 4.

A new formula is proposed based on DDP simulations to describe indentation pressure variation of thin films when applied indentation depth is relatively small. This is followed by a quantitative analysis of the hardness response of a continuum coating system using CPFE calculations when indentation pressure is affected by the substrate. The DDP and CPFE calculations performed in this chapter, while shedding light on interesting aspects of plasticity emerging at different scales, also provide a solid foundation for the implementation of the concurrent coupling method (developed in Chapter 3) to be applied to the planar indentation problem in Chapter 6.

5.1 Introduction

A literature review on the mechanical behaviour and its modelling of materials under micro-scale indention tests has been provided in Section 2.3.2. In this chapter, planar simulations of wedge-shaped indentation problem are conducted using crystal plasticity finite element and discrete dislocation dynamics plasticity. Results are discussed with focus on the role of microstructure and size effect upon the response of specimens. In particular, actual contact size and indentation pressure are investigated in details to understand the normal performance of materials under wedge-shaped contact. Finally, a comparison between results obtained from indentation problem solved with DDP and CPFE is provided in order to further understand the differences in material performance at different scales.

5.2 Indentation Problem Solved using Discrete Dislocation Plasticity

The discrete dislocation plasticity philosophy has been briefly introduced in Chapter 3. In the indentation problem, we still employ the superposition approach (similar to tension case in Chapter 4) to solve displacement and stress field. The application of DDP method in the indentation problem helps further understand dislocation theory and formulations that is mentioned in Chapter 2 and 3 by performing parametric studies on variables that are relevant to dislocation structure. Besides, numerical results of DDP calculations provide comparison data, *e.g.* indentation pressure curves

the upcoming coupling methodology. The successful capture of Indentation Size Effect (ISE) in the DDP simulations enables us to develop a new indentation pressure formula employing fitting parameters being interpreted with physical significance.

5.2.1 Methodology and problem definition

The discrete dislocation plasticity framework in indentation problem is similar to the one mentioned in Chapter 4, and the relevant code is adapted from Balint's previous work [2].

A plane strain analysis of the wedge indentation of a single crystal aluminium-like film of dimension $h \times l$ rigidly bonded to a rigid bottom substrate is conducted. Plasticity in the DD film is described by the collective glide of discrete edge dislocations on predefined slip planes. The indenter is modelled as a rigid wedge generally characterised by small apex angles ($\omega = 5°$, see Figure 5.1) which is blunter than the typical indenters employed in most experimental studies (e.g. Berkovich or Vickers) as larger values of indenter angle ω (sharper wedge) result in large contact area jumps in the discrete dislocation calculations. Perfect sticking contact condition (hence no-slip) between the rigid indenter and the film top surface is assumed, which indicates that the nodes of the film within the contact would share the displacement of the corresponding points of the indenter as soon as the wedge comes into contact. The film is discretized by a biased mesh with the finest mesh allocated in the proximity of the indenter tip in order to obtain a higher resolution within the contact and to accurately capture the gradients in dislocation fields.

The boundary value problem analysed in the DDP model is sketched in Figure 5.1. The length of the dislocation activity process window is fixed as $l = 30\ \mu m$ in a film of length $L = 1000\ \mu m$; the thickness is varied as $h = 2, 5, 10, 20, 50\ \mu m$. According to the rules of planar DDP for FCC systems reported in Chapter 3, there are three potential active slip system oriented $\phi^{(\alpha)}\ (\alpha = 1, 2\ 3) = \pm 35.3°$ and $90°$ with respect to the y-axis. The predefined nucleation source and obstacle density is also varied in the study of their effect on the hardness value. Other parameters in the simulation of DDP-only indentation problem are listed in the following table.

Table 5.1. General DDP material parameters used in the wedge-shaped indentation problem.

Parameter Name	Symbol	Unit	Value
Young's Modules	E	GPa	70
Poisson Ratio	υ	-	0.33
Burger's Vector	b	nm	0.25
Slip Plane Space	-	$\|b\|$	100
Annihilation Distance	L_e	$\|b\|$	6
Source Strength Mean	$\bar{\tau}_{nuc}$	MPa	50
Source Strength S.D.	$\sigma_{\tau_{nuc}}$	MPa	10
Nucleation Period	t_{nuc}	ns	10
Nucleation Dipole Distance	L_{nuc}	nm	15
Drag Coefficient	B	$Pa\ s$	10^{-4}

Obstacle Strength	τ_{obs}	MPa	150

Effects of geometry changes on the momentum balance and lattice rotations are neglected in our DDP calculations. However, the contact between the indenter and the film is based on the deformed film surface. The depth of the indentation is denoted by δ and the true contact length$A$ is defined as the range between the smallest and the largest values of x where the indenter contacts the deformed surface. In general, the true contact length A differs from the nominal contact length $A_N \equiv 2d/\tan\omega$ due to sink-in or pile-up as sketched in Figure 5.1(b), but it does not account for surface roughness (as analysed and discussed by [255])); this can lead to a significantly smaller contact area due to random fluctuations along the contact, especially for sharp indenters.

The boundary conditions of the indentation problem solved using DDP model are set as following:

$$\begin{aligned} &\dot{u}_x = 0, \dot{u}_y = \dot{\delta} \text{ on } S_{contact} \\ &\dot{u}_y = 0 \ on \ y = 0 \text{ and } \dot{u}_x \\ &\qquad\qquad = 0 \ on \ x = 0 \\ &T_x = T_y = 0 \text{ on } x = 0 \notin S_{contact} \end{aligned} \tag{5.1}$$

Here, $T = \sigma_{ij} n_j$ is the surface traction on a surface with outward normal vector n_j.

The displacement of the indenter is set to give:

$$\dot{u}_y = \dot{\delta} = 0.4 \ m/s \tag{5.2}$$

The total reaction force of the film response to the indenter penetration is computed as:

$$F = -\int_{-A/2}^{A/2} T_y(x,0)dx \tag{5.3}$$

Thus the actual indentation pressure p_A and nominal indentation pressure p_N are given by following formulas, respectively:

$$p_A = F/A \tag{5.4}$$

$$p_N = F/A_N \tag{5.5}$$

A small time increment $\Delta t = 0.5 \ ns$ is adopted in order to resolve the dislocation activities.

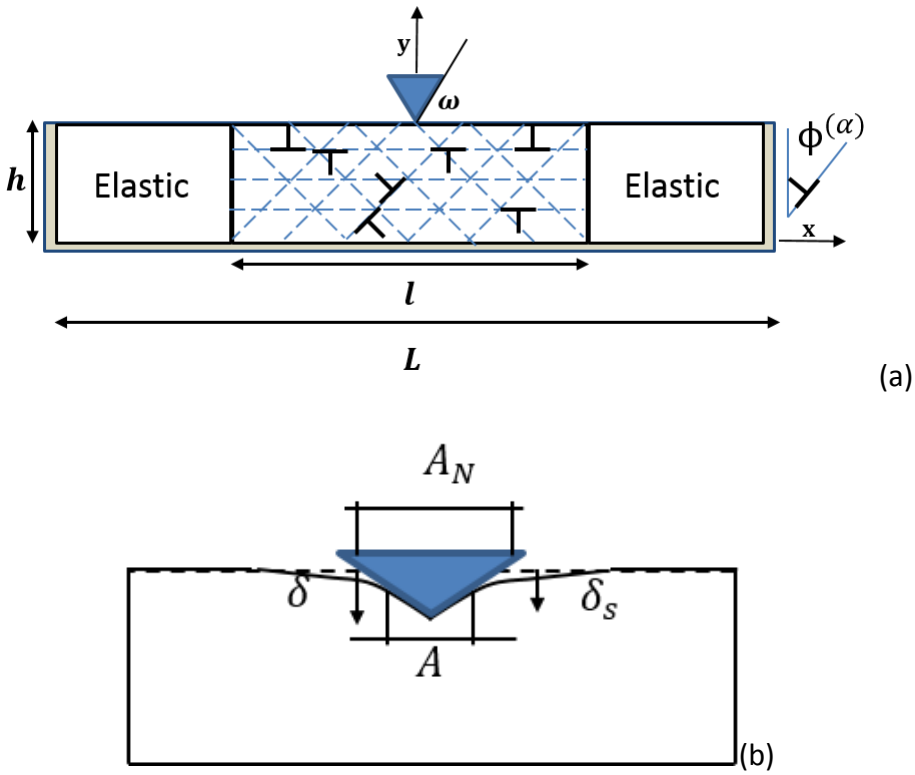
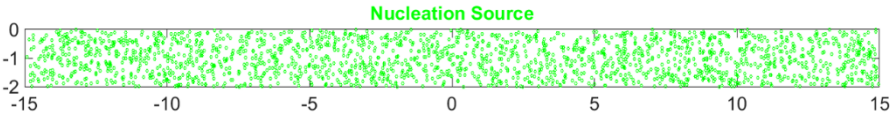


Figure 5.1. (a) Sketch of the indentation boundary value problem solved using the DDP model. (b) The definitions of the actual contact area A, the nominal contact area A_N, the indentation depth δ and sink-in δ_s ignoring the surface roughness.

5.2.2 Results

In this section, parametric studies, including indenter shape, slip system orientation, dislocation source density and film thickness have been conducted in order to understand the microstructure influence on the response of thin films modelling with DDP. Besides, a new formula that describes the indentation pressure variation with indentation depth has been developed based on the phenomenon found in abovementioned parametric studies. Fitting parameters in the newly proposed formula have been provided physics based significance.

The positions of dislocation nucleation sources sites, internal and all obstacles in the reference specimen characterised by $h = 2\mu m$ and $\rho_{nuc} = \rho_{obs} = 42\mu m^{-2}$ are plotted in Figure 5.2(a), (b) and (c) respectively. From that figure, it is seen that both distribution of dislocation nucleation source sites and obstacles are random. Moreover, dislocation sources and obstacles are assigned along the predefined slip planes with orientations: $\phi^{(\alpha)}$ $(\alpha = 1, 2\ 3) = \pm 35.3°$ and $90°$ with respect to the Y axis. It should also be noted that there are boundary obstacles generated along three boundaries of the DDP specimen which, indicates that indented boundary is modelled as free surface.



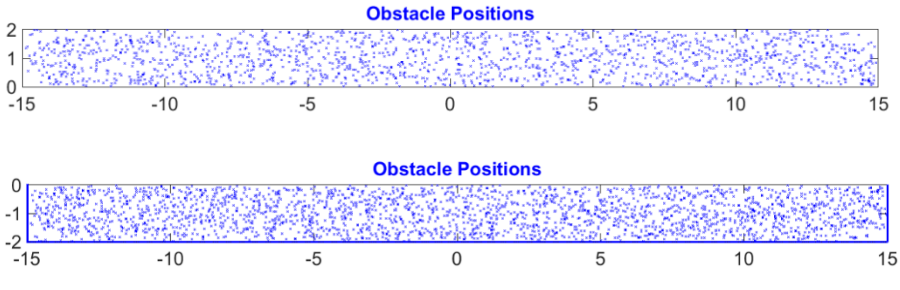
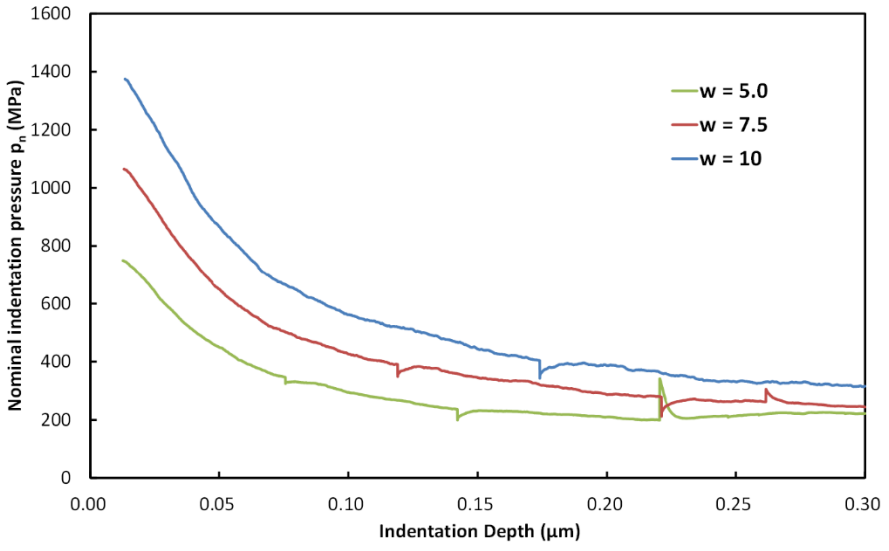
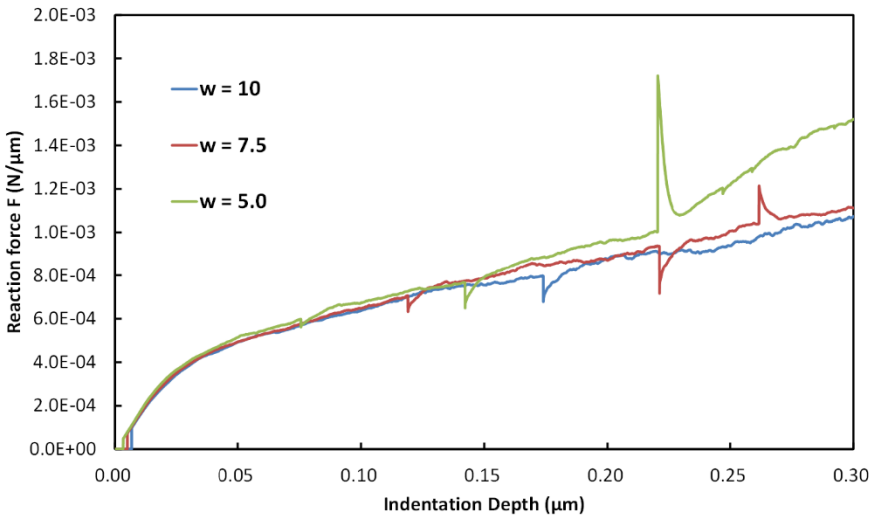


Figure 5.2. The distribution of (a) dislocation nucleation source sites and (b) internal obstacles (c) internal and boundary obstacles predefined in the single reference crystal specimen. The parameters set for the generation of the dislocation structure and the film to be indented are $h = 2\mu m$ and nucleation source and obstacle density $\rho_{nuc} = \rho_{obs} = 42\mu m^{-2}$.

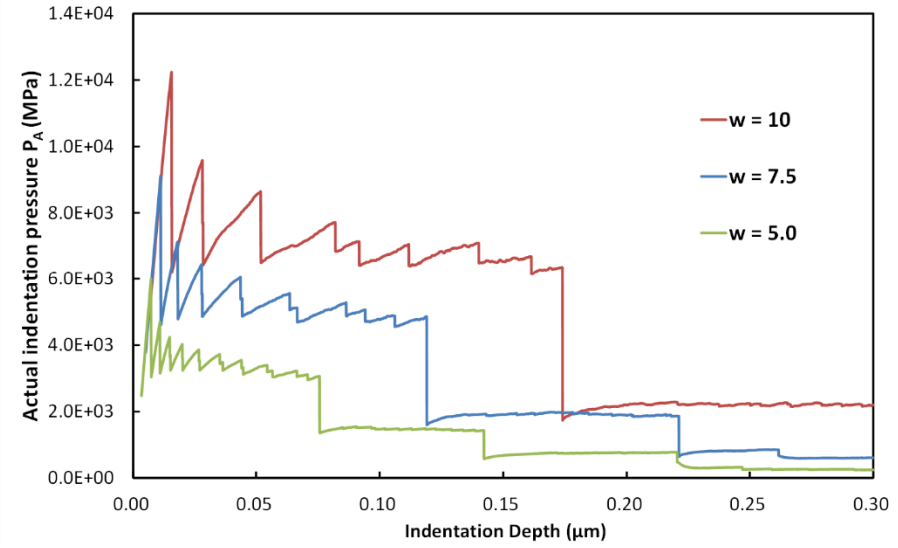
5.2.2.1 Indenter shape effect

Reaction force, F, actual contact area, A, and actual indentation pressure, p_N, curves versus applied indentation depth δ are plotted in Figure 5.3 (a), (b) and (c) respectively. Three values of indenter angle, $\omega = 5.0°, 7.5°$ and $10.0°$, are shown to investigate the indenter shape effect. Films are assigned with same values of nucleation source and obstacle density as $\rho_{nuc} = \rho_{obs} = 8.28\ \mu m^{-2}$. Indentation reaction forces are found to be independent of indenter shape, while actual contact size decreases with indenter sharpness at a given applied indentation depth. Therefore, actual indentation pressure, as the ratio between reaction force and actual contact area, increases with indenter sharpness, at a given indentation depth. There are some sudden jumps in the true contact area and hence the indentation pressure curves. They are caused not only due to the sudden physical attach between indenter and film surface, but also the numerical discreteness of finite element mesh. Thus this large jumps can be relieved by applying a finer mesh near the contact. Please see Section 5.2.3 for more details.





(b)



(c)

Figure 5.3. (a) Reaction force F; (b) Nominal, A_N, and actual, A, contact area; (c) Actual indentation pressure, p_A, curves versus applied indentation depth δ for a film characterised by thickness $h = 10\ \mu m$ with different indenter shapes (different values of indenting angle ω with respect to X axis). The films analysed here have the same dislocation structure.

5.2.2.2 Elastic and elastic-plastic response

Indentation force F versus applied indentation depth δ response of $h = 2\ \mu m$ and $h = 10\ \mu m$ films is plotted in Figure 5.4 with $\omega = 5°$ indenter. Calculations for purely elastic films (*i.e.* preventing all dislocation nucleation activity) are also included for reference. All simulations are carried out until the indentation depth achieves $\delta = 0.1\ \mu m$. Indentation force increases approximately quadratically with indentation displacement in all cases, which is consistent with analytical solutions [256] for indentation force. For elastic materials, at a given indentation depth a larger value of film thickness leads to a smaller value of indentation force due to substrate effects. The plastic response of films are found to be much softer than the corresponding elastic ones, which reveals that plasticity caused by dislocation activity significantly

relaxes internal stresses in films, and thus reduces indentation reaction forces. There are some spikes found in indentation reaction curves of plastic response for both films. Those are due to sudden nucleation (drop) or annihilation (rise) of dislocations within films; this corresponds to sudden changes of the stress field and reaction forces.

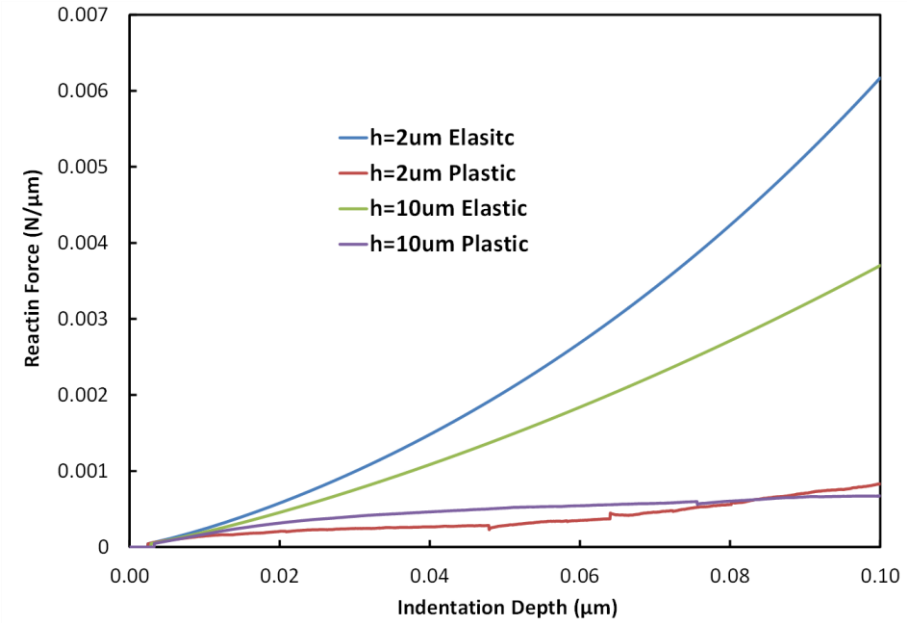


Figure 5.4. Indentation force versus applied indentation depth for $\omega = 5°$ wedge. Results are shown for both elastic and discrete dislocation predictions for the material under investigation.

Actual contact area A versus applied indentation depth δ response of $h = 10\ \mu m$ film is plotted in Figure 5.5 with $\omega = 5°$ indenter. Calculations for a material exhibiting a purely elastic response are also included for reference purposes. All simulations are carried out until indentation depth achieves $\delta = 0.1\ \mu m$. True contact area of elastic response increases approximately quadratically with indentation displacement, and the steps are relatively uniform and small due to the refined mesh size. However, the contact area obtained when the plastic response is considered systematically shows a much lower value which is the result of material sink-in. Besides, the increase of plastic response curve is rather random. A large rise of true contact area occurs because material sink-in results in part of the deformed film surface adjacent to the contact zone to incline nearly parallel to the surface of the indenter. Thus, further indentation leads to the contact area increasing in sudden increments. This discontinuous rise of actual contact area also contributes to the spikes in indentation force diagram shown in Figure 5.4.

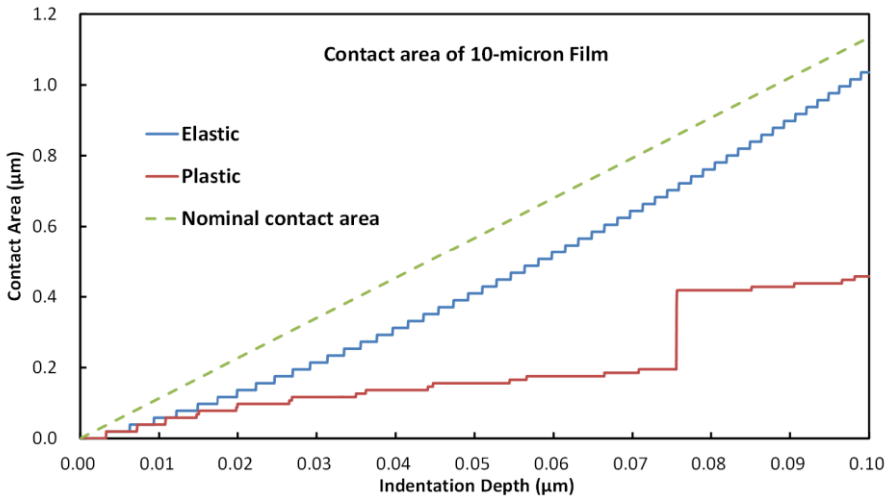


Figure 5.5. Actual contact area A versus applied indentation depth δ for the $\omega = 5°$ wedge. Results are shown for both the elastic and discrete dislocation predictions for the $h = 10\ \mu m$ film. The nominal contact area A_N is also included for reference.

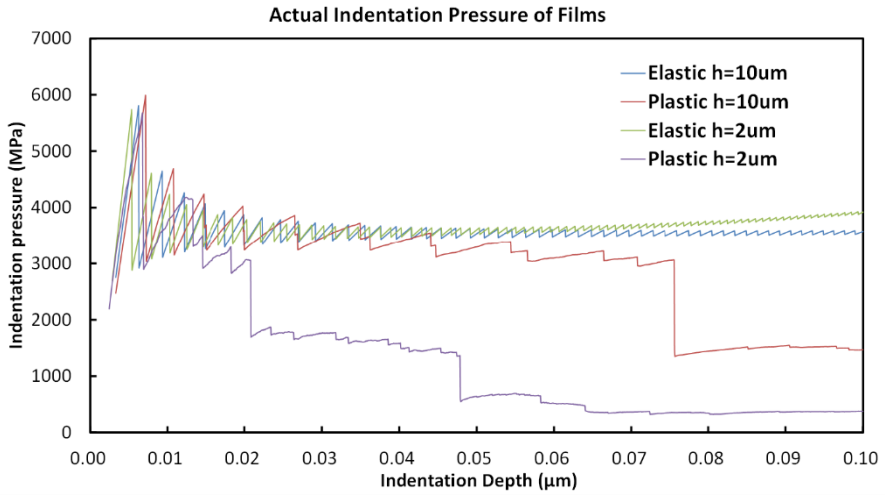


Figure 5.6. Actual indentation pressure p_A versus applied indentation depth δ for the $\omega = 5°$ wedge. Results are shown for both the elastic and discrete dislocation predictions for $h = 2\ \mu m$ and $h = 10\ \mu m$ films respectively.

Actual indentation pressures p_A versus applied indentation depth δ for films characterised by thicknesses $h = 10\ \mu m$ and $h = 2\ \mu m$ are plotted in Figure 5.6 for indentations performed using $\omega = 5°$ indenter. Calculations for purely elastic films are also included for reference purposes. All simulations are carried out until the indentation depth achieves $\delta = 0.1\ \mu m$. The elastic response of $h = 10\ \mu m$ and $h = 2\ \mu m$ films are similar with a stable hardness value $H = 3.5\ GPa$, except the increasing trend obtained for $h = 2\ \mu m$ due to presence of the rigid substrate already felt by the indenter. Besides, both plastic hardness curves are shown to be lower than their corresponding elastic response curves due to dislocation relaxation effect. The plastic hardness response shows significant difference between two films although both simulations successfully capture the indentation size effect. The hardness curve of the film of thickness $h = 2\ \mu m$ decreases more rapidly than that

obtained for film thickness $h = 10\ \mu m$ film. The discrepency of hardness evolution between different films will be discussed in later sections.

5.2.2.3 Contact area response

The variation of actual contact area A with applied displacement δ is plotted in Figure 5.7 with $\omega = 5°$ indenter. Results are included for all five film thicknesses. For reference purposes, the variation of the nominal contact area, $A_N \equiv 2\delta/\tan\omega$ with displacement is also included in the figure. The indentation depth δ achieves up to $\delta = 0.3\mu m$.There are large jumps (much larger than the finite element mesh size) in contact area, especially for $h \geq 5\mu m$ films. These jumps in terms of reaction forces and contact area are stochastic due to dislocation discrete nature and depend on the details of initial source and obstacle distribution.

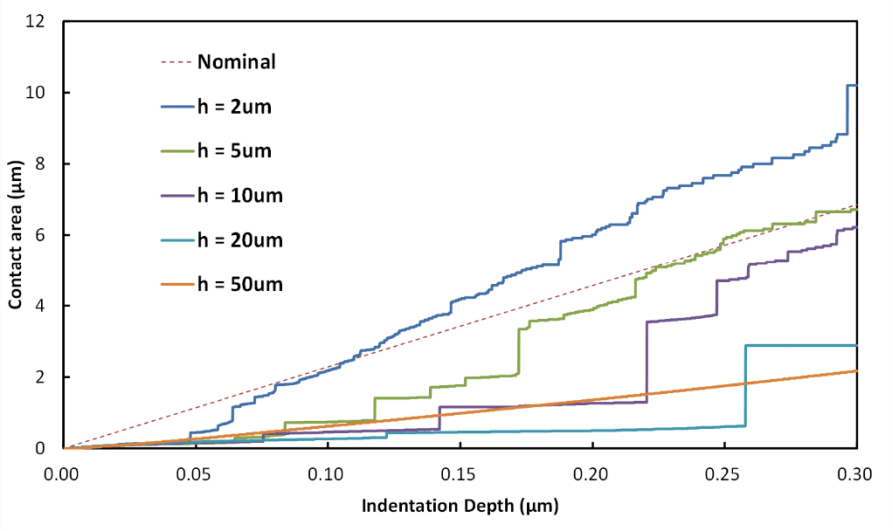


Figure 5.7. the relation between actual contact length, A, and indentation depth δ for indentation of the reference material with $\omega = 5°$ wedge. Results are shown for five films with different thicknesses h. Nominal contact area, A_N, is also shown for reference (dotted line).

Actual contact area A is found less than nominal contact area A_N for $h \geq 10\ \mu m$ (especially so for $h = 50\ \mu m$ and $h = 20\ \mu m$ films) while $A > A_N$ for $h = 2\ \mu m$ and $h = 5\ \mu m$ films at indentation depths greater than $\delta = 0.1\ \mu m$ and$\delta = 0.25\ \mu m$, respectively. This is a result of material pile-up for thin films and sink-in for thick films. Interestingly, the transition relative indentation depths in $h = 2\ \mu m$ and $h = 5\ \mu m$ films for making $A = A_N$ are coincided at $\beta = \delta/h = 0.05$. The phenomenon is also found ($\delta \approx 0.45\ \mu m$) in $h = 10\ \mu m$ when simulation continues to achieve a large indentation depth. This finding is explained as that material pile-up is linked to the plastic zone expansion. When plastic flow that is introduced due to the collective motion of dislocations reaches rigid boundary, dislocations are pinned at the boundary and thus exert a back effect on dislocations near indenter tip. The relative indentation depth $\beta = \delta/h$ is able to reflect indentation progress in terms of the potion of film that indenter has already penetrated and rigid boundary effect. The critical value of relative indentation depth

for material pile-up occurring is predicted as $\beta = 0.4$ for all films with a similar dislocation structure considered herein.

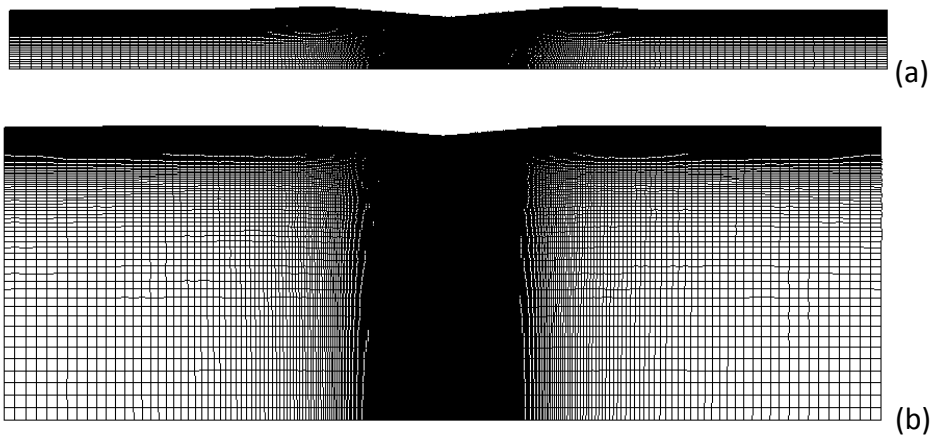


Figure 5.8. deformed mesh (displacements magnified by a factor of 1) with $\omega = 5°$ wedge indentation of (a) $h = 2\mu m$ and (b) $h = 10\ \mu m$ films. Meshes are shown at the time when the applied indentation depth $\delta = 0.3\ \mu m$.

Deformed mesh with $\omega = 5°$ wedge indentation of $h = 2\mu m$ and $h = 10\ \mu m$ films are plotted in Figure 5.8 (a) and (b), respectively. These meshes are generated at the instant when the applied indentation depth$\delta = 0.3\ \mu m$. Apparent material pile-up is observed in $h = 2\mu m$ film while material sink-in is shown in $h = 10\mu m$ film. However, it is worth noting material sink-in (resulting in $A < A_N$ see Figure 5.8 for reference) also occurs in $h = 2\mu m$ crystal when applied indentation depth is $\delta < 0.1\mu m$, and material pile-up starts when plastic flow reaches rigid boundary. Pile-up might eventually occur in thick films when applied indentation depth is large enough to introduce adequate plastic flow into films. The material pile-up phenomenon was once suspected to be attributed to the constraint from left and right sides [2]. By removing traction boundary conditions, material pile-up still presents in $h = 2\mu m$ and $h = 5\mu m$ films that indicates that material pile-up does indeed result from the plastic zone extending to the bottom surface of film rather than side constraint.

5.2.2.4 Dependence of actual indentation pressure evolution curve on thickness and dislocation nucleation source density

The actual indentation pressure p_A evolution curves versus the applied indentation depth δ are plotted in Figure 5.9 for films with different thicknesses indented by the $\omega = 5°$ wedge. The dislocation structure is given by the number of dislocation nucleation sites and obstacles per slip planes. The equivalent values of nucleation source density and obstacle density are different from films with different thickness due to the nucleation sites generation mechanism. The values of nucleation source density and obstacle density for different films are tabulated in Table 5.2. All simulations have successfully captured the indentation decreasing evolution when the indentation depth is small enough. However, the detailed behaviours of curves for different films show significant differences. The indentation pressure curve for $h = 2\ \mu m$ film turns up when the indentation depth $\delta > 0.1\mu m$ due to the rigid

boundary effect. The indentation pressure curve for $h = 5\ \mu m$ and $h = 10\ \mu m$ films level off at a plateau with a value $p_A \approx 200MPa$ that indicates that the indentation process for those two films have exited the indentation size effect zone and finally reached the continuum (indentation size free) zone. The indentation pressure curve for $h = 20\ \mu m$ film still keeps decreasing and has not yet achieved the stable hardness value. It is interesting to observe the elastic like performance of the $h = 10\ \mu m$ film. As seen in Figure 5.6, we cannot simply judge whether the actual indentation pressure evolution curve is determined by film thickness and/or dislocation nucleation density even though the rigid boundary effect can be excluded by focusing on the beginning of the hardness curve of $h = 2\ \mu m$ film. The influence of film thickness and dislocation nucleation density will be investigated separately in the later section.

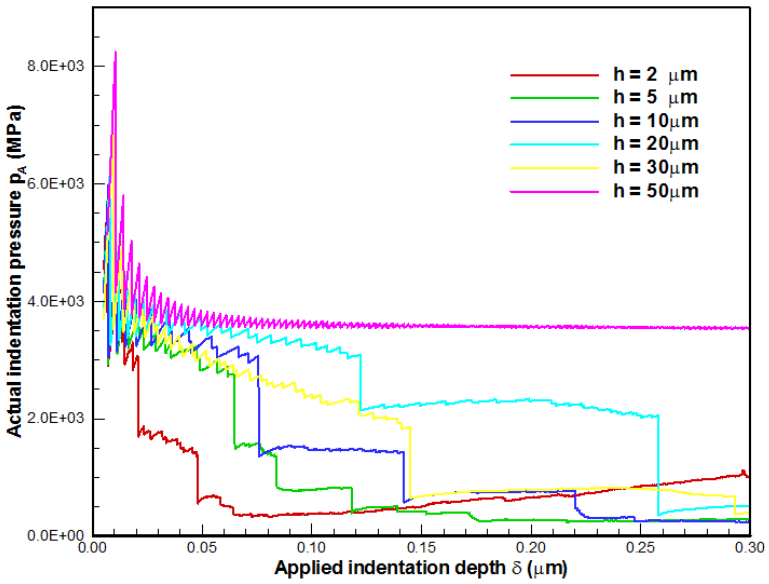
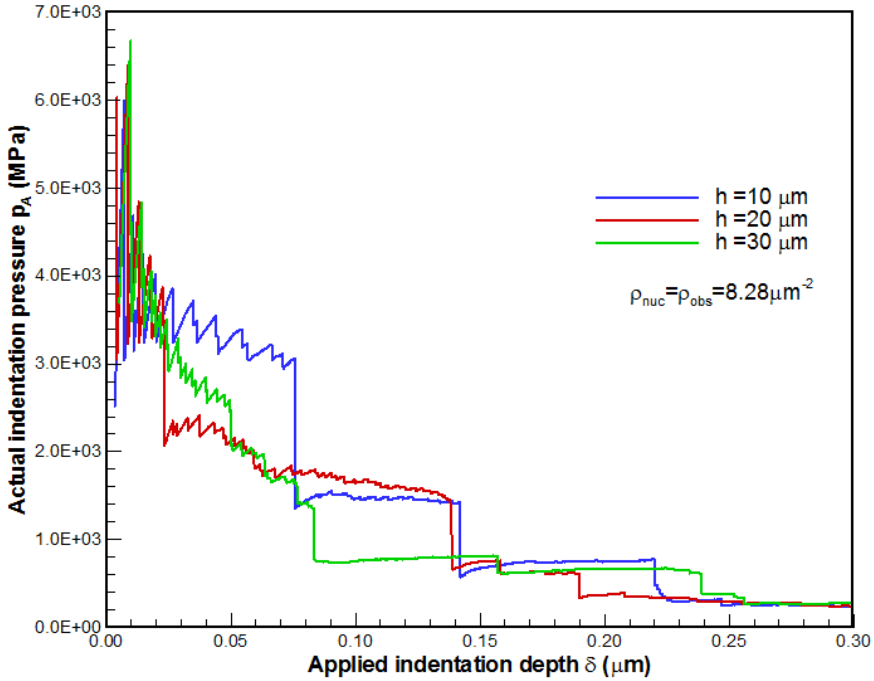


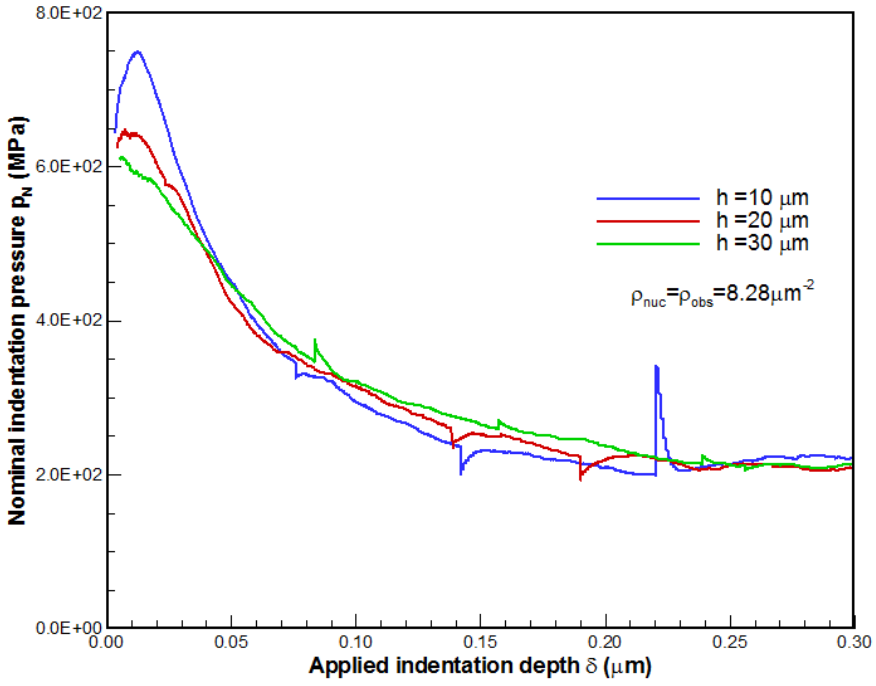
Figure 5.9. Actual indentation pressure evolution p_A curves versus the applied indentation depth δ for five films with different thicknesses indented by the $\omega = 5°$ wedge. Note that the films are also characterised by different values of dislocation nucleation density.

Table 5.2. Values of thickness, nucleation and obstacle density of films in Figure 5.9

Parameter	Symbol	Unit	Values					
Film Thickness	h	μm	2	5	10	20	30	50
Number of sources/plane	-	-	1	1	1	1	1	1
Source density	ρ_{nuc}	μm^{-2}	42	20	8.3	5.0	3.2	1.1
Number of obstacles /plane	-	-	1	1	1	1	1	1
Obstacle density	ρ_{obs}	μm^{-2}	42	20	8.3	5.0	3.2	1.1



(a)



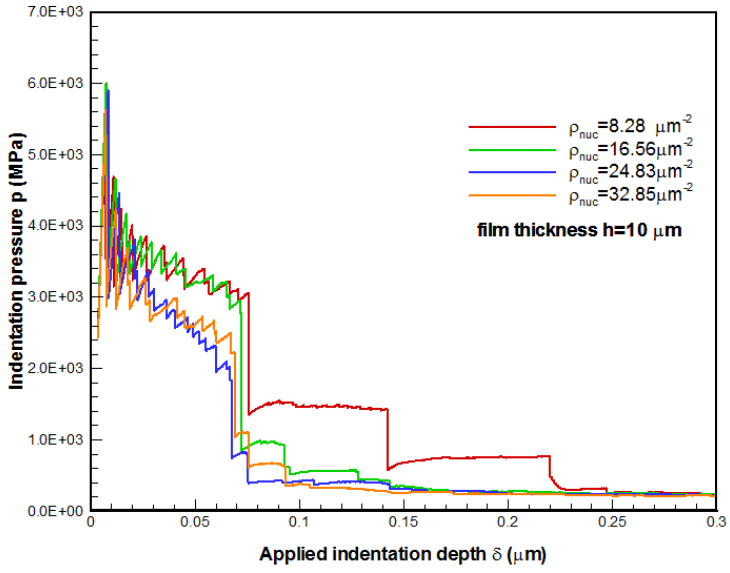
(b)

Figure 5.10. (a) Actual (b) nominal indentation pressure variation of films with different values of film thickness but identical nucleation source density

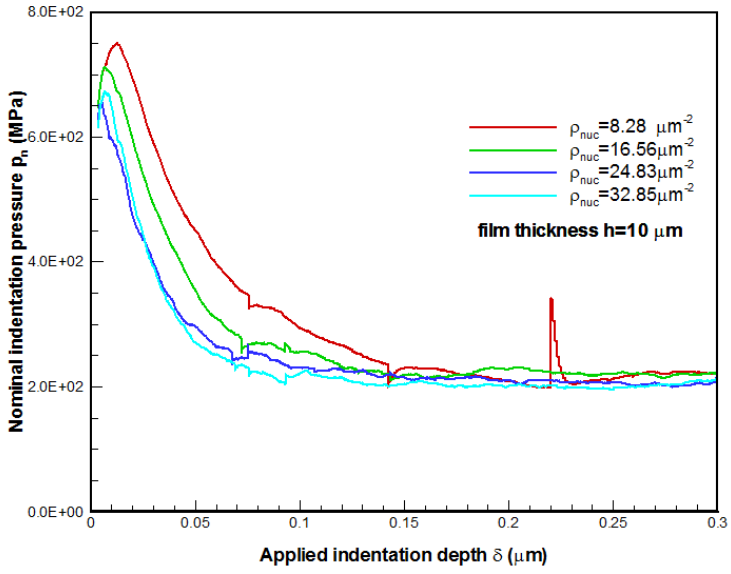
Table 5.3. the micro-structure of the indented films plotted in Figure 5.10

Film Thickness (h μm)	10	20	30
Number of sources per plane	1	2	3
Source density (ρ_{nuc} μm^{-2})	8.28	8.26	8.24
Number of obstacles per plane	1	2	3
Obstacle density (ρ_{obs} μm^{-2})	8.28	8.26	8.24

The actual indentation pressure evolution p_A and nominal indentation pressure p_N evolution curves versus the applied indentation depth δ are plotted in Figure 5.10 (a) and (b) respectively for three films with different thicknesses indented by the $\omega = 5°$ wedges. In order to study whether there is a dependence of the hardness upon the film thickness, the values of source density (as well as the obstacle density) of those films are selected nearly identical as $\rho_{nuc} = \rho_{obs} = 8.28\ \mu m^{-2}$ around. The details are shown in Table 5.3. In Figure 5.10 (a), the beginning parts of three curves generated from films with different thicknesses are nearly overlapped, and the following indentation size dependent performance also show similar trend. The final stable indentation size independent values are found the same as $H \approx 210MPa$ that is taken as the continuum hardness of these thin films. Moreover, the evolution of nominal indentation pressure shows more apparent trend as all three curves are nearly overlapped from beginning to end. The spikes observed in the nominal indentation pressure curves are due to sudden change of dislocation structure, such as nucleation and annihilation. Based on the Figure 5.10 shown, a preliminary conclusion has been drawn that the indentation pressure is not determined by the film thickness as long as the indentation size does not exceeds the threshold value for rigid boundary effect being evolved. From physics perspective, before the indenter feels the rigid boundary, the indentation pressure of material depends on how much material has already damaged and thus is not affected by the total amount of material.



(a)



(b)

Figure 5.11. (a) Actual (b) nominal indentation pressure variation of films of thickness $h = 10\mu m$ but different nucleation source density

Table 5.4. the dislocation structure of the indented films plotted in Figure 5.11

Film Thickness (h μm)	10	10	10	10
Number of sources per plane	1	2	3	4
Source density (ρ_{nuc} μm^{-2})	8.28	16.56	24.83	32.85
Number of obstacles per plane	1	2	3	4
Obstacle density (ρ_{obs} μm^{-2})	8.28	16.56	24.83	32.85

The actual indentation p_A evolution and nominal hardness evolution p_N curves versus the applied indentation depth δ are plotted in Figure 5.11 (a) and (b) respectively for $h = 10$ μm film with different dislocation structure indented by the $\omega = 5°$ wedge. In order to study the dependence of the hardness of films on the nucleation source density, the source density is ranged as $\rho_{nuc} = 8.28, 16.56, 24.83$ and 32.85 μm^{-2} in the $h = 10$ μm film, and the obstacle density is set to be the same as the corresponding source density. The details can be found in Table 5.4. As can be seen in Figure 5.11 (a), the actual hardness with a larger value of dislocation nucleation source density generally decays more, especially for the film with a small value of dislocation nucleation source density. For the films with $\rho_{nuc} = 24.83\mu m^{-2}$ and $\rho_{nuc} = 32.85\mu m^{-2}$, the hardness evolution curves are nearly overlapped especially when the indentation depth δ approaches larger values. This finding is attributed to the dislocation nucleation starvation effect. The mechanism can be explained as follows: the stress field at a certain place has already excessed the critical stress for generating a pair of dislocation dipole; however, there is no dislocation nucleation site available at that place due to a lack of dislocation nucleation source density in the specimen. Therefore, the onset of plastic flow in the specimen will be delayed and thus the crystal will be hardened correspondingly as there are not many dislocations to relieve its internal stress field. Although the size-

dependence hardness of the crystal with different nucleation source density is qualitatively similar, the indentation pressure of a crystal with a lower value of nucleation source density ρ_{nuc} exhibits significantly greater than that of a crystal with a larger value at a given indentation depth. Therefore, a starvation of dislocation sources provides a significant contribution to the indentation response of crystal, especially at a small indentation depth δ and with a small value of nucleation source density ρ_{nuc}. This source-limit plasticity in indentation has analogous feature to that has been discovered in other DDP calculations in tension[1], bending[257], micro-friction[4] and micro-cantilever loading[258]. A conclusion has been drawn from Figure 5.11 that both of the actual and nominal indentation pressure within the size effect zone of crystals strongly depends upon the value of dislocation nucleation density ρ_{nuc}. This dependence is quantitatively studied in Section 5.2.3.

The dependence of indentation pressure variation on slip system orientations are also observed. Please see Appendix V for more details.

5.2.3 Quantitative analysis of indentation pressure evolution

In order to quantitatively predict the actual indentation pressure p_A variation versus the applied indentation depth within the indentation size effect zone for films with different thicknesses and/or with different dislocation structure, the following equation is considered in the DDP simulations.

$$p_A = H_i * \left(1 + \frac{\delta}{a^*}\right)^{-\alpha} \tag{5.6}$$

In Eq. (5.6), H_i is defined as the initial intrinsic material hardness, δ is the applied actual indentation depth, and a^* and α are fitting parameters that are linked to the material property. Parametric studies on these fitting parameters can be found in Appendix VI.

5.2.3.1 Determination and physical interpretation of H_i

As seen in Figure 5.9, all hardness evolution curves start from the same value when the applied indentation depth approaches zero ($\delta \to 0$), and this value shows little dependence on either the film thickness or dislocation nucleation source density. A best-fit of indentation pressure curves in Figure 5.9 using eq.(5.4) is conducted in a MATLAB toolbox, namely CFTOOL (curve fitting tool[259]), which is developed based on trust-region algorithm [260]. The best fit (results are tabulated in Table 5.5) of the curves presented in Figure 5.9 confirms these by showing that there is very little variation of the initial intrinsic hardness for aluminum material H_i, which is evaluated to be $H_i \approx 4870\ MPa$ by averaging the values obtained from films studied here. That predicted value $H_i = 4870\ MPa$ is consistent with the value obtained by extrapolating experimental data [161].

From physical prospect, the initial intrinsic material hardness is interpreted as the hardness value of material when the applied indentation depth approaches 0. The sketch of the physical interpretation of the initial intrinsic material hardness H_i is

illustrated in Figure 5.12. In principle, the value of the initial intrinsic hardness H_i is determined only by the elastic property of material as no plastic flow has yet initiated. Other realisations (including single crystal copper $E = 110GPa$) with different Young's modulus and Poisson's ratio verify the point, and a larger Young's modulus results a larger value of H_i. But the details of atoms arrangement could have a strong effect on its value.

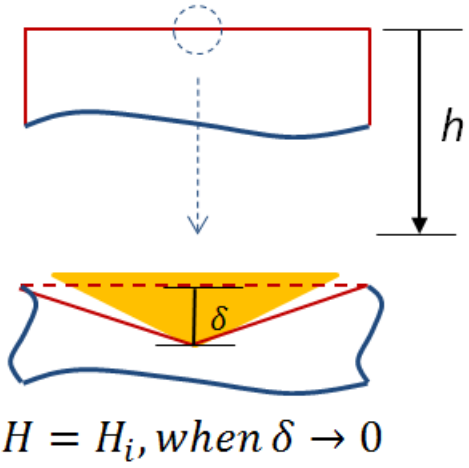


Figure 5.12. Sketch of the physical interpretation of the initial intrinsic material hardness H_i

Table 5.5. The initial intrinsic hardness H_i from best-fit calculations for hardness curves in Figure 5.9 of crystals with dislocation structure in Table

H_i	MPa	4812	4863	4885	4925	4998
ρ_{nuc}	μm^{-2}	42	20	8.28	5.0	1.1
h	μm	2	5	10	20	50

5.2.3.2 Determination and physical interpretation of a^*

The best-fit parameter set a^* against average source spacing (in terms of $1000b$) for $h = 10, 20\ \mu m$ and $30\ \mu m$ films with different dislocation nucleation source density is reported in Figure 5.13. Nucleation source density ρ_{nuc} is directly linked to average spacing of nucleation source in materials as $\rho_{nuc} = 1/s^2$ where s is average source spacing.

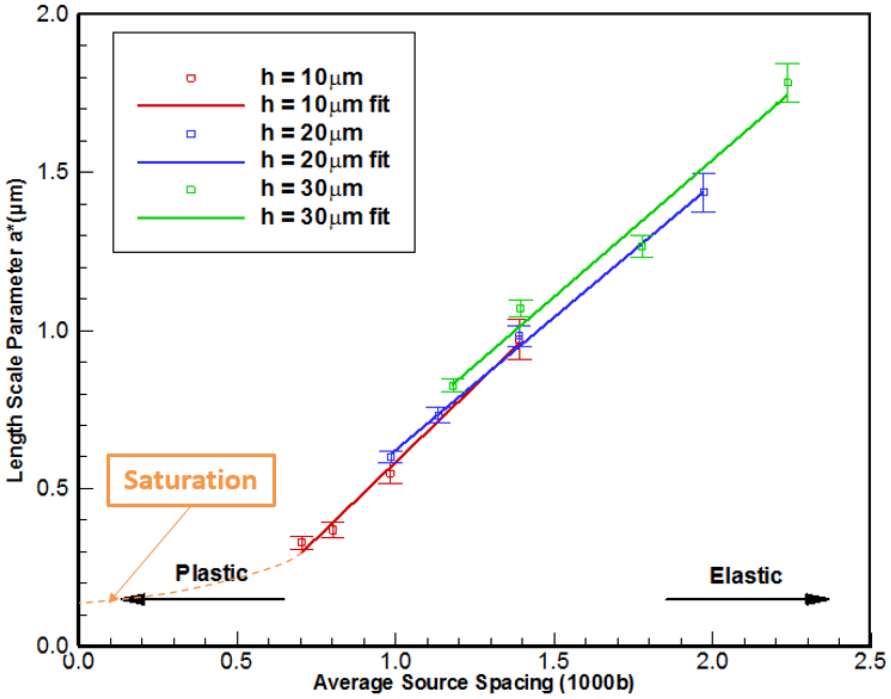


Figure 5.13. the linear relationship between fitting parameter a^* against average source spacing

As clearly seen in Figure 5.13 above, the value of fitting parameter a^* linearly increases with increasing average source spacing s regardless of film thickness h, which gives:

$$a^* = \frac{k}{\sqrt{\rho_{nuc}}} + a_0^* \tag{5.7}$$

Table 5.6. the best-fit parameter sets using eq. (5.7) of the dependence of a^* on ρ_{nuc}

h(μm)	k	a_0^*(μm)	R^2
10	3.8599	-0.3815	0.9858
20	3.3641	-0.2196	0.9992
30	3.4663	-0.1932	0.9937

The best-fit parameters that describe the dependence of a^* on the average source spacing are tabulated in Table 5.6 for films with different thickness. It is noted that the value of the constant of linear proportionality k, which captures the sensitivity of the length scale parameter a^* on nucleation source spacing s, is almost independent of film thickness. This feature is attributed to that the applied indentation depth has not achieved large enough values to yet trigger the rigid boundary effect. Due to the limitation of computational expense, even smaller values of source spacing are not achieved in current DDP simulations. From physic prospect, values of a_0^* should approach a limit that represents the value of length scale parameter a^* where specimens are full of nucleation source density (*i.e.* globally perfect plasticity). On the other hand, the linear dependence of a^* upon source space s would not hold when the latter value approaches 0 due to saturation of nucleation source density.

5.2.3.3 Determination and physical interpretation of α

As discussed above, the decreasing trend of indentation pressure evolution in the size effect zone is strongly dependent on the detailed dislocation structure.

Table 5.7. The best fit parameter set of the actual indentation pressure p_A evolution against the acutal indentation depth δ for $h = 10\ \mu m$ film with different dislocation source nucleation density

Label	$\rho_{nuc}(\mu m^{-2})$	a^*	α
rou-1	8.28	0.1048	14.5
rou-2	16.56	0.09486	14.8
rou-3	24.83	0.07391	15.3
rou-4	32.85	0.07082	15.4

The fitting exponent parameter α determines the gradient of the indentation pressure evolution trend when its value changes from the intrinsic initial hardness H_i to the continuum indentation depth independent hardness value H. We use the indentation pressure curves obtained from $h = 10\ \mu m$ films with different dislocation source nucleation density to show the dependence of α on the source density. Based on the data provided in Table 5.7, a larger value of dislocation nucleation source density ρ_{nuc} leads to slightly larger values of α. It is straightforward to understand that relationship between ρ_{nuc} and α as they both describe the potential status of plasticity in crystals. Dislocation nucleation source, ρ_{nuc}, determines how 'plastic' a crystal is for a given deformation (applied indentation depth δ in indentation simulations), and the fitting exponent parameter α quantitatively describe this status as a consequence. However, the dependence of α on ρ_{nuc} cannot be easily explicitly provided by a mathematical equation. This is not only because the starvation of nucleation sources show less effect when the value of ρ_{nuc} rises to a large value, but also because the orientation of the slip systems has a remarkable influence on the gradient of indentation pressure evolution.

5.2.3.4 Comparison to other formulae aimed at capturing indentation size effect

An indentation pressure evolution formula (5.8) based on the concept of the geometry necessary dislocation (GND) was developed by Nix and Gao [18] to describe the indentation pressure variation during the indentation process.

$$\frac{p}{p_0} = \sqrt{1 + \frac{\delta^*}{\delta}} \tag{5.8}$$

In eq.(5.8), δ^* is a characteristic length parameter, also dependent on the wedge angle and p_0 is the stable hardness in the infinite indentation depth limit.

The Nix and Gao's formula is derived by employing the Taylor relation [18] for strength dependence on dislocation density and the calculations of density of geometrically necessary dislocations (GNDs).

Although the equation worked well for some cases, some researches argued that other power-law exponent instead of 0.5 provided closer results, especially in discrete dislocation predictions [2]. And a range of experiments showed bad agreement of Nix and Gao's formula when the applied indentation depth $\delta < 1.0\ \mu m$. This is due to that this formula is derived for the indentation pressure evolving from the continuum hardness (*i.e.* when the applied indentation depth is large enough for the size effect due to dislocation activity to be negligible) instead of the initial hardness when the applied indentation depth is relatively small. Other possible reasons for its failure were analysed by Balint and co-workers [2]. Moreover, Nix and Gao's equation did not attempt to link the key parameter $\delta^*$to any intrinsic material properties.

In our equation, we firstly focus on the indentation pressure of crystals when the indentation depth is close to 0. The intrinsic initial hardness H_i is employed in the proposed equation based on the finding that the indentation pressure decreases from a fixed value that is independent of film thickness and dislocation structure. The involvement of H_i is able to solve the problem encountered in Nix and Gao's formula application to small indentation depth. Secondly, the fitting parameters in the proposed equation have been shown to be related to some properties of dislocation structure. In particular, physical interpretation has been assigned to a^* and α by parametric study on the dislocation nucleation source density. Thirdly, the exponent fitting parameter α is not fixed as 0.5 which enables the proposed formula to be applied to a wider range of situations, especially crystals with different dislocation structure. Compared to formula proposed in Balint's work [22], we used the actual indentation pressure instead of nominal indentation pressure to represent the hardness in the evolution equation. It is more physical and practical to use the actual indentation pressure as it involves the actual contact area (taking material sink-in or pile-up into consideration) rather than nominal contact although the nominal indentation pressure shows a more smooth trend and relatively easy to be fitted. One drawback of the proposed formula lies in the fact that the continuum hardness (when the applied indentation depth being large enough) cannot be predicted very well due to focus now placed mainly on the initial evolution of the plastic response for very low value of indentation depth. However, the actual indentation pressure for large applied indentation pressures can be described using the coupled DDP-CPFE to determine the indentation pressure (see Chapter 6).

5.2.3.5 Transformations

The proposed indentation evolution formula can also be transformed to another form, where the indentation pressure is dependent on the relative indention depth rather the actual indention depth. This dimensionless analysis is then given as:

$$H = H_i * \left(1 + \frac{\beta}{a}\right)^{-\alpha} \tag{5.9}$$

Since the variable δ in eq.(5.9) is normalized by film thickness h, the length scale fitting parameter a^* needs to be divided by film thickness h. But the exponential fitting parameter α does not need to be re-fitted.

The new equation can illustrate the substrate effect during indentation process by detecting how far it is from the indenter tip to the boundary. Therefore it is suitable to be applied in the comprehensive indentation pressure evolution evaluation of a coating system using the proposed coupling method. That will be shown in the later section.

It is worth noting that both fitting parameters a and α are dimensionless parameters in eq.(5.9) , although the new length scale character length a is not only determined by the average source spacing but also affected by the film thickness. Please recall Section 5.2.3.2 for more details.

5.2.3.6 Fitting experimental data with the new proposed formula

A set of hardness evolution data generated in nano-indentation experiments on Cu single crystals is fitted by our proposed formula in order to further verify its validity and the revealed dependence of indentation pressure on nucleation source density. The experimental data and best fit curves are plotted in Figure 5.14. Experimental data are not available for very small indentation depths due to practical limits but the value of intrinsic hardness can be obtained by extrapolating the fitting to zero indentation depths. The trend that hardness value decreases with the increasing relative indentation depth is successfully captured by our formula, and these corresponding fitting are generally very well as adjusted coefficients of determination is calculated up to $R^2 = 0.9964$. Other fitting parameters are tabulated in Table 5.8. Of more significance, the trend of fitting parameter a^*verifies the determination of nucleation source density on indentation pressure: a larger dislocation source density ρ_{nuc} leads to a shaper decay of indentation pressure, i.e. a smaller value of a^*. The large discrepancy in α between our simulations and the experimental data is due to the different definition of hardness. We use the concept of actual indentation pressure that is directly obtained from indention force divided by true contact area, which may introduce sudden jump in true indentation pressure. While in literature, hardness is usually indirectly calculated from compliance, i.e. the nominal indentation pressure is adopted. In the work of Nix and Gao, the value of exponent α was fixed as 0.5 as it was deducted from a GND argument. A further deduction and fitting of indentation pressure data would be conducted in the future to have a better understanding of the indentation pressure variation with indentation depth.

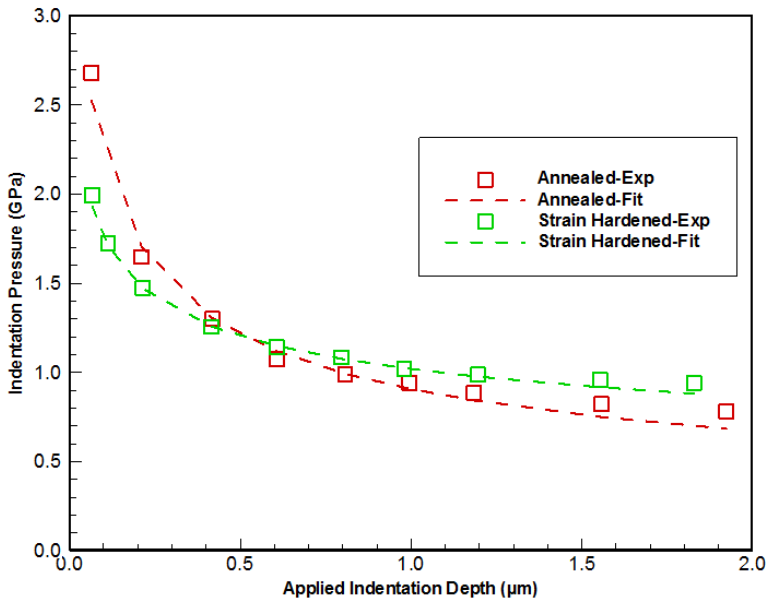


Figure 5.14. Hardness data and their corresponding best fit curves (in discrete data marker) in indentation size effect zone for three Cu single crystals obtained in nano-indentation experiment.

Table 5.8 Best fitting results of experimental data in Figure 5.14 using eq.(5.6)

Specimen	$H_i(MPa)$	a	α	R^2
Annealed	3912	0.009496	0.4416	0.9983
Strain hardened	3895	0.000956	0.2405	0.9873

5.2.4 Summary

Plane strain analyses of the indentation of single crystal films by rigid wedge-shaped indenter are carried out by modelling the film material with dislocation dynamics plasticity (DDP). The calculations are conducted by employing a small-strain DDP framework, and the contact is modelled by applying unidirectional contact boundary conditions to the deformable surface of the films and assuming a perfect stick contact condition between indenter and specimens. Computations are carried out to investigate the role of film thickness, dislocation nucleation source density, slip systems and their combination on the indentation response of single crystal materials. The crystals are initially taken as dislocation-free with dislocation nucleation occurring from mimic-Frank–Read sources randomly distributed in the crystal. Finally, we have proposed a new formula for describing the hardness evolution curve when the contact area is relatively small (i.e. the material response is in the indentation size effect (ISE) zone and not affected by the substrate). The new formula works well for the indentation simulations considered here with physically interpreted fitting parameters, and a practical nano-indentation experiment.

Indentation pressure evolution of a single crystal film is found to be strongly dependent upon the actual indentation depth when the contact area is small. With a

given indentation depth, the indentation pressure value of a single crystal film is determined by the dislocation nucleation source density and the slip system. The film thickness does not affect the indentation pressure until the indenter feels the presence of the rigid boundary (i.e. the plastic zone has extended to the boundary).

Regarding the fitting parameters in eq. (5.8), the initial intrinsic hardness value H_i is defined as that the indentation pressure of films when the applied indentation depth δ shrinks to 0. The value of H_i is found to be independent of dislocation structure and film thickness but affected by the Young's modulus so that it could be linked to the atom bond strength from physical prospect. In order to reflect the indentation process evolution and be further applied in coating system prediction, the length scale parameter a^* is normalized by the film thinness h. The original characteristic length scale parameter a^* is relevant to the average source spacing (i.e. the dislocation nucleation source density) only, while the normalised characteristic length scale parameter a is also affected by the film thinness h.The exponent fitting parameter α which determines the decreasing rate of the indentation pressure evolution is determined by the dislocation structure. A large dislocation nucleation source density leads to a larger value of α and thus a higher rate of decreasing of indentation pressure in the ISE zone which is attributed to the dislocation source starvation effect. The value of exponent fitting parameter α is not affected by the normalization. Although it is relatively more struggling to fit the actual indentation pressure p_A evolution curve compared to the nominal indentation pressure p_N (with a better adjusted coefficient of determination), we still believe actual indentation pressure H is a more physical parameter to represent the hardness of the crystal film as it takes the material pile-up or/and sink into calculations.

The drawback of the new proposed formula is its indentation pressure prediction when the indentation depth is relatively large. From a mathematical investigation, the indentation pressure H decreases to zero when the applied indentation depth δ goes to infinity. Because the focus has been put on the indentation pressure variation within indentation size effect zone, the fitting formula could lead to a large discrepancy on the film continuum hardness prediction. For instance, the fitting formula predicts that $H = 158\ MPa$ for the $h = 10\mu m$ reference film when the applied indentation depth $\delta = 0.4\ \mu m$ but the continuum hardness of the film is actually obtained (independent of dislocation density and film thickness) as $H_0 = 200MPa$.

The new proposed formula will be employed to predict the initial part (i.e. not affected by the substrate) of the indentation pressure evolution curve of a multi-scale modelling coating system by coupling DDP and CPFE. Besides, there are also some other features revealed by the DDP indentation simulations:

- The loading rate does not affect the indentation pressure evolution curve much as there is a 10% change when rate is decreasing to only 1/5.

- Large indenter angle with respect to the film surface (i.e. sharper indenter) leads to a large indentation pressure and a smaller contact area with a given applied indentation depth. But the indenter angle does not affect the total reaction force much.
- Time cost of simulation is strongly dependent on the element number and the nucleation source density.
- Dislocations spread out from the area near indenter tip to the rigid boundary while dislocation density increases linearly with the indentation depth.

Material pile-up for thin films ($h = 2\ \mu m$ and $h = 5\ \mu m$) and sink-in for thick films ($h = 10\ \mu m$, $h = 20\ \mu m$ and $h = 50\ \mu m$) are found by showing the deformed mesh. It is also noticeable that relatively indentation depths when the material pile up initiates are similar for $h = 2\ \mu m$ and $h = 5\ \mu m$, as well as the extrapolated value for film $h = 10\ \mu m$. This finds shows that the material pile-up at contact is also linked to the internal response of crystal and boundary involvement. A further study on the influence of the dislocation activity upon the material pile-up reveals that the both material pile-up and indentation pressure turning up after the indentation size effect zone are related to dislocations pile-up at the rigid boundary. The back effect of piling up dislocations at the grain boundary was reported by other researchers [261, 262]. In indentation problem, this effect is introduced by the rigid boundary, and hence hardens the material response and enables the deformed surface to bump towards indenter.

These studies provide a further understanding of DDP theory and formulations introduced in Chapter 2 and 3, and they are compared to the response of films modelled by CPFE method in the next section. Besides, numerical results, particularly, the indentation pressure curve, contributes as the indention size effect term to the comprehensive hardness curve of a coating system that is discussed in Chapter 6.

5.3 Indentation Problem Solved with Crystal Plasticity Finite Element

In order to capture the response of thin films at larger scales, CPFE simulations (similar to tension case in Chapter 4) are performed in this section. The specimen to be indented is made up of polycrystalline material, whose performance is modelled by a rate-independent formulation as reported in Chapter 3. The indenter is modelled as a wedge-shaped rigid body, and a displacement boundary condition is imposed on the indenter to simulate the indentation process. Results show the hardness response of films characterised by various material properties, substrates and microstructure. At the end, the investigation of continuum hardness transition in a coating system provides a prior foundation for development of a comprehensive indentation pressure formula of a multi-scale coating system, which is shown in Chapter 6.

5.3.1 Methodology and problem definition

In simulations of CPFE material response under indentation, a plane strain analysis of the wedge indentation of a crystal bulk of thickness $H$and length L rigidly bonded to a rigid substrate is carried out. The two-dimensional plain strain indentation problem analysed in CPFE model is sketched in Figure 5.15. Plasticity in the film is calculated by CPFE formulation mentioned above on predefined slip planes. The simulation is performed using ABAQUS and its internal user-defined material subroutine UMAT, as explained in Chapter 3. The indenter is modelled as a non-smoothed wedge-shaped triangular 'analytical surface', and the contact property is set as "frictionless" in tangential behaviour and "hard contact" in normal behaviour, respectively. The CPFE bulk specimen is discretized by a biased mesh with the finest mesh allocated near the indenter tip in order to obtain a higher resolution within the contact zone. Element type is 4-noded non-reduced integration plain strain element with the name CPE4 in ABAQUS element library.

The elastic property of single crystal film is based on aluminium. In single crystal case, there is one grain with varied different orientation angles ranging from 0 to 45 degree with respect to X axis in order to study grain orientation effect. Other CPFE parameters including critical resolved shear stress, hardening parameters and hardening rate are also undertaken parametric study. The reference single crystal properties in CPFE indentation are chosen as in the uniaxial tension problem. Please see Chapter 4 for more details.

Polycrystalline samples are also investigated; in such cases the specimen is generally made of 20 grains unless otherwise specified, and each of the grain is assigned a random grain orientation degree ranging from 0 to 45 degree with respect to the X axis. This polycrystalline case aims to investigate grain boundary and inhomogeneity influence on material response modelling by CPFE under indentation loading.

The boundary conditions are set as following.

$$\begin{aligned} &\dot{u}_y = \ 0 \ \ on \ \ y = 0 \ \text{and} \ \dot{u}_x = \ 0 \ \ on \ \ x = 0 \\ &T_x = T_y = \ 0 \ \ \text{on} \ \ x = 0 \ \ \notin S_{contact} \end{aligned} \tag{5.10}$$

Here, $T = \sigma_{\mathrm{ij}} n_j$ is the surface traction on a surface with outward normal vector n_j.

The displacement rate of wedge-shaped indenter is set as:

$$\dot{u}_y = \ \dot{\delta} = 0.4 m/s \tag{5.11}$$

Indentation process lasts for 0.001s, so that the total applied indentation size is $\delta = 4 \ \mu m$. In order to decrease the expense of computational space, results are taken from ABAQUS calculations every 10 time steps.

Hardness is defined as the reaction force along the Y axis divided by the contact area (that is requested from ABAQUS history output directly), which gives:

$$H \equiv F/A \tag{5.12}$$

In the formula, F is total reaction force within contact, and A is actual contact area, both of which are obtained directly from ABAQUS.

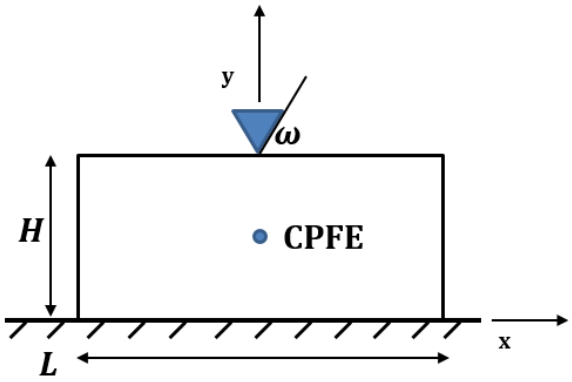


Figure 5.15. Sketch of the boundary value problem of a CPFE crystal indented by a wedge-shaped indenter analysed

5.3.2 Results

In this numerical results section, the response of a crystalline bulk modelled using CPFE under indentation is investigated. In particular, the dependence of hardness of a single crystal upon its material properties have been studied. Besides, a comparison of the response between single crystal and polycrystalline materials has been made to understand the microstructure influence in an indentation process. In the end, we use the formula proposed by Korsunsky [149] to fit the hardness curves obtained in our simulations and other experiments. This formula captures the continuum transition between hardens values of coating film and substrate of a coating system, and will provide the following work of this thesis with resolution at larger scales.

5.3.2.1 Single crystal response

It is essential to understand the response of single crystal under indentation process as single crystal provides the most fundamental microstructure of polycrystalline materials. The general stress field is reported to understand the global stress distribution of a single crystal material, and the general harness evolution curve is illustrated then to show the local response of the film near the contact. Parametric studies on Young's modulus, critical resolved shear stress and crystal orientation are conducted to investigate the factors that can determine the hardness value of a single crystal.

5.3.2.1.1 General stress contour

Mises stress contour of the reference CPFE single crystal (i.e. with grain orientation 0 degree) when indentation depth achieves $\delta = 2\mu m$ is plotted in Figure 5.16. A severe stress concentration is found both in contact and sub-surface that indicates potential micro cracks could possibly nucleate from those highly sensitive regions. In practical applications, indenter tip is usually fitted with a smooth arc instead of an extremely sharp tip in order to reduce this stress singularity. Thus the sub-surface zone

is of more importance when the contact can be considered as 'frictionless'. Besides, plastic flow is found to extend symmetrically from the region adjacent to indenter tip to bottom rigid boundary along an oriented approximately 45 degree plane with respect to X axis. This indicates the most favourable slip direction of a 0 degree FCC single crystal is about 45 degree with respect to indentation direction.

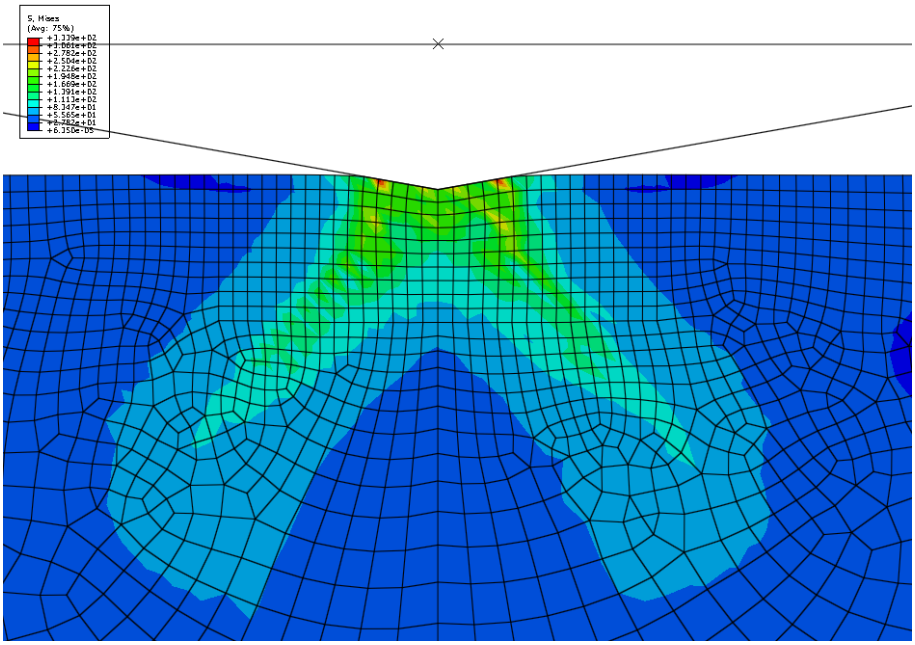


Figure 5.16. Von Mises stress contour plot of the reference CPFE crystal under wedge-shaped indenter indentation when indentation depth achieves $\delta = 2\mu m$ (i.e. the relative indentation depth $\beta = 2\%$).

5.3.2.1.2 General hardness evolution curve

The normal response of CPFE crystals under indentation load is presented by hardness. Figure 5.17 shows the hardness evolution against relative indentation depth of the reference CPFE crystal. It is convenient to use the concept of relative indentation depth, $\beta \equiv \delta/\mathrm{H}$, in our research. It not only provides a dimensionless analysis on fitting of hardness evolution but also it is able to reflect the indentation progress with respect to fixed boundary (in the CPFE or DDP alone case) or the substrate (in the coupling case). There are two stages of the hardness curve in that evolution figure, one of which shows a relative stable plateau and followed by an apparent turning up. The transition occurs at approximately at $\beta = 4\%$, and the subsequent increase in hardness is attributed to the presence of rigid substrate bonded to the CPFE crystal. The transition relative indentation depth obtained in this simulation is relatively smaller than those from experiments shown to be around 10% [162]. This earlier transition phenomenon is attributed to the fact that the substrate in experiments are not perfectly rigid and hence indentation experiments normally show a delayed involvement of the substrate. The following increase of hardness curve is due to the presence of the rigid boundary that prevents the plastic flow the crystal extending further over the boundary. Therefore, the equivalent hardness is also affected by the presence of the boundary which can be taken as substrate with a large value of

hardness. A quantitative analysis of the hardness evolution curve will be discussed in the following section.

Besides, there is no typical Indentation Size Effect captured in CPFE-alone simulations even though indentation depth resolution is rather high. The stable value of hardness curves before transition is taken as the hardness value of a continuum crystal material. The stable hardness value,$H = 150$ MPa, is found as approximately triple as its yield stress ($\sigma_Y = 45\ MPa$) of CPFE bulk, which is consistent with the general conclusion: $\mathrm{H} \cong 3\sigma_Y$

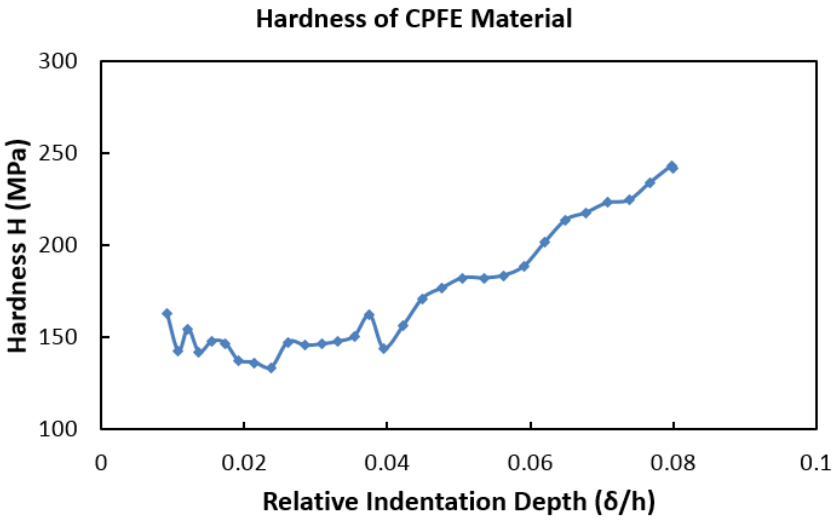


Figure 5.17. hardness evolution curve of the reference CPFE crystal against relative indentation depth, with the trend lines of two different stages in indentation process

Material parameters including Young's modulus (representing elasticity), critical resolved shear stress (representing plasticity) and grain orientation (representing microstructure) are varied in the following sections to investigate their influence on crystal hardness.

5.3.2.1.3 Hardness dependence on Young's modulus

The dependence of hardness of a FCC CPFE single crystal on its Young's modulus is depicted in Figure 5.18. The definition of hardness H is the stable value of indentation pressure evolution curve. Young's modulus E is varied from $3.5\ GPa$ to $280\ GPa$. Both hardness value and Young's modulus are normalized respectively by hardness value ($H_0 = 150MPa$) and Young's modulus ($E_0 = 70GPa$) value of the reference CPFE single crystal. As seen in the figure, it is a positive linear dependence of CPFE single crystal hardness on its Young's modulus with values considered here. It is reasonable to predict that an elastic-harder crystal has a harder normal response in contact. From microstructure view, hardness is a measurement of material flow resistance that is intrinsically linked to the strength of atom bonds that is represented in terms of elastic modulus in macroscopic. Other similar relation between Young's modulus and hardness of materials are also found in other works, e.g. [263-266]

A best-fit of the linear dependence of hardness upon Young's modulus in Figure 5.18 is conducted in a EXCEL toolbox which is developed based on least-squares method [267].The best fit linear equation for describing the relationship between Young's modulus and hardness of CPFE single crystal hardness is given below:

$$H = 0.445 \times E + 109.4 \ MPa \tag{5.13}$$

That linear fit formula eq. (5.13) achieves an adjusted coefficient of determination $R^2 = 0.996$.

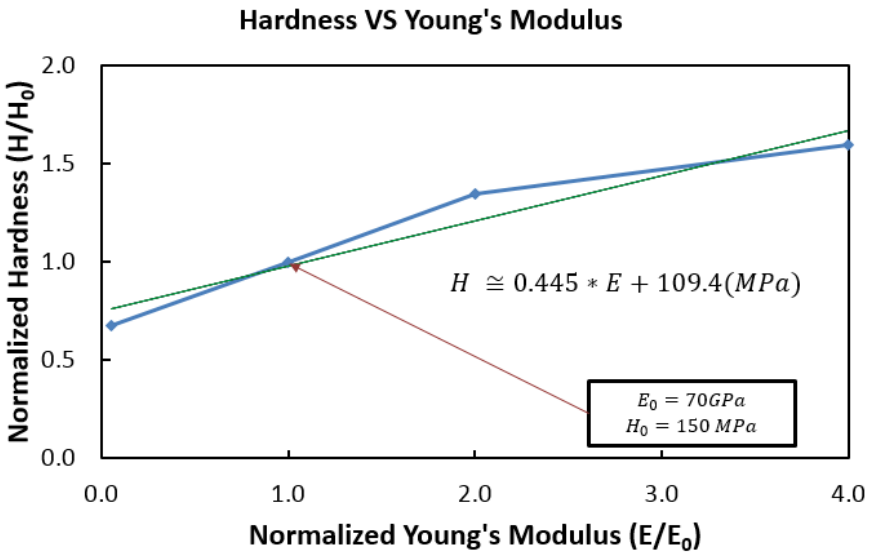


Figure 5.18. the relationship between hardness and Young's modulus of CPFE single crystal. Other CPFE material parameters are set as identical as the reference CPFE single crystal. Both hardness values and Young's modulus are normalized by the hardness value and Young's modulus value of reference CPFE single crystal.

5.3.2.1.4 Hardness dependence on critical resolved shear stress

The dependence of hardness of a single crystal on its critical resolved shear stress (CRSS) is depicted in Figure 5.19. Both hardness value and critical resolved shear stress are normalized respectively by the hardness value ($H_0 = 150MPa$) and CRSS ($\tau_{c0} = 9MPa$) value of reference CPFE single crystal. As seen in the figure, it is also a linear dependence of CPFE single crystal hardness on its CRSS for values considered here. It is reasonable to predict that crystal with a higher yielding stress yields a harder normal response in contact. Hardness is a measurement of highly localized plastic deformation of materials. Thus the value of hardness is related to the yield stress of materials. But as discussed in Chapter 4, critical resolved shear stress is microscopically linked to the yield stress of a crystal. Therefore, it is expected that there is a positive dependence of hardness on critical resolved shear stress of crystals. Experiments including [268-270]also verify similar trends although the detailed relation varies.

The best-fit linear equation for describing the relationship between critical resolved shear stress and its hardness of CPFE single crystal hardness is given below:

$$H = 60 + 10 * \tau_c \tag{5.14}$$

That linear fit eq.(5.14) achieves an adjusted coefficient of determination $R^2 = 0.999$.

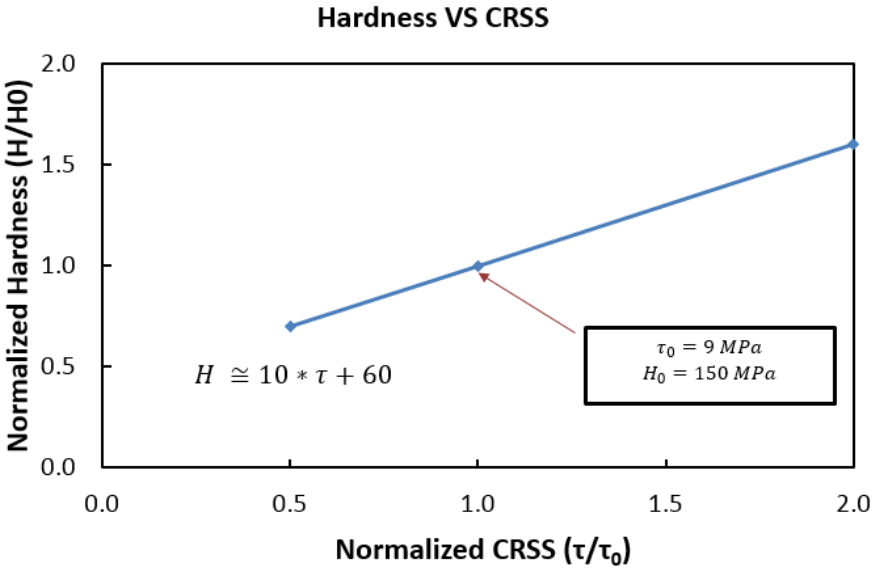


Figure 5.19. the relationship between hardness and value of critical resolved shear stress (CRSS) of CPFE single crystal. Other CPFE material parameters are set as identical as the reference CPFE single crystal. Both hardness value and critical resolved shear stress are normalized by the hardness value and Young's modulus value of reference CPFE single crystal

5.3.2.1.5 Hardness dependence on crystal orientation

The dependence of hardness of a FCC single crystal on grain orientation Φ is depicted in Figure 5.20. Grain orientation Φ is varied from 0 to 45 degree only as cubic crystal slip systems are symmetrical about 45 degree rotation angle. Please see Chapter 3 for more details about Euler Angle notations. All hardness values of different oriented grains are normalized by the hardness value ($H_0 = 150MPa$) of reference CPFE single crystal (0 degree orientation). As seen in the figure, harness value increases with increasing grain orientation and finally achieves a plateau with a hardness value $H_{45} = 180.3MPa$. It is reasonable to obtain a stronger hardness response of a grain with grain orientation closer to 45 degree slip plane as that orientation yields the most strong stress strain response curves in tension problem as well. However, there is an insensitivity of the hardness of CPFE single crystal on grain orientation when its grain orientation approaches 45 degree. This phenomenon is attributed to the fact that the indentation process introduces large plastic deformation highly localized near indenter tip so that flow stress majorly determines the hardness of materials. The corresponding flow stresses are found to be close among CPFE single crystals with different orientations. Please see the parametric study on the dependence of flow stress upon the grain orientation in the uniaxial tension problem (Chapter 4).

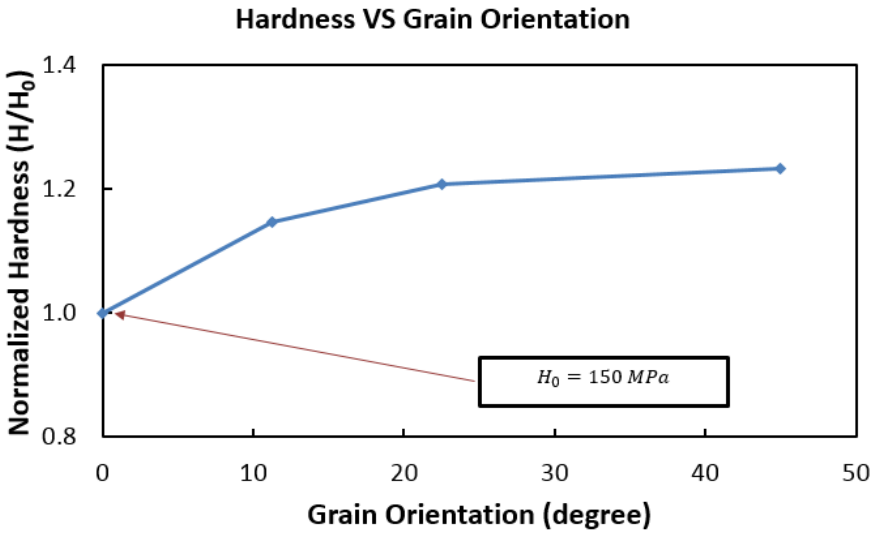


Figure 5.20. the relationship between hardness and grain orientation of CPFE single crystal. Other CPFE material parameters are set as identical as the reference CPFE single crystal. Hardness values of different CPFE films are normalized by the hardness value of reference CPFE single crystal

5.3.2.2 Polycrystalline specimen response

Samples in practical engineering environment are normally composed of grains with random orientations, i.e. polycrystalline material. Thus, it is significant to understanding the response of a polycrystalline specimen under indentation. We herein randomly assign orientation angles of 20 grains in a specimen to represent a anisotropic polycrystalline material.

5.3.2.2.1 Plastic deformation

Accumulated plastic strain (i.e. solution dependent variable SDV (69)) contour of films under wedge shaped indenter indentation is plotted for a single crystal (with a 45 degree orientation grain with respect to X axis) and a polycrystalline material with 20 anisotropic grains in Figure 5.21 (a) and (b) respectively. The shown contour is obtained at the instant when indentation depth achieves $\delta = 2\mu m$ (i.e. relative indentation depth $\beta = 4\%$). Accumulated plastic strain is used to illustrate the plastic formation and slip in crystals and thus to further indicate potential locations for crack nucleation. As can be seen in Figure 5.21, the plastic deformation of single crystal expands more homogenously, and a highly localized strain concentration is found at subsurface underneath indenter. However, anisotropic response of polycrystalline crystal produces random internal strain concentration even including several sites close to rigid bottom boundary. According to the values of accumulated plastic strain, the polycrystalline film generates a contour with a wider range of peak values which depicts the characteristics of inhomogeneity and anisotropy in the polycrystalline material introduced by inter-grain interactions between grains with different orientation angles.

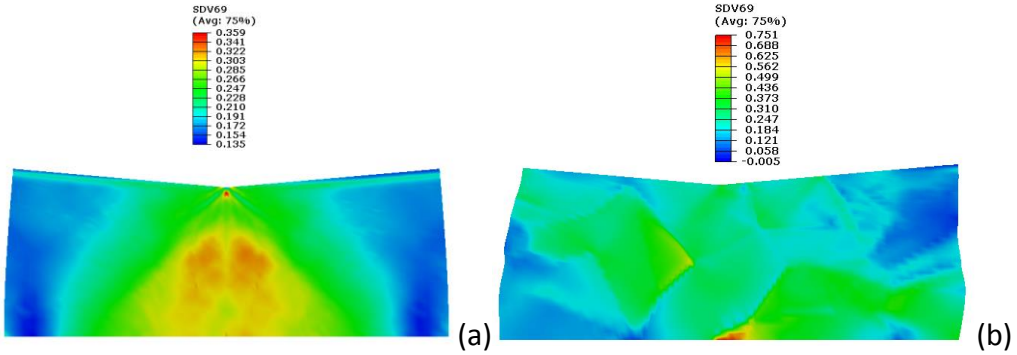


Figure 5.21. accumulated plastic strain contour of (a) a single crystal CPFE film (b) a 20 grains polycrystalline CPFE film under wedge shaped indenter indentation when indentation depth achieves $\delta = 2\mu m$ (i.e. relative indentation depth $\beta = 4\%$).

5.3.2.2.2 Hardness response

Actual indentation pressure p_A evolution curves versus applied indentation depth δ are plotted in Figure 5.22 for a single crystal (with a 45 degree orientation grain with respect to X axis) and the polycrystalline material (20 grains with randomly distributed grain orientations) under wedge indentation. Both curves show a typical hardness curves that there is a plateau with values considered as their hardness values and afterwards a turn up due to rigid boundary effect involved. See Section 5.3.2.1.2 for more discussion. Before the turning up, the single crystal yields a stronger response as the 45 degree orientation slip system is taken as the toughest among all planes. However, after the turning up, indentation pressure of the polycrystalline film is found larger than that of the single crystal. That indicates that the polycrystalline grain structure interacts more with the rigid boundary. This point can also be used to explain the unexpected slip concentration points found in Figure 5.21 (b).

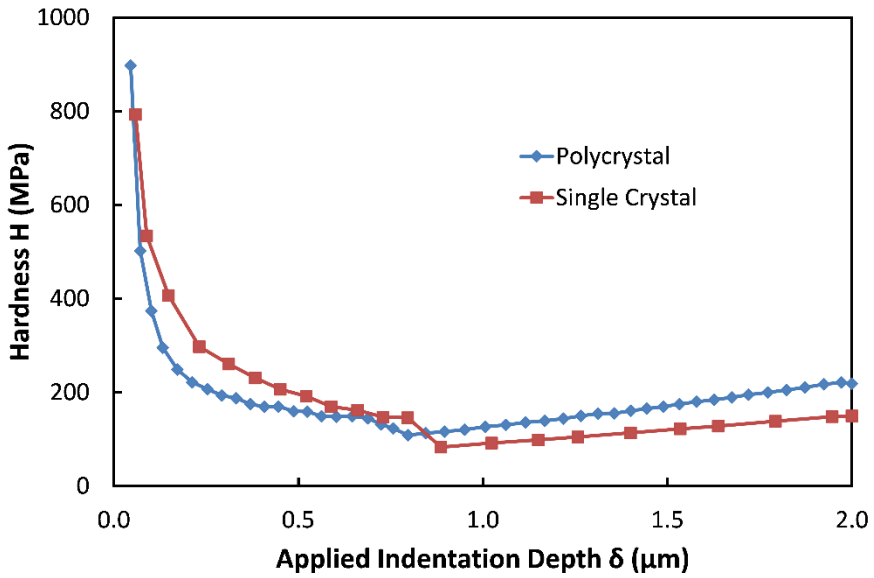


Figure 5.22. actual indentation pressure p evolution curves versus applied indentation depth $\delta$of a single crystal and a polycrystalline material under wedge indenter indentation. The indentation simulation process is carried out up to $\delta = 2\mu m$.

Of more significance, it is worth noting that the polycrystalline structure with a much smaller grain size does not harden the film, compared to response of the single crystal film. This indicates that grain boundary is not explicitly described in the CPFE formulations we adopted in this project. Thus plastic zone can expand from a grain to its adjacent grains without additional energy. Another point is the decreasing trend of hardness values found in Figure 5.22 is not the well-known indentation size effect as there is no specific characteristic length scale in our CPFE formulations. It could be numerical errors due to calculations and sampling frequency.

5.3.2.3 Hardness transition in a coating system

5.3.2.3.1 Simulations

Hardness transition between coating film and substrate of a continuum coating system is simulated using a model sketched in Figure 5.23. A two-dimensional plane strain analysis of wedge indentation of a coating system with dimension thickness $2\mathrm{H} = 200\ \mu\mathrm{m}$ and length $\mathrm{L} = 200\ \mu\mathrm{m}$ rigidly bonded to a rigid bottom boundary is carried out. The film of this coating system is modelled by CPFE description with dimension $\mathrm{L} \times \mathrm{H} = 200\ \mu\mathrm{m} \times 100\ \mu\mathrm{m}$ while the substrate is modelled by purely elastic crystal with dimension $\mathrm{L} \times \mathrm{H} = 200\ \mu\mathrm{m} \times 100\ \mu\mathrm{m}$. Indenter is modelled as a non-smoothed wedge-shaped triangular analytical surface with angle $\omega = 5°$ with respect to the X axis, and contact property is set as “frictionless” in tangential behaviour and “hard contact” in normal behaviour, respectively. Displacement of indenter achieves $\delta = 80\ \mu\mathrm{m}$ i.e. relative indentation depth $\beta = 0.80$ .The compatibility between coating and substrate is ensured in ABAQUS element connection. Coating film domain is discretized by a biased mesh with the finest mesh allocated near indenter tip in order to obtain a higher resolution within contact. The element type is 4-noded non-reduced integration plain strain element with the name CPE4 in ABAQUS element library. The elastic material is discretized by a uniform mesh with the same element type. Substrate domain is discretized by a uniform structured mesh to reduce the expense of calculations.

Coating film is modelled as a single CPFE crystal with the same material parameters as the reference single crystal that yields a hardness value $\mathrm{H} = 150\ \mathrm{MPa}$. Plasticity is calculated by the CPFE formulation mentioned above on predefined slip planes. The simulation is completely calculated by using ABAQUS and its internal user-defined material subroutine UMAT. The substrate is modelled as an isotropic elastic material with $\mathrm{E} = 700\ \mathrm{GPa}$ and $\upsilon = 0.33$, which yields a hardness value $\mathrm{H} = 35\ \mathrm{GPa}$. The dependence of hardness of an elastic material upon its Young’s modulus is shown in Appendix VII.

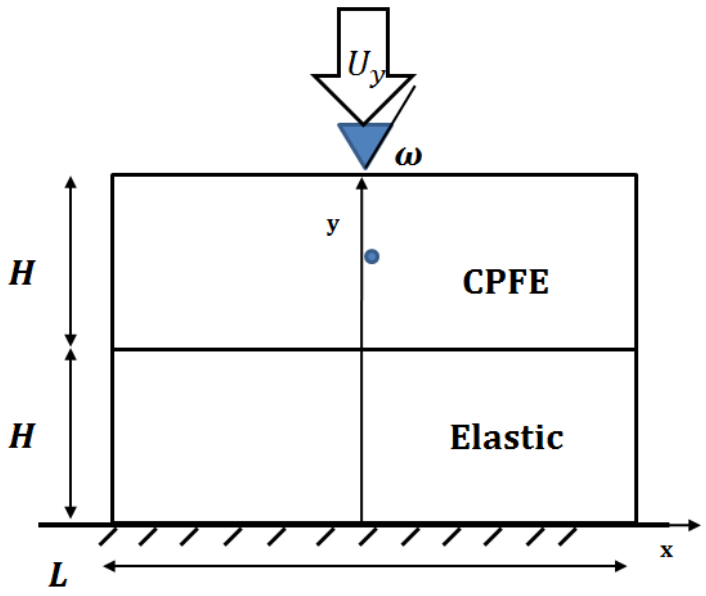


Figure 5.23. Sketch of a coating system indented by a wedge-shaped indenter analysed. The coating film of this coating system is modelled as CPFE single crystal while the substrate is modelled as a purely elastic material.

Hardness revolution of the coating system shown in Figure 5.23 with the reference single crystal as its coating and purely elastic material as substrate is plotted in Figure 5.24. The hardness curve starts with a stable plateau with a value around 150 MPa which is approximately as hardness value of the coating film. After the transition relative indentation depth (approximately $\beta = 0.30$), the composite hardness curve turns up sharply and approaches to the hardness of hard substrate.

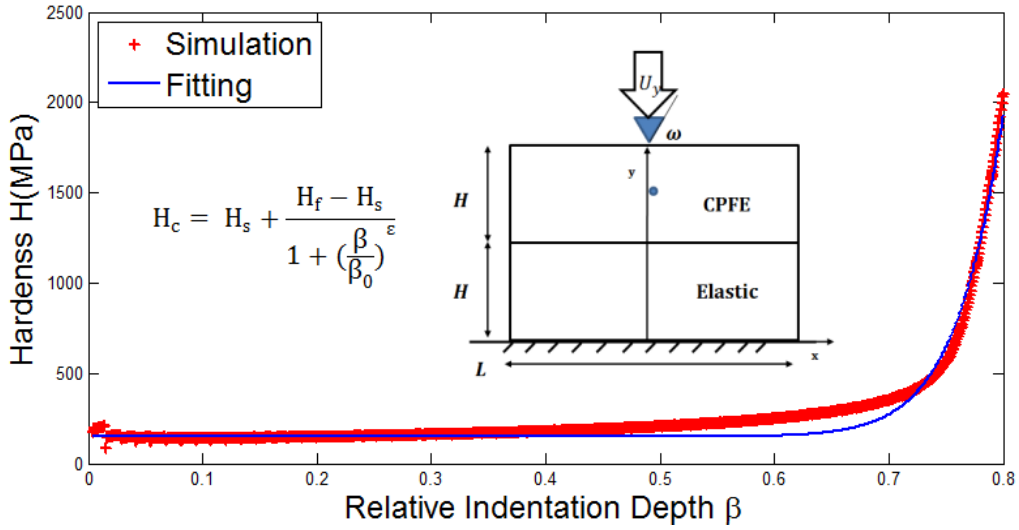


Figure 5.24. hardness revolution of a coating system with the reference single crystal as its coating and purely elastic material as substrate. The best fitting hardness curve of this coating system with eq.(5.15) is also plotted for reference.

In order to quantitatively analyse hardness transition from coating film and substrate, the following formula eq.(5.15) is used to fit the hardness evolution curve of a composite system, especially focusing on the substrate effect[149].

$$H_c = H_s + \frac{H_f - H_s}{1 + (\frac{\beta}{\beta_0})^{\varepsilon}} \tag{5.15}$$

The hardness value of coating film H_f is set as the hardness of reference single CPFE crystal $H_f = 150\ MPa$, the hardness value of substrate H_s is set as the hardness of the elastic substrate $H_s = 35000MPa$ and β_0, ε are fitting parameters. The best fit curve is also plotted in Figure 5.24, and corresponding fitting parameters are tabulated in Table 5.9.

Table 5.9. parameters used to plot the best fit curves using Eq. (5.15) in Figure 5.24

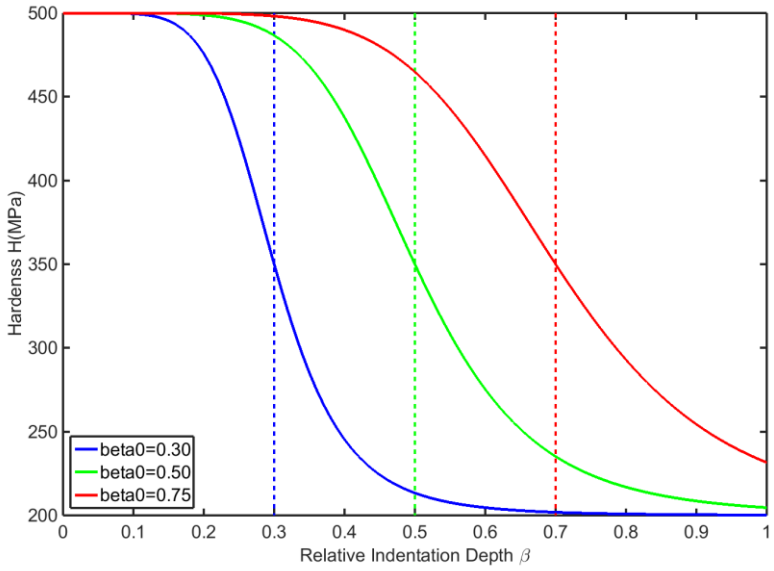
Parameter	Unit	Value
H_s	MPa	35000
H_f	MPa	150
β_0	-	0.9235
ε	-	20.32
R^2	-	0.9871

The fitting curve well matches the simulation data as the adjusted coefficient of determination is calculated as $R^2 = 0.9871$. The relative indentation depth is adopted in transition equation as it is able to represent indentation progress with respect to the substrate. The fitting parameter β_0 determines the middle point of transition, and it should physically link to a length scale parameter. The exponent fitting parameter ε determines the slope of transition, and it can be intrinsically related to the microstructure of coating system

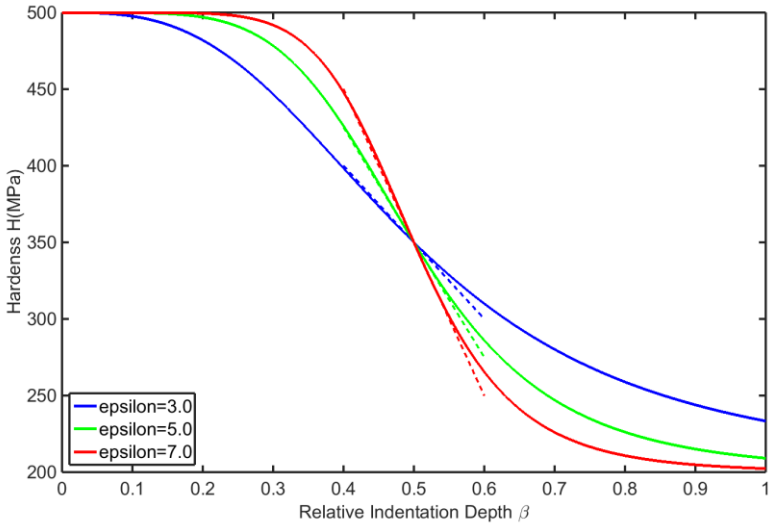
5.3.2.3.2 Parametric study

The influence of fitting parameters in eq. (5.15) upon hardness variation is quantitatively investigated using a parametric study method, and the dependence of fitting parameters β_0 and ε are plotted in Figure 5.25 (a) and (b) respectively. From mathematical perspective, the function of composite hardness value H_c exhibits a monotone transition from the values of film hardness H_f to the substrate hardness value H_s. As the parametric study case mimics the ordinary relationship of a coating system that the coating film is harder than the substrate, $H_f > H_s, H_c$ shows a monotone decreasing function style. The magnitude of decreasing rate is dependent values of relatively indentation depth β. From Figure 5.25 (a), we can see that the magnitude of decreasing rate increases with β until β reaches a transition value β_0, and it starts to decreases with β afterwards. This indicates that the fitting parameter β_0 determines where the maximum value of decreasing rate is in terms of relative indentation depth, and a larger value of parameter β_0 results in a later transition. From Figure 5.25 (b), the exponent fitting parameter ε reflects a

comprehensive decreasing rate of those transition curves. In particular, a larger value of parameter ε results in a more rapid transition of a hardness curve.



(a)



(b)

Figure 5.25. Parametric study of the influence of fitting parameters (a) β_0 and (b) ε of the proposed formula upon hardness transition between the coating film and substrate. Cases are shown with the condition that film is harder than substrate, i.e. $H_f > H_s$

5.3.2.3.3 Fitting experimental data

The continuum transition hardness evolution eq.(5.15) is used to fit a set of nano-indentation data [271]. That indentation was finished by applying displacement on a Vickers indenter indenting into a TiN-M2 steel coating system. The best fit parameters of eq.(5.15) are tabulated in Table 5.10. From fitting results, the transition of coating system in experiment is found to be smoother than in our simulations as the discrepancy between exponent fitting parameters is shown quite large. This finding is

attributed to the finite element feature that elements are modelled more rigid than practical material response.

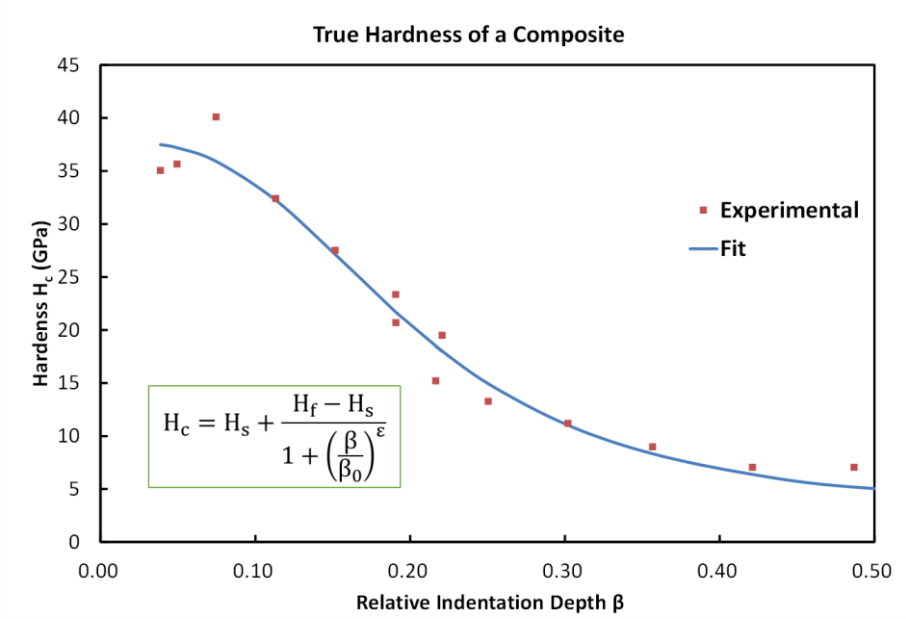


Figure 5.26. Micro (Buehler) and macro indentation data collected from a $3.5\mu m$ TiN coating on M2 tool steel. A best fit curve using eq.(5.15) is also shown in blue line.

Table 5.10. parameters used for fitting an indentation experiment data

Parameter	Unit	Value
H_s	GPa	2.6
H_f	GPa	37.8
β_0	-	0.2023
ε	-	2.89
R^2	-	0.9846

Although the transition equation generally works well for both continuum simulations and experiments, it still lacks of a characteristic length scale for accounting the well-known indentation size effect. In nano or micro-scale, hardness evolution of coating film is taken as a flat curve which is not true in experiments[8].This motivation has driven us to apply dislocation dynamics plasticity (DDP) on indentation problem. Planar indentation problem analysed using DDP will be carefully discussed in the next section.

5.3.3 Summary

Plane strain analyses of indentation of polycrystal films by rigid wedge-shaped indenter are carried out by modelling films with crystal plasticity finite element method (CPFE). The calculations are conducted in ABAQUS using user defined material subroutine (UMAT) and a data file providing the polycrystal microstructure of films. The contact is fully defined in ABAQUS internal algorithm with hard contact n normal direction and 'frictionless' in tangential direction respectively. Computations are firstly carried out to investigate the significance of Young's modulus, critical resolved

shear stress and grain orientation on indentation pressure response of single crystal films. Secondly the number of grains is increased to twenty and orientation angles are randomly assigned to study polycrystalline material response. Finally a formula is used to study the hardness transition of a continuum coating system. The formula works well for the simulations considered here and data from an experiment of indentation on a coating system experiment.

For single crystal's response, general indentation pressure curves keep fluctuation about a stable value when applied indentation depth is relatively small compared to film thickness and then turns up due to rigid boundary after a critical indentation depth. The stable indentation pressure is taken as to be the hardness value of continuum film. The hardness value of a single CPFE crystal modelled is determined by Young's modulus, critical resolved shear stress (CRSS) of material and grain orientation. The linear dependence of hardness value on Young's modulus and the critical resolved shear stress of material are investigated respectively. The relationship between the grain orientation and the hardness is also revealed, but the correlation becomes weak when grain orientation approaches to 45 degree with respect to indentation direction. This phenomenon is explained as hardness value relies on flow stress instead of yield stress because large strain is introduced soon near indenter tip, and the flow stress of grains with large orientation angles are rather similar especially strain is large. Other hardening parameters of CPFE also have an effect on the hardness response which is similar to the tension case. The hardness value found in the single crystal indentation simulation is roughly triple as the yield stress obtained in the corresponding film uni-axial tension simulation. Simulation with film modelled by purely elastic material is also conducted. Their indentation pressure evolution curves also show a "fluctuation and turning up" trend and the hardness value of an elastic material is estimated by the linear dependence on Young's modulus.

For polycrystalline material, the stress contour shows the strong effect of randomly distributed grains on ruining the homogeneity and isotropic behaviour of a typical single crystal. Also, the stress values of polycrystalline material are not increased by small grain size (well-known Hell-Patch effect) compared to single crystal films. It is due to that the CPFE algorithm employed herein does not explicitly describe the grain boundary effect. In particular, the plastic flow in the polycrystalline material is not slowed or blocked by the grain boundary and thus the material is not hardened by the grain boundary. The indentation pressure evolution of polycrystalline material also shows that the response of polycrystalline material under indentation strongly relies on the detail of micro-structure underneath the indenter tip.

For a typical coating system modelled by continuum description, its hardness evolution curve starts from the hardness value of coating film and gradually approaches to the value of substrate. This hardness transition is described by eq. (5.15). This proposed formula works well for results of simulations considered here and nano-indentation experiments. However, the fitting parameters are not interpreted with any physical significance. Besides, the transition rate found in

simulations is much higher than values fitted in experiments. That reveals that the transition behaviour from coating to substrate is dependent on the discrepancy between coating and substrate materials.

The proposed formula will be employed to describe the indentation pressure transition part in the latter multi-scale modelling of a coating system by coupling DDP and CPFE.

5.4 Comparison between responses of CPFE and DDP descriptions in indentation problem

Simulations for thin films indented by wedge-shaped indenter are conducted by modelling films with dislocation dynamics plasticity (DDP) and crystal plasticity finite element (CPFE) methods respectively. CPFE input parameters are obtained by a calibration process which aims to match CPFE stress strain response curve to DDP curve in a uni-axial tension problem. Results from CPFE and DDP modelling both show some key features of indentation process, including stress concentration underneath indenter, plasticity zone spread from indenter tip to rigid boundary. However, the different mechanisms in describing plasticity between DDP and CPFE naturally determines that there are some different findings between there results.

The singularity feature of dislocations provides highly localized stress concentration in films modelled by DDP, especially areas near indenter tip while CPFE models crystal performance using a classical continuum method that enables stress field to be smoothed. Similar to the uniaxial tension case, dislocation activity in DDP modelling ruins isotropy and homogeneity of the overall plasticity flow although general global performance, including reaction forces, total contact area and indentation pressure, is similar to CPFE results. In general, plasticity of CPFE modelling exhibits an average effect of details inside a crystal while DDP addresses a localized small area.

The most significant feature of indentation process captured by DDP simulation is indentation size effect which is demonstrated as indentation pressure of films response decreases with increasing applied indentation depth when contact area is small. This is attributed to dislocation activity explicitly modelled localizing near contact and indenter tip when applied indentation depth is small. However, CPFE modelling is only able to predict a continuum indentation pressure (i.e. the hardness of films) due to its plasticity modelling method. Both calculations using DD and CPFE show that indentation pressure is increased by the presence of rigid boundary when applied indentation depth is large enough. In CPFE calculations, the details of the substrate effect are investigated and described using a mathematical formula based developed by [149]. The formula is able to capture indentation pressure transition between coating film and substrate although the fitting parameters in that formula have not been given any physical meanings.

Although DDP modelling of films is capable of capturing a large amount of details in indentation process, it is not economic in computational space and time to apply DDP

modelling to a film with large dimension. Compared to a CPFE modelling with the same geometry dimension and mesh configuration, it takes up to 40 times expense to finish a simulation with DD modelling. This drawback indeed limits the application of DDP to a large scale region although we use only a two-dimensional computation frame. In contrast, with a typical advantage of traditional continuum modelling method, CPFE modelling can be applied to reasonably large size specimen without losing too much general information.

It is also noting that hardness value of a single crystal material predicted by DDP is around 20% larger than the one obtained from CPFE modelling although uniaxial tension stress strain response curves of them have been matched. This phenomenon reflects that the continuum hardness value is a representative of highly localized at contact material property while the general macroscopic stress strain curve is a comprehensive and global material performance. The stress singularity introduced by dislocations in DDP algorithm effectively hardens the local response of crystal materials and thus its hardness value is higher than CPFE prediction.

Based on the fact that DDP can successfully capture the decreasing style of hardness evolution curve of crystal response, it is feasible to apply DDP to indentation simulation to predict indentation pressure variation when applied indentation depth is small. Besides, parametric study on microstructure influence allows us to describe the indentation pressure decrease using a mathematical formula with physically interpreted parameters. In contrast, CPFE works for computations where the resolution of indentation pressure in ISE zone is not highly required. Therefore, it is reasonable to consider a new multi-scale modelling method that couples the advantages of DDP and CPFE modelling together, in order to completely describe the indentation pressure variation of a coating system over a wider range of indentation depths. In particular, DDP modelling should be used in sensitive regions, for instance, contact surface and subsurface. Meanwhile, the surrounding region of a polycrystalline specimen is modelled using CPFE description in order to reduce simulation cost without loss of accuracy too much. This multi-scale coupling method and its result will be reported in the next section.

5.5 Summary

Planar indentation problem has been simulated by applying crystal plasticity finite element (CPFE) and discrete dislocation plasticity (DDP) at different scales, respectively. The formulations of CPFE and DDP employed herein are introduced in Chapter 3. The adaptation and application of these formulations of CPFE and DDP to the indentation problem focuses on the highly localized plasticity rather than a global response as in the tension problem discussed in Chapter 4.

A large number of parametric study sets have been conducted in CPFE and DDP calculations to study microstructure influence on normal material performance under

indentation, and a comparison between CPFE and DDP results discusses the difference of their material modelling methods at their respective representative scales.

In this chapter, a newly proposed formula describing indentation pressure variation of thin films has been obtained using DDP calculations when the applied indentation depth is relatively small, together with a quantitative analysis of the hardness response of a coating system at continuum level using CPFE calculations. It the latter case, the dependence of indentation pressure on the presence of a substrate has been investigated. Both DDP and CPFE calculations performed in this chapter provide a solid foundation for the application of the proposed multi-scale modelling approach to indentation problems, which is addressed in Chapter 6.

6 Application of the Proposed Multi-Scale Coupling Method to Indentation

In this chapter, planar indentation problem is solved using the multi-scale coupling strategy proposed in Chapter 3 and applied to uniaxial tension in Chapter 4. The application of the coupling method enables us to investigate the effect of the substrate on a coating system without loss of resolution at the very small scales. In doing so, the computational efficiency of indentation simulations is improved due to the fact that dislocation details do not need to be captured throughout the simulations and the substrate can be studied using the crystal plasticity description. Moreover, a new comprehensive formula that quantitatively describes the indentation pressure variation as a function of the indentation depth has been developed by applying the multi-scale modelling techniques to the study of different coating systems. Finally, a comparison between different modelling approaches of grain/substrate boundary conditions between discrete and continuum sub-regions is also reported.

6.1 Introduction

As discussed in Chapter 5, indentation size effect has been studied by applying strain gradient plasticity [18, 161] and/or discrete dislocation plasticity [2, 114]. On the other hand, research on the influence of the substrate on the behaviour of coating systems has mainly been confined to continuum analyses [149, 150]. Therefore, there is a lack of a comprehensive relationship that is effective over the full range of indentation depths encountered in typical experiments. The proposed multi-scale modelling between discrete dislocation plasticity (DDP) and crystal plasticity finite element (CPFE) is in principle capable of investigating coatings' response and size effects across different length scales. Such methodology has not yet been applied to indentation of layered systems and it may prove to be the ideal vehicle to study multi-layer polycrystalline coatings.

Coating systems, usually including one or more thin films deposited and bonded to a bulk substrate, is widely used to enhance the performance (hardness, wear resistance, corrosion resistance, creep resistance, etc.) of the substrate. The process technology and functions of coating served industry for several decades, but understanding the contact response of a coating system remains challenging both in terms of material behaviour and tribological performance. Reliable quantitatively modelling methods are needed to explain and predict the performance of a selected coating film for a certain substrate. Due to the complicated mechanical behaviours of coating components at different scales, it is important to develop a multi-scale model which is able to cover a properly wide indentation depth scales. There is general agreement that the dimension of the contact greatly affects the overall performance of a coating system. In particular, when the contact size is less than the thickness of the coating film, the coating film dominates the mechanical response of the system, and when the

contact size is large enough compared with the thickness of the film, the substrate controls the system behaviour. However, in practice, there are two main problems when trying to model the mechanical performance of a coating system quantitatively.

The first problem is the difficulty of obtaining consistent experimental results, especially when contact size is much less than coating thickness. In this circumstance, environmental disturbance, *e.g.* heat rise [18] and surface roughness[272], can majorly affect measurements and hence result in uncertainty of experimental results[273].The second problem lies in the wide range of scales required to be captured by any proposed model that aims to capture the coating behaviour over a large range of indentation depths. Previous modelling attempts, *e.g.* [149, 274, 275], involve two types of methods: the system model, which separates the behaviour of the coating film and the response of the substrate, without considering the detailed deformation of each component, and the mechanistic model, which considers the effect of a given deformation mechanism on the measured contact response. Both of the models mentioned above have their own shortcomings, when the deformation under the contact conflicts with their original assumptions. In fact, most of coating systems show a mixture of deformation modes, which requires a multi-scale model to capture the general performance over a wide range of scales.

Korsunsky et al. [149, 150, 275] develop and improve formulas that provide the hardness variation of a coated system as a function of indentation depth; it accounts for the effect of the substrate on the hardness of a thin film during the indentation process by looking at the total deforming volume and the work of indentation [150]. This method captures the transition between coating-dominated and substrate-dominated response well for many film-substrate systems, such as Cr-Al and Ni-Cu; the formula is very easy to implement and has a limited number of parameters:

$$H_c = H_s + \frac{H_f - H_s}{(\beta/\beta_0)^{\varepsilon}}, \beta \equiv \delta/h \tag{6.1}$$

where $\mathrm{H_s}$ is the hardness value of the substrate, $\mathrm{H_f}$ is the hardness value of the coating film, and both of these value can be determined independently by fitting to experimental data obtained for the substrate and the film respectively. $\mathrm{H_c}$ is the hardness value of the coating system, while β_0 and ε are material dependent parameters, which incorporate a wide range of composite and indenter properties such as coating brittleness, interfacial strength, indenter geometry, etc. In particular, parameter β_0 determinates where the transition is while exponent parameter ε determines the transition slope between the film and substrate. The detailed parametric study can be found in Appendix VIII.

That formula is based on the concept of total deforming volume and the work of indentation, and it worked well for some typical composite systems, which are listed below.

Table 6.1 Coating systems well fitted with Korsunsky's formula

Specimen	Coating Film	Thickness (micron)	Substrate
ion plating series (SIP)	TiN	2-9.8	M304
PAPVD series	TiN	0.5-25	ASP23
M053	NbN	2.8	M304
M057	CrN	7.8	M304
M059	ZrN	3.2	ASP23

However, it does not account for the indentation size effect observed at small indentation depths. This limitation naturally comes from the fact that there is no length scale parameter in continuum calculations. Please see Section 6.3 for more discussion. Discrete dislocation plasticity was primarily employed to investigate the indentation size effect. However, it is extremely expensive in terms of both time and space to model a coating system wholly with discrete dislocation plasticity, especially we require a comprehensive solution of the coating system response at large indentation depths. This is the subject the Section 6.4. A multi-scale model that couples CPFE and DDP at different scales is principally able to overcome the drawbacks that these individual techniques are limited to. Moreover, the application of the multi-scale model on a coating system helps understand its comprehensive behaviour at a wider range of indentation depth.

In Section 6.2 the general concurrent multi-scale coupling methodology developed in Chapter 3 will be applied to capture the behaviour of coating thin films; the surface film is described by discrete dislocation plasticity while the substrate region is modelled using conventional continuum crystal plasticity. Numerical results are analysed to investigate indentation pressure evolution at scales all through a coating system. Finally, remarkable conclusion points is summarized and suggestions for extending the current work are proposed.

6.2 Methodology

6.2.1 Problem definition

A two-dimensional plane strain analysis of indentation of a polycrystalline material is conducted using the general coupling strategy outlined in Chapter 3. The details of its application on the indentation problem is shown as following.

The key region of the polycrystalline material, i.e. where dislocation activity is likely to be high, is located underneath the tip of the indenter and is modelled using DDP. The surrounding region is modelled using the CPFE description, which is modelled here as a single FCC crystal whose axes are oriented at zero degrees with respect to the reference system, i.e. parallel to the x-axis. The multi-scale modelling of the indentation problem is schematically represented in Figure 6.1.

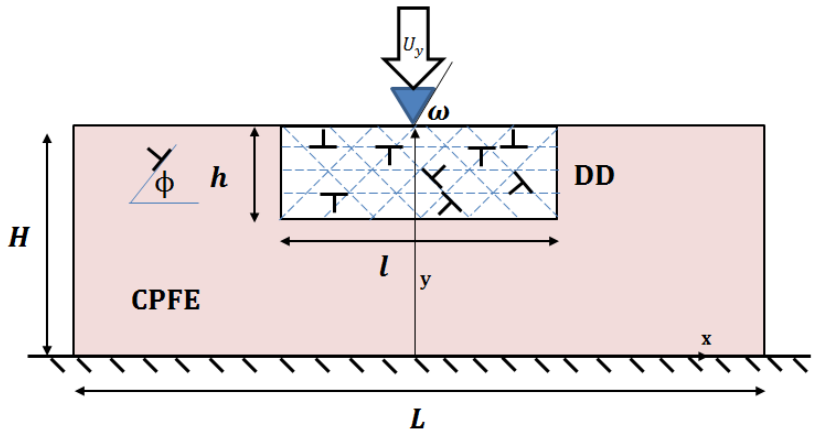


Figure 6.1. Schematic representation of the indentation DD-CPFE coupling problem.

The indenter is modelled as a wedge-shaped rigid body with indentation angle $\omega = 5°$ with respect to the x-axis. This wedge angle is constrained to a smaller value than that used in most experimental studies (e.g. Berkovich or Vickers) because larger indenter angles would lead to large contact area jumps in discrete dislocation calculations [2].

The dimensions of the entire sample are $L \times H = 300\ \mu m \times 100\ \mu m$. Dislocation activity is restricted to a rectangular region underneath the indenter tip. Calculations are performed for different configurations obtained by varying the thickness of the DDP region from $h = 2\ \mu m$ to $h = 20\ \mu m$ for a fixed width $l = 30\ \mu m$. The size of the surrounding CPFE region is varied accordingly. The finite element mesh in the DDP region is highly refined with smallest element size $0.04\mu m \times 0.5\mu m$ in order to model the contact accurately and ensure the effect of the singular ($\tilde{}$) fields is fully captured on the boundary of the ($\hat{}$) problem. The finite element mesh in the CPFE region is characterised by increasingly smaller elements towards the DDP region and a much coarser description away from the DDP region. Another feature of the CPFE mesh is that the node positions and element sizes are exactly the same as the DDP region at the coupling boundary.

Perfect stick (no slip) is assumed at the boundary between the DDP surface and the indenter. Thus, the boundary conditions are:

$$\dot{u}_x = 0, \dot{u}_y = \dot{\delta} \quad \text{on} \quad S_{contact}, \tag{6.2}$$

where $S_{contact}$ denotes the part of the upper surface in contact with the indenter and δ is the indentation depth. The contact between the rigid wedge and the film is calculated based on the deformed top surface; the contact area A (length) is defined as the difference between the x-coordinates of the rightmost and leftmost nodes in the contact. This gives results that are generally different from those based on the nominal contact area, $A_N \equiv 2d/\tan(\omega)$; this is due to material sink-in or pile-up of the deformed surface. The effect of surface roughness is neglected [255]. The other boundary conditions are:

$$\dot{u}_y = 0 \quad \text{on} \quad y = 0 \quad \text{with} \quad \dot{u}_x = 0 \quad \text{at} \quad x = 0 \tag{6.3}$$

$$T_x = T_y = 0 \quad \text{on} \quad x = H \quad \notin S_{contact}. \tag{6.4}$$

Here, $T_i = \sigma_{ij} n_j \ , with \ i,j = x,y$ is the surface traction on a surface with outward normal vector n_j. The total reaction force on the film in response to the indenter is computed as:

$$F = -\int_{-A/2}^{A/2} T_y(x,0)dx \tag{6.5}$$

The indentation pressure p is defined as the ratio of the indentation force to the actual contact area (or length as this is a 2D representation). A relatively high value of indentation displacement rate $\dot{\delta} = 0.4 \ \mathrm{ms}^{-1}$ was used in DDP in order to reduce the computational cost without compromising the accuracy of the results. It should be recalled here that a rate-independent CPFE formulation was adopted after initial calibration against the behaviour of the DDP at the strain-rate given above; this provides a consistent stress-strain response (that can obviously be modified to study different scenarios) across the two regions. All the simulations reported below were done with a maximum indentation depth of $300 \ \mathrm{nm}$.

6.2.2 Boundary conditions passing

The coupling strategy for the indentation problem is illustrated in Figure 6.2. The whole process initiates with DDP calculation alone on the region underneath the tip of the indenter, which is displaced vertically at the prescribed displacement rate. All degrees of freedom are set to zero along the coupling boundary *A*. This initialization produces a preliminary stress field distribution on the coupling boundary *A*. The stress obtained from the DDP initial simulation step is passed to the CPFE region at the nodes distributed along the coupling boundary. CPFE calculations are then performed and the displacements at the coupling interface are re-evaluated and passed back to the DDP region as new boundary conditions for the coupling boundary *A*. The coupling loop ends when the difference between the tractions at the coupling interface is lower than a given threshold. The coupling process will advance to the next step by increasing the indenter penetration, and will terminate when the indenter reaches the prescribed maximum indentation depth.

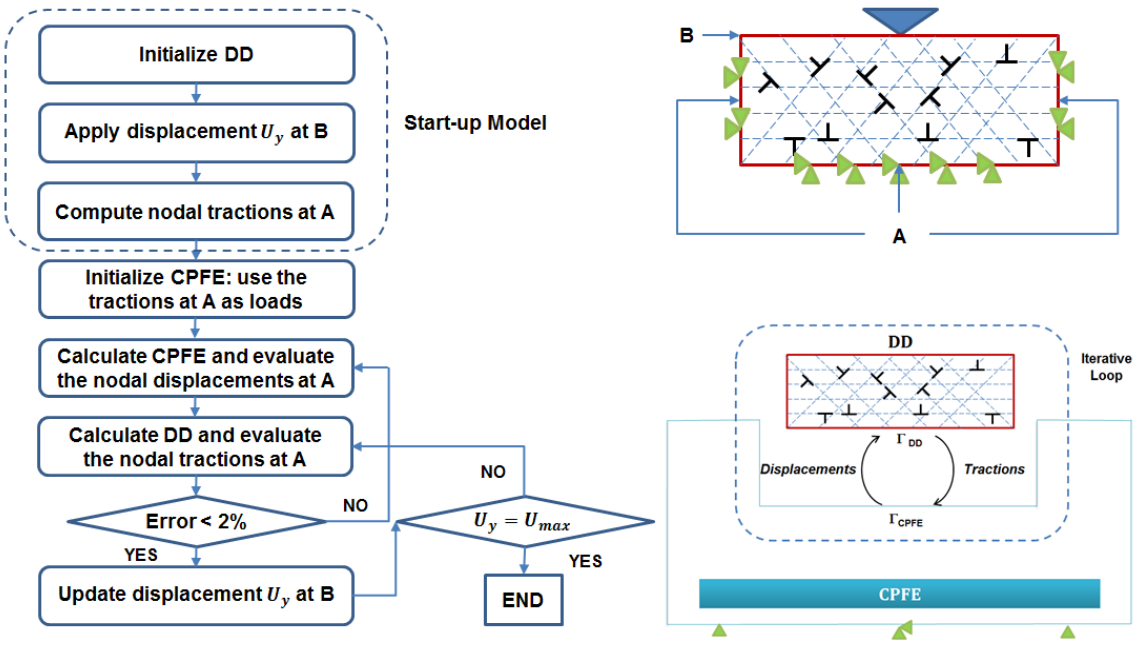


Figure 6.2. The Flow chart of the coupling procedure between crystal plasticity finite element and dislocation dynamics on a displacement-controlled two-dimensional indentation problem.

6.2.3 Interface modelling

There is no explicit dislocation activity description in conventional crystal plasticity finite element region while dislocations in the dislocation dynamics plasticity region can arrive at the coupling boundary between the two regions. Therefore, the flux of dislocations at the coupling interface needs a special treatment in order to obtain dislocation free CPFE region. There are two approaches for dealing with dislocations approaching the coupling boundary, pinning and exiting. The former one is implemented numerically by applying static boundary obstacles on the coupling boundary. Hence, dislocations in the discrete dislocation plasticity region would be pinned at the coupling boundary when they are about to leave. The latter method releases the dislocations that approach to the coupling boundary within a certain distance (for instance, $50nm$ is adopted in our coupling) so that dislocations leave the DDP region and leave a displacement step at the coupling boundary [276]. The coupling boundary modelled as pinning dislocations can be considered as an explicitly description of grain boundary. Thus, the physical model of the former method corresponds to a polycrystalline coating system, shown in Figure 6.3 (a). The latter "transparent to dislocations" model of the coupling boundary enables the coupling strategy to be applied to a bulk crystal without internal grain boundary, and is shown in Figure 6.3 (b).

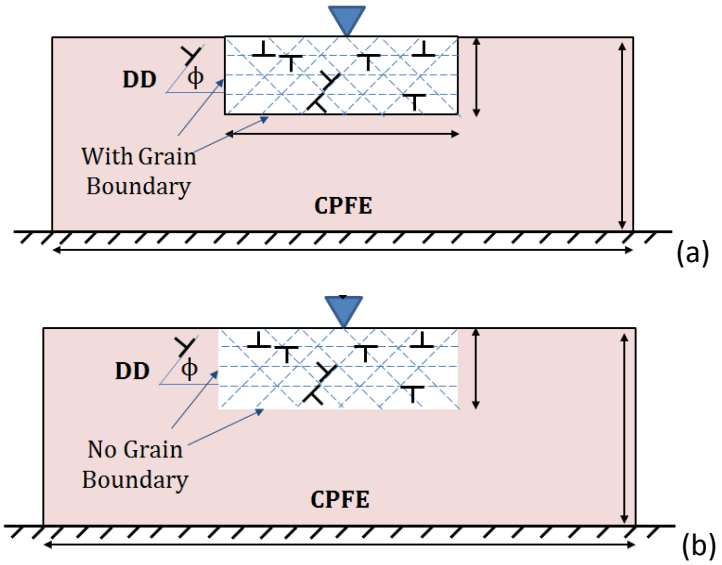


Figure 6.3. Two physical models adopted by describing the coupling boundary as (a) static grain boundary (b) transparent boundary to dislocations

6.2.4 Implementation of the coupling strategy

The whole coupling procedure on the indentation problem is controlled by a BASH script, which is able to call various procedures and to read and write associated files. The BASH shell script is run on the clusters made available for this research project by the Department of Mechanical Engineering using the UNIX operating system.

Before executing the main body of the coupling script, there is still some preparation work to do. Analogy to uniaxial tension problem demonstrated in Chapter 4, geometry and dislocation structure information of DDP sub-region are provided in the *in* and *disl.in* files. Both of them are initialized according to detailed geometry and dislocation structure specification for the DDP executable subroutine (please see Chapter 3 for details), while the "seeds file" is initialized according to the calibration result (see Chapter 3) for CPFE ABAQUS job. Also, the initial boundary condition (that contains zeroes in terms of displacements corresponding to a fixed boundary) is given in the *bcin* file for DDP.

The main BASH script firstly initializes the simulations, including cleaning redundant files and creating new directories. There are two layers of loops in the whole coupling process: an internal loop for the current step convergence (tractions and displacements compatibility) and an external loop for controlling the number of loading steps, *i.e.* total indentation depth desired. The inner loop starts imposing a new boundary condition that is based on the number of loading steps onto the wedge-shaped indenter in the in file. The termination of the DDP code is automatically ensured by the UNIX command line, and the traction information at nodes along the coupling boundary is saved into the *bcout* file by the DDP code. Another subroutine modifies the load section of the **.inp* file of the CPFE model according to the traction boundary conditions from DDP solution.

The inner loop then calls ABAQUS with the updated CPFE job and the subroutine containing CPFE microstructure and material information. The main BASH scripts checks whether the CPFE sub-model job has already finished every five seconds by testing whether an intermediate ABAQUS running status file, **.lck* still exists in the current folder. If the CPFE job has not yet finished, the coupling procedure waits for another five seconds and re-checks it again.

If the result has been generated by ABAQUS successfully, the new boundary condition file of DDP code (*bcin*) is compared to the old file (*bcinOld*). There is a status file monitoring whether the internal loop is finished. This status file informs the main coupling script of convergence status by writing and changing a convergence flash number

If the compatibility of displacements (*i.e.* the difference is less than the imposed convergence – here 5% of result in the last iterative step) has not yet been achieved, the main script returns the beginning of the inner loop. Old traction, displacements and errors files are stored in another folder where the intermediate information is collected when the whole coupling procedure terminates. T

If the convergence between CPFE and DDP sub-regions has been achieved, the main script jumps out of the inner loop and carries on a new external loop for the next coupling loading step.

The external loop starts to update the new displacement boundary condition for the indenter in the DDP code when the compatibility criterion is achieved in the previous internal loop (*i.e.* the convergent flag is checked to be changed in the status file). The increment step of the displacement is predefined by the user, and it is defined as $\Delta\delta = 0.01\ \mu m$ (this is equivalent to $\Delta\beta = 0.05\%$ if the DDP region thickness is $h = 2\ \mu m$ in this project). The DDP code reads the information file (containing dislocation structure, stress, displacement etc.) generated in the last convergent step, and solves the current discrete dislocation plasticity region with new boundary conditions. Thus, a new displacement boundary condition is applied (due to the motion of the indenter) on the top boundary of discrete dislocation plasticity sub-model and a new internal loop is started. Besides, the external loop is also capable of controlling the number of loading steps in the coupling. In this project, the total number of loading steps is set as 30 to achieve a total indentation depth $\delta = 0.3\ \mu m$.

6.3 Results

6.3.1 Validation: DDP zone size effect

Moving now to the results obtained for the indentation case, Figure 6.4 shows the effect of the discrete dislocation region (film thickness) on the coupled results through the response obtained for the indentation pressure. For the coupling calculations with discrete dislocation plasticity region characterized by a film thickness $h = 10\mu m$ on a crystal plasticity substrate, the deviations in the indentation pressure are rather small compared to the curves obtained using discrete dislocation plasticity alone (*i.e.*

assuming that the substrate of the DDP layer is rigid). However, for the case of a film thickness $h = 2\mu m$, the difference is more significant and the presence of the CPFE substrate leads to a smaller indentation pressure with increasing indentation depth. A least-squares error estimate is used to quantify the difference between the same films modelled using DDP only and the coupled DDP/CPFE approach, results shown in Table 3 for three discrete dislocation plasticity region film thicknesses:

$$Mismatch_{Coupled} = \sqrt{\frac{1}{\delta_0}\int_0^{\delta_0}\left(\frac{P_{Coupled} - P_{DDP}}{P_{DDP}}\right)^2 \mathrm{d}\delta} \tag{6.6}$$

The results obtained using the coupling strategy proposed here begin to differ considerably from those obtained using DDP alone (i.e., a rigid substrate) when the discrete dislocation plasticity film thickness decreases below 5 μm; the solution obtained for thicker films is further validation of the coupling methodology in capturing the known DDP limit. Hence it is capable of capturing the effect of a non-rigid substrate (in this case characterised by a CPFE description matching the elasto-plastic behaviour of the film) when performing indentation, without the associated computational cost of modelling the entire system using DDP. This effectively expands the potential applications of discrete dislocation plasticity in modelling indentation and other problems to potentially much larger systems where the details of dislocations activity are only relevant in a region of interest; therefore the coupling method can predict the hardness of thin films and multi-layers on substrates more accurately than was possible in [277].

Figure 6.5 shows the normal stress component in the coupled simulation with a 0.2 μm indentation depth. The dislocation activity within the domain is clearly visible, as is the continuity in the stress across the DDP/CPFE boundary and the pinning of the dislocation at the boundary between the two domains.

Table 6.2. Relative deviation in indentation pressure with different discrete dislocation plasticity film thickness; based on Eq. (6.6).

DDP region $h \times l$ $(\mu m \times \mu m)$	20×30	10×30	5×30	2×30
$Mismatch_{Coupled}$	0.0	0.01	0.04	0.15

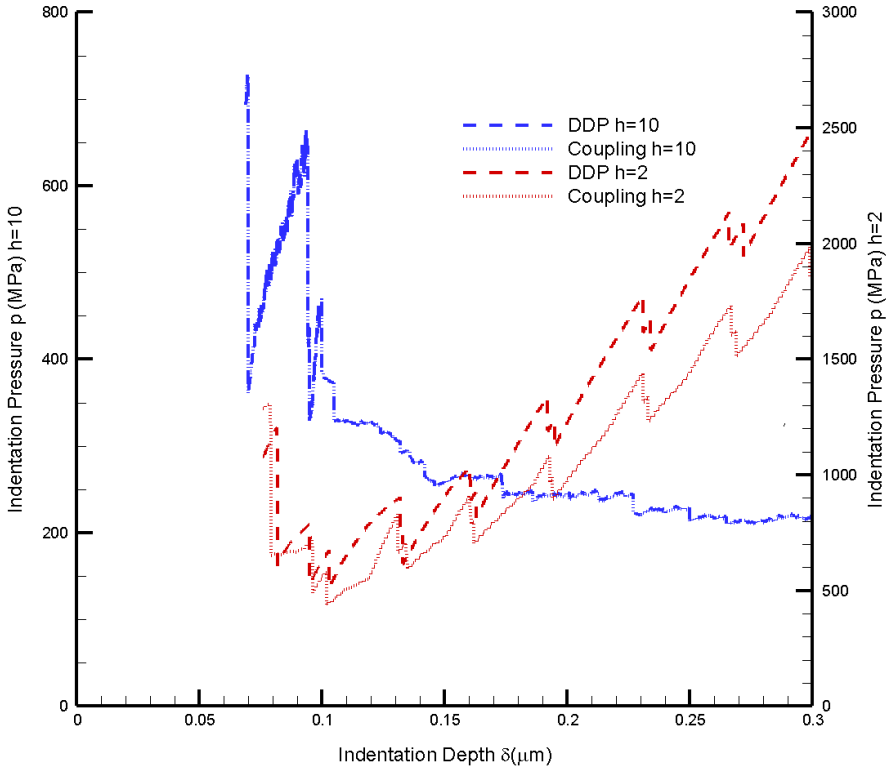
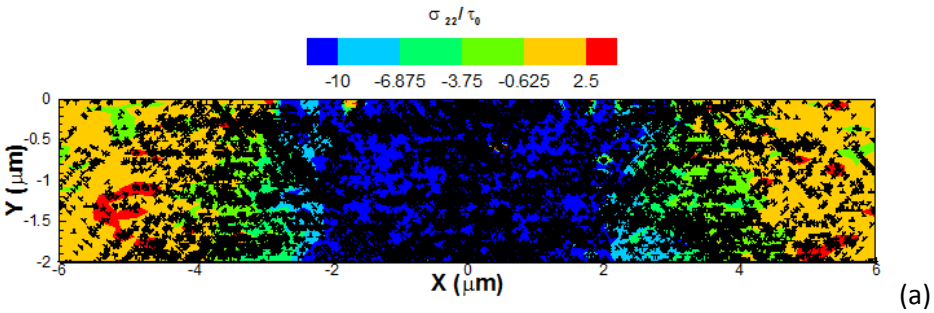
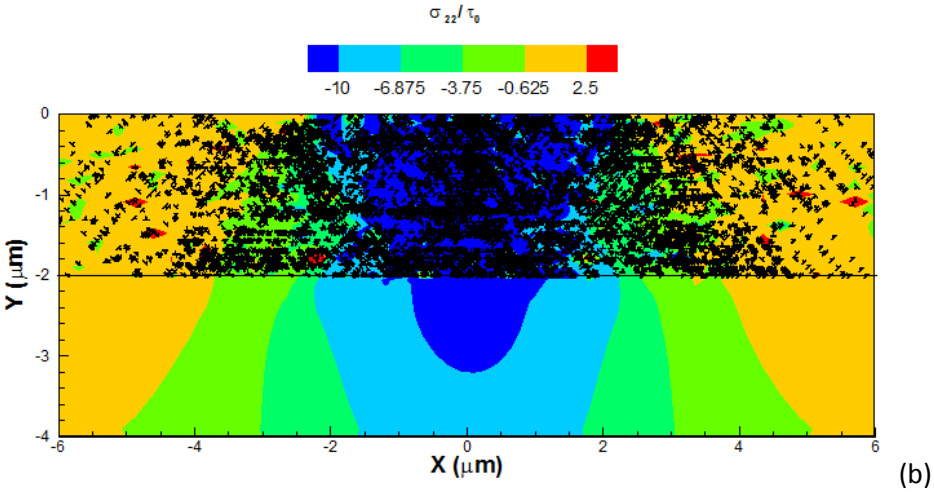


Figure 6.4. Curves of indentation pressure p versus applied indentation depth δ for two film thicknesses: $h = 2\mu m$ and $h = 10\mu m$.



(a)



(b)

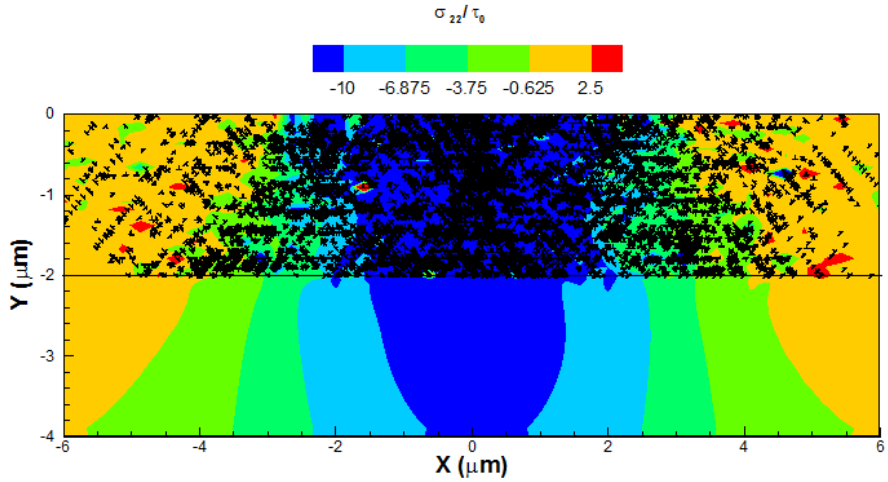


Figure 6.5. Normalized stress $\sigma_{22}/\tau_0$and dislocation structure of the indentation problem solved by (a) DDP film on a rigid boundary (b) DDP film coupled with a CPFE substrate (c) DDP film on an elastic substrate. All stress contours are plotted at the instant $\delta = 0.2\ \mu m$.

Contours of normalized stress in the vertical direction are plotted in Figure 6.5 for the different modelling cases, along with the corresponding dislocation structure. It is evident that the coupling method improves the accuracy of the calculations compared to the stress and dislocation structure obtained in the simulations where the substrate is assumed by a rigid boundary or a purely elastic substrate.

Table 6.3. The normalized dislocation density at the instant $\delta = 0.2\ \mu m$, both of the DDP only and the coupling responses are included.

DDP region $h \times l$ $(\mu m \times \mu m)$	20×30	10×30	5×30	2×30
DDP ρ_{dis}/ρ_{nuc}	3.72	4.56	5.94	12.6
Coupling ρ_{dis}/ρ_{nuc}	3.70	4.52	5.06	10.6

The normalized dislocation density evolution versus the discrete dislocation film thickness *h* is plotted in Table 6.3. Both of total and mobile dislocations are unaffected by the coupling approach when the DDP domain size is sufficiently large. However, the coupling effect, which manifests itself as the influence of the CPFE zone as substrate in these simulations, becomes more apparent on the dislocation density when the DDP domain is reduced in size.

The deformed contact surface profiles of the $\mathrm{h} = 2\mu\mathrm{m}$ film obtained from DDP only and our coupling simulations are shown in Figure 6.6. Results are shown when the applied indentation depth $\delta = 0.4\mu\mathrm{m}$. The pile-up of material at the contact surface obtained by the coupling calculation is observed more apparent than the DDP only method. This indicates the presence of CPFE substrate relieves the deformation and thus the dislocation activity in the DDP film.

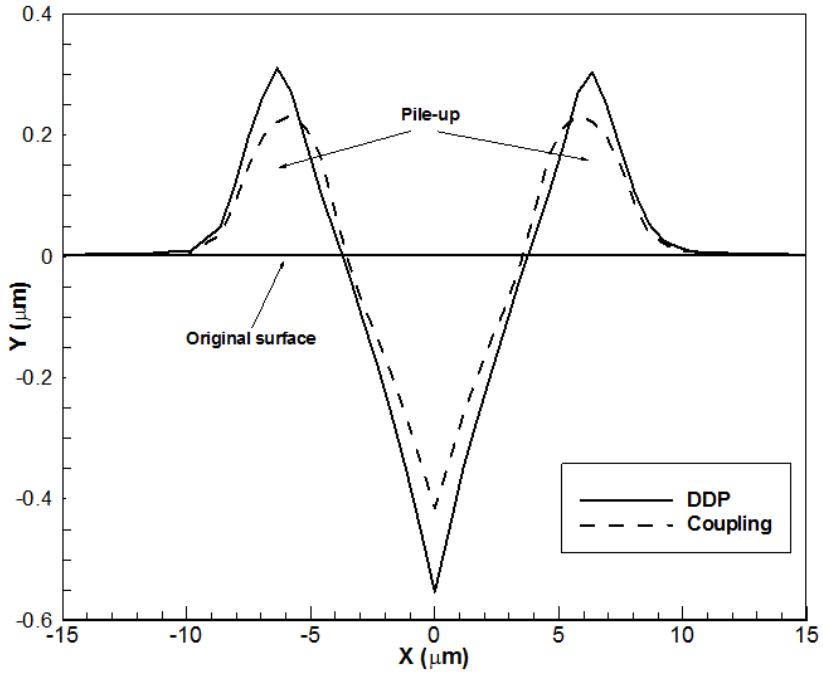


Figure 6.6. The deformed contact surface in the $\omega = 5°$ wedge indentation of the $h = 2\mu m$ film. The displacements are shown at the instant when the applied indentation depth $\delta = 0.3\mu m$. The initial nucleation source density is set as $\rho_{nuc} = 42\mu m^{-2}$. The DDP only results are also included for reference.

The dislocation density evolution curves during indentation process on films with two different thicknesses of DDP regions are shown in Figure 6.7. Compared to the results of DDP-only calculation, the model with larger discrete dislocation plasticity region sizes exhibits a nearly identical dislocation density evolution in terms of total and mobile dislocations. This further verifies that the proposed multi-scale modelling is sufficient to represent the whole system performance when the discrete dislocation plasticity region is large compared to the applied indentation depth considered here. However, dislocation density increase is slowed down by the crystal plasticity finite element region when the discrete dislocation plasticity thickness is shrunk to $h = 2\ \mu m$ with the applied indentation depth $\delta = 0.3\mu m$. This result reveals that the crystal plasticity finite element region has a significant effect when modelling the whole coating system performance.

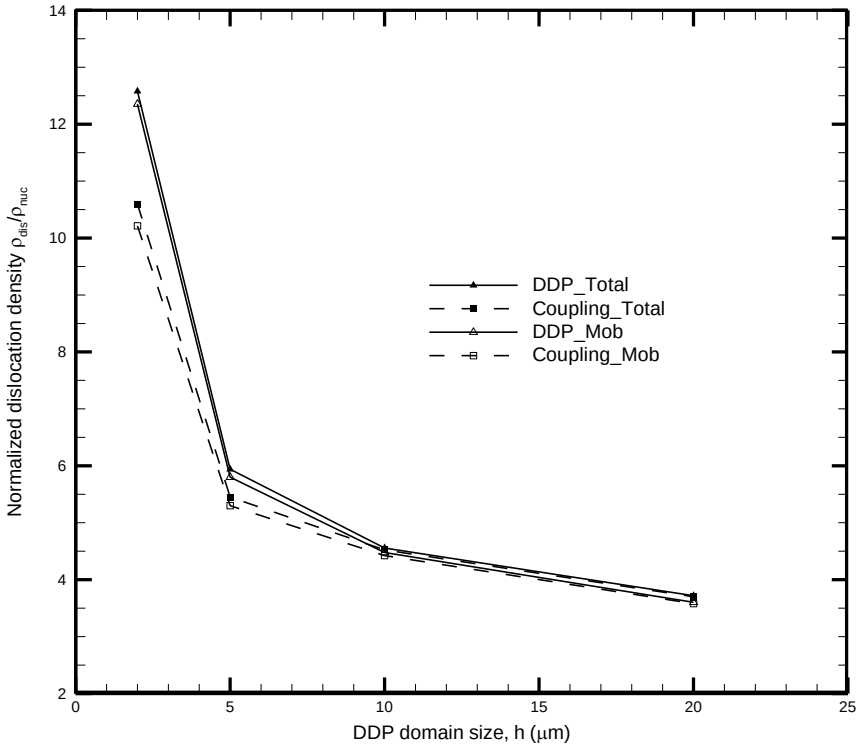
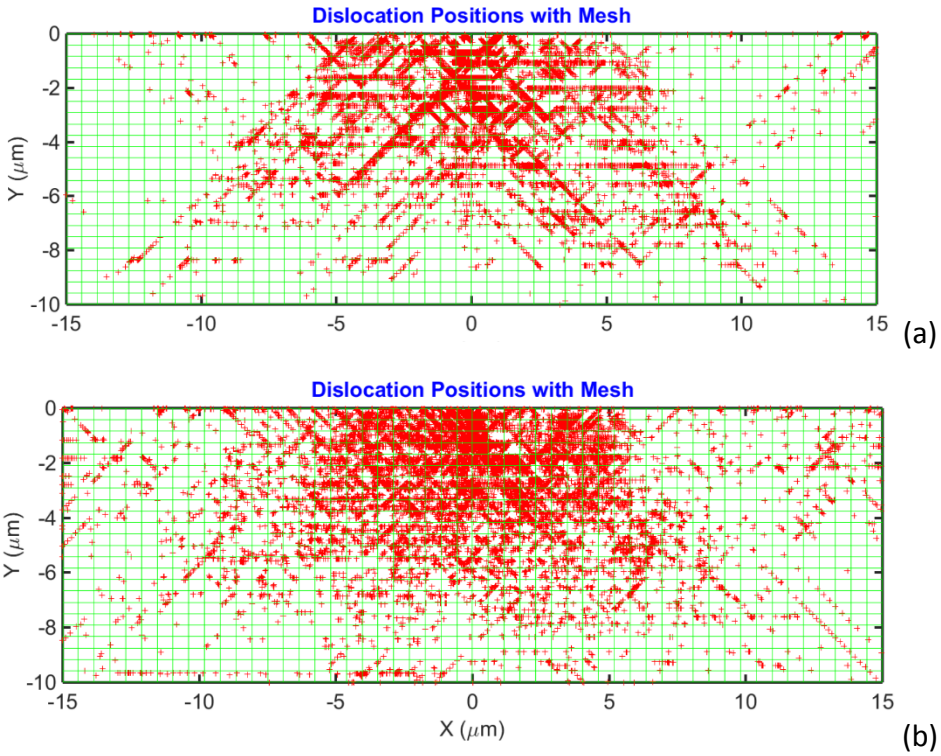
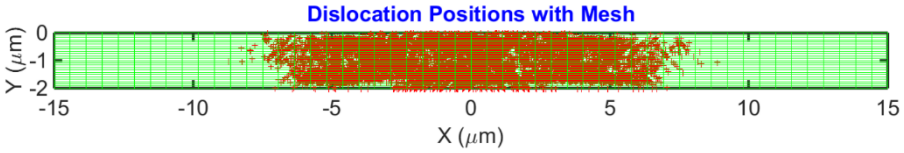


Figure 6.7. Dislocation density evolution curves of the indentation process on the coupling model with discrete dislocation plasticity region sizes (a) $l \times h = 30\ \mu m \times 10\ \mu m$ and (b) $l \times h = 30\ \mu m \times 2\ \mu m$. The dislocation density is averaged within the corresponding DDP sub-region

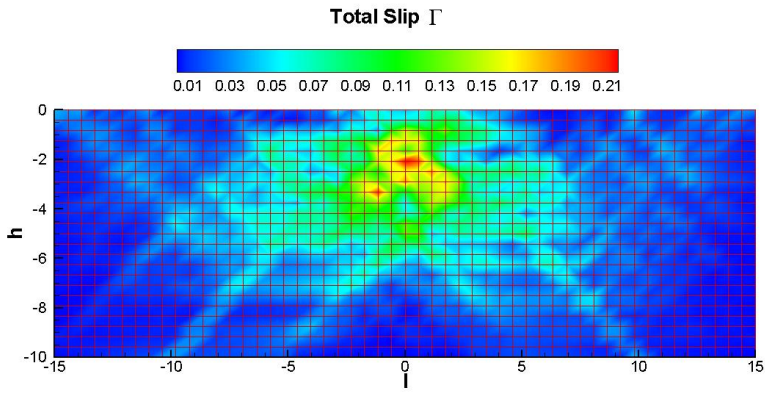




(c)

Figure 6.8. The dislocation structure in the discrete dislocation plasticity region modelling by the DD-CPFE coupling approach with discrete dislocation plasticity region size (a) $l \times h = 30\ \mu m \times 20\ \mu m$ (results are shown within $h = 10\ \mu m$), (b) $l \times h = 30\ \mu m \times 10\ \mu m$ and (c) $l \times h = 30\ \mu m \times 2\ \mu m$ respectively. Results are obtained at the instant $\delta = 0.3\ \mu m$. The distributions are shown on the undeformed film.

The dislocation structure intrinsically determines the plastic behaviour of material. The dislocation structure in the discrete dislocation plasticity region modelling by the DDP-CPFE coupling approach with various sizes of discrete dislocation plasticity region are plotted in Figure 6.8. These dislocation distributions are obtained with modelling the coupling boundary as static grain boundary. The pattern of dislocation structure obtained from a thinner discrete dislocation region $h = 10\ \mu m$ is preserved similarly to that from a thicker discrete dislocation region $h = 20\ \mu m$ including the slip style and the pile ups. Therefore, this similarity of dislocation structure leads to the similar response of the stress and thus the indentation pressure of the whole system. However, the dislocation structure of the coupling method with discrete dislocation plasticity region size $l \times h = 30\ \mu m \times 2\ \mu m$ exhibits a large amount of dislocation pile-up at the grain boundary and some dislocations moving out of the film from the indented boundary. The pile-up of dislocations at the grain boundary hardens the material thus resulting in the turn up of the indentation pressure. The exiting of dislocations from the free surface introduces displacement steps at the contact, leading to the material pile-up near the indenter tip.



(a)

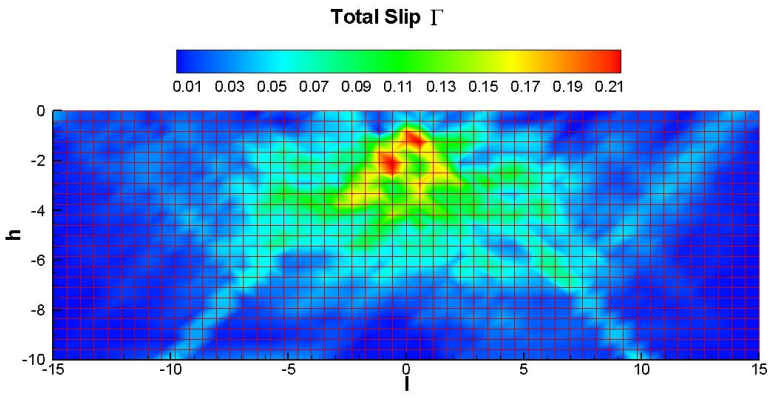


Figure 6.9. The distribution of total slip contour Γ in the $h = 10\ \mu m$ film modelled by (a) the proposed coupling method and (b) discrete dislocation dynamics plasticity indented by the $\omega = 5°$ wedge-shaped indenter. Results are obtained at the instant $\delta = 0.3\ \mu m$ (the actual contact area$A \approx 7.2\mu m$).The distributions are shown on the undeformed film.

The fidelity of our coupling approach is further proven using the total slip contour in the discrete dislocation plasticity region. The quantity totally slip Γ , which is given as following:

$$\Gamma = \sum_{\alpha=1}^{3} \left|\gamma^{(\alpha)}\right| \tag{6.7}$$

Where $\gamma^{(\alpha)}$ is given by:

$$\gamma^{(\alpha)} = s_i^{(\alpha)} \varepsilon_{ij} m_j^{(\alpha)} \tag{6.8}$$

Here, $s_i^{(\alpha)}$ and $m_j^{(\alpha)}$ are tangential and normal unit vectors respectively of slip system α. Both of the displacement field of the region modelled by discrete dislocation dynamics and the coupling method are not continuous because dislocations gliding along slip systems results in displacement jumps. Thus, in order to visualize the deformation, Γ is computed on a uniform mesh with the cell dimension $0.52 \times 0.4\ \mu\mathrm{m}$. The strain field is calculated based on the numerical differentiation of displacement field $\mathrm{u} = \tilde{\mathrm{u}} + \hat{\mathrm{u}}$ using a bilinear displacement shape function. The total slip Γ can picture the plastic deformation of the dislocation region clearly, although it is not a direct measure of slip as $\gamma^{(\alpha)}$ takes the effect of dislocations from all slip systems.

Distributions of Ω at an indentation depth $\delta = 0.3\ \mu m$ in the $h = 10\ \mu m$ film ($= 5°$) are plotted in Figure 6.10 (a) and (b) using the DD-CPFE coupling and discrete dislocation plasticity descriptions, respectively. The values of Γ in (a) and (b) give a measure of slip averaged over approximately 10 slip planes (the grid size used to evaluate strain is $0.25\ \mu m$ while the slip plane spacing in the discrete dislocation plasticity simulations is $0.025\ \mu\mathrm{m}$). The patterns of slip contours of dislocation dynamics predictions and the coupling method are quite similar. Compared to the discrete dislocation plasticity result, the coupling simulation gives a bit larger values

of the total slip along slip planes. This finding shows that a softener substrate (i.e. the bulk modelled using crystal plasticity finite element description) allows the slip to develop further in the discrete dislocation plasticity film. Both of results generated by the coupling and the discrete dislocation plasticity show a larger plastic zone than the continuum CPFE calculation (please see Chapter 5). In detail, the plastic zone exists only underneath the contact in CPFE calculations while slip can develop along the ± 45 slip systems. Thus, the plastic zone is able to spread outside of the contact zone. Our results are different from those in previous work [2] due to involving different dislocation structure and geometry dimension.

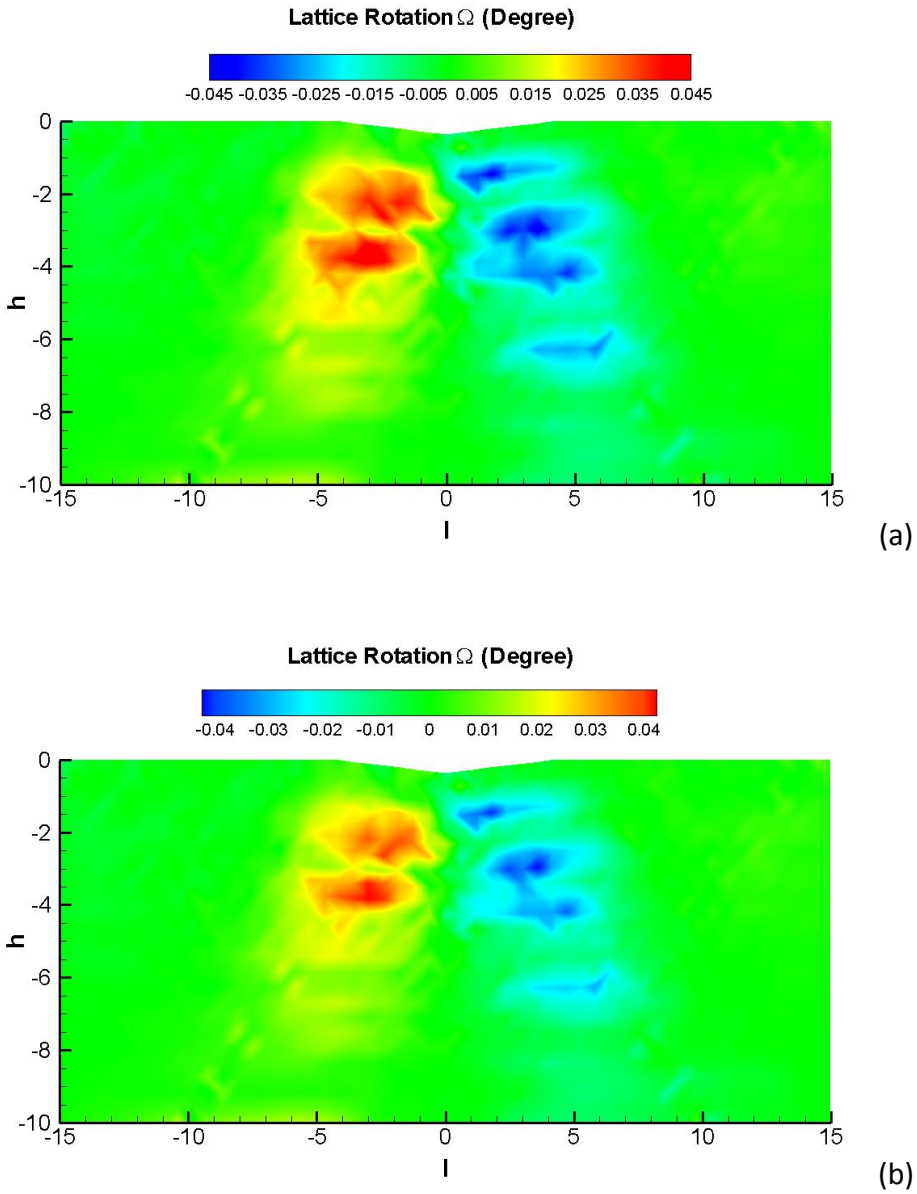


Figure 6.10. The distribution of lattice rotations under the indenter tip in the $h = 10\ \mu m$ film modelled by (a) the proposed coupling method and (b) discrete dislocation dynamics plasticity indented by the $\omega = 5°$ wedge-shaped indenter. Results are obtained at the instant $\delta = 0.3\ \mu m$ (the actual contact area$A \approx 7.2\mu m$

Besides the quantity total slip Γ, the lattice rotation Ω can also be considered as a variable to show the plastic deformation in the material. We define the lattice rotation Ω as following:

$$\Omega = \frac{1}{2}(\hat{u}_{2,1} + \hat{u}_{1,2} - u_{2,1} - u_{1,2}) \tag{6.9}$$

In eq.(6.9), the spatial differentiation is performed analytically to exclude the slip components of the $\tilde{u}$ field.

The validity of our proposed coupling method is further highlighted by comparing the lattice rotation in the coating film generated by the discrete dislocation plasticity method and our coupling method. Contours of the lattice rotation at the applied indentation depth $\delta = 0.3\ \mu m$ using the discrete dislocation dynamics predictions and the coupling method in the $h = 10\ \mu m$ film ($\omega = 5°$) are plotted in Figure 6.10 (a) and (b) respectively. Similar to pervious CPFE-DDP simulations and experimental results [278, 279], there is an abrupt change of the lattice rotation at $x = 0$ underneath the indenter. In [278], the experimental data showed the magnitude of lattice rotation was in the range from -10 to +10 degrees when the indentation depth is $\delta = 130\ \mu\mathrm{m}$. Our simulation results match the correlation between the lattice rotation and the indentation depth of experimental data. In the research by [279], the slip contour was illustrated symmetrically about the $x = 0$ line, although the magnitude of those slips were relative large than our coupling simulations. Compared to the lattice rotation of the dislocation dynamics prediction, the contour pattern obtained in coupling method is identical, and the magnitude is also consistent to the result of purely discrete dislocation predictions. This further shows that our coupling method is generally capable of accurately modelling a large size of material with focusing on one or more sensitive region using discrete dislocation plasticity. For details, the values of lattice rotations are moved positive in the coupling, which is due to the anisotropic property of the CPFE substrate.

6.3.2 Computational efficiency

The most important motivation of developing a multi-scale coupling is to improve the current simulation efficiency by avoiding applying discrete dislocation dynamics to the whole material to be modelled. The computational time used in the indentation process from the applied indentation depth up to $\delta = 0.10\ \mu\mathrm{m}$ is tabulated in Table 6.4. Results are obtained from coupling simulations with various sizes of discrete dislocation plasticity regions. The corresponding computational time spent in the simulation of the whole system (dimensions 300 μm×100 μm) with discrete dislocation plasticity is listed for reference.

Table 6.5 shows that the application of our proposed coupling approach substantially reduces the computational time required for the planar indentation problem, especially when the size of discrete dislocation plasticity sub-region is small. The time savings is a factor in the range of 5-10. For larger plastic zone sizes the reduction of computational time will be even greater. All the examples shown below have been

run in a cluster equipped with a one single Quad-Core AMD Opteron(tm) Processor 8384 2.7 GHz processor and 2GB RAM.

Table 6.4. The fraction of computational time and time saving for the indentation depth from $\delta = 0.05\ \mu m$ to $\delta = 0.10\ \mu m$. Results are shown for various sizes of the discrete dislocation plasticity region and the time consumed of modelling the whole material $300\ \mu m \times 100\ \mu m$ with discrete dislocation plasticity is included for reference.

DD region size ($\mu m \times \mu m$)	30×2	30×10	30×20
$\Delta t_{Coupling}$(hours)	~11	~15	~18
$\Delta t_{300\times100}$(hours)	~100	~100	~100
Time saving	1/9	1/6.5	1/5.6

6.4 Application: Indentation Pressure Evolution of a coating system

The coupling simulation results (please see Figure 6.4) of the modelling with a thin DDP sub-region has shown that the CPFE sub-region has affected the comprehensive response of polycraylline materials. Along with Indentation Size Effect fully captured by DDP film (please see Section 5.2), this involvement CPFE sub-region motivates us to apply the proposed multi-scale modelling approach to a coating system.

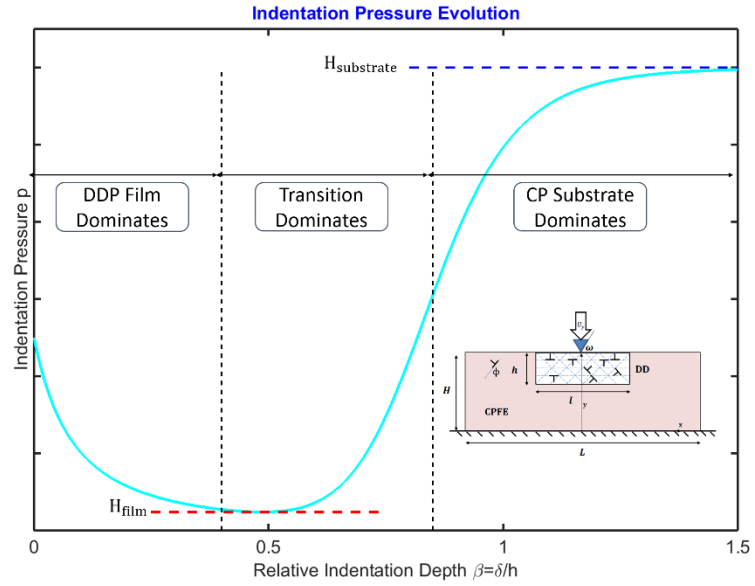
The indentation pressure evolution of a coating system that is typically composed of a coating film and a substrate undergoes a transition process when it is subjected from indentation loading. The comprehensive indentation pressure variation that covers the whole range of indentation depth is still required, although Korsunsky and co-workers [150] developed an empirical formula that describes the transition between continuum film and substrate.

In this project, we aim to apply the newly proposed multi-scale coupling approach to a coating system composed of polycrystalline material. In particular, its coating film contains a single crystal that is modelled and solved using discrete dislocation plasticity while its substrate incorporates a polycrystalline crystal that is modelled and solved using crystal plasticity finite element. Hence, this application aims to achieve describes good description of the three indentation pressure regimes experienced by the material during a typical wedge indentation process (also please see Figure 6.1 for this detailed illustration):

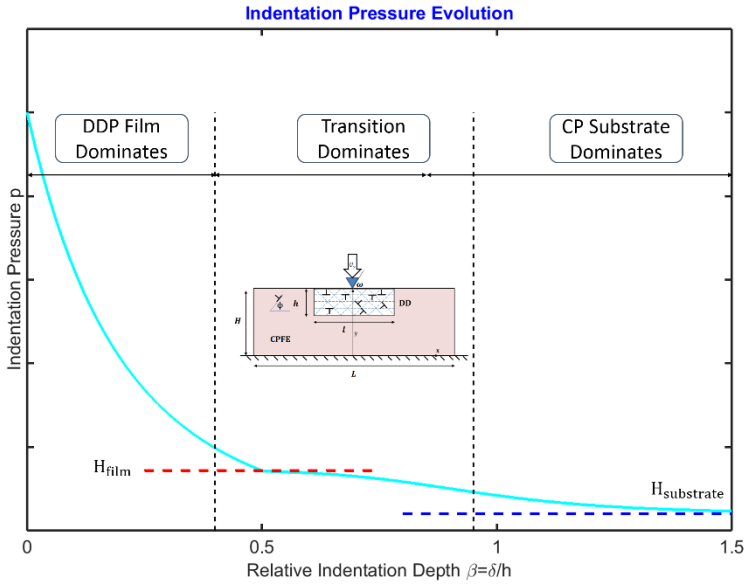
- Fully capture the indentation size effect when the applied indentation depth is relatively small compared to the film thickness (Regime I: DD film dominating zone in Figure 6.1)
- Fully capture the transition between different regimes when the indentation process enters the indentation pressure transition zone between the film and substrate (Regime II transition dominating zone in Figure 6.1)

- Fully capture the transition process when the indentation response of the coating system enters the substrate dominating zone (Regime III CP substrate dominating zone in Figure 6.1).

It is noticing that the thickness of coating film (DDP sub-region) is assigned a relatively small value ($h = 2\mu m$ in the following discussion) as this configuration decreases the computational time for taking CPFE substrate involved during a micro-indentation process.



(a)



(b)

Figure 6.11. Schematic illustration of the indentation pressure variation against relative indentation depth that is aimed to be solved applying the newly proposed multi-scale coupling approach on a coating system with (a) substrate harder than film and (b) film harder than substrate

Since formulas for the indentation size effect (ISE) and continuum transition of indentation pressure have been quantitatively discussed in Section 5.2 and Section 5.3 (also eq.(6.1)), respectively, the major target of the application is to quantitatively describe the size-dependent transition between response of film (DDP sub-region) and substrate (CPFE sub-region).

As stated in Chapter 3 and Section 6.2.3, there are two approaches to model the coupling boundary between DDP and CPFE sub-regions. The first approach models the coupling boundary as a static grain boundary that pins dislocations that are about to pass, and hence it naturally models the whole coating system as a polycrystalline composite, where the interface between the two domains act as an impenetrable grain boundary. The second one models the coupling boundary as transparent to enter and exit of dislocations, and hence it models the coating system as a bulk single crystal. The two physical models will be discussed separately in the following sections.

6.4.1 Models with coupling boundary as static grain boundary

In this section, results of simulations modelling the coupling boundary as a static grain boundary are shown and discussed. The general indentation pressure response of the investigated coating system is illustrated at the beginning. Based on this indentation pressure response, a formula that describes its trend and combines the results in Chapter 5 is proposed. At the end, a parametric study on the substrate hardness is performed on the newly proposed indentation formula.

6.4.1.1 General indentation response

The actual indentation pressure p_A curves of DDP and coupling calculations of a coating system against the applied indention depth δ are presented in Figure 6.12. The coupling approach models the coupling boundary between DDP and CPFE sub-regions as a static grain boundary. Both curves clearly show that the indentation pressure of a polycrystalline coating system increases after a critical applied indentation depth ($\delta = 0.1\mu m$ for this case). This increment has generally been attributed to the rigid boundary effect that affect the results of discrete dislocation plasticity calculations when performed in isolation [2]. However, here this increment is due to the presence of the grain boundary and the pinning of dislocations as the substrate is able to deform in this coupling case. The sketch in Figure 6.13illustrates the static grain boundary and deformable geometry boundary in this type of coupling model.

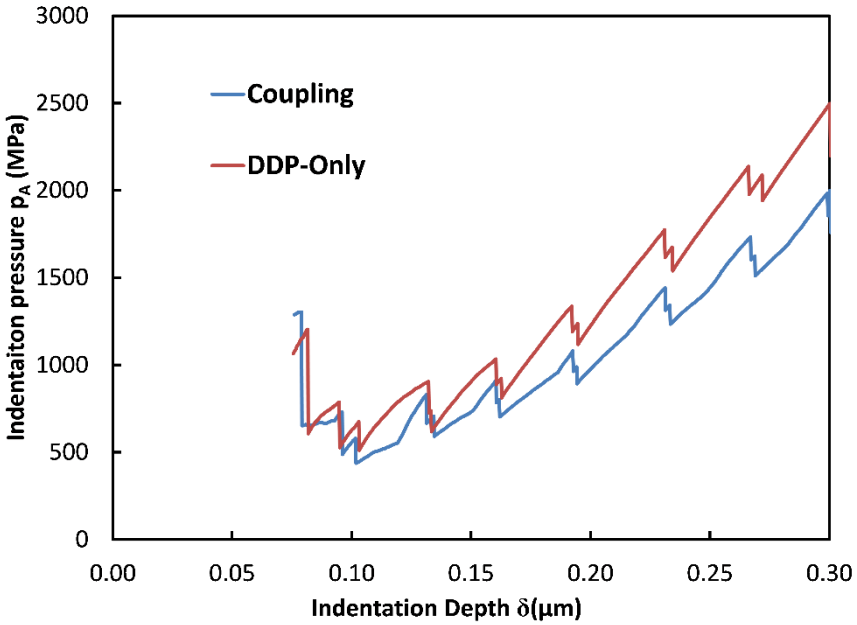


Figure 6.12. The actual indentation pressure p_A curves versus the applied indentation depth δ for the film $h = 2\mu m$ indented by the $\omega = 5°$ wedge. Results are shown for discrete dislocation plasticity alone and the DDP-CPFE coupling method with the same mesh configuration.

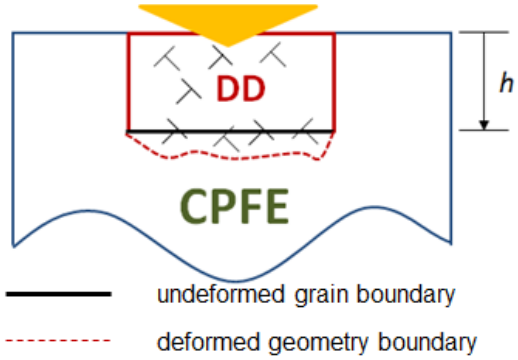


Figure 6.13. Sketch of the coupling model where a static grain boundary pins dislocations. The deformed geometry boundary is also shown for reference.

There are some jumps in the indentation pressure curves of Figure 6.4, and their jump magnitudes are generally larger than the result obtained in Section 5.2 as the mesh size is much coarser in coupling calculations. Both of the coupling and DDP alone results exhibit indentation size effect, although the decreasing of indentation pressure loses more details due to the coarse mesh size.

Of more significance, the indentation pressure curve of the coupling modelling still increases when indentation depth exceeds the value $\delta = 0.1\mu m$, although the substrate in the coating system modelled by CPFE is softener than the coating film modelled by discrete dislocation plasticity, $H_{film,\ \ stable} > H_{substrate}$ (recall Section 5.2 and 5.3 for these values).

This turning up in indentation pressure curve of the coating system is rationalized that the static grain boundary effectively pins dislocations and thus the back effect of pinned dislocations hardens the coating system behaviour. Therefore, the general trend of indentation pressure curve of the coating system is analogy to the one obtained in DDP calculation with same film thickness. To summarize the general indentation pressure response of a polycrystalline system:

There is Indentation Size Effect when the applied indentation depth is relatively small compared to the coating film thickness.

The transition in indentation pressure evolution of a polycrystalline coating system is dominated by the grain boundary between the coating film and substrate, when the applied indentation depth increase to a critical value.

6.4.1.2 Formula for indentation pressure

In order to quantitatively describe the indentation pressure curve of a polycrystalline coating system (*e.g.* Figure 6.13), the following eq.(6.10) is developed to capture the indentation variation trend. Eq.(6.10) is assembled by combining the indentation pressure formula in ISE zone (See section 5.2) and eq.(6.1) that describes the hardness transition in a continuum coating system. In particular, we replace the assumed stable hardness of the coating film with the indentation pressure variation formula (i.e. eq. (5.9)) at ISE regime.

$$\mathrm{H_c} = \mathrm{H_G} + \frac{\mathrm{H_i}\left[(1+\frac{\beta}{\mathrm{a}})^{-\alpha}\right] - \mathrm{H_G}}{1+(\frac{\beta}{\beta_{\mathrm{G0}}})^{\varepsilon_{\mathrm{G}}}} \tag{6.10}$$

In eq.(6.10), $\mathrm{H_c}$ is the indentation pressure of a polycrystalline coating system, H_i is the intrinsic hardness of the coating film material, β is the relative indentation depth.H_G is the presumed hardness of the grain boundary, and its value is obtained as $H_G = 35GPa$ by simulating an elastic bulk with a large Young's modulus (please see Section 5.3 for its calculation). Parameter β_{G0} and ε_{G} specify the transition feature of indentation curves that are analogical from eq. (5.14). The introduction of grain boundary term originates from the grain boundary influence discussed in Section 6.4.1.1. Other fitting parameters are with the same physical interpretation that is discussed in Section 5.2.

6.4.1.3 Parametric study

In order to investigate the substrate influence on indentation pressure of a polycrystalline coating system, coupling simulations with substrates having various continuum hardness values modelled are performed. The substrates with different continuum hardness values are realized by varying critical resolved shear stress (τ_c) in the crystal plasticity finite element description (please see Section 5.3 for more details) and holding elastic properties.

The indentation pressure curves of polycrystalline coating systems composed of these substrates are reported in Figure 6.14. As can be seen, the indentation pressure, especially the general turning up feature, of a polycrystalline material coating system is not affected by substrate hardness too much. For instance, the discrepancy of indentation pressure between the coating systems with $\mathrm{H_{substrate}} = 102\mathrm{MPa}$ and $\mathrm{H_{substrate}} = 240\mathrm{MPa}$ substrates is only 6% at relative indentation depth $\beta = 0.15$. An extremely softened substrate with $\mathrm{E} = 70\mathrm{MPa}$ and $\mathrm{H_s} = 39\mathrm{MPa}$ is also plotted in Figure 6.14 with label "Soft". The difference becomes more evidently as expectedly.

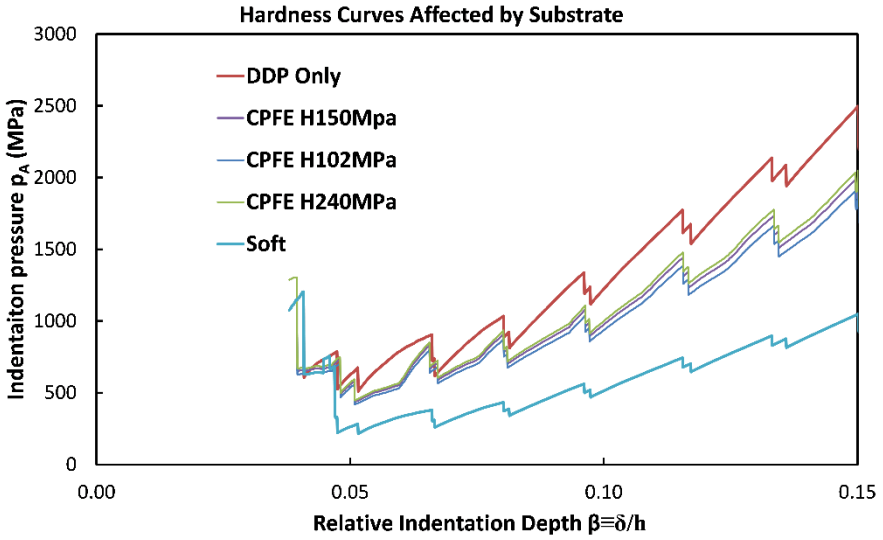


Figure 6.14. The actual indentation pressure p_A curves versus the relative indentation depth β for the polycrystalline coating system with the coating film $h = 2\mu m$ and various substrates with different continuum hardness values indented by the $\omega = 5°$ wedge. Results of discrete dislocation plasticity alone with a rigid boundary with the same mesh configuration are also included for reference.

Fitting parameters of the best-fit results with eq.(6.10) on indentation pressure curves in Figure 6.14 are tabulated Table 6.5. The best-fit is performed using the MATLAB CFTOOL toolbox whose details can be found in Chapter 5.

As can been in Table 6.5, the value of transition relative indentation depth β_{G0} (which represents the critical relative indentation depth where indentation pressure curve occurs to turn up) shows weak dependence upon the hardness of CPFE substrate. The "Soft" case exhibits a different trend on β_{G0} because there is a mismatch of elastic modulus between the coating film and substrate in this case. The sudden drop of the indentation pressure curve also verifies this mismatch effect. Besides, the value of transition exponent parameter ε_G decreases with the increasing hardness of CPFE substrate. This is attributed to that harder substrates hinders the plastic flow in the coating film and thus hardens the comprehensive performance of the polycrystalline coating system. Values of other fitting parameters take the same as the corresponding DDP only calculation that can be found in Section 5.3.

Table 6.5. the substrate hardness values and the corresponding fitting parameters of indentation pressure in Figure 6.14 curves fitted by equation (6.10) in Figure 6.14

Case Label	H_{CPFE} (MPa)	β_{G0}	ε_G
Soft	39	0.8412	2.405
CPFE 102MPa	102	0.9286	1.572
CPFE 150MPa	150	0.9335	1.569
CPFE 102MPa	240	0.9264	1.484
DDP Only	-	0.9154	1.365

The best-fit curve with the fitting parameters for the polycrystalline coating system with a CPFE substrate having its hardness $H_s = 150MPa$ is presented in Figure 6.15. The best-fit result reflects the general indentation pressure variation well (the coefficient of determination $R^2 = 0.8832$) with the relative indentation depth and the domination of the grain boundary.

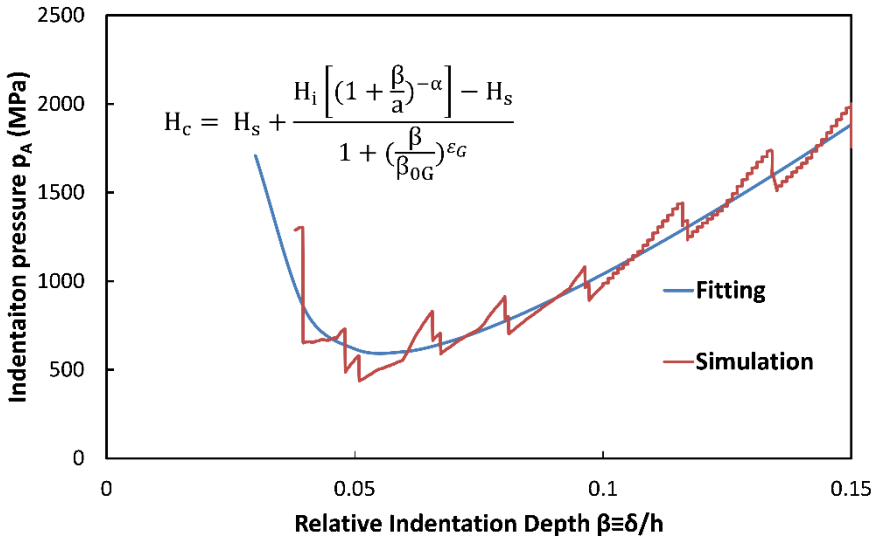


Figure 6.15. the actual indentation pressure against the relative indentation depth of a polycrystalline coating system. Results are shown for both coupling simulations and the best fit curve with eq.(6.9).

6.4.2 Models with coupling boundary transparent to dislocations passing

In this section, results of simulations modelling the coupling boundary dislocation-transparent boundary are shown and discussed. The dislocation flux passing from DDP to CPFE sub-region is illustrated. The general indentation pressure response of the investigated coating system is illustrated at the beginning. Based on this indentation pressure response, a formula that describes its trend and combines the results in Chapter 5 is proposed. At the end, a parametric study on the substrate hardness is performed on the newly propose indentation formula.

6.4.2.1 General indentation response

The actual indentation pressure p_A curves of DDP and coupling calculations of a single coating system against the applied indention depth δ are presented in Figure 6.16. The indentation pressure curve obtained from a DDP calculation with film

thickness $\mathrm{h} = 10\ \mu\mathrm{m}$ is included for reference as this reference film can be considered as being composed by two identical materials. The hardness value of CPFE substrate ($\mathrm{H_{CPFE}} = 150\ \mathrm{MPa}$) is included for reference. The indentation pressure curve of coupling simulation shows a decreasing trend following the indentation size effect. However, the indentation pressure of the coating system approaches the continuum hardness of CPFE substrate instead of the continuum hardness of DDP coating film. This further decrease in indentation pressure of the single crystal coating system is due to the introduction of the softer CPFE substrate.

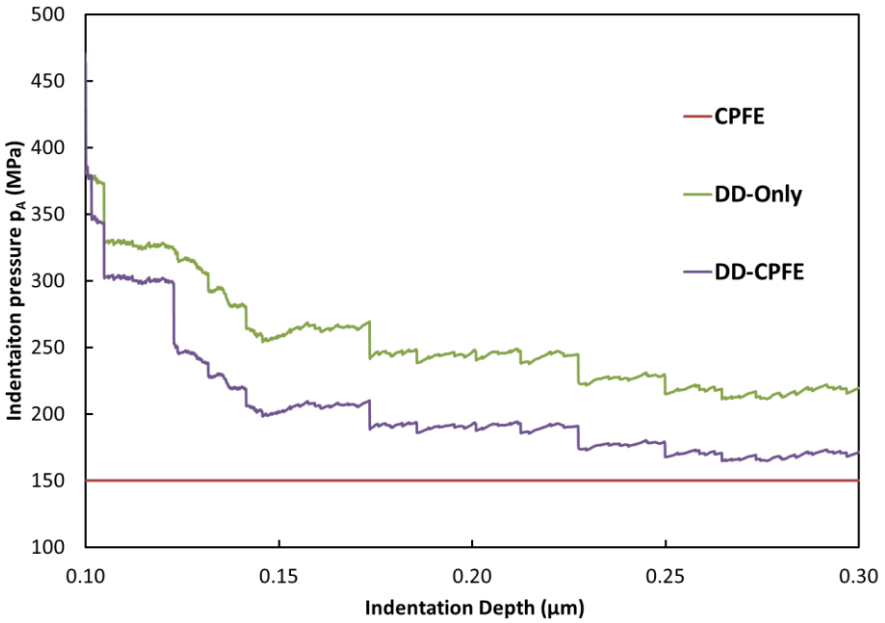


Figure 6.16. The actual indentation pressure $\mathrm{p_A}$ evolution curve of a coating system without internal grain boundary against the applied indentation depth δ. Indentation pressure curves generated by other modelling methods are also included for reference.

Compared to the result of DDP film bonded to a fixed rigid boundary and polycrystalline coating system (see Figure 6.13), this single crystal coating system is not hardened as there is no increase in its indentation pressure curve for large values of applied displacements. This feature verifies that the coupling boundary is indeed transparent to dislocations passing through the interface.

The modelling of transparent coupling boundary between DDP and CPFE sub-regions is illustrated in Figure 6.17. At the ith iteration, there are dislocations that are about to pass the coupling boundary (*i.e.* their cores are within an "absorption" thickness h_{absorb}) from the DDP sub-region. CPFE sub-region absorbs these dislocations virtually via receiving the stress field produced by them and they are removed from the DDP sub-region rather than piling up at the coupling boundary. The compatibility of traction and displacement field between CPFE and DDP region is achieved by adopting small load step and the proposed iteration scheme in our coupling method.

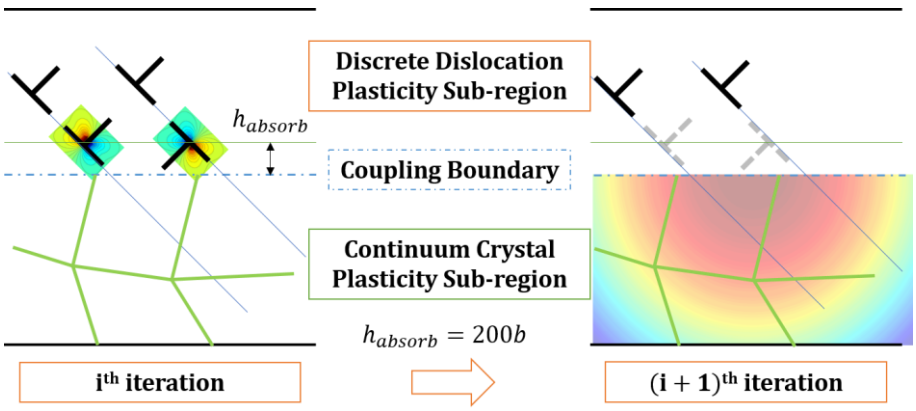


Figure 6.17. Sketch of the coupling model where a boundary transparent to dislocations presents. The stress field transfer is also illustrated.

6.4.2.2 Formula for indentation pressure

In order to quantitatively describe the indentation pressure curve of a single coating system (*e.g.* Figure 6.13), the following formula eq.(6.11) is developed to capture the indentation variation trend. Eq.(6.10) is assembled by combining the indentation pressure formula in ISE zone (See section 5.2) and eq.(6.1) that describes the hardness transition in a continuum coating system. In particular, we replace the assumed stable hardness of the coating film with the indentation pressure variation formula (i.e. eq. (5.9)) at ISE regime.

$$H_c = H_s + \frac{H_i\left[(1+\frac{\beta}{a})^{-\alpha}\right] - H_s}{1+(\frac{\beta}{\beta_0})^{\varepsilon}} \tag{6.11}$$

In eq.(6.10), H_c is the indentation pressure of a single coating system, H_i is the intrinsic hardness of the coating film, β is the relative indentation depth. H_s is the substrate, Parameter β_0 and ε specify the transition feature of indentation curves that are similar to those obtained from eq. (5.14). Other fitting parameters have the same physical interpretation as discussed in Section 5.2.

The best-fit curve using eq.(6.11) for the single crystal coating system is shown in Figure 6.18. This fitting curve captures the indentation pressure variation well (the adjusted coefficient of determination $R^2 = 0.9012$ with the relative indentation depth. Besides, compared to Korsunsky's formula (eq.(6.1)), the new formula captures the indentation size effect with the modified indentation pressure instead of a size-independent coating film hardness. The substrate starts to affect the single crystal coating system behavior at applied indentation depth $\delta = 0.1\mu m$ (*i.e.* equivalent to relative applied indentation depth $\beta = 5\%$) which is similar to the value at the polycrystalline coating system modelling (see Figure 6.13). The influence of CPFE substrate on the single crystal coating system is captured by the multi-scale coupling model and quantitatively described by eq.(6.11).

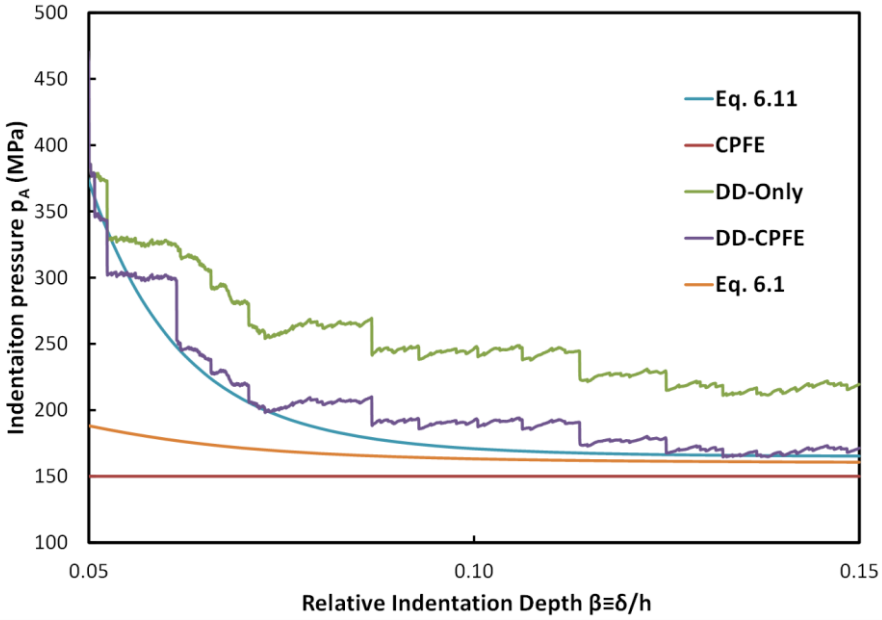


Figure 6.18. The actual indentation pressure against the relative indentation depth of a typical coating system. Results are shown for both coupling simulations and the best fit curve with eq.(6.11). The indentation pressure of discrete dislocation plasticity and crystal plasticity finite element simulations are also included for reference. The prediction of the coating system using the traditional formula eq.(6.1) is also plotted in orange.

6.4.2.3 Parametric study

In order to investigate the substrate influence on indentation pressure of a single crystal coating system, coupling simulations with substrates having various continuum hardness values modelled are performed. The substrates with different continuum hardness values are realized by varying critical resolved shear stress (τ_c) in the crystal plasticity finite element description (please see Section 5.3 for more details) and holding elastic properties.

The substrate effect of a single crystal coating system is illustrated in Figure 6.19 by terms of indentation pressure p_A curves versus relative indentation depth β. TAs can be seen in purple and blue curves, the indentation pressure of the coating system is decreased by softer substrates at a given relative applied indentation depth compared to the reference value, and the curves gradually approach to the continuum hardness value of substrates with increase of relative indentation depth. Bounded to a harder substrate (see the red curve), the indentation pressure curve is lifted up. In general, the substrate affects the comprehensive performance of the coating system by hardening or softening its coating film. This effect is rationalized as the discrepancy of plastic flow resistance between coating film and substrate. Besides, the effect becomes more evident with the increase of relative indentation depth.

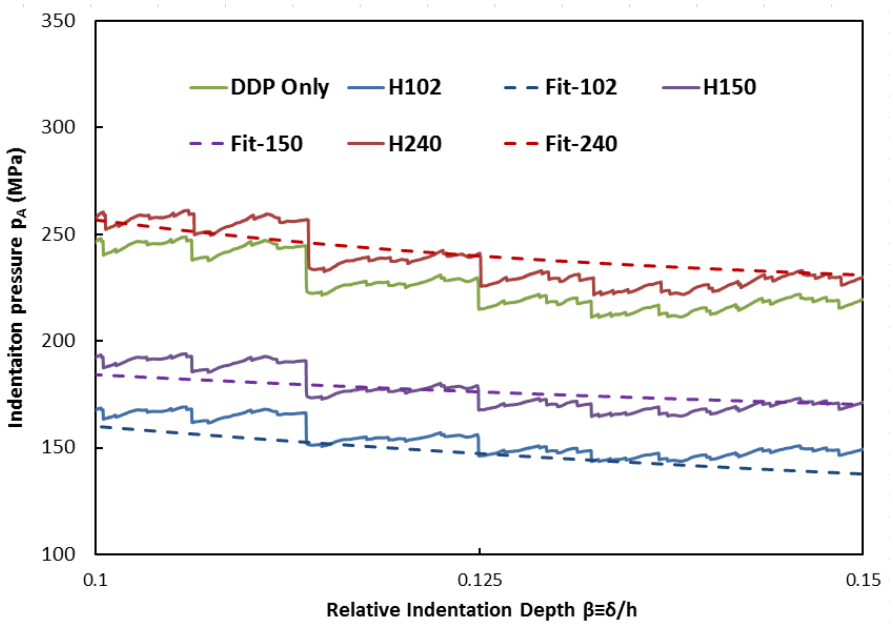


Figure 6.19. The actual indentation pressure p_A curves versus the relative indentation depth β for the single crystal coating system with the coating film $h = 2\mu m$ and various substrates with different continuum hardness values indented by the $\omega = 5°$ wedge. Results of DDP alone with a process window $h = 10\ \mu m$ with same source density are also included for reference.

The corresponding best-fit curves using eq.(6.11) are also reported in Figure 6.19. The of indentation pressure are plotted in same colour but in dash line. Fitting parameters are tabulated in Table 6.6.

The fitting parameters of Case H102 and H150 show a similar trend as in the polycrystalline coating system *i.e.* the transition parameter β_0 is not affected much by the substrate hardness and the exponent parameter ε increases with the increasing substrate hardness (please recall Section6.4.1 for more information). However, Case H240 representing a coating system with a harder substrate shows a change in values of β_0 and ε. This is due to the turning up of the indentation pressure following ISE regime. It is also noticing that this turning up of indentation pressure is attributed to the harder response of substrate rather than the grain boundary.

Table 6.6. the substrate hardness values and the corresponding fitting parameters of the indentation pressure curves fitted by using eq.(6.11). The values of fitting parameter α and α are the same as the corresponding discrete dislocation plasticity simulation fitting results.

Case Label	H_{CPFE} (MPa)	β_0	ε
H102	102	0.0985	1.976
H150	150	0.0945	2.069
H240	240	0.0429	0.393

The fitting parameters in the modified term ($H_i\left[(1+\frac{\beta}{a})^{-\alpha}\right]$) are found to be similar to results obtained by corresponding DDP calculations (please see Section 5.2), which

indicates that the single crystal coating film performance at ISE regime is still predominated by the DDP coating.

However, the fitting parameters β_0 and ε for the substrate effect are changed much compared to fitting results of hardness transition using Korsunsky formula eq.(6.11). The coating film hold its presence on indentation pressure of the coating system even though the applied indentation depth exceeds the ISE regime.

6.5 Discussion

The proposed coupling approach between DDP and CPFE sub-regions covering different scales improves computational efficiency of indentation problem while maintaining the fidelity of the material response. The substrate effect is involved when the size of DDP sub-region region decreases to a certain value. The application of the multi-scale coupling approach on polycrystalline and single crystal coating system motivates developing new equations for their indentation pressure variation. In particular, the newly proposed indentation pressure formulas (eq.(6.10) and eq.(6.11)) focus on the transition regime between DDP film and CPFE substrate. Hence, they are capable of predicting the comprehensive indention pressure variation covering a wider indentation depth range after incorporating ISE formula (See Section 5.2) and continuum transition formula (See Section 5.3).

The newly proposed multi-scale coupling approach improves the work by Curtin [130] in terms of focusing on localized plasticity at interface instead of achieving compatibility at an average sense. Besides, the flexibility due to the sub-region modelling strategy enables us to replace the current CPFE/DDP formulations with state-of-art and/or appropriate techniques. For instance, we can also incorporate a rate- and length scale-dependent CPFE algorithm e.g. [79, 81] into the multi-scale coupling. Two different type of coupling boundary intrinsically provide the indentation pressure response of coating systems composed of polycrystalline and single crystal.

The application of the proposed coupling approach on indentation problem illustrates the grain boundary and substrate effect, respectively, and the newly developed indentation pressure formula enlarges the application scales of previous work using strain gradient plasticity [152], discrete dislocation plasticity [2] and continuum plasticity [150] on predicting the hardness evolution of a composite coating system.

The fitting parameters in the modified film hardness term hold their physics significance (please see Section 5.2) and values as in DDP calculations. However, parameters in substrate hardness term are varied much due to the coupling effect. Some parameters in the proposed formulas still need physics-based interpretations, particularly in the transition regime.

In most of our coupling calculations, applied indentation depth was limited to $\delta = 0.3\mu m$ due to computational expense and numerical convergence issue. It still needs more investigation on fidelity of the proposed coupling results and coupling interface

performance when larger strains/strain gradient, higher dislocation densities and larger indentation depths present.

Meanwhile, our coupling framework is at present limited to a two-dimensional calculation. A number of crucial issues, especially when dealing with dislocation loop transmission between the DDP and the CPFE interface, in order for the proposed multi-scale coupling method to be extended to three dimensions.

Finally, the proposed indentation pressure formula needs further verification by experimental tools. Nano-indentation experiments would be conducted to further improve the current formula and provides the fitting parameters with physical interpretations based on specimen microstructure.

6.6 Summary

Planar wedge indentation problem has been simulated using the proposed multi-scale modelling method that is introduced in Chapter 3 on polycrystalline films. The application further shows the effectiveness and validity of the newly developed multi-scale coupling technique between CPFE and DDP. For a given applied indentation depth, the CPFE substrate takes stronger effects on the comprehensive response of the coupled material when the DDP film is relatively thin. Besides, the computation efficiency is improved by a factor up to 10.

The indentation pressure variation curve is obtained after applying the multi-scale coupling method to a coating system. Incorporating the previous study on the indentation pressure variation at ISE regime (see Section 5.2) and the hardness transition at continuum level (see Section 5.3), a new formula that quantitatively describes the indentation pressure variation at different scales has been developed for a polycrystalline coating system. The new formula successfully bridges the gap between indentation solutions at discrete and continuum scales. Besides, two different techniques that can be used to model the interface between DDP and CPFE sub-regions are discussed.

The application of the proposed coupling approach has investigated the normal response of films under contact at different scales. In the following Chapter 7, numerical efforts will be focused on the tangential response (including response under cyclic loading) of thin films in contact and subjected to normal load and shear for different sizes.

7 Nano-Sliding and Fretting Problems

In this chapter, planar sliding and fretting calculations of thin films under various contact shapes and sizes are carried out by adopting crystal plasticity finite element (CPFE) and discrete dislocation plasticity (DDP) material descriptions to capture plastic flow and study the origin of contact fatigue at different scales. The relevant codes are adapted from the formulations introduced in Chapter 3.

Parametric study on plastic slip and grain orientations are performed using CPFE modelling, while dislocation structure and evolution, surface profile variation, contact size effect (CSE) and influence of indentation performed prior to sliding are addressed in DDP modelling. Numerical results shown in this chapter reveal that the application of tangential forced to materials subjected to contact loads produces a highly localized plasticity zone, which is analogous to the indentation problem in Chapters 5 and 6. The study in this chapter also shifts focus from the global plasticity of specimens discussed in Chapter 4 to the analysis of localized sensitive regions were damage accumulation is likely to take place.

The link between dislocation structures that are captured by DDP at the micro-scale to fatigue crack initiation that can be incorporated within CPFE meso-scopic continuum models is discussed. The preliminary work carried out by the author reveals the role of dislocation structure and local energy dissipation in the micro-crack initiation process experienced in fretting problems. Results and discussion shed light on multi-scale material response under sliding and fretting loading. A plan for future work that describes the potential coupling between DDP and CPFE in fretting problems will be suggested in Chapter 8.

7.1 Introduction

A literature review on the mechanical behaviour of materials and its modelling under fretting has been provided in Section2.3.4. In this chapter, the thesis first reports on a number of sliding and fretting simulations that are performed using crystal plasticity finite element and discrete dislocation plasticity in order to investigate general features of fretting problems and nano- and micro-sliding, and the sensitivity of material performance to the microstructure. In particular, results of CPFE simulations focus on stress and deformation in different regions of the indented material, while DDP calculations apply dislocation structure and shear stress to investigate contact size effect in both sliding and fretting problems. Finally, the possibility of applying a multi-scale modelling technique that would enable to embed information obtained using DDP calculations into CPFE damage initiation models is proposed and discussed.

7.2 Sliding and Fretting problems Solved using the Crystal Plasticity Finite Element Technique

7.2.1 Methodology

The investigated specimen is made up of polycrystalline materials that are modelled by a rate-independent formula as illustrated Chapter 3. The indenter is modelled as a flat rigid body, and a displacement boundary condition is imposed on the indenter to simulate sliding and fretting. Results show the response of a polycrystalline film indented by a flat punch to the application of tangential forces, as a function of various material properties and microstructures.

7.2.2 Problem definition

In simulations of CPFE material response under sliding and fretting, a plane strain analysis of the contact between a polycrystalline film and a flat indenter sliding is conducted. The specimen studied using the CPFE description is characterised by thickness $H = 10\ \mu m$ and length $L = \ 20\ \mu m$ and is bonded to a rigid substrate. Sketches of the problem under investigation is shown in Figure 7.1 Plasticity in the film is calculated by the CPFE formulation on predefined slip planes. The simulation is performed using ABAQUS and its internal user-defined material subroutine (UMAT). The indenter is modelled as a non-smoothed rectangular 'analytical surface' with thickness $h = 2\ \mu m$ and contact length $\mathrm{l} = \ 10\ \mu m$, and the contact property is set as "hard contact" in the normal behaviour and the frictional interactions are treated using a penalty algorithm. Lagrange Multiplier algorithm commonly works as a more accurate algorithm for tangential behaviour option because additional parameters are applied to refine constraints [280-282]. However, Lagrange Multiplier would meet difficulties when a direct solution technique is applied [283] as zero term are introduced into the diagonal of matrix. Penalty algorithm, on the other hand, represents the contact governing equations with approximation by introducing a penalty parameter [284, 285]. Penalty option is able to achieve a high accuracy when adopting a sufficiently large value of penalty parameter[283]. The adoption of penalty algorithm in this project also decrease the complexity of contact and thus the computational expense.

The CPFE specimen is discretized by a biased mesh with the finest mesh at the surface in order to obtain a higher resolution within the contact area. The element type is 4-noded non-reduced integration plain strain element with name "CPE4" in ABAQUS element library.

Elastic properties of the crystals composing the film is based on typical values of aluminium, set as Poisson's ratio $v = 0.33$ and Young's modulus $E = 70\ GP$. While investigating the general plastic material behaviour under sliding and fretting, the coefficient of friction was varied to study its effect on the system response. On investigating the microstructure effect of materials in sliding and fretting problems, a single grain with a crystalline orientation angle ranging from 0 to 45 degree is assigned

to the investigated specimen. Please refer to Chapter 3 and Chapter 4 for more details on the notation of grain orientation. Other CPFE parameters, including the critical resolved shear stress, hardening parameters and hardening rate are fixed as their influence has been discussed in Chapter 4. Parameters of the reference single crystal in CPFE sliding and fretting simulations are chosen as the following Table 7.1 shown. These parameters are obtained by a calibration process to match the macroscopic stress strain response curve of DDP material under a uniaxial tension case. Please refer to Chapter 4 for more details on the calibration.

Table 7.1. Parameters of reference CPFE single crystal in sliding and fretting problems

Parameter	Symbol	Unit	Value
Young's Modulus	E	GPa	70
Poisson's ratio	v	-	0.33
Grain Orientation	ϕ	degree	0
CRSS	τ_c	MPa	9
	H_F	-	98
	H_R	-	45
	H_{exp}	-	1525
Lateral Hardening rate	q	-	1.01

In the polycrystalline case, there are 20 grains in CPFE film, and each of them is assigned a random grain orientation degree ranging from 0 to 45 degree. Please refer to Chapters 3 and 4 for more details on this rotation definition. This polycrystalline case aims to investigate grain boundary and inhomogeneity influence on material response modelling by CPFE under sliding and fretting.

The bottom surface cannot displace in the Y-direction of its centre node is fixed. Left and right edges of the CPFE specimen are set as free boundaries. The fixed boundary conditions of sliding problem are summarized as following:

$$\begin{aligned} &\dot{u}_y = 0 \text{ on } y = 0 \text{ and } \dot{u}_x = 0 \text{ on } x = 0 \\ &T_x = T_y = 0 \text{ on } x = H \notin S_{contact} \end{aligned} \tag{7.1}$$

Here, $T = \sigma_{ij} n_j$ is surface traction on a surface with outward normal vector n_j.

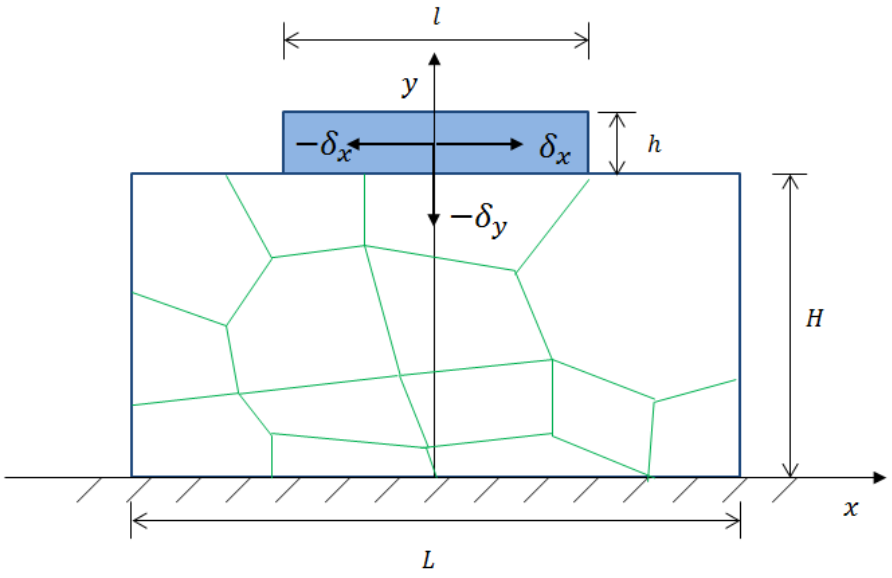


Figure 7.1. Sketch of the boundary value problem of a CPFE crystal under a sliding and fretting loading by a flat-shaped indenter

A flat indenter indents into the CPFE specimen with an applied indentation depth $-\delta_y = 0.2\mu m$ to initialize a contact. Afterwards, the flat contact slides monodirectionally in the sliding problem or cyclically in the fretting problem with a maximum sliding distance $\delta_x = 0.2\mu m$. In order to decrease the expense in terms of post-processing, the results are taken from ABAQUS calculations every 1000 increments during the sliding step, which effectively achieves a resolution of $\Delta\delta_x = 0.02\mu m$.

We herein integrate a damage initiation and evolution criterion that is based on the accumulated plastic strain of elements into the UMAT subroutine. Regarding the damage initiation, accumulated plastic strain representing plastic slip within an element is considered as the main contribution to crack initiation due to fretting fatigue. The microscopic damage initiation criterion is stated as the onset of damage of a finite element will occur when the accumulated plastic strain during the whole fretting process exceeds a critical value, which is given as:

$$D = \int_0^t \frac{\gamma}{\gamma_D} \geq 1 \tag{7.2}$$

where D is a state variable that increases monotonically with plastic deformation, γ_D is an empirical material dependent parameter, and γ is the current value of plastic strains accumulated throughout the loading cycles, which is given by the time evolution of:

$$\gamma = \sum_1^3 \left|\Gamma^{(\alpha)}\right|, \alpha = 1,2,3 \tag{7.3}$$

where $\Gamma^{(\alpha)}$ is the slip along the αth slip system.

Materials usually undergo softening after their onset of damage initiation. The damage parameter D, which evolves with the accumulation of damage in materials, quantitatively assesses damage in materials. At the onset of damage, the value of damage parameter D is zero. When a material is completely damaged, *i.e.* failed, the value of damage parameter D is one. Two types of damage evolutions are considered in simulations, namely the linear form and the exponent form[286], which are shown in Figure 7.2 respectively. The exponent evolution form (eq. (7.4)) describes the damage parameter D variation on the accumulative plastic strain γ using two parameters (a and b in the adopted equation).

$$D = \frac{1 - e^{(-a*\frac{\gamma-\gamma_s}{\gamma_f-\gamma_s})}}{1 - e^{-a}} \tag{7.4}$$

The effect of exponent parameter a is illustrated using a parametric study in eq.(7.4), where a larger value of exponent parameter a leads to a larger value of damage parameter D (see Figure 7.2). The linear evolution form that describes a linear relation between the damage parameter D and the accumulative plastic strain γ is obtained by specifying parameter value $\mathrm{a} \to 0$ in eq.(7.5).

$$D = \frac{\gamma - \gamma_s}{\gamma_f - \gamma_s} \tag{7.5}$$

The value of damage onset parameter and complete parameter stands for the accumulative plastic strain where the damage initiates (*i.e.* $\mathrm{D} = 0$) and material fully fails (*i.e.* $\mathrm{D} = 1$). The choice of corresponding accumulated plastic values for the damage onset parameter (γ_s) and complete damage (γ_f) should be determined by experiments and further calibration, potentially using DDP simulations. However, simulations herein employ a pair of empirical values that are obtained from fatigue simulations [287, 288]. Further efforts should be placed on the development of suitable fatigue experiments to provide more physically-based parameters.

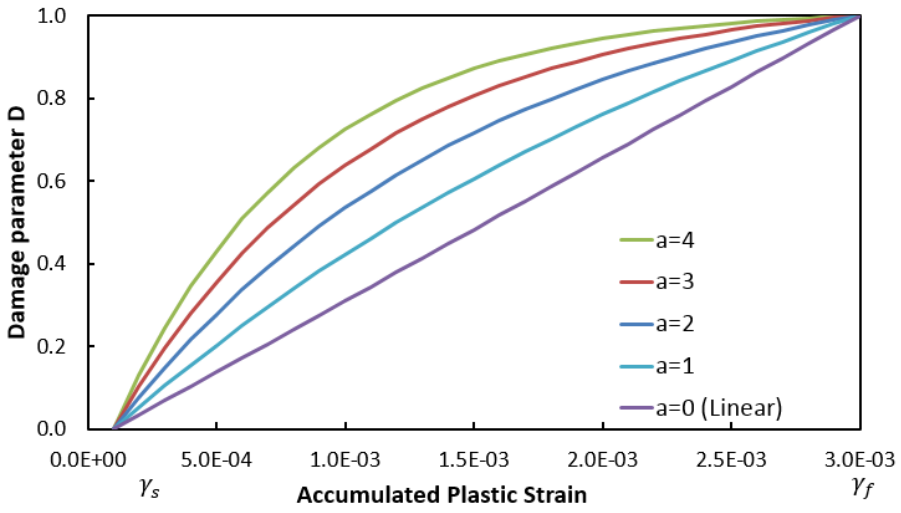


Figure 7.2. Linear and exponential types of damage evolution based on the accumulated plastic strain in finite elements

7.2.3 Results

In this section, results will be shown in sliding and fretting problems, respectively. The sliding process is obtained by applying a relative displacement between indenter and films, while the fretting process is realized by applying oscillating tangential displacements to the indenter. In each set of simulations, we first define the sampling coordinates where the response information is collected. After that, parametric studies is conducted to investigate the microstructure influence. At the end, the relation between accumulated plastic strain and micro-crack initiation is discussed. Numerical results reported here provide a systematic study of a specimen subjected to tangential contact forces modelled with CPFE. This study complement the previous work on the performance of polycrystalline material when subjected to normal load presented in Chapter 5, and will be further linked to the DDP simulations results in the following section.

7.2.3.1 Sliding simulations

7.2.3.1.1 Path definition for results collection

In order to demonstrate stress, deformation and damage status in different partitions of specimen, five paths of nodes have been defined to track the evolution of the system: at surface, subsurface, bulk, leading edge and trailing edge, respectively. The definitions of the five paths are shown in Figure 7.3. In particular, Path Surface (a_1) is defined as the first layer i.e. the nodes in direct contact with the indenter. Path Subsurface (a_2) and Path Bulk (a_3) are defined 5 and 10 layers of nodes (which are equivalently $0.218\mu m$ (0.0218% of the thickness) and $0.633\mu m$ (0.0633% of the thickness) respectively away from Path Surface. The vertical distributed nodes near the right edge of contact compose to the Path Trailing Edge (b_2), while the nodes near the left edge of contact compose to the Path Leading Edge (b_1). The definition of leading and trailing edges is based on the imposed boundary condition, namely the

indenter slides towards the left (negative direction) with respect to specimen during sliding or in the first stroke of the fretting simulations.

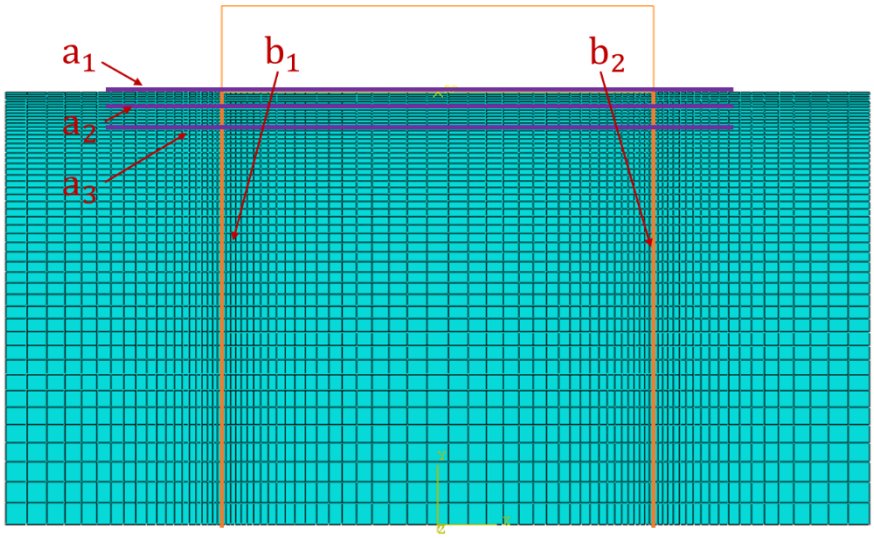


Figure 7.3. The nodal path definitions in sliding simulations solving with CPFE method. The horizontal path definitions labelled as a_1, a_2 and a_3 represent surface, subsurface and bulk behaviour, while vertical path definitions labelled as b_1 and b_2 represent the trailing and leading edge behaviour.

7.2.3.1.2 General slip/plastic deformation distribution

A reference simulation is carried out to investigate the general material response at different positions for a sliding loading configuration. The reference specimen is a single crystal material with 0 grain orientation, and the coefficient of friction between the indenter and the specimen is fixed as 0.2.

Figure 7.4 shows a general plastic deformation distribution represented by a solution dependent variable (SDV69) (accumulated plastic strain γ) near indenter leading edge. This contour plot shows the typical behaviour of a material plastically deforming under a flat sliding indenter. It is found that a high plastic strain concentration is generally located underneath the indenter's edge. The strain concentration is a consequence of the ploughing effect of the indenter. Another important feature of this plastic strain contour is about its plastic flow direction. The plastic flow in a material under sliding expands from the surface towards the bulk in two directions. The major "branch" of accumulated plastic strains heads far away from contact, while the other branch showing large plastic flow moves towards the zone underneath contact. The orientation of plastic flow is not only determined by external loading but is also affected by crystal orientation.

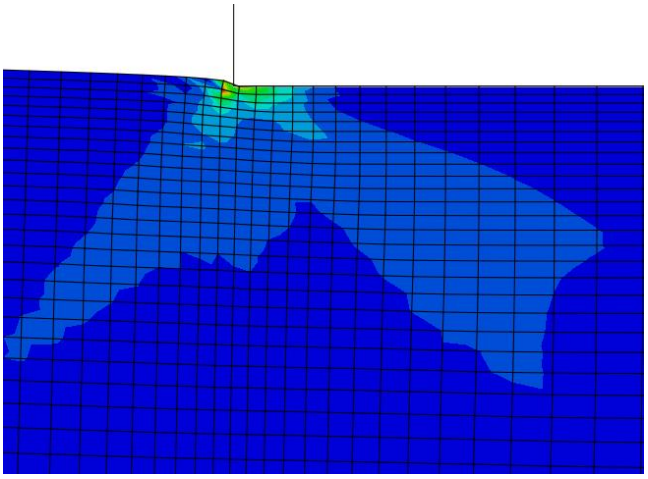


Figure 7.4. A general plastic deformation contour of the specimen under flat contact sliding. Figure shows the accumulated plastic strain contour near the leading edge.

Accumulated plastic strain γ along Path Surface, Path Subsurface and Path Surface is reported in Figure 7.5, against normalized position along the contact. Peak of accumulated plastic strain of all paths are found to be near the contact edges. Nodes along Path Surface are found to exhibit the most severe plastic deformation peak due to highly localized stress concentration at the contact edges. Accumulative plastic strain at nodes along Bulk Path exhibit a lower peak and a contact-oriented trend, which is consistent with the plastic deformation contour in Figure 7.4. However, there is highly localized plastic deformation found at nodes closer to contact edges along Surface and Subsurface Path

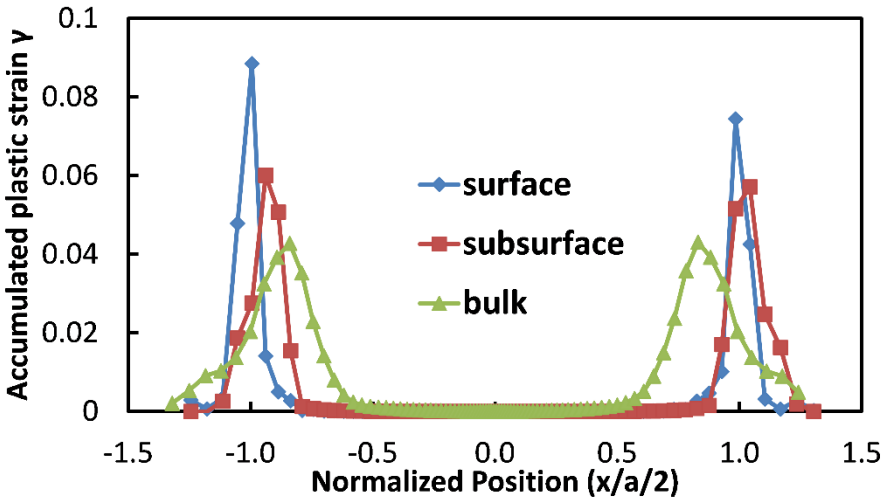


Figure 7.5. Accumulated plastic strain γ computed at nodes along Path Surface, Path Subsurface and Path Bulk.

Accumulated plastic strain γ along Path Leading Edge and Path Trailing Edge are reported in Figure 7.6 against the normalized specimen's depth. Accumulated plastic strain achieves their peaks near the contact (surface) for both leading and trailing edges. Trailing edge suffers from a larger plastic deformation at a shallower layer, but nodes along the leading edge are damaged more inside material bulk.

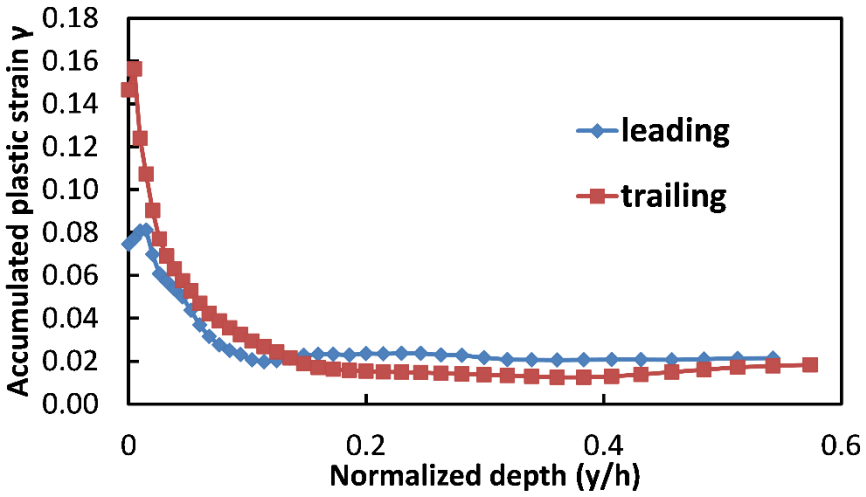


Figure 7.6. The accumulated plastic strain γ of nodes along Path Leading Edge and Path Trailing Edge.

7.2.3.1.3 Plasticity introduced by sliding

The influence of sliding on the response of the material after indentation is evaluated by a parameter named the sliding index. It is defined as the accumulated plastic strain after sliding over the accumulated plastic strain after indentation process, which is given by:

$$\zeta = \gamma_{sliding}/\gamma_{indentation} \tag{7.6}$$

The sliding index ζ along Path Surface, Path Subsurface and Path Bulk is reported in Figure 7.7, against normalized position along the contact. It is clear that the bulk of the material is not affected much by the sliding process *i.e.* the plastic deformation inside material undergoing indentation and sliding is mainly caused by indentation process for the configurations under investigation here. The contact surface is found to be largely affected by the sliding process, especially in the zones near the contact edges. The sliding index is found to be up to 1.6 at certain nodes near those zones.

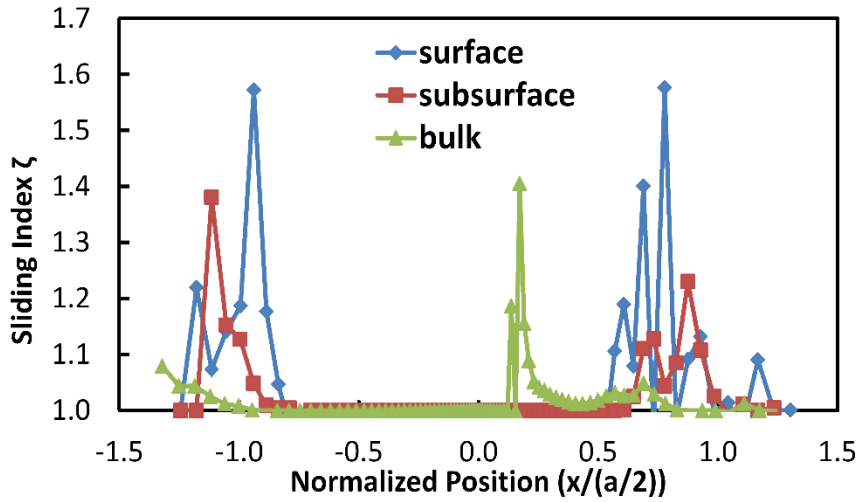
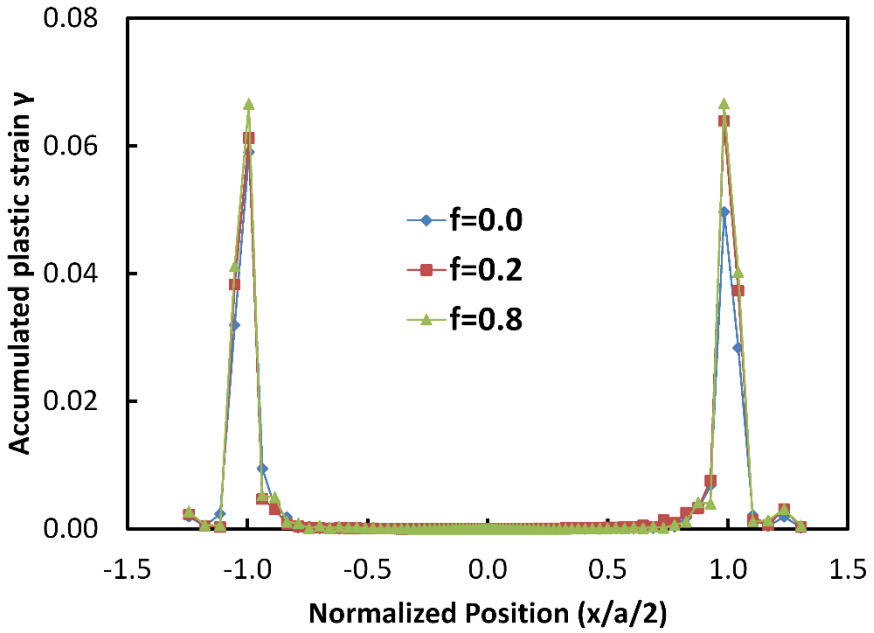


Figure 7.7. Sliding index ζ of nodes along Path Surface, Path Subsurface and Path Bulk.

A set of simulations with different values of coefficient of friction (COF, represented by f in the figure) between indenter and specimen are carried out to investigate the coefficient of friction effect on material behaviour. The specimen is modelled as a reference crystal material, i.e. 0 grain orientation with respect to X axis. The accumulated plastic strain γ of nodes along Path Surface and Path Leading Edge are reported in Figure 7.8 (a) and (b) respectively. For surface nodes (see Figure 7.8 (a)), higher coefficient of friction leads to a higher peak value of accumulated plastic strain near the leading edge. This finding indicates that the increase of friction results in a higher plastic deformation and thus a lager probability to nucleate micro-crack. But coefficient of friction exhibits less influence on plastic strain within the contact interior. For leading edge nodes (see Figure 7.8 (b)), besides contact edge effect motioned above, coefficient of friction does not affect plastic deformation of nodes inside of the material bulk.



(a)

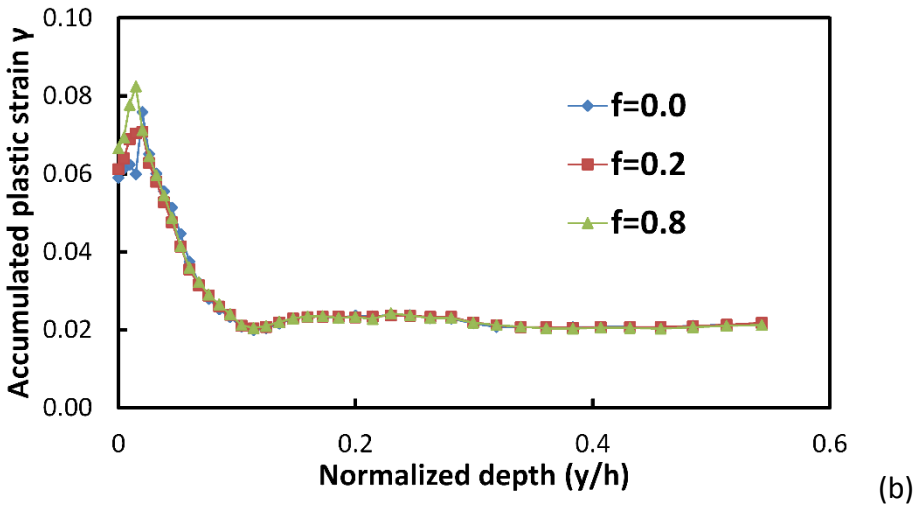


Figure 7.8. The influence of coefficient of friction on the plastic deformation of nodes at different positions (a) nodes along the specimen surface (b) nodes along the leading edge

7.2.3.1.4 Microstructure influence

In order to investigate the influence of the crystalline microstructure on the material response, two sets of simulations using materials with different crystal microstructure are conducted. On one hand, a single crystal with its crystal axes representing different grain orientations with respect to the geometry of the specimen and the applied load is studied; this aims at investigating the effect of the global grain orientation of crystals on its plastic response. On the other hand, a polycrystalline aggregate is also studied, with a different specific grain orientations assigned to the grains in the zone underneath the leading edge; these investigations look at the localized effect that grain orientation has on the material response.

Figure 7.9 (a), (b) and (c) show the accumulated plastic strain γ at nodes along Path Surface, Path Subsurface and Path Bulk with 0, 22.5 and 45 degree oriented single crystals respectively. For nodes along the surface, the crystal with 45 and 0 degree orientation show greatest and smallest plastic strain respectively. For nodes along Path Subsurface and Path Bulk, the grain with 0 orientation shows the smallest value of plastic strain. However, the grain with 22.5 grain orientation shows the greatest value of plastic strain at those positions, especially underneath contact leading edge. This comparison indicates that the plastic deformation during a sliding process is strongly dependent on the orientation of local slip systems. Besides, from the practical engineering perspective, a specific grain orientation should be adopted in order to obtain an optimal microstructure design of specimens.

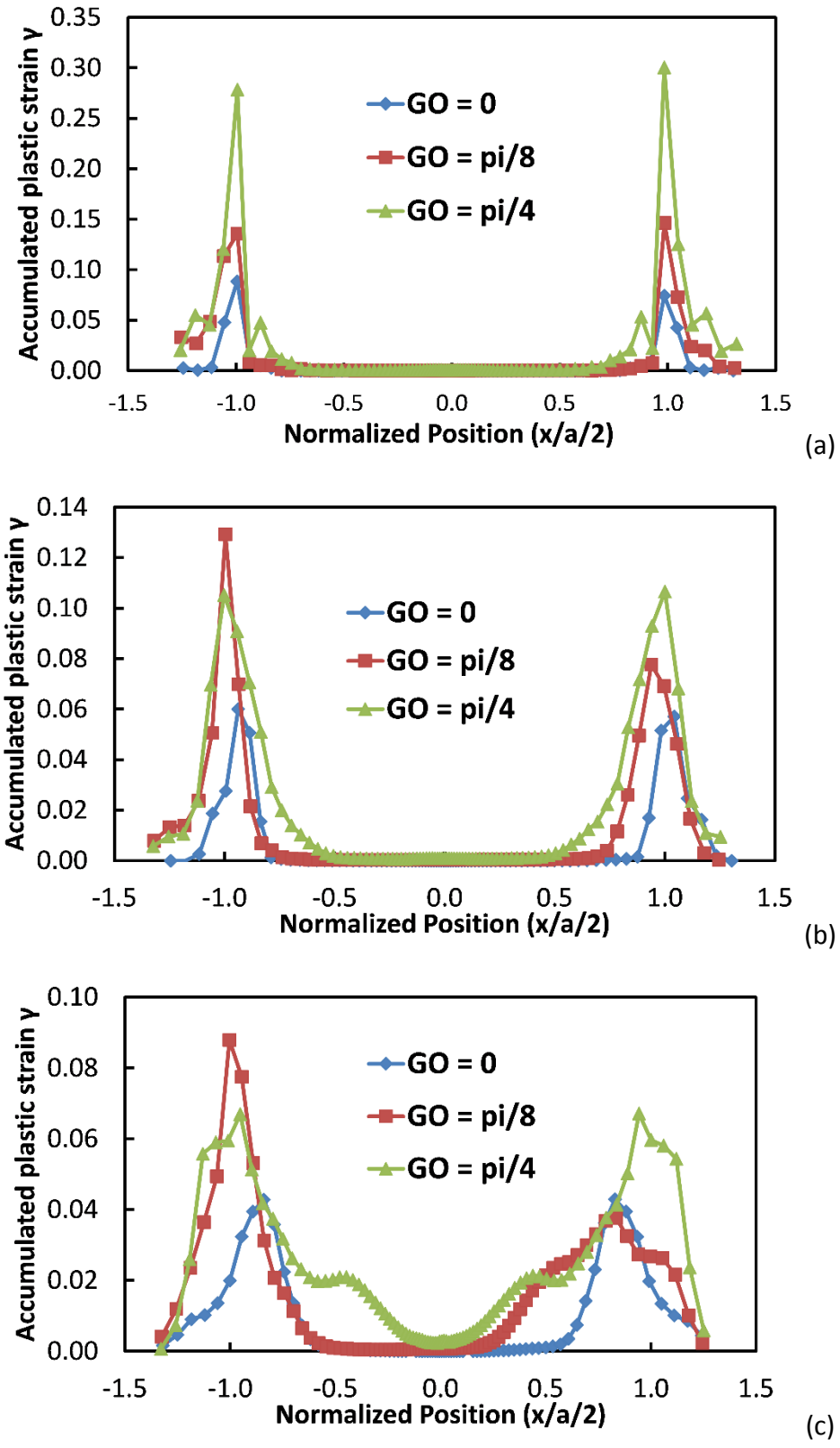


Figure 7.9. Accumulated plastic strain γ of nodes along Path Surface (a), Path Subsurface (b) and Path Bulk (c). Results are shown from films assigned single crystals with grain orientations (GO) 0, $\pi/8$ and$\pi/4$, respectively.

A polycrystalline material model with 20 grains is adopted to investigate the localized crystal orientation effect on material performance. A sketch of a general microstructure of the polycrystalline material model is illustrated in Figure 7.10. There are two potentially sensitive grains, labelled as X, underneath the contact leading edge. They are assigned a varied crystal orientation to study the effect of local grain orientation variation near the contact edge. All other grains are assigned a fixed grain orientation with a random distribution ranging from 0 to 45 degree.

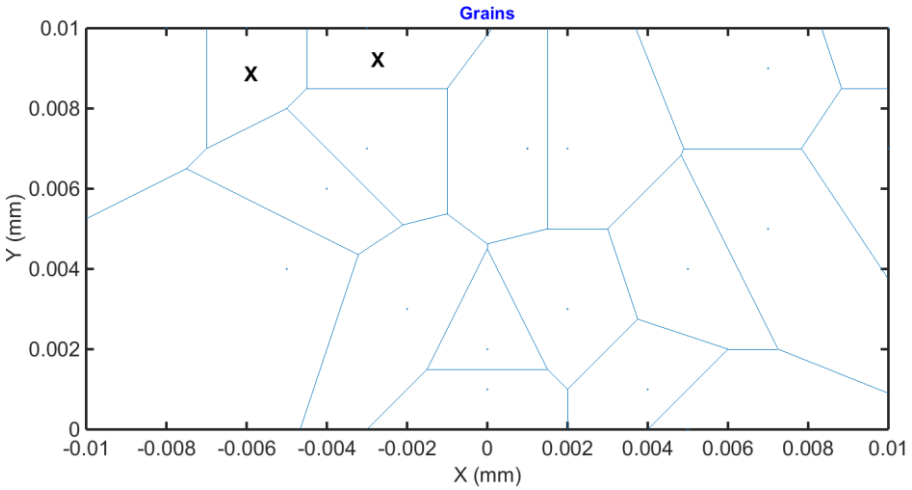


Figure 7.10. A sketch of polycrystalline microstructure of the specimen under flat contact sliding. X represents potentially sensitive grains.

Figure 7.11 shows the accumulated plastic strain γ of nodes along Path Surface with the two grains labelled as X in Figure 7.10 oriented at 0, 22.5 and 45 degree on the horizontal respectively. We can see that crystals with 22.5 degree as grain orientation show the greatest value of localized plastic deformation. This indicates that grains with 22.5 degree orientation have the most favourable slip system for the leading edge zone. As the leading edge is the most favourable zone for plastic strain accumulation, these results highlight the importance of the local microstructure in the neighbourhood of the leading edge in controlling the fatigue process. This has important implications in terms of designing the near-surface microstructure of a specimen undergoing indentation and sliding. Besides, the significance of microstructure near the geometrical features that show stress concentrations revealed. The combination effect of geometry characteristics (near leading edge of contact) and a favorably oriented grain lead to increase probability of fatigue crack initiation.

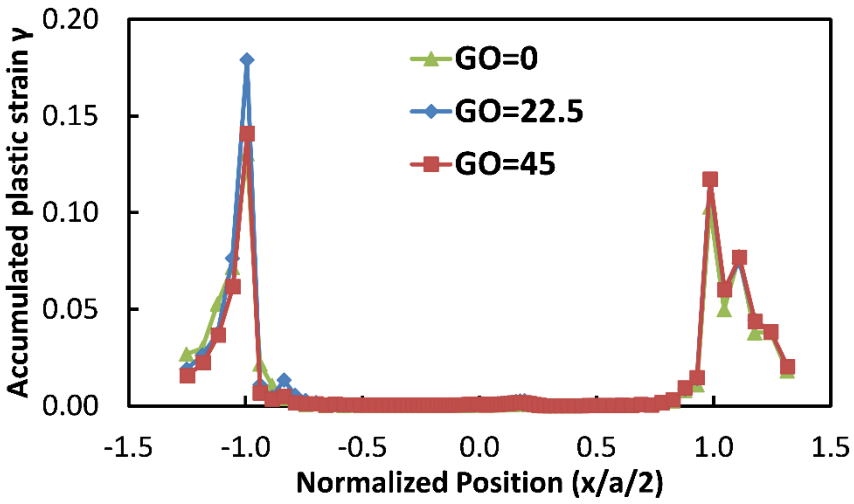


Figure 7.11. Accumulated plastic strain γ along Path Surface. Results are shown for polycrystalline specimens with grains near the contact leading edge oriented at 0, 22.5 and 45 degree, respectively.

7.2.3.2 Fretting simulations

Fretting simulations herein are realized by cyclic conducting the sliding calculation mentioned in Section 7.2.2 which follows a preceding indentation process. Three number of cyclic sliding strokes $\delta_x = 0.2\mu m$ are conducted the beginning stage of a fretting process. The definition of fretting problem and corresponding boundary conditions are similarly sketched in Figure 7.2.

7.2.3.2.1 Path and intersection nodes definition for results collection

The definitions of nodal paths in fretting simulations are identical to the definitions used for the sliding cases described above. In order to track the plastic deformation evolution of in sensitive zones, focus is placed on stresses and plastic strains

According to the highly localized plastic strain and thus damage (*i.e.* the highest probability of crack initiation) observed discovered in sliding problem (see Section 7.2.3.1), we investigate the plastic deformation at six intersections between leading /trailing contact and Path Surface/Subsurface/Bulk, respectively. The location of these investigated nodes are shown in Figure 7.12. Plastic strain is calculated at Gaussian points nearby and then interpolated to the nodes of interest. The plastic strain obtained at these nodes is considered as a comprehensive response along slip systems nearby within a crystal under cyclic sliding loading.

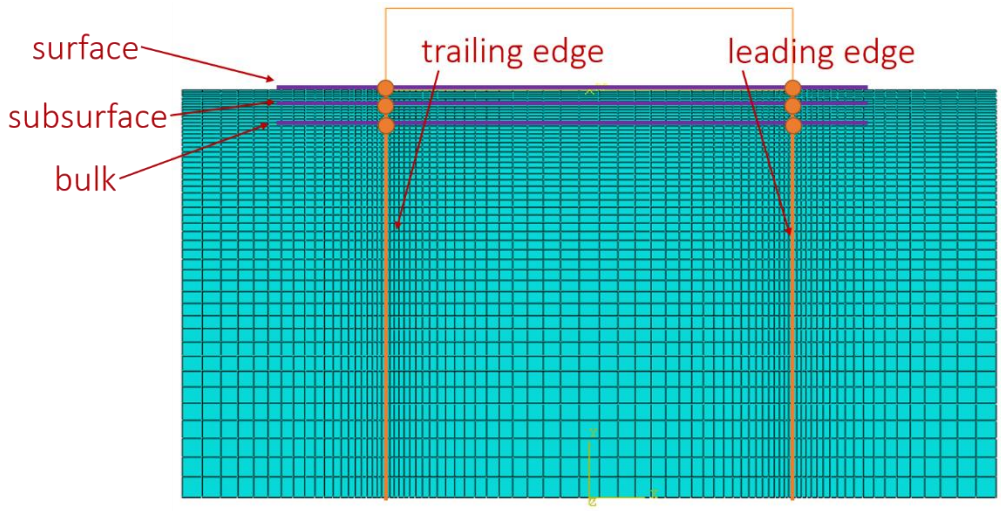


Figure 7.12. Points of interest on the specimen in fretting simulations solving with CPFE method. A focused mesh is also shown for reference

7.2.3.2.2 The general evolution of accumulated plastic strain

Results are obtained from simulations with a single crystal oriented 0 degree assigned to the specimen and $f = 0.2$ as the coefficient of friction between specimen and indenter. As expected, plastic strain is highly localized and accumulated at nodes close to leading and trailing edges. Regarding the values of accumulative plastic strain, the preceding indentation process contributes a dominating portion of the total plastic strain after three fretting cycles. For fretting process, plastic deformation is founded to be more accumulative at the leading contact point. For nodes within the contact, the accumulation of plastic strain is not apparently observed during the fretting process. This indicates that plastic shakedown phenomenon (*i.e.* deformation recover) occurs for the material within the contact regime.

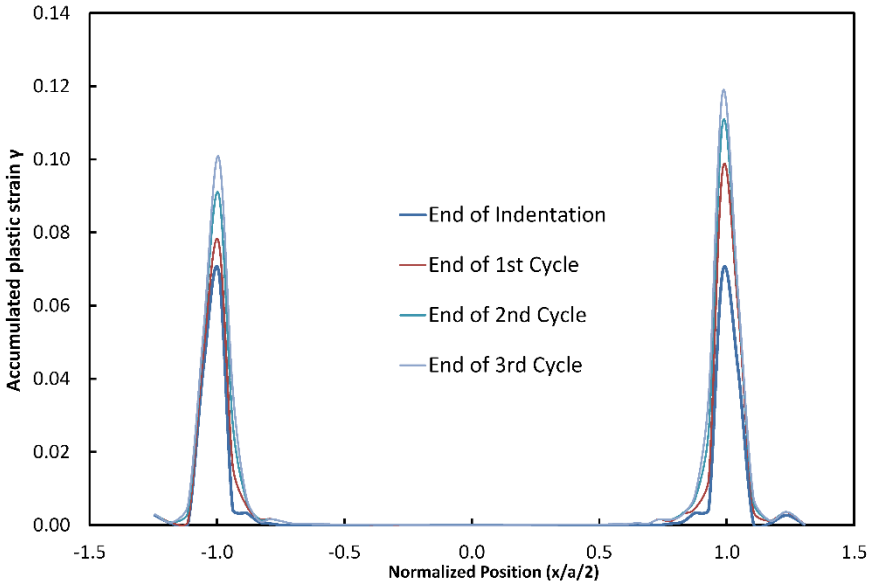
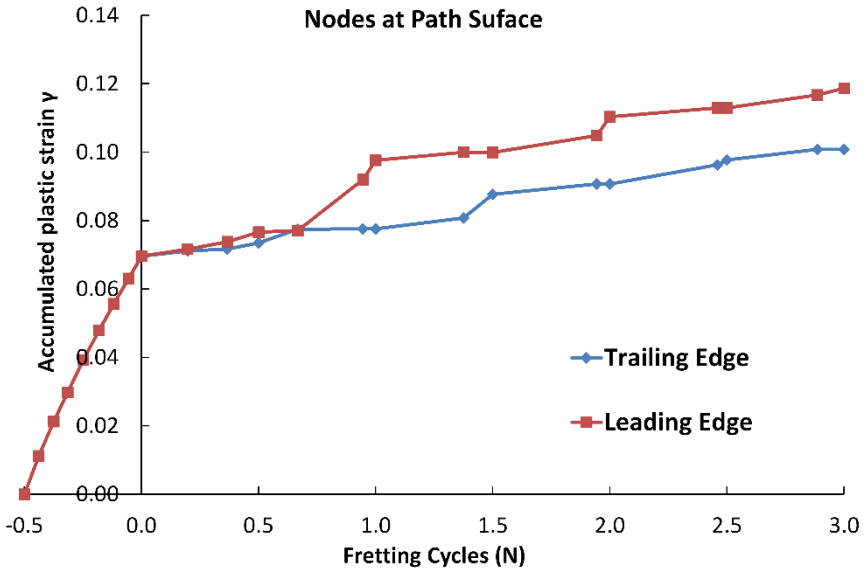
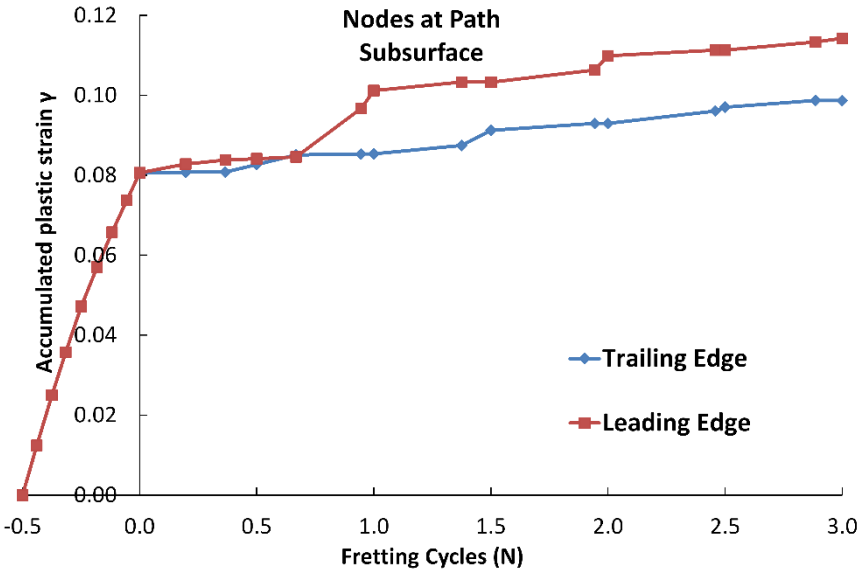


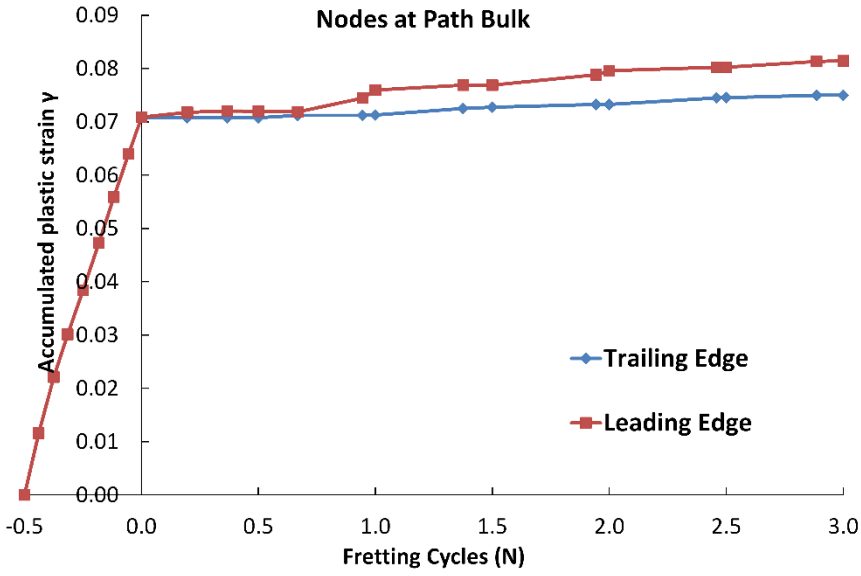
Figure 7.13. Evolution of accumulated plastic strain γ of nodes along Path Surface during three cycles of sliding. Results are obtained from a single crystal oriented 0 degree and coefficient of friction $f = 0.2$ between the indenter and specimen.

Evolution curves of accumulated plastic strain γ of nodes at the intersections defined in Section 7.2.3.2.1 during three cycles of fretting are presented in Figure 7.14 (a), (b) and (c), respectively. Results are obtained from simulations with a single crystal oriented 0 degree as specimen and f=0.2 as the coefficient of friction between specimen and indenter. The fretting cycle N from -0.5 to 0 stands for the prior indention process. Nodes at the contact surface suffers from the most severe plastic deformation; and the plastic deformation at the surface and subsurface keeps gradually accumulated. Compared to the counterpart at the trailing edge, material near the node at the leading edge exhibits a higher value of plastic deformation. This is attributed to the mono-direction sliding effect (please see Figure 7.2). However, the plastic deformation of nodes in bulk of material shows little discrepancy between leading and trailing edges, and plastic strain accumulation effect is not that apparent during fretting process. Therefore, the plastic shakedown phenomenon is observed during subsequent cycles in the deep bulk of materials.


Nodes at Path Suface
Accumulated plastic strain γ
0.14
0.12
0.10
0.08
0.06
0.04
0.02
0.00
-0.5
0.0
0.5
1.0
1.5
2.0
2.5
3.0
Fretting Cycles (N)
Trailing Edge
Leading Edge


Nodes at Path Subsurface
Accumulated plastic strain γ
0.12
0.10
0.08
0.06
0.04
0.02
0.00
-0.5
0.0
0.5
1.0
1.5
2.0
2.5
3.0
Fretting Cycles (N)
Trailing Edge
Leading Edge

(b)

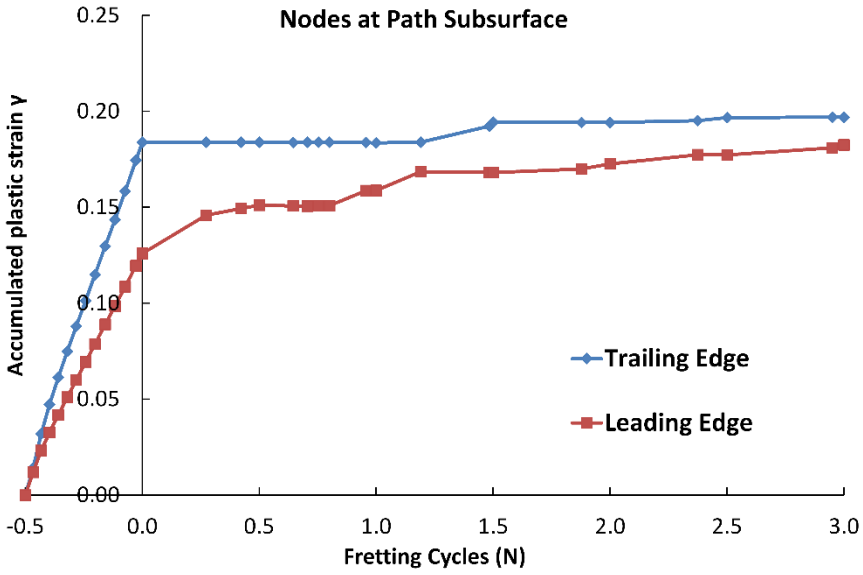

Nodes at Path Bulk
Accumulated plastic strain γ
0.09
0.08
0.07
0.06
0.05
0.04
0.03
0.02
0.01
0.00
-0.5
0.0
0.5
1.0
1.5
2.0
2.5
3.0
Fretting Cycles (N)
Trailing Edge
Leading Edge

(c)

Figure 7.14. Evolution of accumulated plastic strain γ of nodes at the intersection between contact edges and (a) Path Surface, (b)Path Subsurface and (c)Path Bulk during three cycles of fretting. Results are obtained from simulations with a single crystal oriented 0 degree as specimen and 0.2 as the coefficient of friction between the specimen and indenter.

7.2.3.2.3 Microstructure effect on fretting

In order to investigate the crystal microstructure influence on the plastic strain accumulation during the fretting process, similar cyclic sliding simulations are conducted with a specimen characterised by a 22.5 degree oriented single crystal. The coefficient of friction between the indenter and the single crystal specimen is set to$f = 0.2$. Evolution curves of accumulated plastic strain γ of nodes at intersections between leading/trailing edge and Path Surface/Subsurface/Bulk during three cycles of sliding are presented in Figure 7.15(a), (b) and (c) respectively. Compared to Figure 7.13, the variation of grain orientation introduces much more plastic strain at the trailing edge. The discrepancy of accumulative plastic strain is systematically observed in surface, subsurface and bulk of materials. This microstructure influence is attributed to that the adopted grain orientation (i.e. 22.5 degree) leads to a much more favoured slip system near the trailing edge. The revealed microstructure effect is able to direct designers to specifically select a single crystal orientation according to practical loading conditions.



(a)

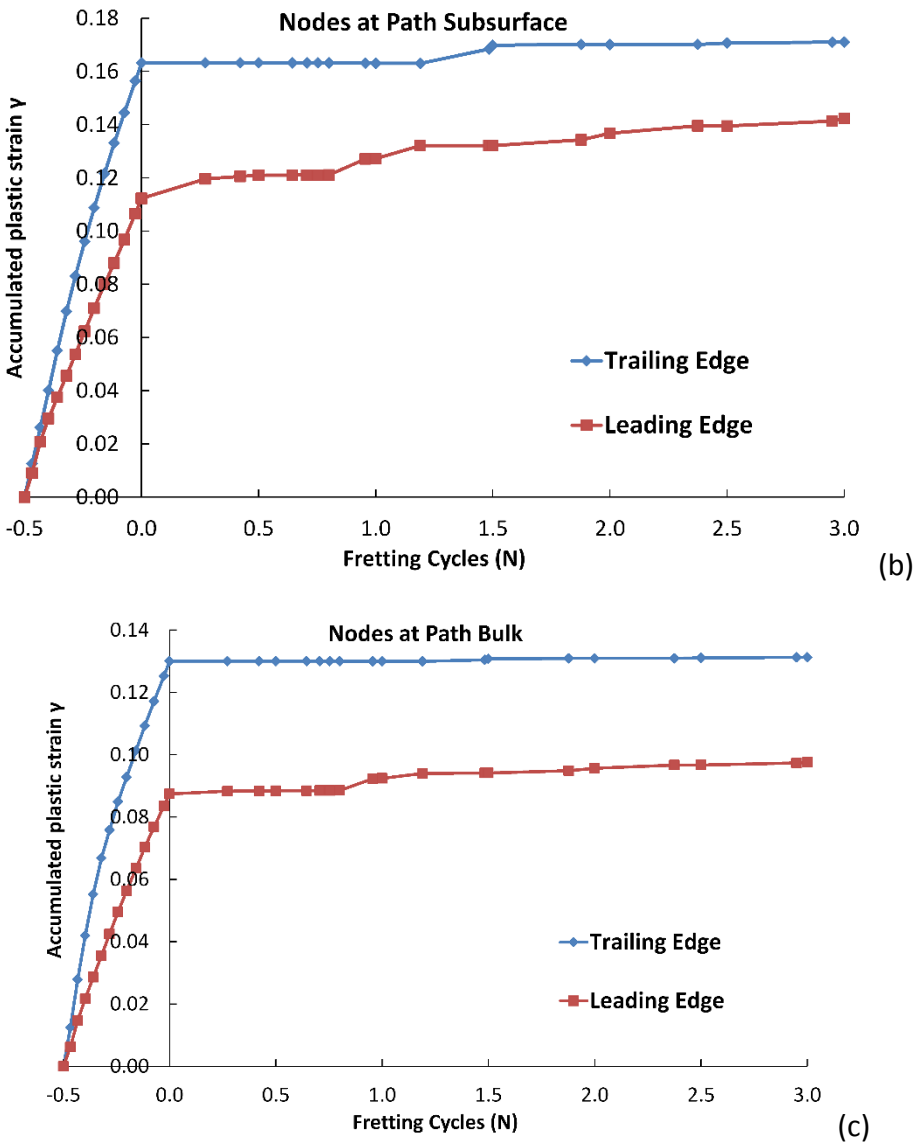


Figure 7.15. Evolution of accumulated plastic strain γ of nodes at the intersection between contact edges and (a) Path Surface, (b)Path Subsurface and (c)Path Bulk during three cycles of fretting. Results are obtained from simulations with a single crystal oriented 22.5 degree as specimen and 0.2 as the coefficient of friction between the specimen and indenter.

7.2.3.2.4 Contact shape effect

In practical engineering applications, contact edges or asperities are always naturally or manually rounded to avoid stress concentrations. In order to simulate this case and eliminate stress singularity induced by sharp edges, rounded edges are introduced in the indenter, as shown in Figure 7.16. The radius of the filleted arc is also varied to study its effect on contact performance.

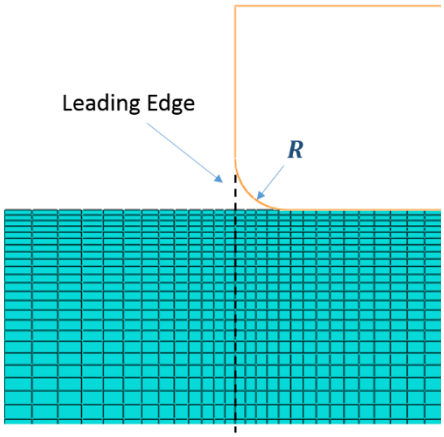
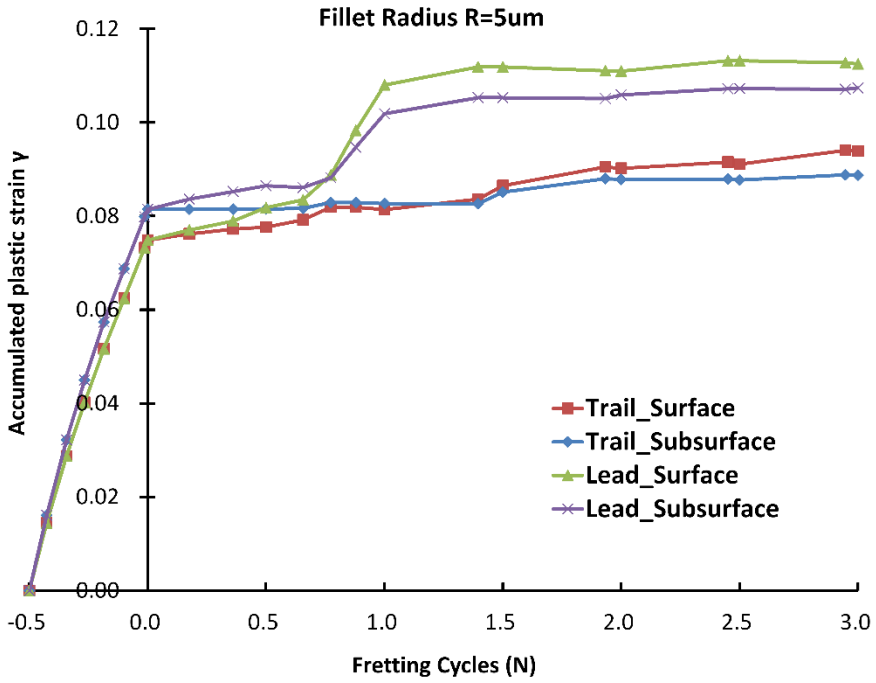
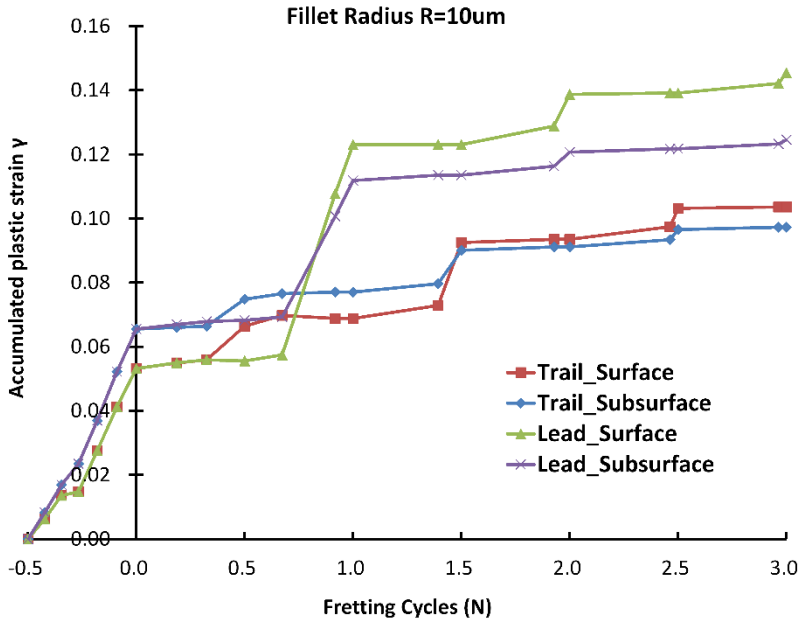


Figure 7.16. Contact between film and a rounded rectangular indenter with a fillet radius $R = 1\mu m$.

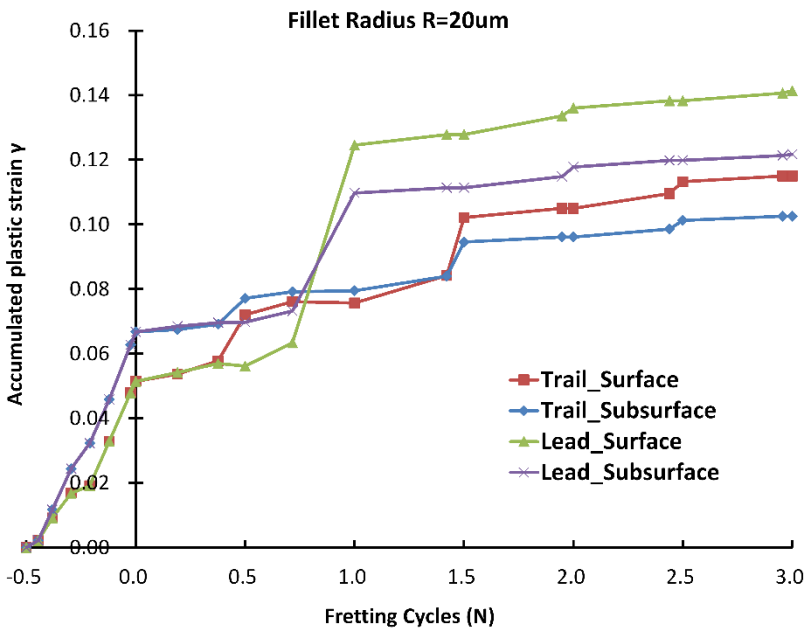
Evolution of accumulated plastic strain γ at nodes undergoing severe stress concentration at the surface and subsurface are plotted in Figure 7.17 for different shapes of indenter. The maximum sliding distance is set as $\mathrm{U} = 0.05\mu\mathrm{m}$, and the film is modelled as a single crystal oriented at 0 degrees. For a flat and rounded contact, the node near the trailing edge always accumulates more plastic strain, i.e. subjecting from more damage, during fretting process. For slider shape effect, it is observed that a larger fillet radii (i.e. a sharper slider) lead to a large accumulative plastic strain at all positions at a given stage of fretting process. A sharp slider displaces ploughs material more effectively when sliding on a specimen and thus the plastic strain induced by its sliding is observed more apparent. Besides, the accumulation of plastic strain in specimens introduced by a sharper slider is increased gradually without a sudden jump, especially compared to the results of blunt sliders. This indicates that the damage evolution of specimens introduced by a sharper slider (or indenter) is stable and thus predictable in practical applications. The extreme condition of a fillet radii indenter makes it be shaped as a cylinder that forms a single point contact at the beginning. According to the discussion on shape effect of indenter in fretting, the extreme case would help develop a physics based model for calculating corresponding plastic deformation and thus damage during a fretting process.


Fillet Radius R=5um
Accumulated plastic strain γ
0.12
0.10
0.08
0.06
0.04
0.02
0.00
-0.5
0.0
0.5
1.0
1.5
2.0
2.5
3.0
Fretting Cycles (N)
Trail_Surface
Trail_Subsurface
Lead_Surface
Lead_Subsurface

(a)


Fillet Radius R=10um
Accumulated plastic strain γ
0.16
0.14
0.12
0.10
0.08
0.06
0.04
0.02
0.00
-0.5
0.0
0.5
1.0
1.5
2.0
2.5
3.0
Fretting Cycles (N)
Trail_Surface
Trail_Subsurface
Lead_Surface
Lead_Subsurface

(b)



(c)

Figure 7.17. Evolution of accumulated plastic strain γ of nodes at the most sensitive nodes during three cycles of sliding under contact edges with radius (a) $R = 0.5\mu m$ (b) $R = 1.0\mu m$ (c) $R = 2.0\mu m$ respectively. Results are obtained from simulations with a single crystal oriented 0 degree as specimen and 0.2 as the coefficient of friction between the specimen and indenter.

7.2.4 Summary

A couple sets of sliding and fretting simulations have been conducted with crystal plasticity finite element material description used for films. The contact simulates both of a smoothed/non-smoothed flat indenter with variable coefficient of friction between indenter and specimen. The general response of a plastic material under sliding and fretting has been simulated using a reference simulation. The crystalline microstructure influence on material performance has been reported using various single and polycrystalline material models. Some remarkable conclusions have been summarized as:

- Highly localized plastic concentration has been found in both sliding and fretting simulations near contact edges. There is much less plastic strain accumulated inside contact.
- Plastic strain concentration gradually decreases from the zone near contact surface to the specimen bulk.
- Sliding and coefficient of friction affects the behaviour of material surface, especially the zone underneath contact edge, but their influence becomes weaker at nodes inside the specimen bulk.
- For a single grain microstructure, grains with 22.5 degree oriented are found to have the most favourable slip system for surface nodes. Grains with 45 degree is found to have the most favourable slip system for subsurface and bulk nodes.

- For a polycrystalline grain microstructure, plastic strain is found to be highly dependent on the specific grain underneath contact edges. Also, grains with 45 degree is found to have the most favourable slip system for the sensitive zone.
- In fretting simulations, plastic strain accumulates with cyclic process although preceding indentation process contributes a large portion of the total value. Regardless of the specimen microstructure, nodes at the trailing edge accumulate more plastic strain than those at the leading edge during fretting process. Also, nodes near leading edge tend to accumulate plastic deformation during a first half cycle (sliding left) and nodes near trailing edge tend to accumulate plastic deformation during a second half cycle (sliding right).
- In the future, more effort should be focused on the work finding the microstructure dependent damage parameter. Therefore, the damage initiation and thus the crack initiation can be directly linked to the microstructure, instead of using empirical parameters in the damage assessment.

The adaption and application of CPFE formulations on sliding and fretting problems not only help reviews the feature of its modelling method introduced in Chapter 3, but also extends the study on the global plasticity in Chapter 4 to a localized zone under contact. Besides, the work here also supplies the tangential behaviour of a specimen to the study on the normal behaviour in Chapter 5.

7.3 Sliding and Fretting Problems Solved with Discrete Dislocation Plasticity

7.3.1 Methodology

In analogy to the tension (Chapter 4) and the indentation (Chapter 5 and 6) problems, we adopt the small strain formulations of discrete dislocation plasticity developed in [139] to study contact problems undergoing indentation, sliding and fretting. Dislocation parameters of details of the dislocation calculations can be found in Chapter 3 and 4.

7.3.2 Problem definition

Calculations are conducted on films of two different thicknesses, $\mathrm{h} = 2\mu\mathrm{m}$ and $\mathrm{h} = 10\mu\mathrm{m}$ (see Figure 7.18). The first geometry considered is a rounded micro-asperity. The asperity shape is sinusoidal (that is the same indenter shape in previous simulations [3, 4]) with a variable wavelength (here taken as $\lambda = 10\mu\mathrm{m}$ or $\lambda = 20\mu\mathrm{m}$) and a fixed amplitude $\Delta = 0.5\mu\mathrm{m}$. Dislocation activity in a film of dimension $\mathrm{L} \times \mathrm{h}$ (where the length is fixed as $\mathrm{L} = 1000\ \mu\mathrm{m}$) is confined to a process window of dimension $\mathrm{l} \times \mathrm{h}$ (where the length is fixed as $\mathrm{l} = 30\ \mu\mathrm{m}$). There are three general types of simulations calculated using discrete dislocation dynamics: sinusoidal indentation calculations, sliding calculations and fretting (cyclic micro-sliding) calculations. The pure sliding and fretting computations are used to investigate the tangential behaviour of materials under contact while sinusoidal indentation

computations provide the following sliding and fretting simulations with contact, stress and dislocation structure information. Also, preceding indentation effect is illustrated by comparing the results of pure sliding/fretting and simulations with a prior indentation.

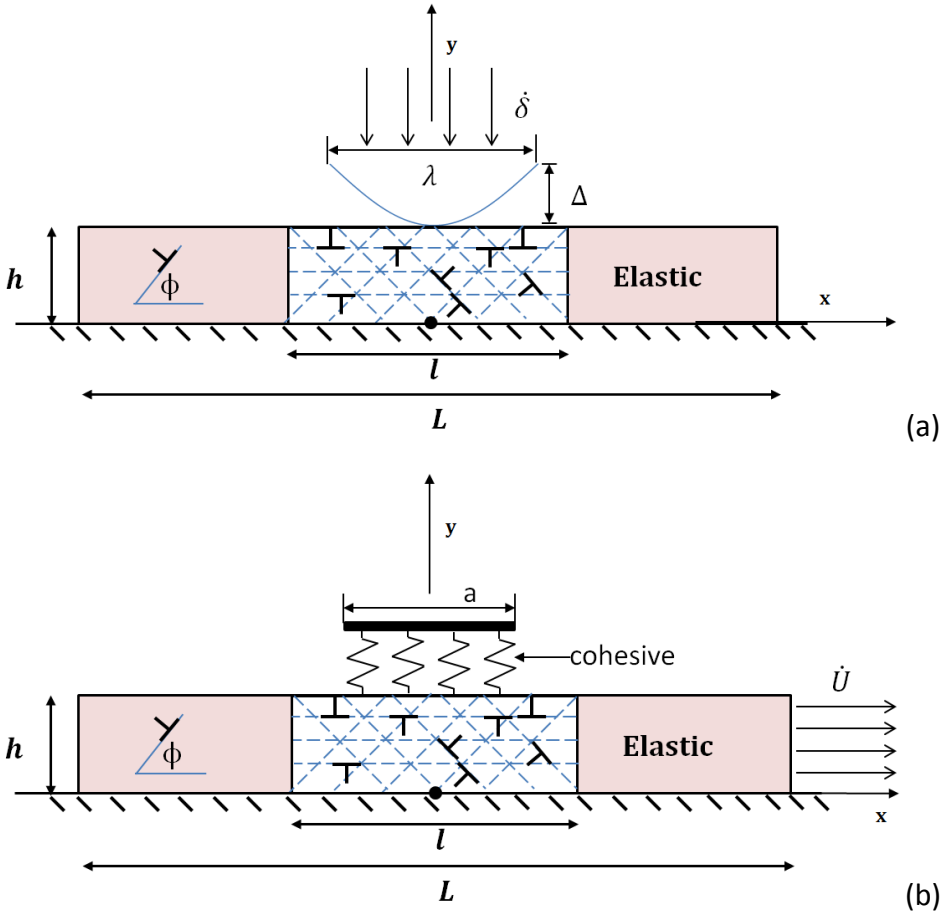


Figure 7.18. Sketches of (a) sinusoidal indentation and (b) sliding and fretting boundary value problems analysed using discrete dislocation plasticity. The origin of the coordinate system employed is marked as a filled-in circle (•) in (a) and (b).

7.3.2.1 Sinusoidal indentation

In sinusoidal indentation DDP calculations, effects of geometry changes on the momentum balance and lattice rotations are neglected. However, the contact between the indenter and the film is controlled by the displacement of the indenter, which deforms the film surface. During the indentation stage, the depth of the indentation is denoted by δ and the true contact length a is defined as the region delimited by the first and the last node where the indenter is in contact with the deformed surface.

For the bottom boundary, the boundary conditions of the sinusoidal asperity indentation problem solved using the DDP model are set as following:

$$\dot{u}_x = 0, \dot{u}_y = \dot{\delta} \text{ on } S_{contact}$$

$$\dot{u}_y = 0 \ on \ y = 0 \ \text{and} \ \dot{u}_x = 0 \ on \ x = 0$$
$$T_x = T_y = 0 \ \text{on} \ x = 0 \notin S_{contact} \tag{7.7}$$

Here, $T = \sigma_{ij} n_j$ is the surface traction on a surface with outward normal vector n_j.

The displacement of sinusoidal indenter increases from zero to a maximum indentation depth δ_{max} at the following loading rate. The

The displacement rate of sinusoidal indenter is set as:

$$\dot{u}_x = \dot{\delta} = 0.4 \ m/s \tag{7.8}$$

The maximum applied indentation depth δ_{max} is determined according the contact size required by following sliding/fretting simulations.

The total reaction force of film response to indenter penetration is computed as:

$$F = -\int_{-a/2}^{a/2} T_y(x,0)dx \tag{7.9}$$

And thus the indentation pressure p is defined by:

$$p \equiv F/a \tag{7.10}$$

where a is the end-to-end length of contact area.

The process window with dimension $l \times h$ is discretised by a finite element mesh that is highly focused towards the centre of the contact area. The finite element mesh is commonly made up of 180×100 elements with a typical mesh size of $0.01 \ \mu m$ in a sensitive zone of dimension$1\mu m \times 1\mu m$. A small time increment $\Delta t = 0.5 \ ns$ is adopted in order to resolve the dislocations' activity.

7.3.2.2 Sliding

In sliding calculations, the contact between sinusoidal asperity and specimen is modelled via a cohesive zone between the indenter and the crystalline surface. The application of cohesive zone model A cohesive zone mode l(CZM) is commonly applied in a fracture problem analysis [289]. Cohesive zone model is considered as the most useful method [290]for modelling contact behavior between surfaces, e.g. [291, 292]. Herein, we apply a cohesive zone mode on the contact between indenter and specimen to simulate the shear traction resistance within the contact.

The contacting zone is of length a and the relation between local shear tractions and displacements is given by:

$$T_t = \begin{cases} -\tau_{max} \dfrac{\Delta U}{\delta_t}, if \ |\Delta U| < \delta_t \\ -\tau_{max} sign(\Delta U), if \ |\Delta U| > \delta_t \end{cases} \tag{7.11}$$

where $\Delta t = u_1(x,h)$ is the tangential displacement jump across the cohesive surface, and T_t represents the shear traction. Traction free boundary conditions are applied on the surface outside of the contact region:

$$T_x = T_y = 0 \text{ on } x = 0 \notin S_{contact} \text{ and } y = h \tag{7.12}$$

The maximum cohesive strength τ_{max} is set to be $\tau_{max} = 300MPa$ and the threshold displacement jump is $\delta_t = 0.5nm$. Those values are chosen to be the same as those used in Ref. [3]. Regarding the cohesive relation between the shear traction and the displacement jump, it should be noted that Deshpande et al. [4] have applied another equation to incorporate a softening cohesive law:

$$T_t = -\sqrt{e}\tau_{max}\frac{\Delta U}{\delta t}\exp(-\frac{\Delta U^2}{2\delta_t^2}) \tag{7.13}$$

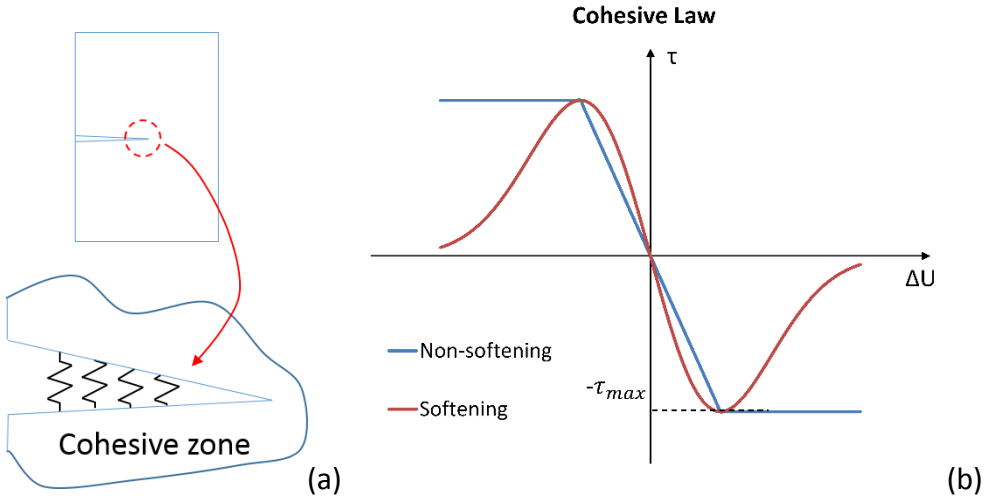


Figure 7.19. Sketches of (a) a cohesive zone model (b) the softening and non-softening cohesive laws prescribing the relationship between the shear traction and the displacement jump at the nodes belonging to the contact partition. The non-softening relation is adopted in sliding and fretting calculations.

The softening and non-softening cohesive shear-displacement laws are plotted in Figure 7.19. However, since it was found that the onset of material sliding is not strongly dependent upon the form of cohesive law, the non-softening form of the cohesive law is used in this thesis.

The displacement rates,

$$\dot{U}_x = U, \dot{U}_y = 0 \tag{7.14}$$

are imposed on the specimen boundaries $x = \pm L/2$ and $y = 0$ to simulate the relative sliding of the contact surface with the magnitude $\dot{U}/a = 10^4 s^{-1}$. It is worth noticing that the sliding configuration simulates the indenter moving towards the left (in the negative x-direction). The averaged shear stress τ in the contact is given by:

$$\tau = -\frac{1}{a}\int_{-a/2}^{a/2} T_x(x,h)dx \tag{7.15}$$

and, correspondingly, the friction coefficient μ is defined as:

$$\mu = \tau/p \tag{7.16}$$

A sinusoidal indentation simulation is carried out to evaluate the relation between the contact area and the applied normal load. Based on a certain value of contact area obtained in the preceding indentation simulation,

In one set of sliding calculations, an independent “pure slide” simulation of the initiation of sliding, as proposed in paper [3], is conducted using the predefined traction-displacement relation (eq.(7.13)) in the contact portion; the specimen is characterised by a stress and dislocation free status at eh beginning of the simulations. However, these calculations are only capable of approximately representing the sliding phenomenon to the traction resistance introduced by the cohesive zone model, since the effect of material deformation on the contact surface due to the normal load has not been taken into consideration in this set sliding calculations.

In the other set of sliding calculations, the simulations are designed to capture the characteristics of sliding explicitly accounting for the contribution of the applied normal load. The sinusoidal indentation simulation is beforehand carried out to evaluate the relation between the contact area and the applied normal load; then pure sliding calculations are performed with the contact size obtained at the end of corresponding indentations. In fact, in these simulations sliding is also initiated with the stress and dislocation structure inherited from the application of the normal load during the indentation process. Results from these two sets of sliding simulations will be compared.

7.3.2.3 Fretting

In fretting simulations, the geometry of the specimens and the cohesive relation between specimen and indenter is the same as the one used to solve the sliding problem. However, in order to simulate the cyclic micro-sliding motion representative of fretting conditions, the displacements are inverted and the end of each stroke. Micro-sliding simulations are sub-divided into half-cycles, with stresses and dislocation structures evolution preserved and recorded throughout the simulations. A Bash Shell script has been developed to conduct fretting calculations automatically. Loading rates are kept as uniform to avoid rate-dependent effects. As for the sliding simulations, fretting cyclic calculations are performed with and without accounting for the effect of the initial indentation process on the dislocation structure before sliding.

7.3.3 Results

Numerical results are categorized as sinusoidal asperity indentation, nano-sliding and nano-fretting and they are reported in the following sub-sections. The sinusoidal

asperity indentation produces the initial stress field, contact size and, thus, indentation pressure to be used in the following sliding and fretting process. Contact size and dislocation source density effects are addressed in the nano-sliding section. Fretting results focus on the evolution of film performance within the contact due to the repeated application of the load, including shear stress, dislocation densities and surface profile variation.

7.3.3.1 Sinusoidal Asperity Indentation

Indentation pressure p versus contact length a is plotted in Figure 7.20 (a) and b for indentation of films of thickness $h = 10\ \mu m$ and $h = 2\ \mu m$ by rigid sinusoidal asperities with amplitude $\Delta = 0.5\ \mu m$ and wavelengths $\lambda = 20\ \mu m$ and $\lambda = 10\ \mu m$ respectively. These curves are obtained by calculating the indentation pressure as a function of the applied indentation depth $p(\delta) = F/a$ and of the evolution of the contact area with the applied indentation depth $a(\delta)$. For the thicker film, $h = 10\ \mu m$, the indentation pressure curve initially increases linearly with the contact length a, and then levels off towards a stable value after a pressure peak. For the thinner film, $h = 2\ \mu m$, the indentation pressure consistently increases with the contact area as the plastic flow under the indenter has been constrained by the presence of the rigid substrate, which is "felt" by the indenter much sooner than for the thicker film. Also, at a certain contact length, indentation pressure of film $h = 2\ \mu m$ is found to be considerably higher than the response of film $h = 10\ \mu m$. The sharpness effect of sinusoidal indenter is investigated by increasing the ratio Δ/λ. The indentation pressure is found to increase with increasing sharpness of asperity for $h = 10\ \mu m$ film. This is attributed to the fact that a sharper asperity needs to penetrate more into specimen to achieve the same contact length. However, this phenomenon is not that apparent in $h = 2\ \mu m$ film . This can also be explained by the fact that for the thin film the volume of material that can undergo plastic flow is limited due to the presence of the rigid substrate. This leads to material pile-up at contact surface when thickness of film is relatively small, while material sink-in is observed when the thickness of the film is relatively large. Thus, the effect of asperity sharpness on indentation pressure is then relieved.

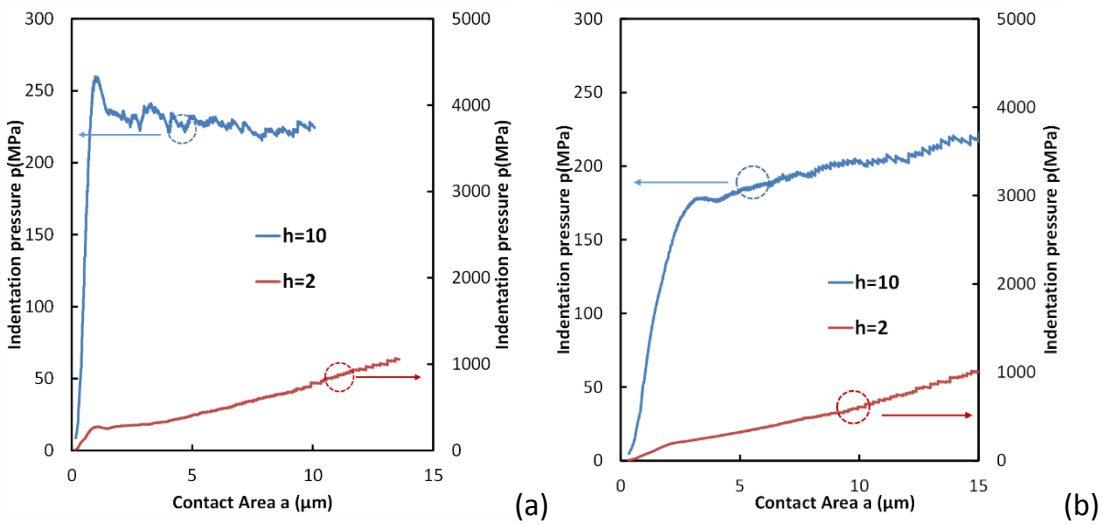


Figure 7.20. Indentation pressure *p* versus contact length for sinusoidal asperity indentation with amplitude $\Delta = 0.5\ \mu m$ and wavelengths (a) $\lambda = 20\ \mu m$ and (b) $\lambda = 10\ \mu m$. Results are shown for $h = 10\ \mu m$ and $h = 2\ \mu m$ films.

7.3.3.2 Sliding

7.3.3.2.1 Contact size effect

The boundary value problem sketched in Figure 7.18 (b) is analysed for an initially dislocation-free crystal, i.e. pure sliding simulation is conducted. Curves of shear stress τ versus applied sliding displacement U are plotted in Figure 7.21 (a) for $h = 10\ \mu m$ film for different predefined values of contact length a. Curves of shear stress τ (*i.e.* defined as averaged along contact, see eq.(7.15)) firstly increase approximately linearly with increasing applied sliding displacement U, and then approach a plateau, whose value is shown to be strongly dependent on the contact length a. In general, large contact size leads to a smaller value of stable shear stress. For the smallest contact size selected here, $a = 0.04\ \mu m$ no dislocation is nucleated before shear stress attains the cohesive strength $\tau_{max} = 300MPa$.

The average shear stress over a specific sliding distance (*i.e.* averaged in terms of simulation time) range , τ_{ave} , is defined as the average value of shear stress τ calculated over the indenter displacement range $0.015\ \mu m \leq U \leq 0.020\ \mu m$. This range of sliding distance U is selected to obtain the average shear stress as the evolution curves of shear stress of different contact sizes have already achieve a relatively stable plateau. Also, this range is identical as the previous calculations[3]. For a larger contact size, the shear stress τ has achieved a stable value of plateau, *i.e.* no longer depends on the applied sliding displacement. In order to exclude the randomness effect of dislocation source and obstacle distribution [3], simulations that use three realizations with identical density values are conducted to obtain a mean value. Curves of averaged shear stress τ_{ave} against contact length a are plotted in Figure 7.21(b) for $h = 10\ \mu m$ and $h = 2\ \mu m$. It is found that the average shear stress is insensitive to film thickness, at least for the range calculated here. The insensitivity is attributed to the phenomenon that the plasticity zone

induced by pure sliding is rather shallow, usually less than $0.5\mu m$. Therefore, the plastic response of contact is not affected much by the thickness of films.

The qualitative features of the results displayed in Figure 7.21 (b) shows similar trends to those found in the work by Deshpande and co-workers (see Refs. [4] and [3]). There are three regimes of average shear stress τ_{ave}. For large contacts, *e.g.* $a = 10\ \mu m$, τ_{ave} is approximately equal to the shear flow strength (that is determined by the source strength). For a small contact size, *e.g.* $a = 0.04\ \mu m$, τ_{ave} attains the cohesive strength τ_{max}. In the intermediate regime, τ_{ave} decreases as a function of the square root of a. This relation between average shear stress τ_{ave} and contact size a is found to be similar as calculations[3] is written in the form as:

$$\tau_{ave} = Aa^{-\frac{1}{2}} + B \tag{7.17}$$

In eq.(7.17), A and B are fitting parameters. This contact size effect is not only caused by the strain gradient near the contact introduced by geometrically necessary dislocations, but also as a result of the discrete characteristics of dislocations [3].

The dependence of shear stress on the size of the contact area is consistent with experimental observations. For the regime of large contact size, the average shear stress value is similar to the experimental results obtained using a surface force apparatus [293]. For the regime of small contact size, a larger value of shear stress is observed in experiments performed using atomic force microscopy[294]. For the transition regime, recent experimental measurements [295] confirmed the square root inverse dependence between average shear stress and contact area.

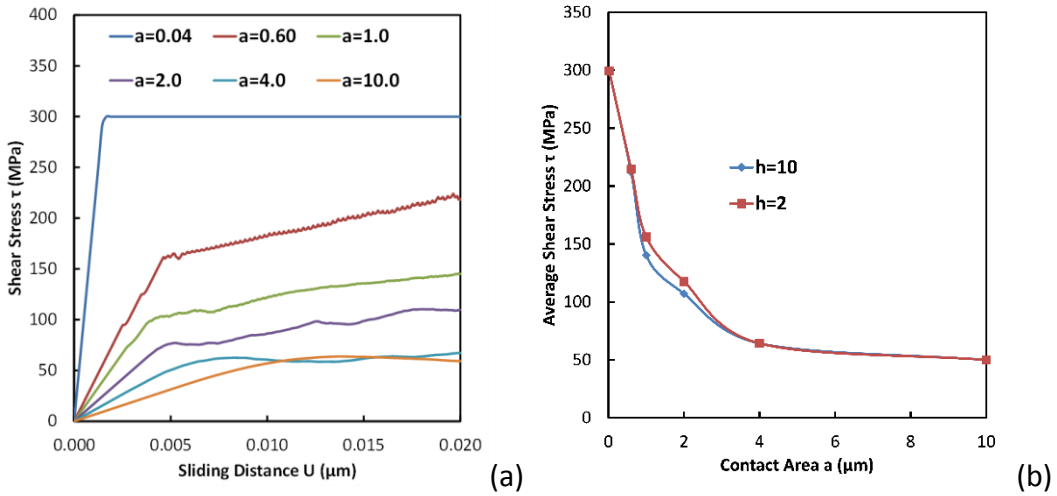


Figure 7.21. (a) shear stress τ versus sliding displacement U curves for $h = 10\ \mu m$ film for selected values of contact length a. (b) average stress stress τ_{ave} versus contact length a for two values of film thickness h. These results are obtained from sliding simualtions with no prior indentation.

The values of the coefficient of friction $\mu = \tau/p$ for different values of contact length a versus sliding displacement U and for $h = 10\ \mu m$ are reported in Figure 7.22. The indentation pressure p is obtained by the initial sinusoidal asperity

indentation with indenter shape $\Delta = 0.5\ \mu m$ and wavelength $\lambda = 20\ \mu m$. For all contact sizes, coefficients of friction μ increases with increasing sliding distance until it reaches a steady-state when sliding distance is greater than about $U = 5\ nm$. Looking at contact size effect, coefficients of friction increase with decreasing contact size.

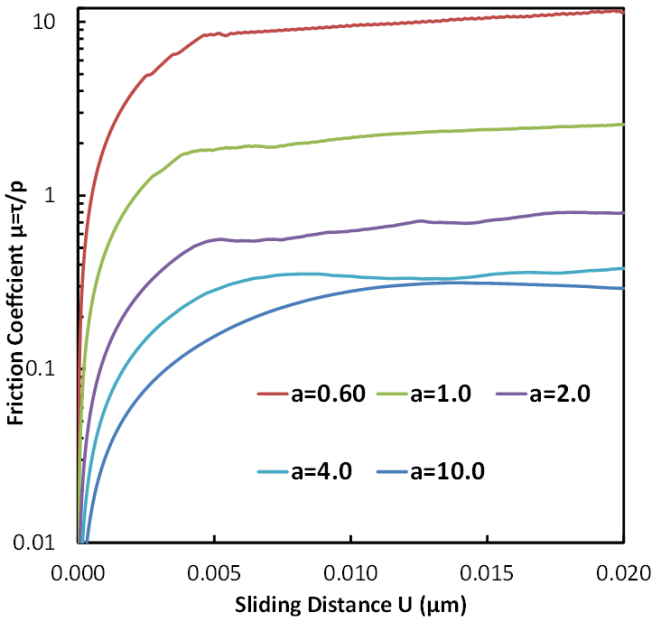


Figure 7.22. The coefficient of friction μ versus sliding displacement U for a $h = 10\ \mu m$ film. Indentation pressure p is from the sinusoidal asperity indentation with $\Delta = 0.5\ \mu m$and wavelength $\lambda = 20\ \mu m$. The sliding calculations are carried out for an initially stress and dislocation-free crystal, while the pressure p for each a is the value needed to achieve this contact length under indentation.

7.3.3.2.2 Rate effects

Shear stress τ evolution versus applied sliding displacement U is plotted in Figure 7.23 for film of thickness $h = 10\ \mu m$ with different values of contact length under different sliding rates. The loading rate is evaluated by the ratio $\dot{U}/a$. It appears that the shear stress response under a sufficient small loading rate ($\dot{U}/a < 10^4 s^{-1}$) is not affected by the rate. However, shear stress increases at a given sliding displacement with a higher loading rate. It should be noted that the loading effect always begins to act on the shear response after the first nucleation of dislocations. The rate dependency is explained as that dislocations are not allowed enough time to achieve the most stable pinning or gliding status when an applied loading rate is relatively high. Thus, the shear response of material is hardened. In order to eliminate this loading rate influence, a relatively low loading rate $\dot{U}/a = 10^4 s^{-1}$ is generally adopted in following sliding and fretting calculations.

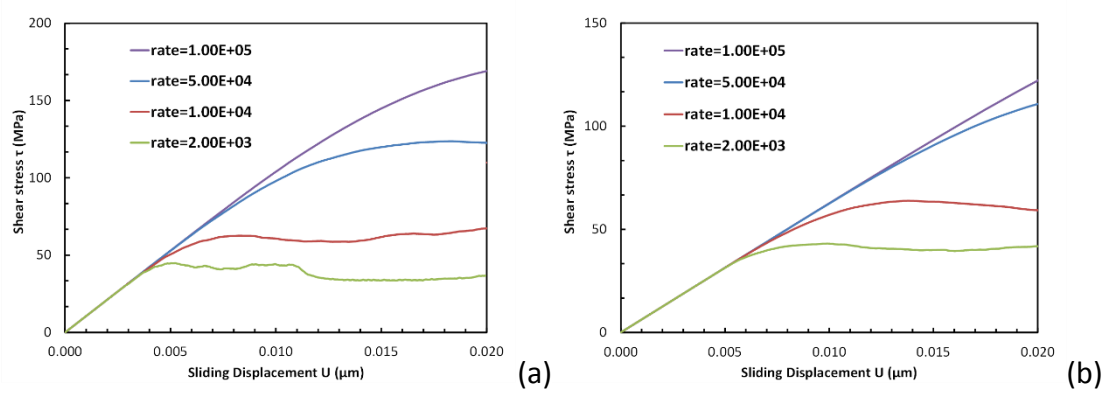
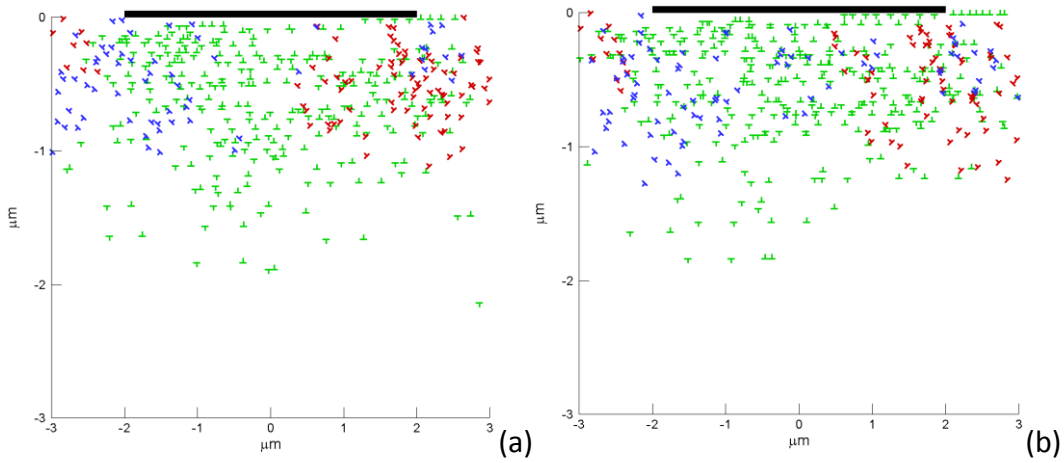


Figure 7.23. The shear stress τ versus sliding displacement U curves for $h = 10\ \mu m$ with contact length (a) $a = 4.0\ \mu m$ and (b) $a = 10.0\ \mu m$. Results are obtained from pure sliding simualtions with different loading rates.

The dislocation structures of a $h = 10\ \mu m$ film with contact size $a = 4.0\ \mu m$ but under different loading rates are plotted in Figure 7.24. Results are obtained at the end of a sliding process $U = 0.20\ \mu m$. It is clearly seen that loading rate affects the distrbition of dislocations, and thus the shear stress response. An optimum sliding rate is considered herein to obtain a balance of quasi-static response and computation efficiency. The creterieon of optimum sliding for a sliding calculation with specific contact size claims that it is the most fast loading rate that allow shear stress response of contact to be independent of loading rate. Seen from figures, in order to obtain an optimum loading rate, results achieve a stable solution when dislocation pairs have backwardly glided with a sufficiently large distance from their nucleation site. Besides, the optimum loading rate is able to allow a sufficient number of dislocation dipoles nucleating.



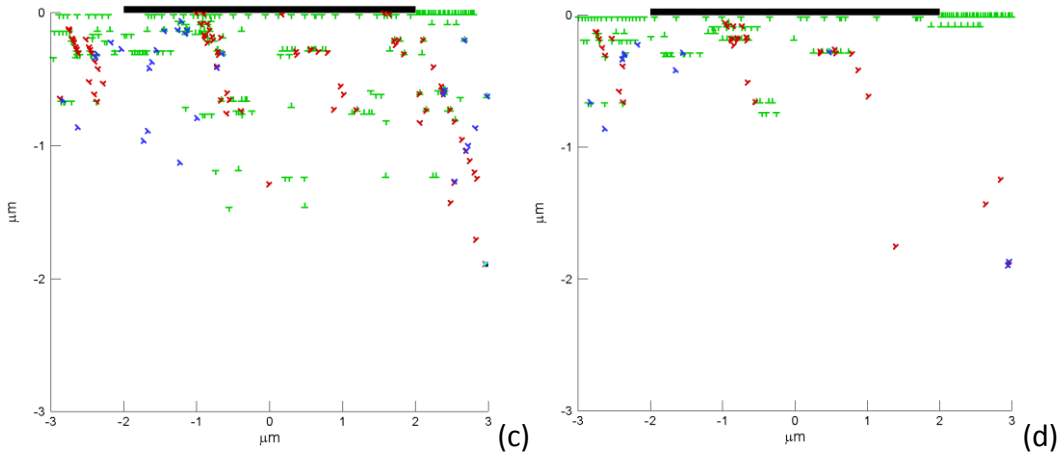


Figure 7.24. Dislocation structure for $h = 10\ \mu m$ film with the contact length $a = 4.0\ \mu m$ and loading rate (a) $\dot{U}/a = 1e5s^{-1}$, (b) $\dot{U}/a = 0.5e5s^{-1}$ (c) $\dot{U}/a = 0.1e5s^{-1}$ and (d) $\dot{U}/a = 0.05e5s^{-1}$.

7.3.3.2.3 Dislocaiton structure evolution

Dislocation structure evolution in a film of thickness $h = 10\ \mu m$ is plotted in Figure 7.25 under pure sliding conditions and contact size $a = 2.0\ \mu m$. Results are obtained for different applied sliding distance U, up to $U = 0.02\ \mu m$. From the evolution of the dislocation struture, the actitvation order of potention slip systems is obtained. The horizontal slip system $\phi^{(\alpha)} = 0$ is the most favourable one to be activated, following by the inclined slip systems $\phi^{(\alpha)} = \pm 45°$. Besides, the contribution of dislocations to plastic flow appears to depend upon their slip systems. For dislocations nucleated on the horizontal slip system $\phi^{(\alpha)} = 0$, their glide and piling up mainly leads to the rectangular plastic zone underneath the contact. For dislocations nucleated on the inclined slip systems $\phi^{(\alpha)} = \pm 45°$, their gliding from the contact edge to the bulk of the specimen and piling up results in the slip pattern that the specimens experience near the contact edges. This pattern is potentially linked to micro crack nulceation by indicating the initial micro crack orientation, the crack initiation creterion and damge calculations (due to the fact the number of dislocations monotonically increases with the applied sling distance, as will be shown later on). Furthermore, the number of dislocations piling up near the traling edge is found to be larger than the proximity of the leading edge.

U=+8nm U=+12nm

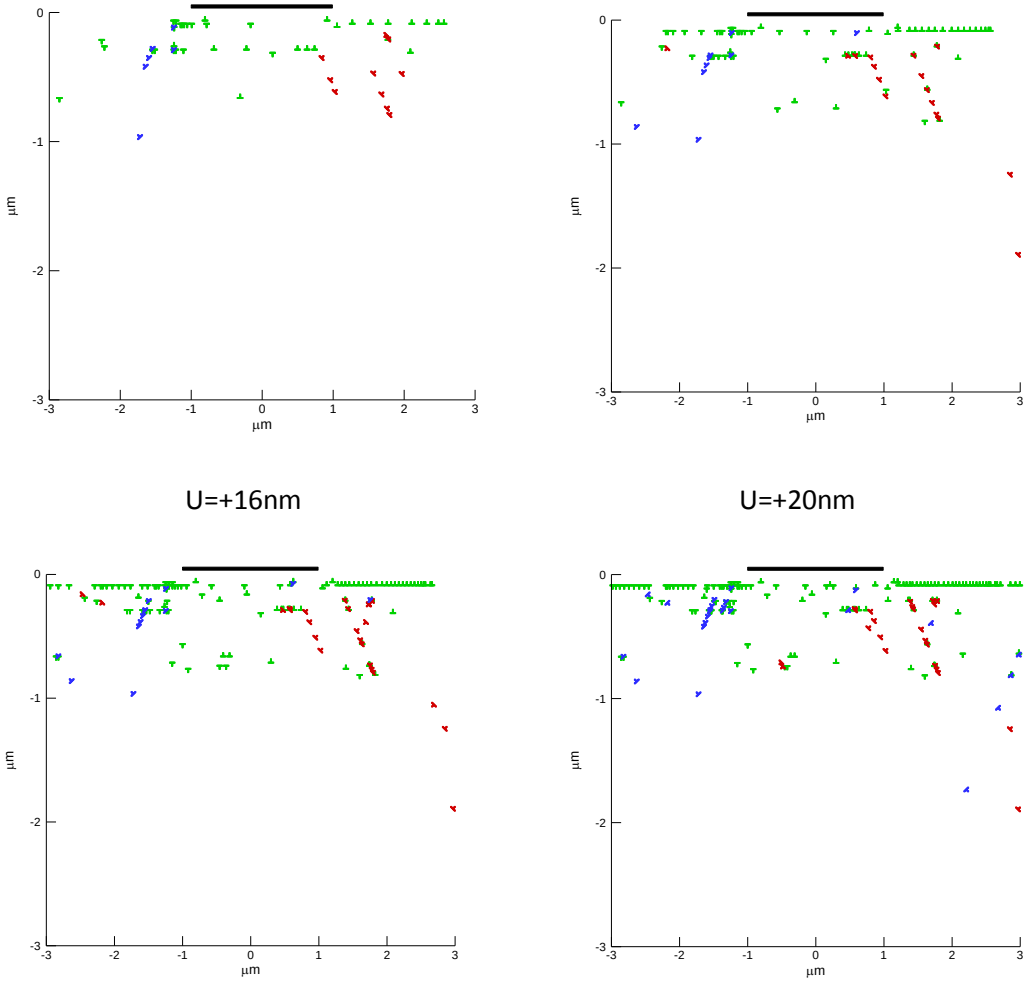


Figure 7.25. The dislocation structure in a $h = 10\ \mu m$ film at different applied sliding displacement for pure sliding. The flat contact length $a = 2.0\ \mu m$ is illustrated by a black filled bar.

Dislocation density evolution versus applied sliding distance is plotted in Figure 7.26 with different slip systems. Results are from pure sliding simulations. Dislocation densities are increased with the increasing applied sliding distance *U* for both horizontal and inclined slip systems. However, the increasing rate of dislocation gliding on the horizontal slip system is found to be significantly higher than the inclined slip systems. This indicates that the plastic deformation underneath contact (which is caused by dislocations gliding on the horizontal slip systems) dissipates much more energy (that is input from the relative sliding of indenter) than the plastic deformation along the inclined slip systems.

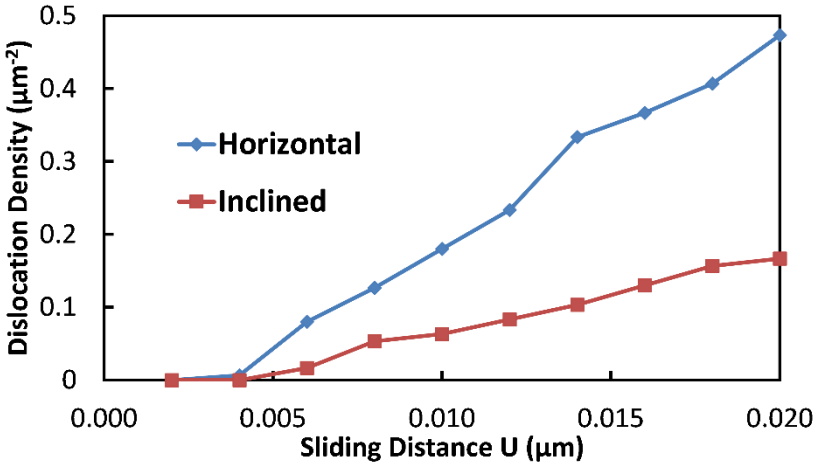


Figure 7.26. Dislocation density evolution in $h = 10\ \mu m$ film at different applied sliding displacement for pure sliding. The flat contact length is $a = 2.0\ \mu m$, and results are shown for dislocation gliding on different slip systems.

7.3.3.2.4 Dislocation source density effect

The microstructure of the films under investigation is varied by changing dislocation source and obstacle density in order to investigate the dependence of source density effect on the shear response of films. Microstructure of different realizations are tabulated in Table 7.2.

Table 7.2. Parameters for realizing microstructure with different average source spacing $d_{avg.}$ in $h = 10\ \mu m$ film. The obstacle density is varied with the source density $\rho_{obs} = \rho_{nuc}$ in this set of calculations.

# source /plane	# obstacle /plane	$\rho_{nuc}\ (\mu m^{-2})$	$\rho_{obs}\ (\mu m^{-2})$
1	1	9.71	9.71
2	2	19.41	19.41
3	3	29.12	29.12
5	5	48.53	48.53
7	7	67.94	67.94

The shear stresses τ averaged along the contact between an equivalent asperity characterised by a contact size $a = 4.0\ \mu m$ and a $h = 10\ \mu m$ film with various microstructural features (in terms of source densities) are illustrated in Figure 7.27. The general shape of the shear stress response curve is observed to be consistent with both experimental results [293-295] and simulations [1, 4]. Of more significance, dislocation source density is found to have a strong effect on the shear stress response of films. A smaller value of source density is able to delay the onset of sliding between asperity and film. Meanwhile, it also hardens the shear response of films in terms of the shear stress plateau. Both phenomena are attributed to the well-known dislocation source starvation effect. Local stress would further increase when there is no dislocation nucleation sources available locally. Therefore, films are hardened by a source-limited strengthening that is a universal observation in discrete dislocation

simulations under various loading conditions [1, 258, 296]. Results of sliding simulations show that a source density value $\rho_{nuc} = 48.53\ \mu m^{-2}$ is able to saturate a $h = 10\ \mu m$ film in contact with $a = 4.0\ \mu m$ indenter

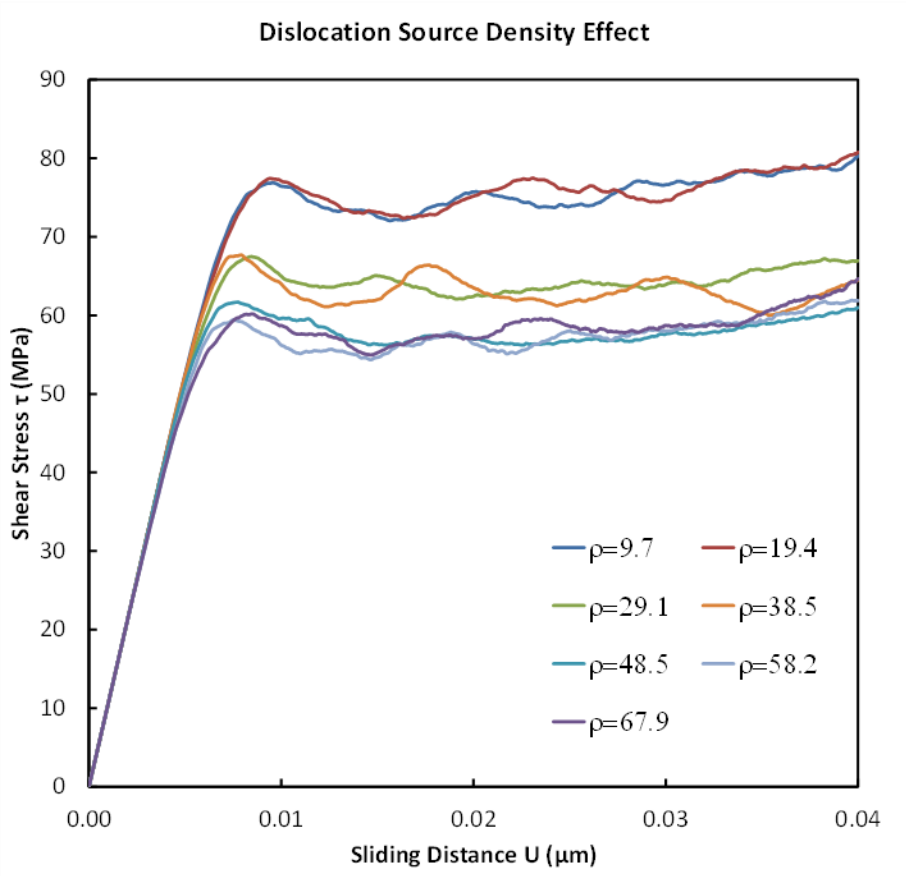


Figure 7.27. Shear stress τ versus sliding displacement U curves for a $h = 10\ \mu m$ film in contact with an asperity (contact size $a = 4.0\ \mu m$) for selected values of dislocation source densities, ρ.

The averaged friction stress τ_{ave} is calculated as the average value of τ over the range $0.015\ \mu m \leq U \leq 0.02\ \mu m$ and $0.035\mu m \leq U \leq 0.040\ \mu m$. Separate ranges of sliding distance are considered to obtain more information along the shear stress evolution curves and thus exclude numerical errors. For contact size $a = 4.0\ \mu m$, τ has attained a steady-state value for displacements in both of ranges. The $\tau - U$ curves depend on the specific distribution of dislocation sources and obstacles and not only just on the densities [3]. Here, calculations were carried out for three realizations, and the values obtained for these realizations differed by less than 5 % in all cases and the values of τ_{ave} reported are mean values. The averaged friction stress against averaged dislocation source spacing is plotted in Figure 7.28. A linear relation between the average shear stress and the average source spacing is obtained when the source density does not saturate the film, i.e. $\rho_{nuc} < 48.53\ \mu m^{-2}$ nor too small $\rho_{nuc} > 19.41\ \mu m^{-2}$. Thus the average shear stress for the contact size $a = 4.0\ \mu m$ can be given as:

$$\tau_{ave} = \frac{A}{\sqrt{\rho_{nuc}}} + \tau_0 \tag{7.18}$$

where A is a stress proportionality constant which depends on boundary conditions and material properties, and $\tau_0 = 48MPa$ approaches the dislocation nucleation strength. The best fit result of the relation of shear stress on average source spacing is as $A = 218.4\ \mathrm{MPa/\mu m}$ and $\tau_0 = 48MPa$ with coefficient of determination $R^2 = 0.9804$.

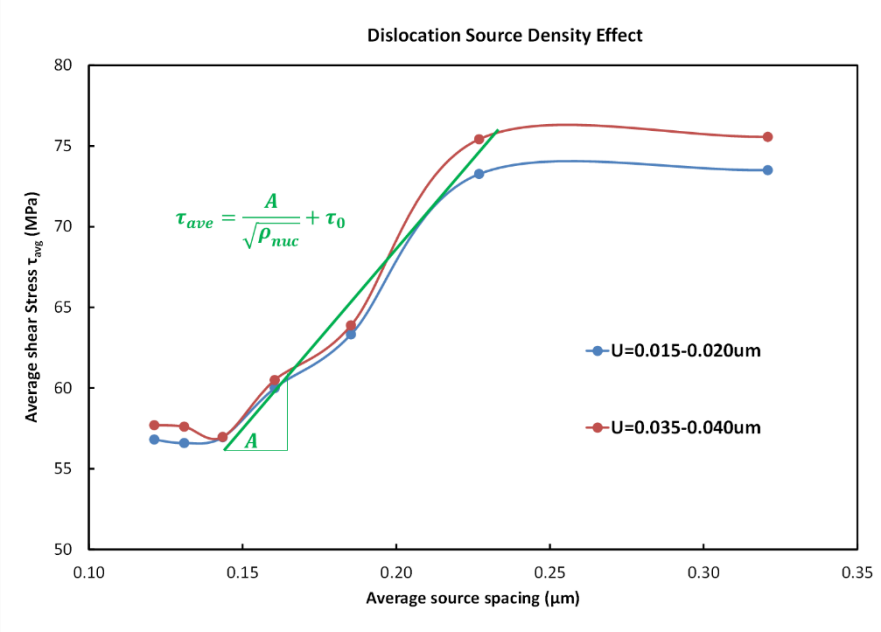


Figure 7.28. The average shear stress τ_{ave} versus average source spacing $d_{avg.}$ curves for a $h = 10\ \mu m$ film with contact size $a = 4.0\ \mu m$ for selected values of dislocation source densities.

The values of the coefficient of friction μ calculated for a contact between an equivalent asperity of nominal contact sizes $a = 4\ \mu m$ and $a = 8\ \mu m$ and a $h = 10\ \mu m$ film characterised by different microstructural features are illustrated in Figure 7.29. It is generally found that the coefficient of friction along the contact is independent of dislocation source density, at least for the contact sizes considered here. Indentation pressure of films is, in actual fact, also increased when there is a source limited strengthening present. Besides, the values of the coefficient of friction along a smaller contact size are systematically higher compared to the values obtained from a larger contact size. This is consistent with simulations carried out in Ref. [3], and it is attributed to the predominant influence of the shear-displacement relation when the contact size is relatively small. Results with contact size $a = 8.0\ \mu m$ are reported in Appendix IX.

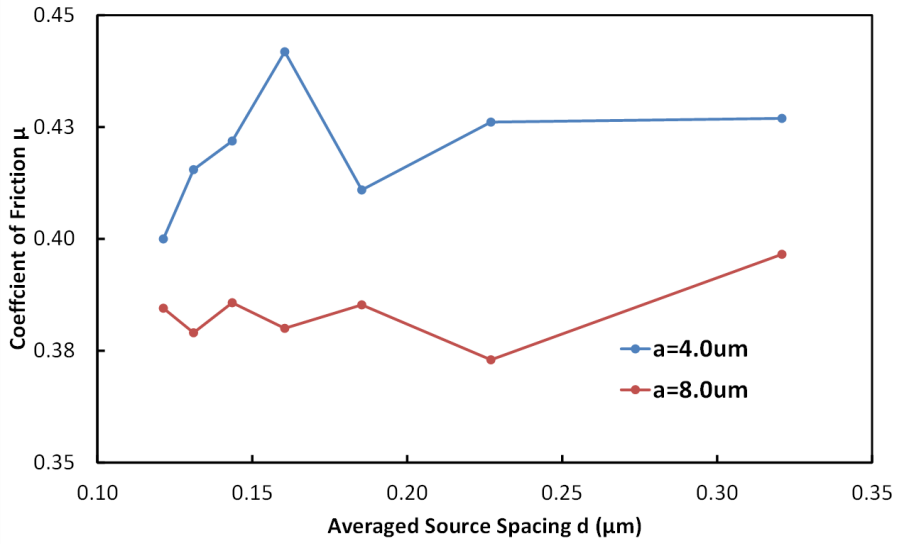


Figure 7.29. The coefficients of friction μ versus the average source spacing $d_{avg.}$; curves for a $h = 10\ \mu m$ film with contact sizes $a = 4.0\ \mu m$ and $a = 8.0\ \mu m$ for selected values of dislocation source densities.

Figure 7.30 and Figure 7.31 show dislocation structures in a $h = 10\ \mu m$ film with a low and high source density for $a = 4.0\ \mu m$ and $a = 8.0\ \mu m$ respectively. Results are obtained at the instant when the asperity slides to the maximum stroke, $U = 0.040\ \mu m$ for $a = 4.0\ \mu m$ and $U = 0.080\ \mu m$ for $a = 8.0\ \mu m$. The difference is clearly observed in dislocation structures between films with a low and high source density. In particular, a larger number of dislocations piling up at the surface and subsurface along horizontal slip systems are obtained in a film with higher source density. Thus the plastic flow induced by these dislocations softens the shear stress response of the film. The source limit strengthening in sliding problem is therefore explained using the dislocation structure in the films under investigation.

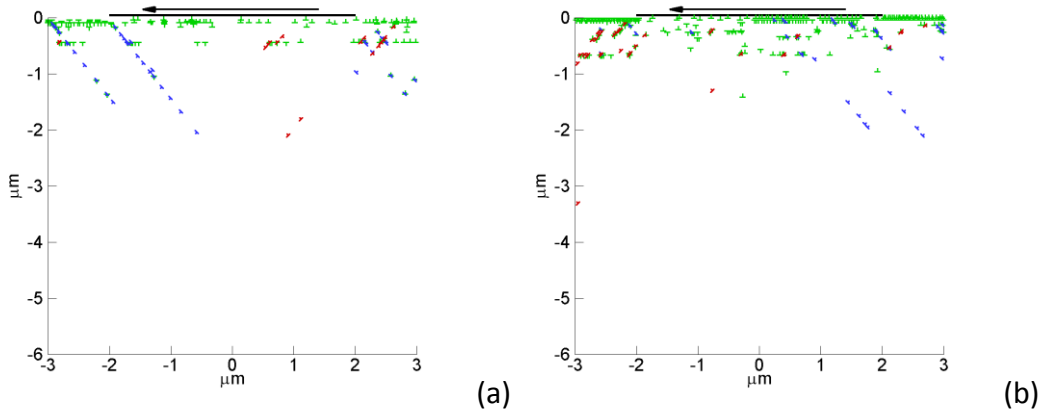


Figure 7.30. Dislocation structure in a $h = 10\ \mu m$ film for $a = 4.0\ \mu m$. Results are obtained for films with (a) $\rho_{nuc} = 9.71\ \mu m^{-2}$ and (b) $\rho_{nuc} = 97.18\ \mu m^{-2}$ at the instant when the sliding displacement is $U = 0.04\ \mu m$.

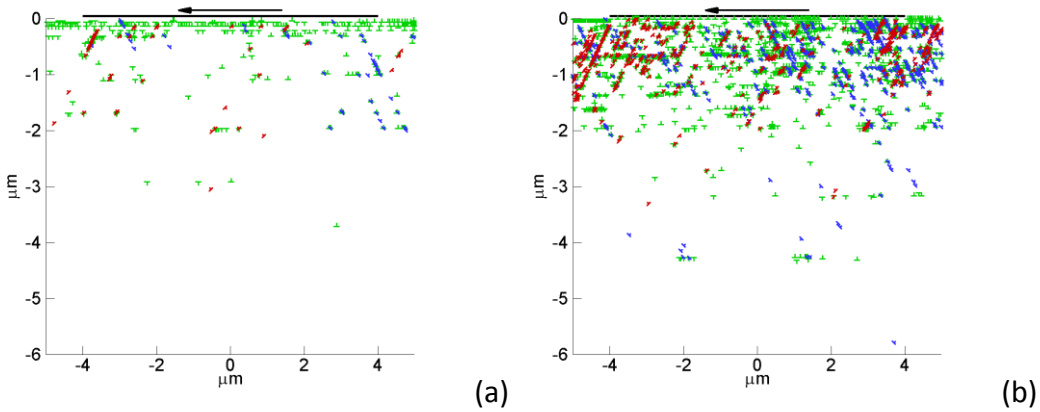


Figure 7.31. Dislocation structure in a $h = 10\ \mu m$ film for $a = 8.0\ \mu m$ size. Results are obtained for films with (a) $\rho_{nuc} = 9.71\ \mu m^{-2}$ and (b) $\rho_{nuc} = 97.18\ \mu m^{-2}$ at the instant when the sliding displacement $U = 0.08$ μm.

Obstacles that are predefined along slip systems also affect the shear stress response of thin films under contact loading. A large value of obstacle density leads to a stronger response. Detailed results showing this effect are reported in Appendix X.

7.3.3.2.5 Initial indentation effect

The influence of dislocation structure and stress induced by the initial sinusoidal asperity indentation process and applied normal load is investigated by simulating sliding after indentation has taken place and an initial dislocation activity has taken place.

The shear stress τ versus applied sliding distance U curves for selected values of contact length size a are plotted in Figure 7.32 (a) for $h = 10\ \mu m$ film with an initial indentation by a $\lambda = 20\ \mu m$ sinusoidal asperity. The shear stress response is similar to the results of pure sliding. The shear stress tends to a steady state value when the contact size is large, but there is no distinct stable value for small contact sizes. Also, the dislocation nucleation source starvation zone of shear stress τ is not found in sliding with preceding indentation simulations for small contacts, see Figure 7.32 (b). Compared to the pure sliding results, the shear stress predicted in sliding with preceding indentation is observed to yield smaller values of shear stresses, especially for large contacts. The initial indentation has induced a stress field and existing dislocation structure that helps easier nucleation and gliding for dislocations, especially for dislocations along the $\Phi^{(\alpha)} = 45°$ slip systems.

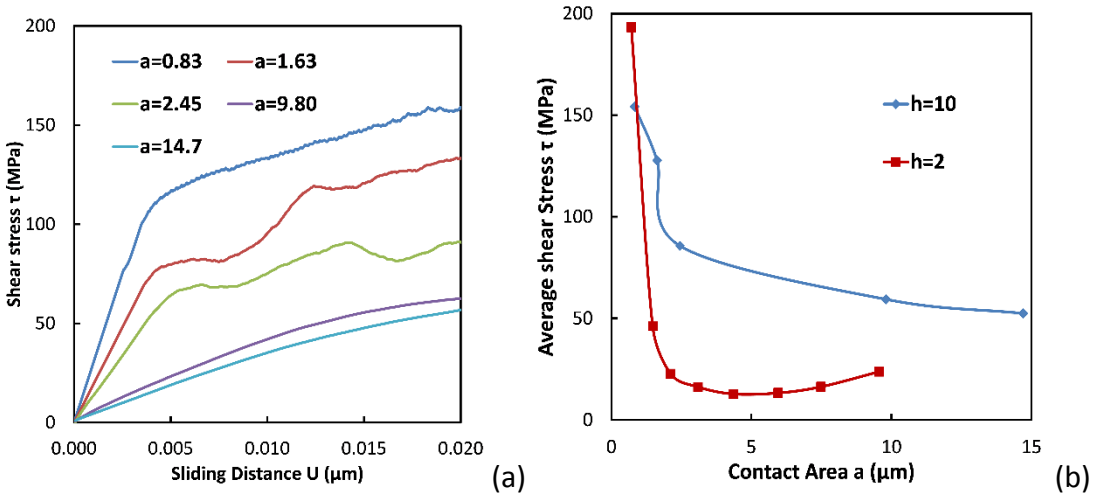


Figure 7.32. Effect of preceding indentation on frictional response. (a) Shear stress versus displacement response for a $h = 10\ \mu m$ film. (b) Average friction stress τ_{ave} versus contact size for $h = 10\ \mu m$ and $h = 2\ \mu m$ films. In these calculations, the films were firstly indented by a sinusidial asperity with amplitude $\Delta = 0.5\ \mu m$ and wavelength $\lambda = 20\ \mu m$, which produced the pre-existing stress field and dislocation structure that determine the subsequent response during sliding.

In order to further investigate the difference between pure sliding and sliding with preceding indentation, the dislocation structure and corresponding slip contours are plotted in Figure 7.33. Results are shown for sliding for a $h = 10\ \mu m$ film at the instant $U = 0.02\ \mu m$ and $a \approx 10\ \mu m$; the preceding indentation is performed with a sinusoidal asperity characterized by amplitude $\Delta = 0.5\ \mu m$ and wavelength $\lambda = 20\ \mu m$. The dislocation structures are quite visually different between the simulations without (Figure 7.33 (a)) and with (Figure 7.33 (b)) a preceding indentation process. Dislocation structures obtained from a pure sliding calculation typically show a "strip" of dislocation activity (whose width is dependent on the contact area) just underneath the contact surface of the film. The dislocation patters induced by sliding with a preceding indentation has been affected by the persisting indentation structure, which leads to more extensive and dense structures.

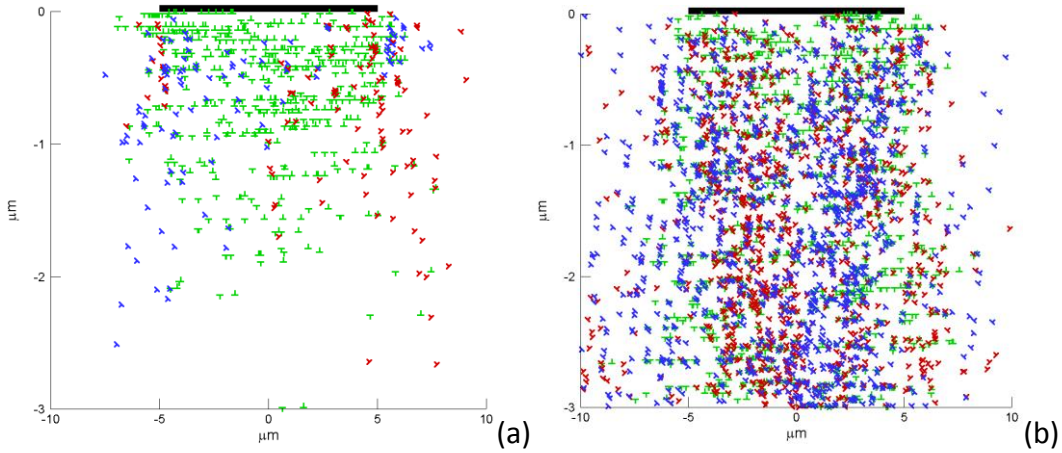


Figure 7.33. Effect of preceding indentation on dislocation structure. Dislocation patterns are obtained at the instant $U = 0.02\ \mu m$ of simulations (a) pure sliding with contact size $a = 10\mu m$ (b) sliding with a preceding indentation that introduces a contact size $a \approx 10\ \mu m$.

The corresponding slip distribution in a $h = 10\ \mu m$ film under pure sliding and sliding with preceding indentation is plotted in Figure 7.34 (a) and (b) respectively to illustrate the deformation field. The slip is computed as the numerical differentiation of the displacement field using the finite element shape functions of a four-noded linear element. For a certain element containing three potential slip planes, the total slip Γ is computed as the sum of slips $\gamma^{(\alpha)}, \alpha = 1,2$ and 3 along all three slip planes, which is given as:

$$\Gamma = \sum_{\alpha=1}^{3} \left|\gamma^{(\alpha)}\right|, \gamma^{(\alpha)} = \ s_i^{(\alpha)} \varepsilon_{ij} m_j^{(\alpha)} \tag{7.19}$$

In the equation above, ε_{ij} stands for the strain at the Gaussian point of a certain four-noded element, $s_i^{(\alpha)}$ and $m_j^{(\alpha)}$ are the slip and normal unit vectors of slip plane α within the element.

Although this numerical calculation eliminates dislocation singularities over single elements, it still provides reasonable information of deformation in the bulk of the films [1]. Sliding with preceding indentation results in slip spreads to at least $3.0\ \mu m$ underneath the contact, while slip induced by pure sliding is only observed up to a depth of $1.5\ \mu m$. Although dislocation and slip fields of the two types of sliding calculations are significantly different, the values of the coefficient of friction are similar.

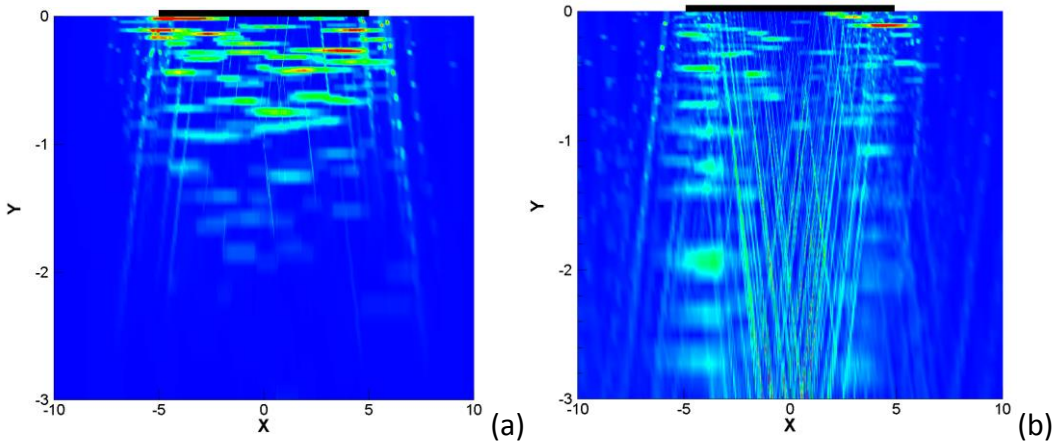


Figure 7.34. Slip contours obtained in simulations for (a) pure sliding, and (b) sliding with a preceding indentation on a $h = 10\ \mu m$ film by a sinusidial asperity with amplitude $\Delta = 0.5\ \mu m$ and wavelength $\lambda = 20\ \mu m$ at the applied sliding distance $U = 0.02\ \mu m$. The contact area is $a = 10\ \mu m$ indicated as a filled black bar in both cases.

Another comparison is made between results shown in Figure 7.35 and Figure 7.36 which show the dislocation structure and corresponding slip contours obtained from simulations with a smaller contact length, $a = 2.45\ \mu m$. The other conditions are similar. For a smaller contact length, a thinner plastic zone formed by gliding dislocations is found to be confined underneath the asperity. Also, the preceding indentation influence is weakened in this small contact area calculation as the effect of the preceding indentation is relatively small in depth.

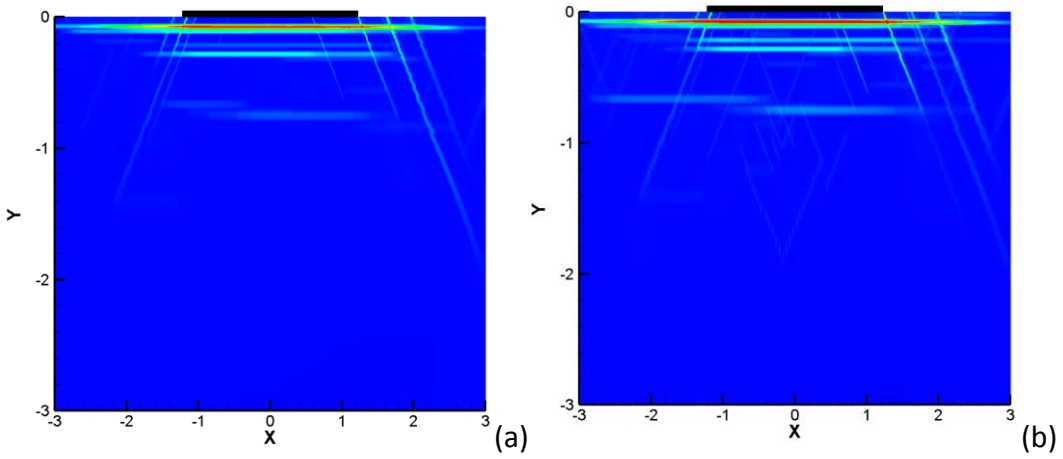


Figure 7.35. Slip contours obtained in simulations for (a) pure sliding, and (b) sliding with a preceding indentation on $h = 10\ \mu m$ film by a sinusidial asperity with amplitude $\Delta = 0.5\ \mu m$ and wavelength $\lambda = 20\ \mu m$ at the applied sliding distance $U = 0.022\mu m$. The contact area is $a = 2.45\ \mu m$ indicated as a filled black bar in both cases.

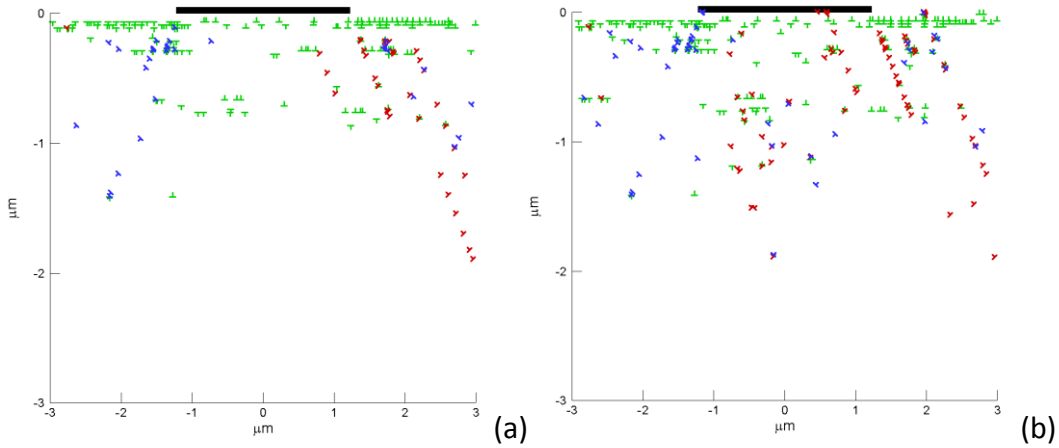


Figure 7.36 Dislocation structure obtained in simulations for (a) pure sliding, and (b) sliding with a preceding indentation on a $h = 10\ \mu m$ film by a sinusidial asperity with amplitude $\Delta = 0.5\ \mu m$ and wavelength $\lambda = 20\ \mu m$ at the applied sliding distance $U = 0.022\ \mu m$. The contact area is $a = 2.45\ \mu m$ indicated as a filled black bar in both cases.

7.3.3.3 Fretting

An investigation on fretting problems, which is simulated by cyclic micro sliding calculations on a $h = 10\ \mu m$ film with and without a preceding indentation process, is carried out. The sliding half-stroke length is set as $U = 0.02\ \mu m$, which is applied with a relatively low loading rate $\dot{U}/a = 10^4 s^{-1}$ in order to eliminate the loading rate effect. Contact size ranges from $a = 2.0\ \mu m$ to $a = 10.0\ \mu m$ in order to study contact size effect in fretting problems. Besides, there are studies on dislocation evolution within specimens to reveal a link between dislocation structure and potential processes linked to crack initiation and its location.

7.3.3.3.1 Cyclic effect on shear stress

The evolution of the calculated shear stress, τ, averaged over the contact length is shown as a function of the applied sliding distance U in Figure 7.37. For all cycles, the shear stress curve during a loading (sliding forward) half-cycle is systematically higher than the one during corresponding unloading (sliding backward) half-cycle. This behaviour is similar to the well-known Bauschinger effect experienced by materials under a cyclic uniaxial tension loading. This phenomenon indicates that the film has been plastically deformed due to dislocation piling up and other activities even after the first cycle of sliding. The area enclosed by loading and unloading shear stress curves is the energy dissipated during a sliding cycle. The values of areas become smaller with fretting cycles, which indicates that plastic shakedown has generally occurred.

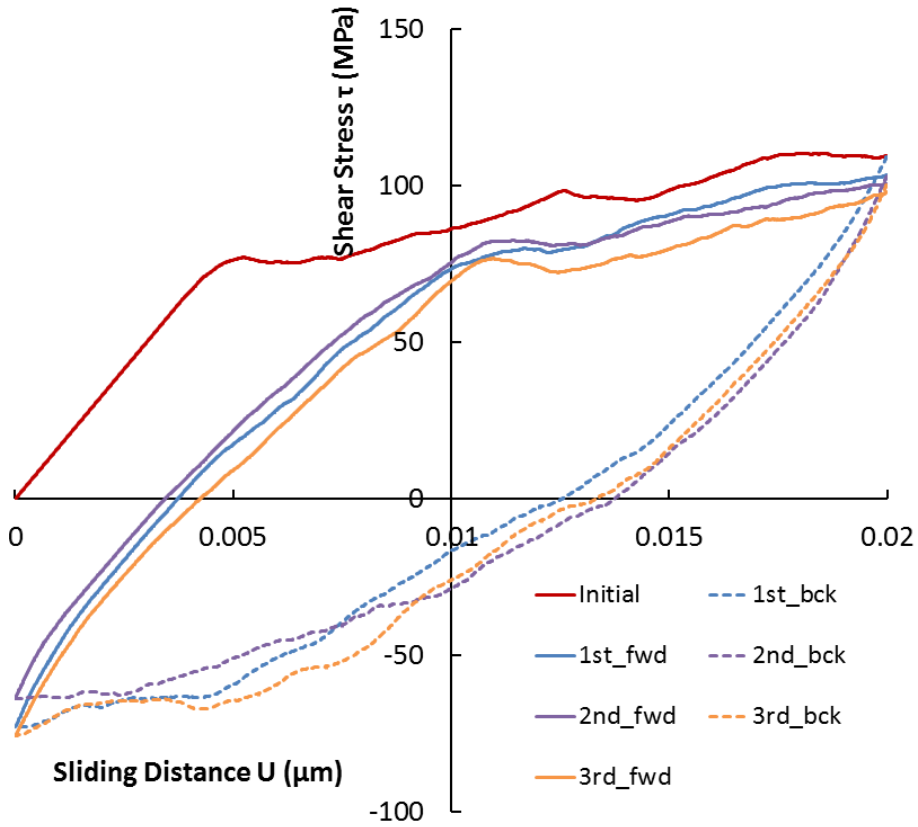
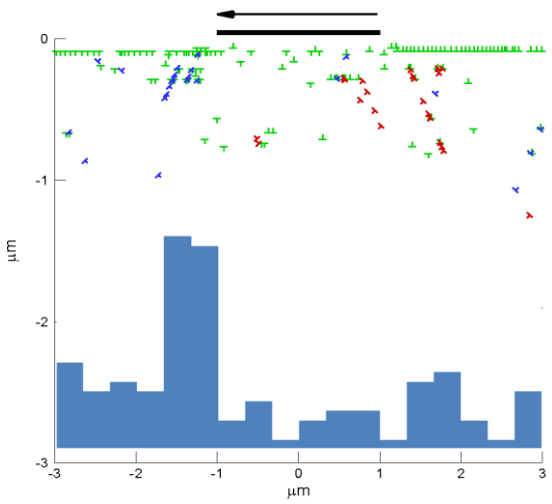


Figure 7.37. Shear stress τ evolution during a fretting process. Results are obtained by cyclic sliding for a $h = 10\ \mu m$ film with a stress- and dislocation-free status initially. The contact length is set as $a = 2.0\ \mu m$.

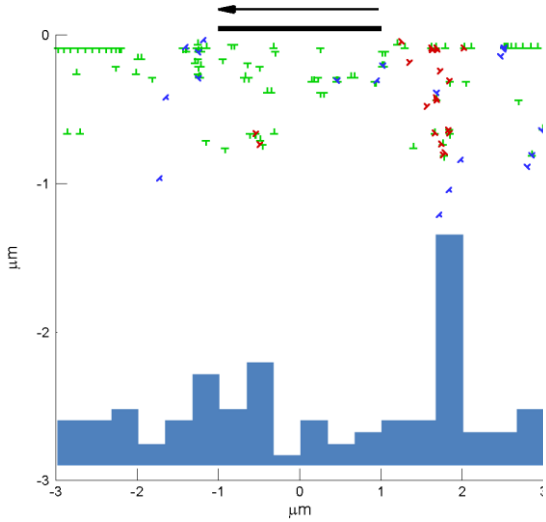
7.3.3.3.2 Dislocation structure evolution

Dislocation structures are plotted in Figure 7.38 at instants when the contact reaches the leftmost and rightmost positions (*i.e.* at the end of each half sliding cycle). Similar to a dislocation structure obtained from a pure sliding calculation, dislocations gliding on the horizontal slip system are confined to a thin strip just underneath the contact. Dislocations gliding on the inclined slip systems move from the surface to the bulk of the film with a certain pattern. Also, the dislocation structure does not significantly change except for the first cycle. This implies that the majority of damage to the film is produced during the first sliding cycle and the contact undergoes plastic shakedown for the conditions under investigation, which is consistent with the shear stress evolution (Figure 7.37). Besides, dislocations are binned (blue histograms) according to their X coordinates. Dislocations tend to pile up near the contact edges, and dislocation distribution appears to be more even during fretting cycles. Calculations with other values of contact sizes show similar trends and can be found in Appendix XI.

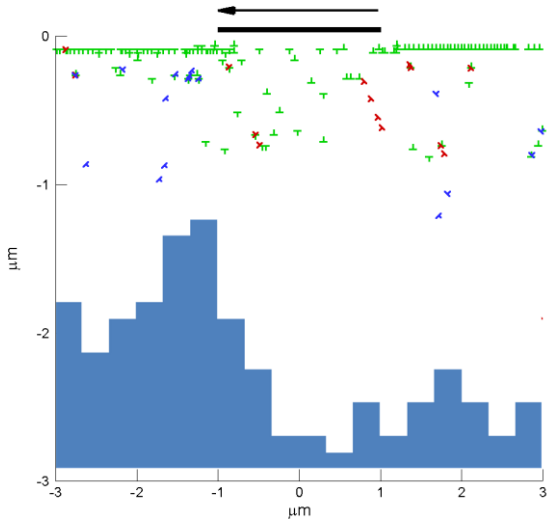
U=+20nm/



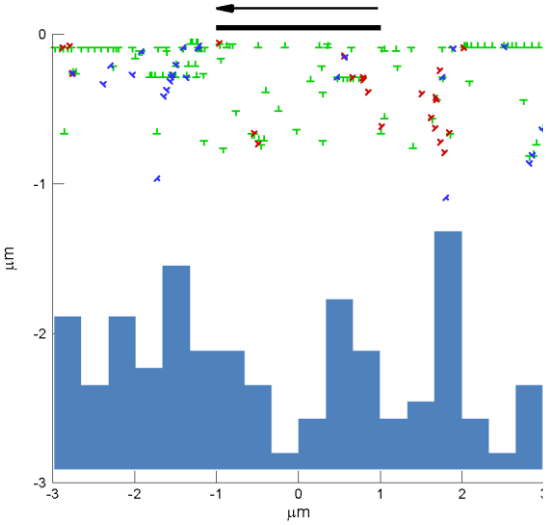
U=0/4000



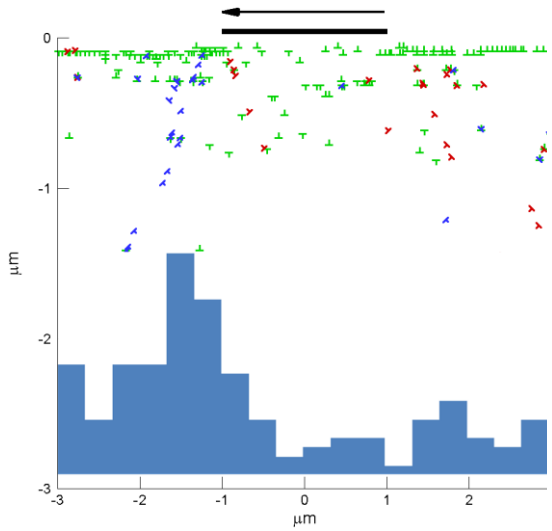
U=+20nm/6000



U=0/8000



U=+20nm/10k



U=0/12k

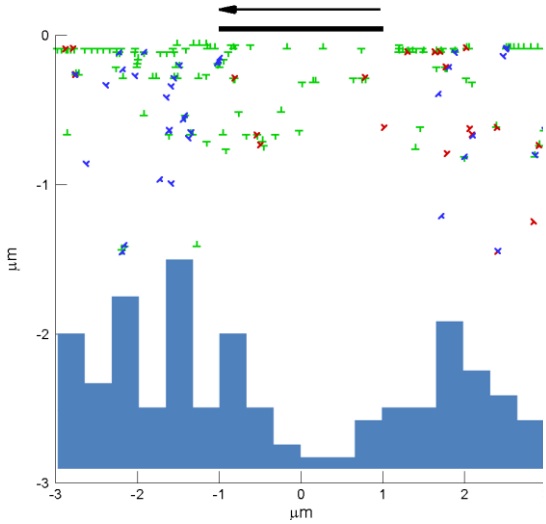


Figure 7.38. Dislocation structure evolution during the fretting process. Results are obtained for cyclic sliding on a $h = 10\ \mu m$ film with a stress- and dislocation-free status initially. The contact length is set as $a = 2.0\ \mu m$.

In order to quantify the link between dislocation activity and plastic damage during the fretting process, dislocation density evolution on different slip systems are plotted in Figure 7.39. For dislocation gliding on the horizontal slip system, the density goes up in the first half-cycle and decreases suddenly at the end of it , and then it alternates between increasing during the loading half cycle and deceasing during the unloading half cycle. The overall dislocation density increases with cycles as the number of newly nucleated dislocations is apparently larger than the number of dislocations eliminated during unloading. However, the total number of the dislocations gliding on the inclined slip systems increases slowly. It is due to the alternating performance for dislocations near the leading edge and the trailing edge during loading and unloading half cycles. As discussed in the sliding section, the general plastic accumulation of film is majorly dominated by dislocations gliding on the horizontal slip system while the accumulation of slip and dislocations along the inclined slip systems is probably linked to crack initiation, which has been experimentally been confirmed to coincide with the contact edges in fretting contacts characterized by sharp edges[210]. The crack initiation process can potentially be linked to the dislocation density along the inclined slip systems, and the slow increase is consistent to literature and experiments, e.g. [211, 297, 298] on the damage accumulation during a typical fretting fatigue.

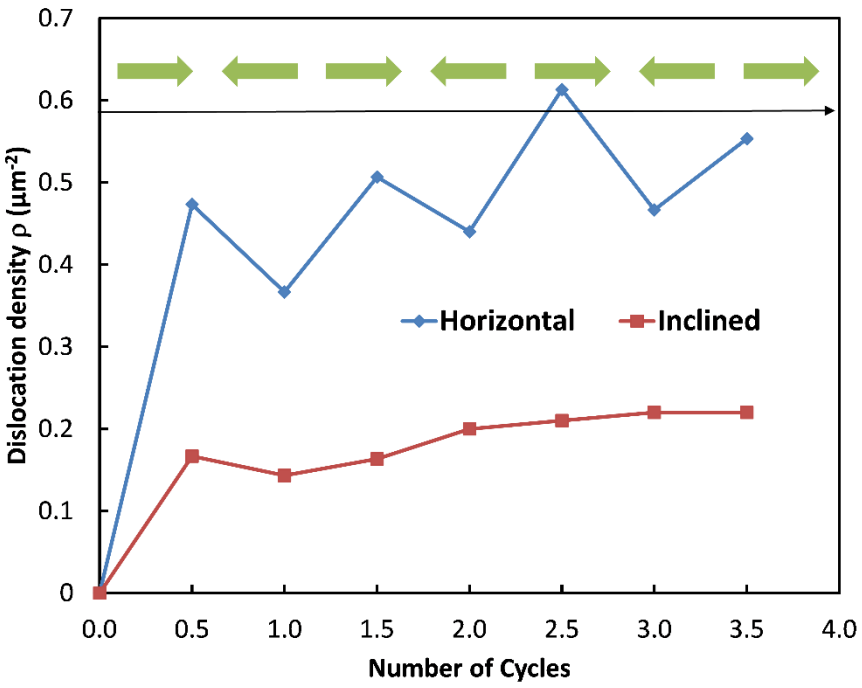


Figure 7.39. Dislocation density evolution during the fretting process. Results are obtained by cyclic sliding on the $h = 10\ \mu m$ film with a stress- and dislocation-free status initially. The contact length is set as $a = 2.0\ \mu m$. The evolution of dislocations gliding on horizontal and inclined slip systems are separated to discuss their roles during the fretting process.

7.3.3.3.3 Surface profile evolution

The surface profile variation during a fretting process is characterized by the Y component of nodal displacements along contact surface that is shown in Figure 7.40. Results are shown at end of each labelled cycle. The surface is generally lifted up during the fretting process due to the fact that normal pressure is absent during simulations, and therefore such loading scenarios are probably more typical of contacts undergoing sliding in the presence of adhesive forces rather than contact. These results will be further compared to results with preceding indentation (Section 7.3.3.3.5).The magnitude of the normal displacement increases with the number of cycles, and it is distributed uniformly within the contact. However, at the edge of contact there tends to be abrupt discontinuities corresponding to material intrusion and/or extrusions. They are formed by certain dislocations pile-up patterns on favourable slip systems. This pile-up of dislocation mechanism [299] is illustrated in Figure 7.41. The distribution of dislocation structure near contact edges during fretting process, shown in Figure 7.42, is consistent with the surface profile.

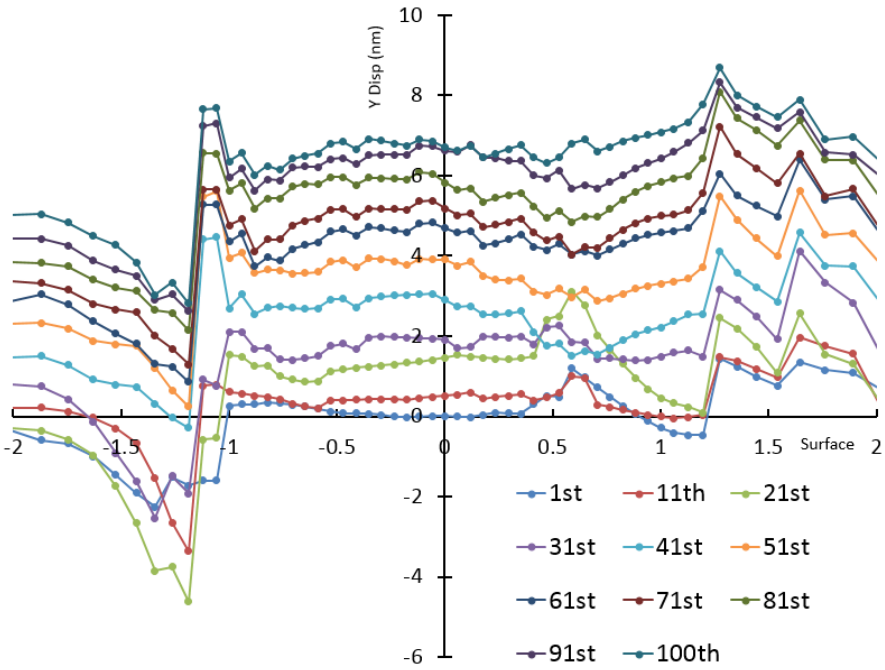


Figure 7.40. Displacements in the Y direction along the contact surface of the specimen during the fretting process without preceding indentation.

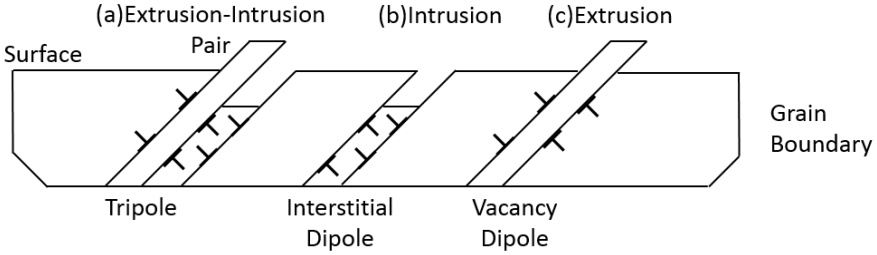


Figure 7.41. Dislocation motion in a most favourably oriented grain and the formation of extrusion and intrusion of surface due to dislocation pile-up with certain patterns.

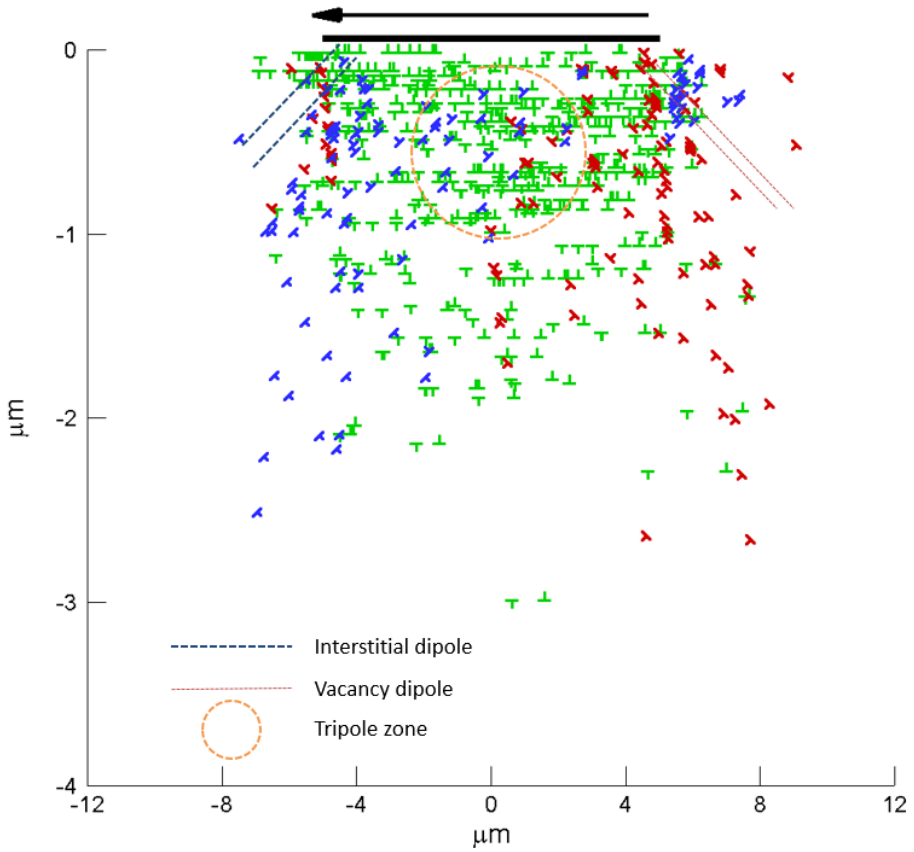


Figure 7.42. A typical dislocation structure near the contact in fretting process. Results are obtained at the end of 71st cycle.

Parameters of surface roughness, including arithmetic average R_a and root mean squared R_q, are plotted against the number of fretting cycles N in Figure 7.43. Both R_a and R_q linearly increase with the number of fretting cycles N, in terms of the whole surface and the nominal contact partition only. Also, it is seen that the roughness within the contact zone is more severe than the whole surface. This indicates that, as expected, the partition of surface out of contact has not been affected much during the fretting process. The roughness is introduced by ploughing effect at the micro-scopic scale and by the formation of dislocation pile-up along slip systems at subsurface of specimen in microscope.

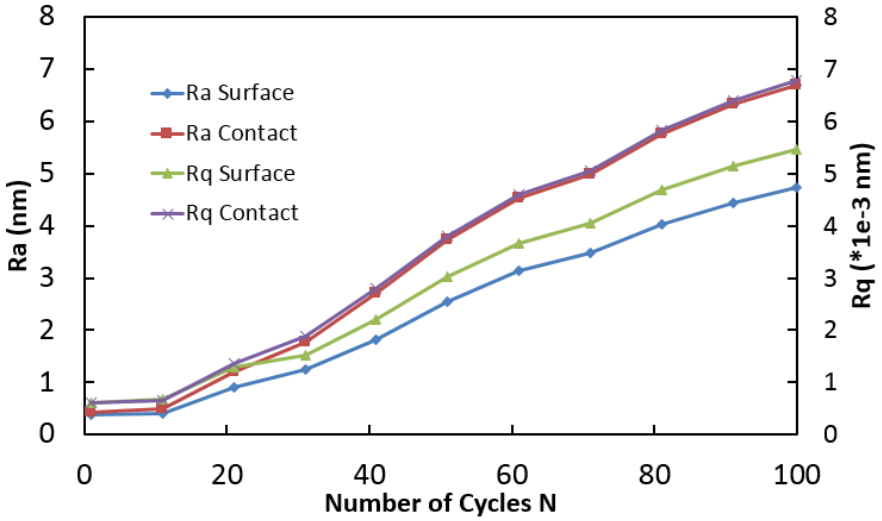


Figure 7.43 Surface roughness, including arithmetic average R_a and root mean squared R_q, along the contact surface variation during fretting process

7.3.3.3.4 Size effect

Fretting simulations with three values of contact size ($a = 2, 4$ and $10\ \mu m$) and up to 100 cycles have been performed in order to further study material response and contact size effect in fretting problem. Size effect is illustrated in terms of the following aspects: shear stress evolution, dislocation structure and density evolution, and surface profile variation.

The shear stresses,τ, averaged over the contact length and calculated at the end of the stroke of each fretting cycle are plotted in Figure 7.44 for different contact sizes, $a = 2.0, 4.0, 10.0\ \mu m$. The stroke length for all simulations with various contact sizes is set identical $U = 20\ nm$ as For all contact sizes, the average shear stress gradually decreases during the fretting process, while the initial shear stress differs between the different contact sizes. Besides, for a relatively small contact size, $a = 2.0\ \mu m$, the variation of average shear stress is found to be more pronounced. For medium and large contact sizes, $a = 4.0$ and $10.0\mu m$, the change in shear stress is almost negligible. This indicates that a fretting process introduces more damage on contact with smaller contact sizes due to the higher intensity of stress and energy. Finally, it seems that all values of average shear stress tends to approach the stress level $\tau = 50\ MPa$, which is the dislocation nucleation strength. This reveals that the material would reach a steady-state equivalent to the behavior that would be obtained assuming a size-independent continuum behaviour when the number of fretting cycles is sufficiently large.

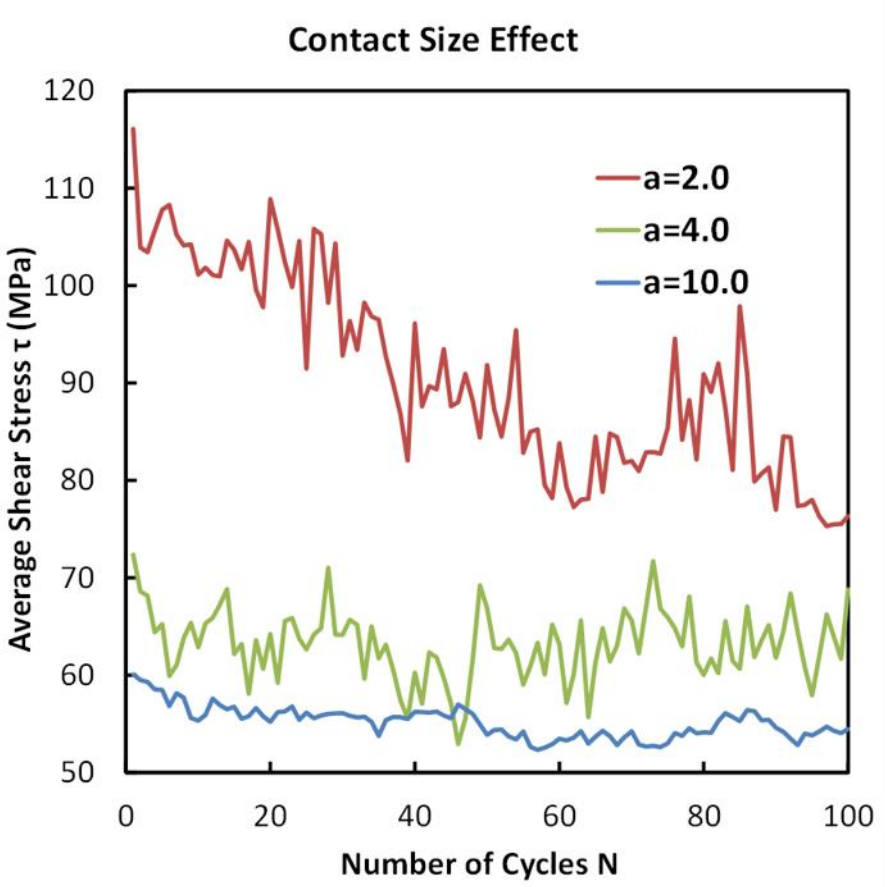


Figure 7.44. Shear stress τ evolution during the whole fretting process of 100 cycles. Results are obtained at the end of the stroke for each cycle from the simulation performed for a $h = 10\ \mu m$ film with a stress- and dislocation-free status initially and various values of contact size.

Dislocation density ρ for all slip systems at the end of the stroke is plotted against the number of fretting cycles in Figure 7.45. Results are shown for three values of contact sizes, $a = 2.0, 4.0, 10.0\ \mu m$. Similar trends i.e. the dislocation density increases linearly with number of fretting cycles are found for all contact sizes. However, the coefficient of determination R^2 increases with the values of contact sizes. This indicates that the nucleation of dislocation dipoles under large contact is more stable. There are more sudden and irregular jumps along dislocation density evolution curves of smaller contact sizes due to the increase of fretting energy intensity.

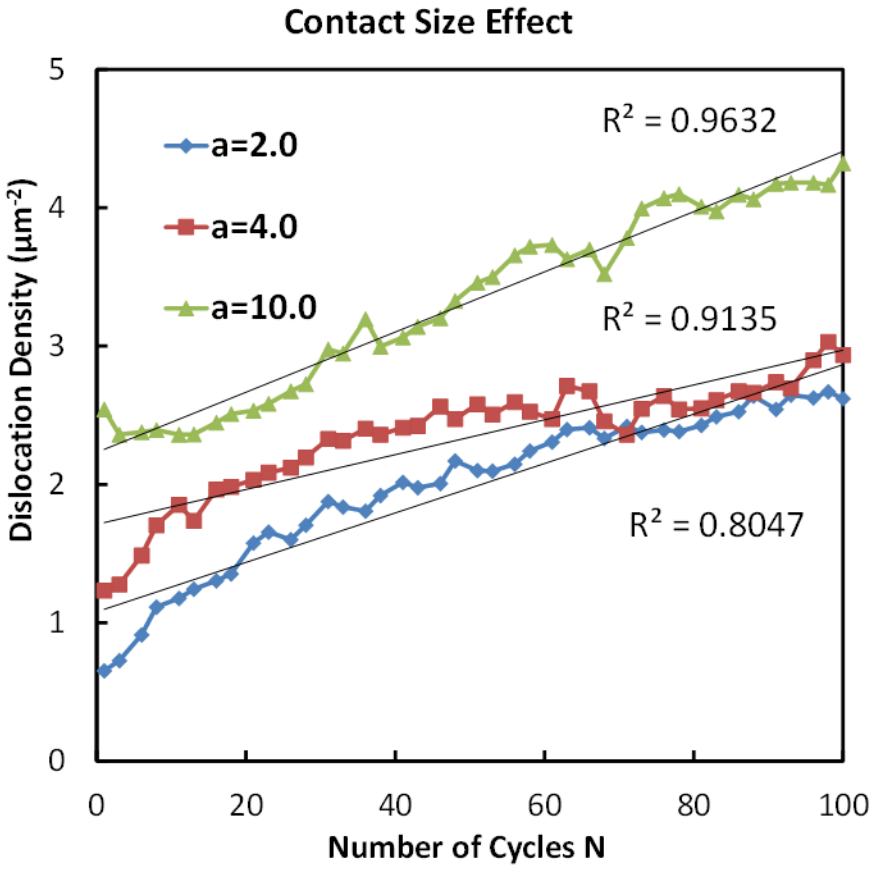


Figure 7.45 Total dislocation density evolution during a fretting process. Results are obtained at the end of the stroke for each cycle from simulations of a $h = 10\ \mu m$ film with a stress- and dislocation-free status initially and various values of contact size.

The residual displacements in the Y-direction of surface nodes along the contact during fretting process are plotted in Figure 7.46. Results are reported at the last cycle of the fretting process and for three values of contact sizes, $a = 2.0, 4.0, 10.0\ \mu m$. Contacts with a relatively small contact length exhibit a more severe deformation along the surface. This is due to the fact that contacts with smaller sizes are more sensitive to the external fretting loading energy input. Contacts with larger contact size are able to distribute input fretting energy more evenly along the surface.

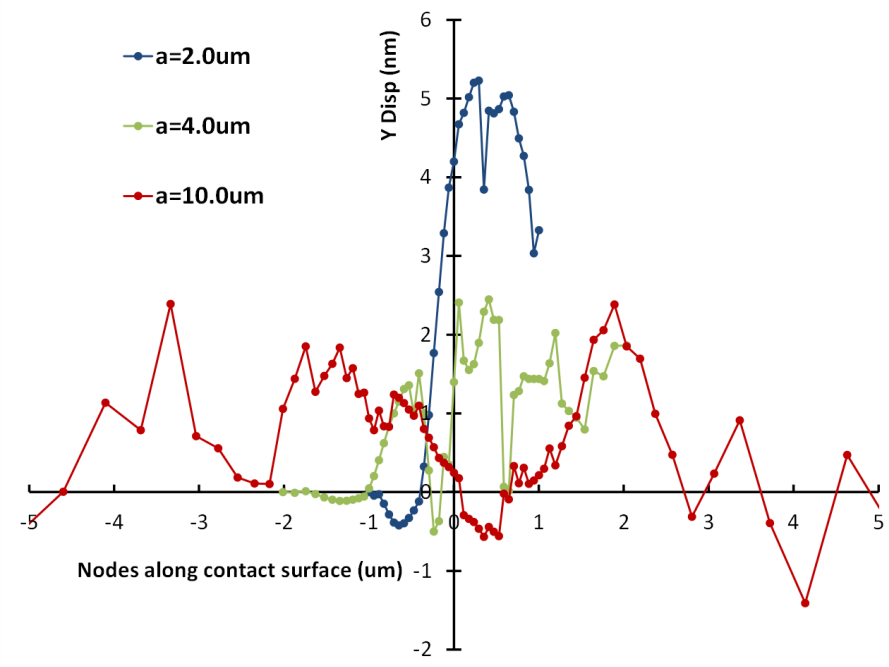


Figure 7.46. Displacement profiles of surfaces at the end of the 100th fretting cycle. Results are obtained from a simulation performed for a $h = 10\ \mu m$ film with a stress- and dislocation-free status initially and various values of contact size.

The evolution of surface roughness parameters, R_a and R_q, with number of fretting cycles is plotted within the contact partition in Figure 7.47. Results are reported for three values of contact sizes, $a = 2.0, 4.0, 10.0\ \mu m$. Similar trends are found for all three values of contact sizes, but contact with relatively smaller sizes are found to undergo much larger deformations during the fretting process as the surface roughness parameters increase at a higher rate. With the increase of contact length, the surface roughness becomes more insensitive to fretting cycles. For instance, the roughness increase of contact with $a = 10.0\mu m$ during 100 fretting cycles is very limited.

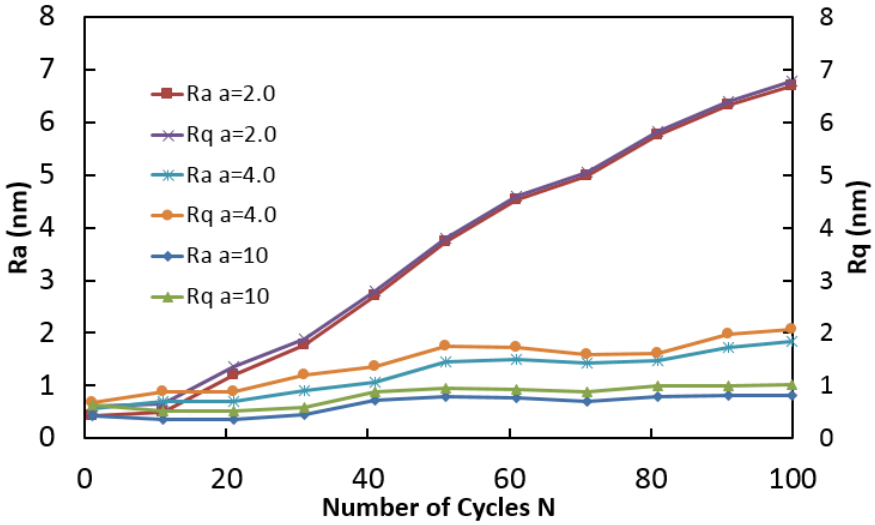


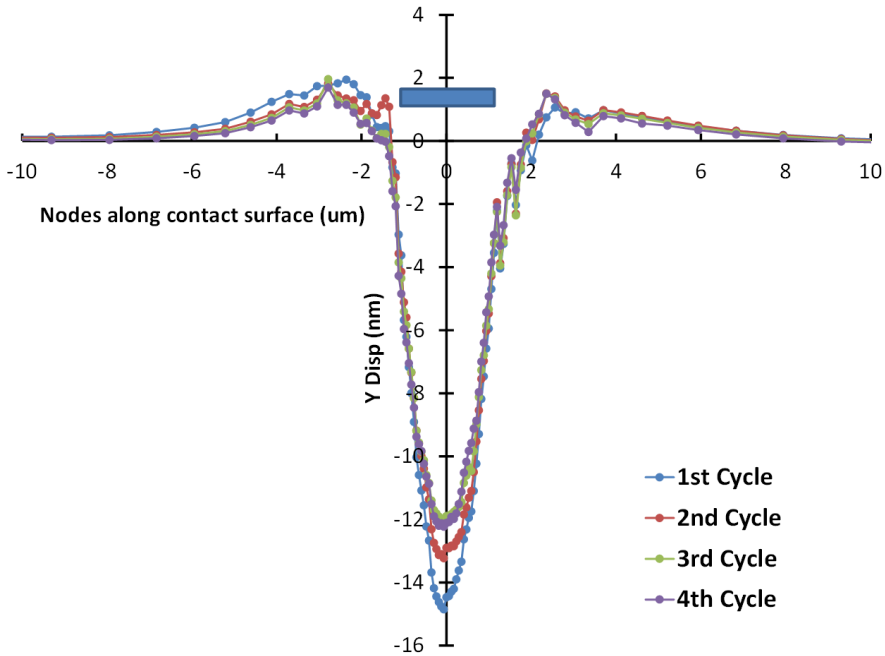
Figure 7.47. Roughness parameters of contact partition and the whole surface during a fretting process. Results are obtained from simulations on $h = 10\ \mu m$ film with a stress- and dislocation-free status initially and various values of contact sizes.

7.3.3.3.5 Effect of initial indentation

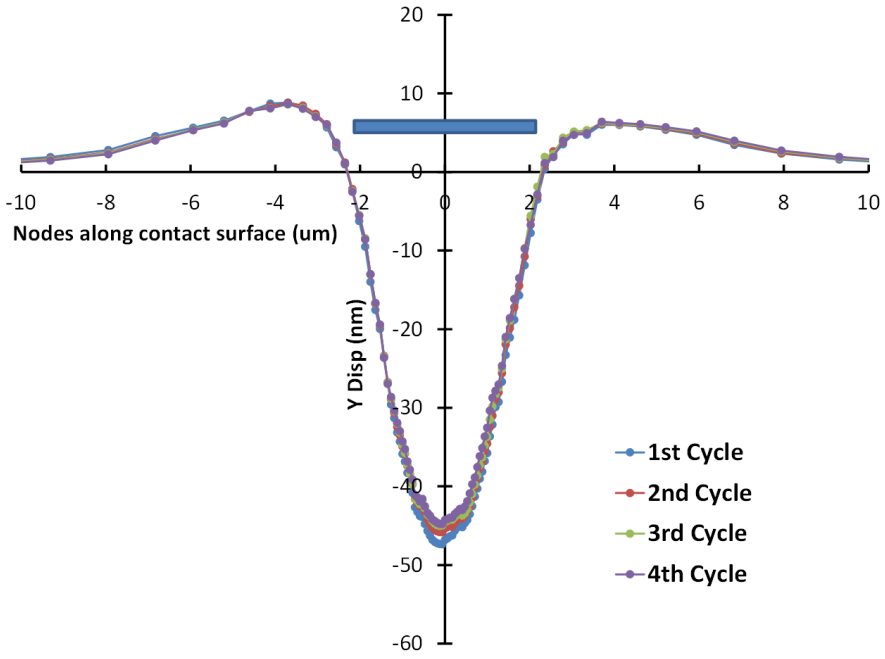
Results that are reported above are based on calculations without the application of indentation and normal load, and the positive surface displacements measured in the direction perpendicular to the contact during fretting (see Figure 7.40 and Figure 7.46) is a result of the absence of indention pressure. The following paragraphs show the surface profile and shear stress evolution, respectively, when the fretting process is applied in the presence of a constant normal load after indentation has taken place. Results aim to reveal the indentation effect that is commonly experienced during a more conventional fretting loading. The number of cycles are limited to four due to computational expense introduced by the much larger number of dislocations generated during the process.

Displacements on Y direction of nodes along specimen surface with different contact sizes during fretting process following a preceding indentation are plotted in Figure 7.48. Results are reported at the end of first four cycles during fretting process and for three values of contact sizes, $a = 2.4, 4.1, 9.3\mu m$, respectively. Compared to the displacement profiles obtain in the pure fretting calculations (see Figure 7.40 and Figure 7.41), surfaces with preceding indentation surface tend to keep at the originally deformed position due to the preceding indentation normal pressure . This phenomenon is more apparent when contact size introduced by the preceding indentation is relatively large (*i.e.* indentation pressure is larger). Besides, the deformed surface shape is dominated by the sinusoidal indenter rather than sudden spikes observed near the contact edge. These explicitly indicates the preceding indentation effect on the surface profile variation during following fretting cycles. Surface roughness, in terms of Ra and Rq reported in Figure 7.49 decreases during fretting process. This ploughing which is introduced by both fretting and preceding indentation process also further exhibits the preceding indentation effect. For

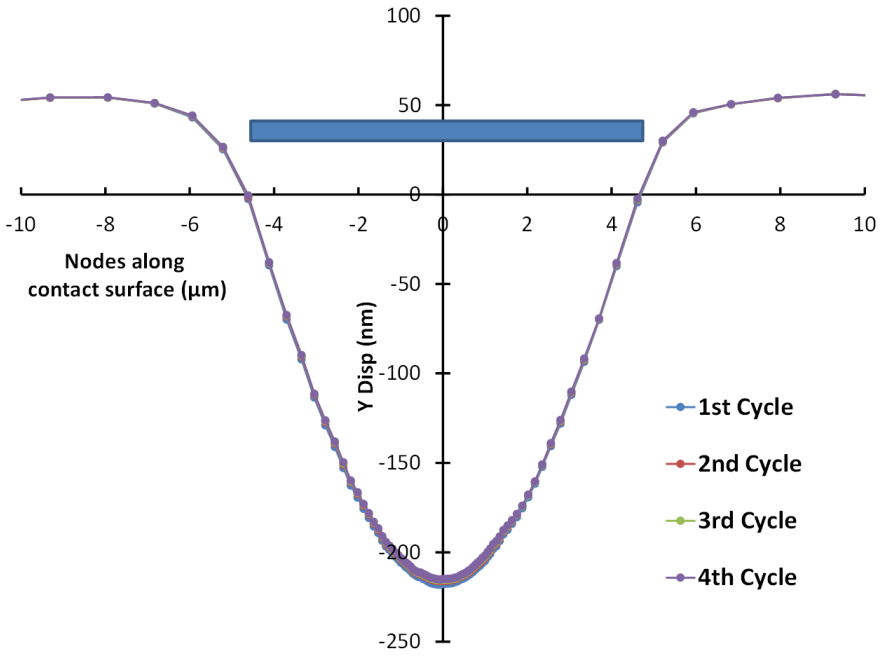
different contact sizes, surface profile is even more insensitive to number of cycles when the contact size is larger (*i.e.* indentation pressure is larger).



(a)

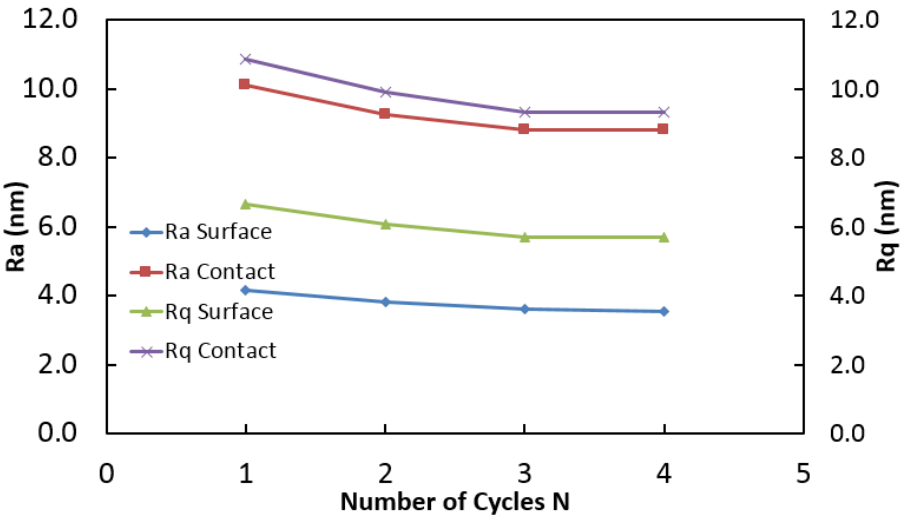


(b)



(c)

Figure 7.48. Displacement profiles of surfaces at the end of each cycle. Results are obtained from simulations performed for a $h = 10\ \mu m$ film preceding indented with contact sizes (a) $a = 2.4\mu m$ (b) $a = 4.1\mu m$ (c) $a = 9.3\mu m$, respectively



(a)

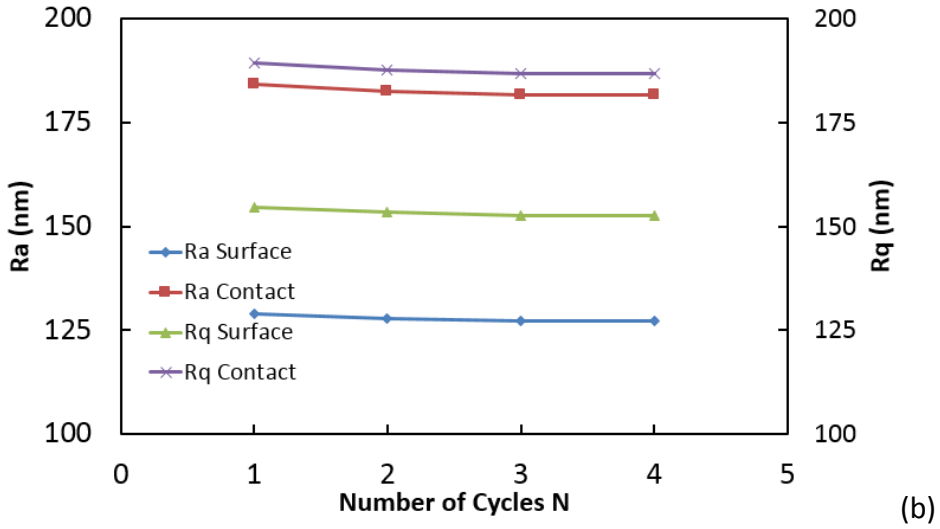
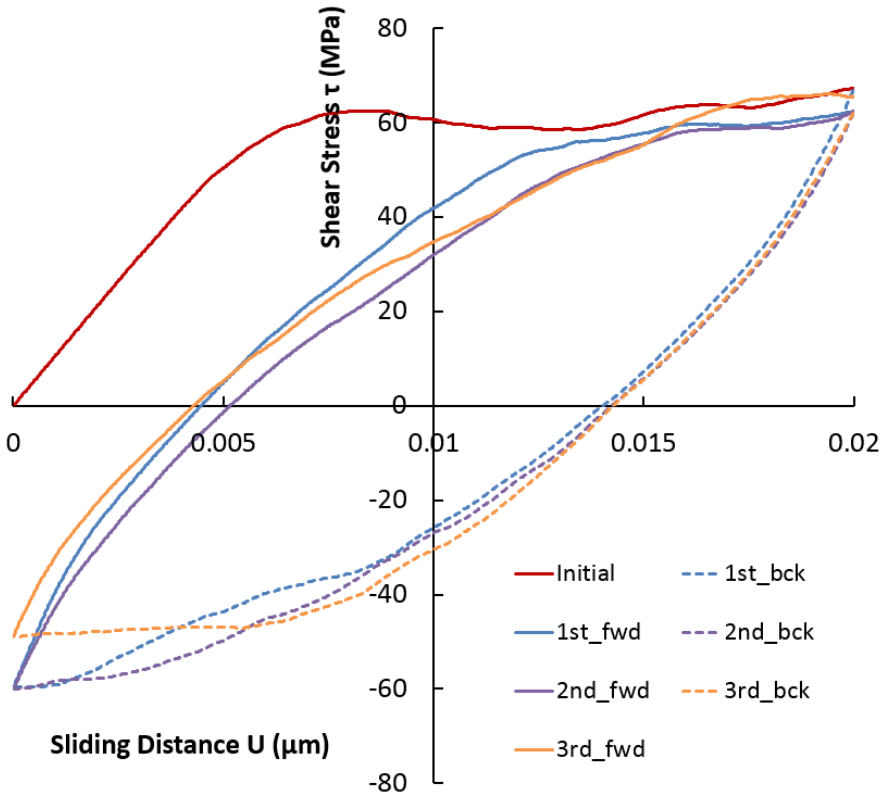
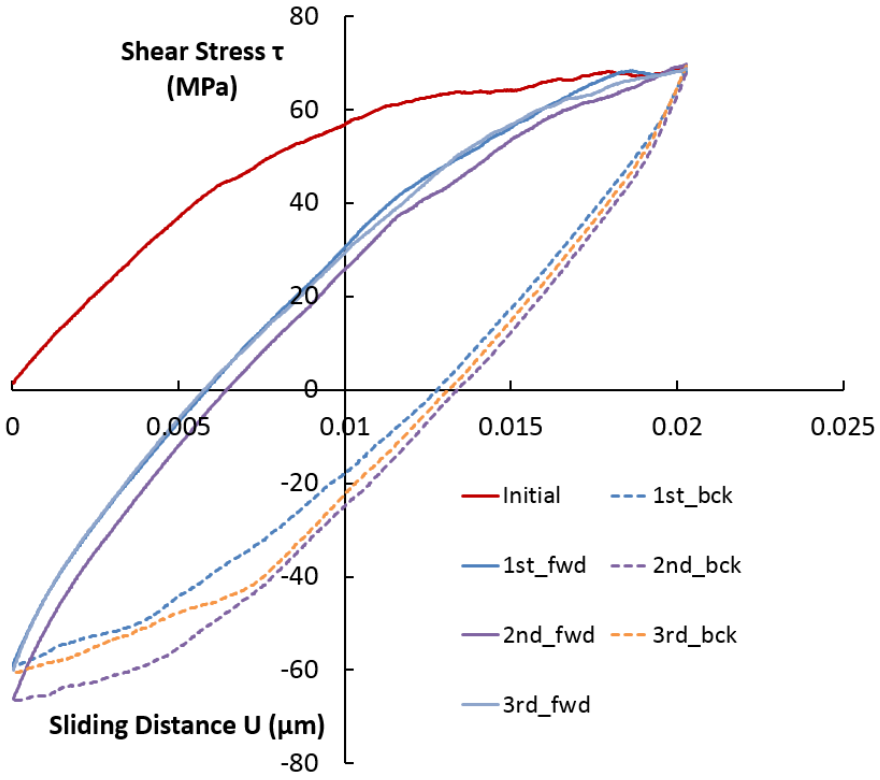


Figure 7.49. Surface roughness parameters including arithmetic average Ra and root mean squared Rq along specimen surface during fretting process that starts from a preceding indentation with contact size (a) $a = 2.4\mu m$ (b) $a = 9.3\mu m$ repectively

Evolution of shear stresses, τ, averaged over the contact area obtained from fretting calculations after the indentation process versus applied sliding distance U is plotted in Figure 7.50. Results are shown for three contact sizes: (a) $a = 2.4\ \mu m$ (b) $a = 4.1\ \mu m$ (c) $a = 9.3\ \mu m$, which are controlled by the initial indentation process. We can clearly see the Bauschinger effect is less apparent in fretting with preceding indentation compared to the results obtained when shear is applied in the absence of indentation pressure. Besides, energy dissipation during each fretting cycle decreases with increasing contact size. This phenomenon is also attributed to the presence of normal indentation pressure that has already produced much dislocation activity and plasticity in the thin films. Fretting processes characterized by small stroke length and relatively large contact size only add a limited dislocation activity to the films under investigation.

Results reported above have shown that relative magnitude of indentation and frictional forces both play a key role in determining the system response and that, therefore, a much larger set of parameters should be explored to have a full picture of the fretting process at these scales. However, due to the large number of dislocations having nucleated during the preceding indentation process, retting calculations with preceding indentation requires more computational time to finish. Thus the number of cycles is confined to four to preliminarily reveal the features. Moreover, the geometry shape and dimensions of a sliders (indenter) also affects the response of thin films during fretting. Thus, the tip and/or contact edges can be filleted to round in the future research so that the dislocation activity can be further explored.


Shear Stress τ (MPa)
80
60
40
20
0
-20
-40
-60
-80
0
0.005
0.01
0.015
0.02
Sliding Distance U (μm)
Initial
1st_bck
1st_fwd
2nd_bck
2nd_fwd
3rd_bck
3rd_fwd


Shear Stress τ (MPa)
80
60
40
20
0
-20
-40
-60
-80
0
0.005
0.01
0.015
0.02
0.025
Sliding Distance U (μm)
Initial
1st_bck
1st_fwd
2nd_bck
2nd_fwd
3rd_bck
3rd_fwd

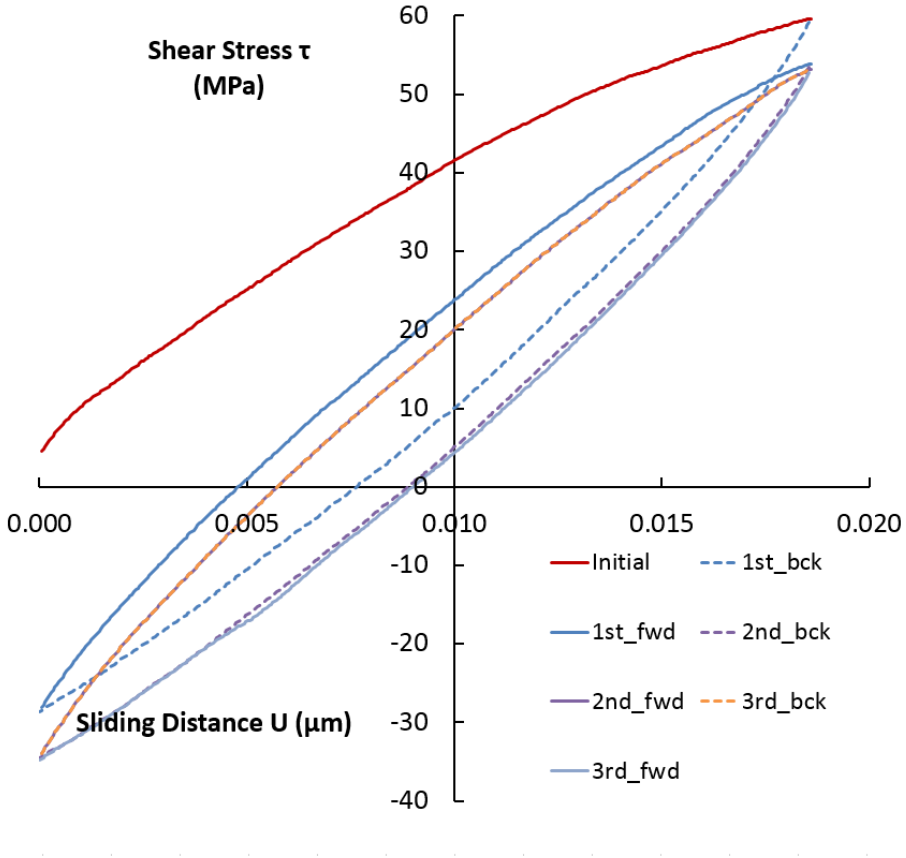


Figure 7.50. Shear stressτ evolution during a fretting process. Results are obtained on $h = 10\ \mu m$ film cyclically sliding from a preceding indentation with contact size (a) $a = 2.4\mu m$ (b) $a = 4.1\mu m$ (c) $a = 9.3\mu m$ repectively

7.3.3.4 Computational Efficiency

Computation time, in terms of hours taken to implement half cycle fretting without preceding indentation, is tabulated in Table 7.3. All simulations have been performed in clusters of Mechanical Engineering Department, Imperial College London, using a single Quad-Core AMD Opteron(tm) 8384 2.7 GHz processor and 2GB RAM. The loading rate $\dot{U}_x/a$ is set identical for all calculations so that simulations with a small contact size takes more time to finish in order to achieve the same stroke distance. Simulations with contact size $\mathrm{a} = 0.04\mu m$ and $0.6\mu m$ are also performed with a higher loading rate to reduce time expense.

Table 7.3. Time consumed for fretting simulations with different contact sizes a.

Contact size a	μm	0.04	0.6	1.0	2.0	4.0	10.0
Time consuming per half cycle	hours	60	25	7	6	5	3

7.3.4 Summary

A couple of sets of indentation, sliding and fretting simulations have been conducted between a rigid asperity and a single crystal film, which is modelled with discrete dislocation dynamics plasticity description for specimens. Two types of sliding

simulations have been conducted. In one set, sliding commences in an initially stress and dislocation-free crystal, while in the other case there is a stress and dislocation state inheriting from a preceding sinusoidal indentation. Plastic flow arises from the collective motion of dislocations which nucleate from initially predefined Frank–Read sources in the bulk of materials. The contact between the asperity and the crystal is modelled using a shear cohesive law. The indenter shape and the film thickness are varied in the indentation calculations, and the influence of contact area has been focused on in the sliding and fretting simulations. The shear stress and dislocation structure represent the deformation of surface contact and internal slip during the sliding and fretting process. Main results are summarized as following:

For sliding:

- Indentation pressure versus contact size relation is both film size (thickness) and indenter size (shape) dependent.
- Highly localized plastic concentration has been found in both sliding and fretting simulations near the contact edge. There is little plastic strain accumulated inside the contact.
- For both types of sliding simulations, macroscopic plasticity dominates when the contact area is large enough and the friction shear stress approaches the flow strength of the film crystal. When the contact area is sufficient small, the friction shear stress approaches the strength of the adhesion zone. Within the intermediate contact area zone, the friction shear stress is found to be determined by the contact size with a square root relation.
- The relation between shear stress and contact area size is not significantly changed by preceding indentation for the cases with a thicker film ($\mathrm{h} = 10\ \mu\mathrm{m}$).
- The relation between coefficient of friction and contact area size is found to be strongly dependent on asperity shape.
- Coefficient of friction predicted for the thicker film ($\mathrm{h} = 10\ \mu\mathrm{m}$) are similar in simualations with or without preceding indentation, although their dislocation distribution structure and slip contour are found to be significantly differently.
- The shear stress evolution in sliding is found to be loading rate-dependent, even though the discrete dislocation plasticity algorithm adopted herein is quasi-static.
- Dislocations gliding on different slip systems take different responsibility of plastic flow in flat contact sliding, regardless of with or without a preceding indentation. The horizontal slip system, which is found to be active at subsurface of specimen, mainly contributes the plastic zone underneath the asperity. The inclined slip systems, which are found to be active at contact-edge-affected zone, manly contributes the plastic slip from the contact to the bulk of film.
- Based on the different roles of dislocations on plastic flow in specimen, crack initiation in the specimen can further be linked to dislocation structure evolution, especially for those gliding on the inclined slip systems.

For fretting:

- The major contribution of damage (related to total slip) comes from the first cycle of sliding. During subsequent cycles, dislocation density along the inclined slip systems increase slightly, although the slip underneath the flat contact due to dislocations piling up along the horizontal slip system.
- The reversed shear stress is lower than the corresponding forward shear stress during a cyclic sliding period. It implies that the material has suffered from being damaged during fretting process, although the damage becomes weaker during the subsequent cycles.
- Contact size effect has been addressed in terms of shear stress, dislocation density evolution and surface profile variation.
- Preceding indentation effect has been discussed in terms of shear stress and surface profile variation.
- Besides investigation on micro-crack initiation, the newly adapted discrete dislocation dynamics codes on sliding and fretting can also be applied to study other aspects of contact, including average shear stress evolution, friction coefficient due to asperity sliding and variation of contact surface profile, etc.

The adaption and application of DDP formulations on sliding and fretting problems not only help reviews the feature of its modelling method introduced in Chapter 3, but also extends the study on the global plasticity in Chapter 4 to a localized zone under contact. Besides, the new computational framework in fretting work here also complements the tangential behaviour of a specimen to the study on the normal behaviour in Chapter 5.

In future, more effort should be focused on the work finding relevant sliding or fretting experimental results in order to find a corresponding relation between the dislocation density on certain slip systems and the crack initiation. Once that relation is revealed, the discrete dislocation plasticity model in sliding/fretting would be able to provide all calibration damage parameters for a larger scale, for instance, crystal plasticity finite element, calculations. This would help understand the damage mechanism and crack initiation under contact in a more physical aspect. This future work will be discussed in Chapter 8.

7.4 Linking Dislocation Activity to Crack Initiation for Sliding and Fretting Problems

It is evident for researchers to understand fatigue as over 50% of engineering components failing to work due to fatigue[300] and approximately 4% of grand national product of USA is spent on dealing with these failures[301]. Not only for economy reasons, we also need to improve and refine the current fatigue theories that are not completely capable of explaining experimental and practical phenomenon.

Researchers have been spending several decades on relating fatigue crack initiation mechanisms to microstructure of materials. The service life of a part can be decomposed into two parts: (1) the number of cycles that need to initiate a micro-crack and (2) the number of cycles that need to propagate an existing crack to ultimate failure. For a typical low cycle fatigue, the crack initiation process contributes a large portion of the total service life [302]. Macroscopic crack initiation results from irreversible microscopic slip existing and accumulating during fatigue loading. At the scale of defects, the irreversibility of slips are introduced by net dislocation activities during each loading cycle. Therefore, the consequent localized strain in sensitive regions leads to persistent slip bands where micro-crack initiation could potentially occurs.

While investigating the relevant mechanisms, parameters that can be employed to predict the initiation, propagation of micro-cracks and thus the fatigue life of a component have also become the focus of researches. In the pioneering study, the amplitude of loading stress used to be employ to predict the fatigue life in terms of S-N curves [303], especially in uniaxial cyclic loading. Strain-life relation, normally expressed as Coffin-Manson relation[304, 305], predicts the life using the strain amplitude range. Recently, accumulated plastic strain is widely used as a key empirical parameter for indicating crack initiation under fatigue [193, 227, 306-308]. Plastic strain that is intrinsically linked to the irrecoverable displacement along slip systems during loading cycles. Thus this parameter phenomenally becomes a bridge between the atom bonds separation in micro scale to the deformation in macroscopic. However, accumulated plastic strain does not have a sound physics background and thus it is not able to visually illustrate a micro-crack imitation process. Besides, the assessment approaches using accumulative plastic strain are still based on continuum computational framework that lacks of a characteristic length scale. This shortcoming stops the common continuum framework from predicting micro-crack initiation associated with size effects (e.g. the contact size effect revealed in this chapter).

Dislocation density and patterns have already captured researchers' focus on predicting the micro-crack initiation due to its more physics based mechanisms in producing persistent slip bands [309, 310]. Therefore, discrete dislocation plasticity method is capable of predicting the initiation of fatigue cracks.

There are two potential approaches to couple DDP into a macro-scale scheme in order to fully take advantages of multi-scale coupling philosophy. In the first approach, a concurrent coupling philosophy that is analogical to the approaches employed in uniaxial and indentation problems of this project paper applies to obtain a discrete dislocation resolution. The sketch of the sub-region concurrent coupling approach on the sliding and fretting problems are shown in Figure 7.51. By applying this type of coupling, micro-crack initiation will be fully captured in terms of dislocation activities in the sensitive zones near the contact edges ($l \times h$ rectangular zones in the sketch).

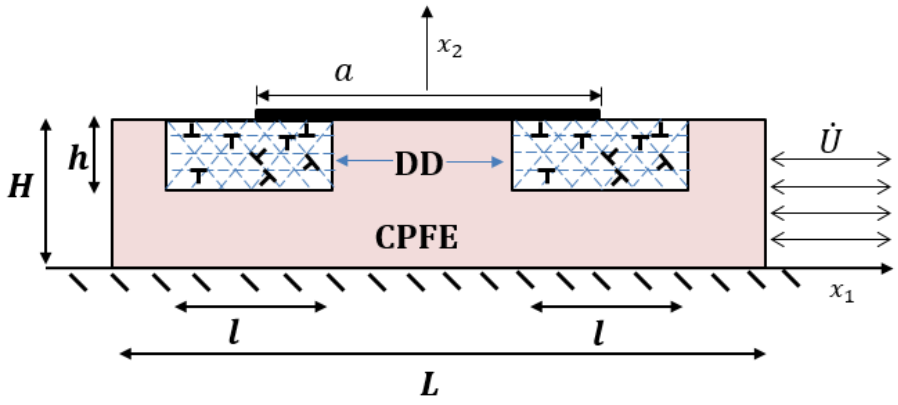


Figure 7.51. the sketch of the concurrent multi-scale coupling method in sliding and fretting problems

The other approach requires a hierarchical and single directional information passing from DDP solution to CPFE region. In this method, dislocations density is considered as the most appropriate variable in DDP calculations to be passed to CPFE fatigue crack initiation. In particular, when focusing on asperity-scale fretting problems, the dislocation density along inclined systems located near contact edges should work well as a fatigue parameter in CPFE calculations. Based on an analysis of discrete dislocation plasticity, dislocation density is an effective variable to reflect slip, and plastic deformation and the residual plastic deformation during a cyclic loading process. Besides, dislocation density along inclined slip systems with special piling up patterns intrinsically represents the crack initiation potentials. Finally, based on results in our fretting simulations, dislocation density increases linearly with the number of loading cycles, regardless of contact size. Thus, this feature allows us to implement a quantitatively analysis on predicting the onset of micro-crack initiation

A new crack initiation criterion for films under fretting conditions would be proposed that is based on the dislocation density evolution. After experimental variation and support, damage parameters in CPFE calculations can be calibrated according to comparable discrete dislocation simulations. By carrying out this procedure, the current CPFE model would be improved by integrating more physics based fatigue parameters rather than empirical ones. Besides, the problem domain would be enlarged to part dimension level rather than focusing on the typical DDP problem dimension (*i.e.* ten times tens of micrometres). Furthermore, computational efficiency will be elevated as CPFE simulations take much less computational expense than DDP ones (*e.g.* please see Chapter 4). Although it is a hierarchical coupling as there would be no information feedback from CPFE to DDP scale, the method will be still able to shed some light on fatigue crack initiation of thin films under asperity fretting conditions.

7.5 Summary

Planar sliding and fretting problems have been simulated by applying crystal plasticity finite element (CPFE) and discrete dislocation plasticity (DDP) at different scales,

respectively. The formulations of CPFE and DDP employed herein are introduced in Chapter 3. The adaption and application of these formulations of CPFE and DDP on the indentation problem focuses on the highly localized plasticity rather than a global response as in tension problem discussed in Chapter 4. Also the numerical results on the tangential behaviour of specimens shown in this chapter complements the study on the normal behaviours in Chapter 5.

A large number of parametric study sets have been conducted in CPFE and DDP calculations to study microstructure influence on shear material performance under indentation contact, and a comparison between CPFE and DDP results discusses the difference of their material modelling methods at their own scales.

In this chapter, a newly proposed computational framework simulating fretting on thin films has been devised in DDP calculations. Results from this framework reveal the relation between dislocation structure and micro-crack initiation in fretting problems. An innovated crack initiation criterion is proposed based on these results and new coupling methods in the future. Details of this future work will be addressed in Chapter 8.

8 Conclusion and Future Work

This Chapter presents concluding remarks on this research project, and it consists of five sections. Section 8.1 briefly reviews the research results and how the initial objectives introduced in Introduction have been met and highlights the main innovations and contributions of this research project. Section 0 discusses the significance of the research results and implications for further engineering and research application. Section 8.3 describes limitations of the work presented in this thesis. Section 8.4 presents potential opportunities to extend the current study based on the proposed framework and limitations. Section 8.5 draws the final conclusions from the work presented in this thesis.

8.1 Summary and Key Contributions

This thesis has investigated main modelling approaches of material performance under various loading conditions and focused on microstructure influence. Mechanisms and codes of discrete dislocation plasticity (DDP) and crystal plasticity finite element (CPFE) are studied in details by applying their descriptions on specimens with various microstructures under several working conditions.

A method of concurrent coupling of planar discrete dislocation plasticity (DDP) and a crystal plasticity finite element (CPFE) method has been devised for simulating plastic deformation in specimens consisting of polycrystalline materials. This multi-scale material modelling is conducted with discrete dislocation resolution in a single grain or cluster of grains for computational efficiency; computation time using the coupling method can be reduced by at least an order of magnitude compared to DDP simulations only. The method is based on an iterative scheme initiated by a sub-model calculation, which ensures displacement and traction compatibility at all nodes at the interface between DDP and CPFE sub-regions.

The proposed multi-scale modelling approach has been validated by a benchmark uniaxial tension problem, and further applied to planar wedge-shaped indentation problems. A different coupling approach, where field information between DDP and CPFE sub-regions can be passed hierarchically between the scales has been suggested to be applied to sliding and fretting problems in future investigations.

The main results of this research are presented below together with the direct link to the initial research objectives introduced in Chapter 1.

Objective A: We aim to develop a general multi-scale modelling framework between DDP and CPFE by using a sub-model scheme. The multi-scale modelling framework should be able to cover different scales using DDP and CPFE, capture the material deformation details via dislocation activity in the sensitive region and improve the computational efficiency compared to modelling the whole region with DDP. The arrangement of sub-regions and corresponding microstructure should be flexible,

and the external boundary conditions should be applied according to different engineering problems.

Chapter 3 describes the proposed multi-scale coupling approach between discrete dislocation plasticity and crystal plasticity finite element methods. The coupling philosophy, boundary conditions passing between different sub-regions, the iterative scheme, convergence and validation are illustrated in a general way. The approach is innovated in that the iterative scheme adopted in boundary conditions passing inherently satisfies full characteristics of concurrent coupling method. This ensures the compatibility of tractions and deformations all through the problem domain. Most coupling tools reported [130, 311, 312] in literature were developed as a hierarchy method, *i.e.* there is only mono-directional information passing between sub-regions.

In Chapter 4 and Chapter 6, the proposed multi-scale coupling approach has been applied to uniaxial tension and wedge-shaped indentation problem, respectively. The uniaxial tension problem has also been used to validate effectiveness and robustness of the coupling approach, and boundary conditions passing between sub-regions at different scales; the iterative scheme and convergence have also been discussed in details.

Objective B: The proposed multi-scale coupling framework is to be applied to study the uniaxial tension problem. The specimen is modelled with the multi-scale polycrystalline and sub-region approach, and a uniaxial displacement is imposed on one boundary of the specimen while the other boundary is fixed. The traction and displacement compatibility must be satisfied along the nodes at the coupling boundary between CPFE and DDP sub-regions.

In Chapter 4, the proposed multi-scale coupling framework has been applied to the uniaxial tension problem. The specimen is modelled as two sub-regions with single crystals described by DDP and CPFE, respectively. Uniaxial displacement boundary condition is applied to simulate a tension test on the specimen. Compatibility of tractions and displacements are both satisfied at nodes along the coupling boundary between sub-regions. Both of the curves of stress strain response and dislocation density evolution are used to illustrate the effectiveness of this coupling technique in calculating stress and displacements across the sub-regions to be coupled using the two different descriptions. The size effect of uniaxial tension problem is also discussed by using both DDP simulations only and the coupled approach.

Objective C: The proposed multi-scale coupling framework is to be applied to wedge-shaped indentation problem. The specimen is modelled with the multi-scale polycrystalline and sub-region approach, and a uniform displacement rate is imposed on the indenter. The traction and displacement compatibility must be satisfied along the nodes at the coupling boundary between CPFE and DDP sub-regions.

In Chapter 5 and Chapter 6, the proposed multi-scale coupling framework has been applied to wedge-shaped indentation problems. The specimen is modelled as two sub-regions with the deformations and stresses of crystals described by DDP and CPFE formulations respectively. The primary region underneath indenter is modelled as DDP description, while the surrounding bulk material is modelled as CPFE description. Compatibility of tractions and displacements are both satisfied at nodes along the coupling boundary between sub-regions. The indentation pressure evolution curve, dislocation structure and slip contour are used to illustrate the coupling and substrate effect.

The application of the multi-scale modelling approach on a typical coating system quantitatively reveals the hardness evolution of a composite specimen. Based on the qualitative analysis of indentation pressure in DDP simulations, we have proposed a new formula describing indentation pressure variation on applied indention depth. Furthermore, the parameters in the newly proposed formula are provided with physical interpretations rather than simply empirical fitting. Besides, integrating the new indention pressure formula of thin films and the overall indentation pressure response of a coating system that is obtained by applying the proposed multi-scale modelling approach, a new formula that covers both of indentation size effect in discrete primary region with a characteristic length scale and the hardness transition from coating film to substrate has been proposed. This formula is the first effort to provide hardness prediction and analysis of a coating system with a physics based description.

Objective D: The proposed multi-scale coupling framework is to be applied to sliding and fretting problems. The specimen is modelled with the polycrystalline model and sub-model approach, and a uniform displacement rate is imposed on the sliding asperity. The application on the sliding and fretting problems aims to investigate the material performance under combined shear and pressure loading using DDP and CPFE. Also, the crack initiation of a polycrystalline film under a sliding or fretting loading should be investigated by studying the dislocation activities in the sensitive regions. A quantitative study of dislocation activity in DDP should provide intrinsic damage parameters for CPFE damage predictions.

In Chapter 7, simulations at different scales have been applied to sliding and fretting problems and suggestions have been made for the application of a multi-scale coupling strategy to these problems. Various simulations were firstly carried out for sliding problems using DDP and CPFE respectively, and dislocation activities from DDP calculations at sub-micron scale were considered to be able to provide damage parameters in terms of accumulated plastic strain for CPFE damage calculations at larger scales. Calculations were also carried out with DDP and CPFE methods to investigate parameters' influence in their own framework. The linkage between the dislocation structure/density and damage parameters in CPFE simulations has been investigated in the sliding and fretting problems. The damage parameters adopted in crystal plasticity simulations were once strongly relied on the experimental results [81,

194, 218, 313]. The dislocation structure and thus the consequent plastic discovered using DDP provides CPFE simulations with necessary damage parameters. Those parameters from DDP simulations with identical boundary condition as CPFE calculations are of more physical significance that sheds insight in predicting fatigue micro-crack initiation.

A new and independent discrete dislocation plasticity routine has been developed for planar fretting calculations. Although DDP framework has been applied to solve various problems at meso-scale, it has never been employed to investigate the cyclic micro-sliding, *i.e.* fretting problem. In this project, a Bash Shell script has been developed to cyclically conduct an adapted micro-sliding DDP code, and this effectively simulates fretting loading condition with an asperity at micro-scale. The evolution of shear stress and dislocation structure has been reported to verify the validation and robustness of this new computational framework.

8.2 Discussion and Applications of the Proposed Framework

This Section discusses the implications of this research for the use of the methodologies I developed for potential application to a wide set of engineering problems.

First, the proposed multi-scale coupling framework extends the domain of application of DDP simulations. Also, boundary value problem in continuum sub-region is solved using the commercial FEM package ABAQUS and relevant user subroutines. This ensures flexibility and reliability when the proposed coupling approach is applied on other engineering problems (different boundary value problems that can be solved using the concurrent coupling framework) and/or crystal plasticity formulations (*e.g.* can be easily adapted to use strain-dependent CPFE formulations).

Second, the application of the proposed multi-scale coupling framework on a coating system allows researchers to investigate its performance in a wide range of applied indentation depths. Compared to the previous coating film study performed using discrete dislocation plasticity and strain gradient plasticity [2, 18, 114], the proposed methodology is able to extend the range of indentation depths without sacrificing the indentation size effect regime captured by discrete dislocation plasticity. The technique can also be applied to predict indentation pressure and hardness of polycrystalline coatings.

Third, application of the DDP framework to sliding and fretting problems has been shown to be able to predict the dependence of surface properties, including friction coefficient and roughness, on dislocations' activity for thin films at the sub-micron scale.

Fourth, application of multi-scale coupling approaches to sliding and fretting problem allows for the first time to link macroscopic damage to the development of plastic flow and damage initiation at dislocations' level. The linkage between dislocation

structure/density and macroscopic damage provides researchers and engineers with a prospective computational tool to assess the origin of damage, and therefore to predict fatigue life and prevent possible catastrophic failure of key components.

Finally, the proposed coupling approach between DDP and CPFE provides a general concurrent framework that can also be extended to other scales and type of simulations. The general philosophy of the proposed coupling strategy is based on the compatibility of tractions and displacements at the boundary between different domains; hence this framework can be adapted to perform coupling between e.g. molecular dynamics and dislocation dynamics (although this would require performing evaluation of stresses in discrete systems before the information is passed across the scales) and between crystal plasticity and conventional continuum plasticity.

8.3 Limitations

Although this thesis contributes significantly to the development of multi-scale modelling tools, there still exist some limitations with the current approach and work carried out by the author. This Section addresses some of the general limitations in this research.

Firstly, the modelling of the coupling boundary between DDP and CPFE sub-regions has not been tackled using a unified approach. For example, in the uniaxial tension problem the coupling boundary is modelled as transparent to dislocations; however, under the loading conditions studied there are no dislocations passing through the coupling boundary due to characteristics of the problem under investigation. However, in the indentation problem, dislocations were found to pass through the coupling boundary when the coupling boundary is considered transparent to their motion as well. The injection of dislocations flux into CPFE sub-region caused unphysical behaviours in continuum sub-region and thus computational difficulty. The proposed multi-scale modelling could be improved if unified and automatic routines were made available to handle different transitions between the DDP and the CPFE regions.

Secondly, the proposed concurrent multi-scale coupling has not been applied in full to the sliding and fretting problems. It is suggested instead that information is passed using a one-way coupling scheme whereby parameters are obtained from the DDP sub-region to inform the CPFE sub-region; no information is passed from the CPFE sub-region to DDP sub-region to achieve compatibility of traction and displacement. The use of concurrent coupling in these scenarios is, however, easy to implement, with the major limitation being the large computational effort required to perform many loading cycle in the case of fretting simulations.

Finally, the general coupling framework and its application to different problems has not been generally verified against experiments. Although our simulation results are able to reflect the major features of corresponding experimental observations in general, further supporting experiments are still needed to fully verify the effectiveness of this coupling approach and its various applications. It is for example

essential to link the generation of damage and dislocation's activity to experimental evidence at the sub-micron scale.

8.4 Future Work

Based on the discussion of limitations of the current work, potential future work is proposed in the following paragraphs to extend the content of this project.

First, full consideration needs to be given to the modelling of the coupling boundary. On one hand, the coupling boundary can be considered as a rigid boundary, where dislocations cannot be transferred from discrete sub-regions to continuum sub-regions. On the other hand, the coupling boundary can also be considered as a transparent geometric boundary, where dislocations move freely from and to any sub-regions and thus the whole specimen can be considered as a single crystal. The physical understanding and numerical techniques that effective emission and absorption of dislocations between discrete sub-region and continuum sub-region needs take into consideration (see paper [130]).

Second, supporting experiments are needed to further prove the validity of the coupling framework and its application to the problems investigated iiinnn this thesis. Focus could be placed on the dislocation density and its structure pattern in sensitive regions (*e.g.* contact corners) and coupling boundaries.

Third, the mathematical foundation of the proposed coupling framework still needs improving, for example by performing an optimization of the iterative scheme. For instance, a relaxation approach could be employed to improve the convergence of traction and displacement between sub-regions and thus the overall coupling efficiency.

8.5 Conclusions

A key challenge of material modelling is that it needs to capture stresses and deformation mechanisms with high resolution in sensitive regions while simultaneously limit computational costs to be able to effectively model materials' behaviour from the micro- or sub-micro scales to the macro-scale. The proposed multi-scale coupling method has been shown to be capable of bridging the gap between modelling approaches working at different scales. In addition, the application of a multi-scale modelling method on engineering problems allows improving computational efficiency without loss of resolution in sensitive regions, were stress concentrations give rise to plastic deformations and damage.

The proposed multi-scale modelling approach, which links discrete dislocation plasticity (DDP) and crystal plasticity finite element (CPFE) methods via concurrent coupling, has been successfully applied to various common engineering problems, covering a wide range of scales.

The proposed multi-scale coupling approach has been validated by being applied on a uniaxial tension problem. Furthermore, the application of multi-scale modelling method on contact problems reveals the microstructure influence on the material performance under normal and shear loading. Besides, size effects are also investigated by applying discrete dislocation plasticity, crystal plasticity and the coupling approach to relevant problems.

In recent years, with the rise of demand from microstructure application and rapid development of computational tools and resources, the role of multi-scale modelling of material behaviour has become increasingly important in engineering analysis and risk assessment. The research presented in this thesis provides a valuable contribution to the development of the new generation of engineering predictive tools.

Reference

1. Balint, D.S., et al., *Size effects in uniaxial deformation of single and polycrystals: a discrete dislocation plasticity analysis.* Modelling and Simulation in Materials Science and Engineering, 2006. **14**(3): p. 409-422.
2. Balint, D.S., et al., *Discrete dislocation plasticity analysis of the wedge indentation of films.* Journal of the Mechanics and Physics of Solids, 2006. **54**(11): p. 2281-2303.
3. Deshpande, V.S., *Size effects in single asperity frictional contacts.* Modelling and Simulation in Materials Science and Engineering, 2007. **15**(1): p. S97-108.
4. Deshpande, V.S., *Discrete dislocation plasticity analysis of static friction.* Acta Materialia, 2004. **52**(10): p. 3135-49.
5. de Pablo, J.J. and W.A. Curtin, *Multiscale modeling in advanced materials research: Challenges, novel methods, and emerging applications.* Mrs Bulletin, 2007. **32**(11): p. 905-911.
6. Hall, E.O., *The Deformation and Ageing of Mild Steel: III Discussion of Results.* Proceedings of the Physical Society. Section B, 1951. **64**(9): p. 747.
7. Poole, W.J., M.F. Ashby, and N.A. Fleck, *Micro-hardness of annealed and work-hardened copper polycrystals.* Scripta Materialia, 1996. **34**(4): p. 559-564.
8. Ma, Q. and D.R. Clarke, *Size-Dependent Hardness of Silver Single-Crystals.* Journal of Materials Research, 1995. **10**(4): p. 853-863.
9. Stelmashenko, N.A., et al., *Microindentations on W and Mo Oriented Single-Crystals - an Stm Study.* Acta Metallurgica Et Materialia, 1993. **41**(10): p. 2855-2865.
10. Fleck, N.A., et al., *Strain Gradient Plasticity - Theory and Experiment.* Acta Metallurgica Et Materialia, 1994. **42**(2): p. 475-487.
11. Toupin, R.A., *Elastic materials with couple-stresses.* Archive for Rational Mechanics and Analysis, 1962. **11**(1): p. 385-414.
12. Mindlin, R., *Micro-structure in linear elasticity.* Archive for Rational Mechanics and Analysis, 1964. **16**(1): p. 51-78.
13. Smyshlyaev, V.P. and N.A. Fleck, *The role of strain gradients in the grain size effect for polycrystals.* Journal of the Mechanics and Physics of Solids, 1996. **44**(4): p. 465-495.
14. Gurtin, M.E., *On the plasticity of single crystals: free energy, microforces, plastic-strain gradients.* Journal of the Mechanics and Physics of Solids, 2000. **48**(5): p. 989-1036.
15. Sluys, L. and Y. Estrin, *The analysis of shear banding with a dislocation based gradient plasticity model.* International Journal of Solids and Structures, 2000. **37**(46): p. 7127-7142.
16. Wei, Y.G. and J.W. Hutchinson, *Steady-state crack growth and work of fracture for solids characterized by strain gradient plasticity.* Journal of the Mechanics and Physics of Solids, 1997. **45**(8): p. 1253-1273.
17. Begley, M.R. and J.W. Hutchinson, *The mechanics of size-dependent indentation.* Journal of the Mechanics and Physics of Solids, 1998. **46**(10): p. 2049-2068.

18. Nix, W.D. and H.J. Gao, *Indentation size effects in crystalline materials: A law for strain gradient plasticity.* Journal of the Mechanics and Physics of Solids, 1998. **46**(3): p. 411-425.
19. Shu, J.Y. and N.A. Fleck, *The prediction of a size effect in micro-indentation.* International Journal of Solids and Structures, 1998. **35**(13): p. 1363-1383.
20. Shu, J.Y., et al., *Boundary layers in constrained plastic flow: comparison of nonlocal and discrete dislocation plasticity.* Journal of the Mechanics and Physics of Solids, 2001. **49**(6): p. 1361-1395.
21. Roters, F., et al., *Overview of constitutive laws, kinematics, homogenization and multiscale methods in crystal plasticity finite-element modeling: Theory, experiments, applications.* Acta Materialia, 2010. **58**(4): p. 1152-1211.
22. Bishop, J.F.W. and R. Hill, *CXXVIII. A theoretical derivation of the plastic properties of a polycrystalline face-centred metal.* Philosophical Magazine Series 7, 1951. **42**(334): p. 1298-1307.
23. Bishop, J.F.W. and R. Hill, *XLVI. A theory of the plastic distortion of a polycrystalline aggregate under combined stresses.* Philosophical Magazine Series 7, 1951. **42**(327): p. 414-427.
24. Sachs, G., *Zur ableitung einer fliessbedingung*, in *Mitteilungen der deutschen Materialprüfungsanstalten*. 1929, Springer. p. 94-97.
25. Taylor, G.I., *Analysis of plastic strain in a cubic crystal.* Stephen Timoshenko 60th Anniversary Volume, 1938: p. 218-224.
26. Kroner, E., *On the plastic deformation of polycrystals.* acta metallurgica, 1961. **9**(2): p. 155-161.
27. Courant, R., *Variational methods for the solution of problems of equilibrium and vibrations.* Bull. Amer. Math. Soc, 1943. **49**(1): p. 1-23.
28. Zienkiewicz, O.C., *The finite element method in structural and continuum mechanics : numerical solution of problems in structural and continuum mechanics*. 1967, London: McGraw-Hill.
29. Simo, J.C. and T.J.R. Hughes, *Computational inelasticity*. Interdisciplinary applied mathematics. 1998, New York: Springer. xiv, 392 p.
30. Nematnas. and E.H. Lee, *Discussion of Elastic-Plastic Deformation at Finite Strains.* Journal of Applied Mechanics, 1970. **37**(1): p. 243-&.
31. Curtin, W.A. and R.E. Miller, *Atomistic/continuum coupling in computational materials science.* Modelling and Simulation in Materials Science and Engineering, 2003. **11**(3): p. R33-R68.
32. Arsenlis, A., et al., *On the evolution of crystallographic dislocation density in non-homogeneously deforming crystals.* Journal of the Mechanics and Physics of Solids, 2004. **52**(6): p. 1213-1246.
33. Cetinkaya, M., S.B. Xiao, and F. Grater, *Bottom-up computational modeling of semi-crystalline fibers: from atomistic to continuum scale.* Physical Chemistry Chemical Physics, 2011. **13**(22): p. 10426-10429.
34. Vitek, V., M. Mrovec, and J.L. Bassani, *Influence of non-glide stresses on plastic flow: from atomistic to continuum modeling.* Materials Science and Engineering a-Structural Materials Properties Microstructure and Processing, 2004. **365**(1-2): p. 31-37.

35. Sachtleber, M., Z. Zhao, and D. Raabe, *Experimental investigation of plastic grain interaction.* Materials Science and Engineering a-Structural Materials Properties Microstructure and Processing, 2002. **336**(1-2): p. 81-87.
36. Raabe, D., et al., *Grain-scale micromechanics of polycrystal surfaces during plastic straining.* Acta Materialia, 2003. **51**(6): p. 1539-1560.
37. Peirce, D., R. Asaro, and A. Needleman, *An analysis of nonuniform and localized deformation in ductile single crystals.* Acta metallurgica, 1982. **30**(6): p. 1087-1119.
38. Becker, R., *Analysis of texture evolution in channel die compression—I. Effects of grain interaction.* Acta metallurgica et materialia, 1991. **39**(6): p. 1211-1230.
39. Becker, R., et al., *Analysis of an aluminum single crystal with unstable initial orientation (001)[110] in channel die compression.* Metallurgical Transactions A, 1991. **22**(1): p. 45-58.
40. Anand, L. and M. Kothari, *A computational procedure for rate-independent crystal plasticity.* Journal of the Mechanics and Physics of Solids, 1996. **44**(4): p. 525-558.
41. Asaro, R.J., *Micromechanics of Crystals and Polycrystals.* Advances in Applied Mechanics, 1983. **23**: p. 1-115.
42. McGinty, R.D. and D.L. McDowell, *A semi-implicit integration scheme for rate independent finite crystal plasticity.* International Journal of Plasticity, 2006. **22**(6): p. 996-1025.
43. Peirce, D., R.J. Asaro, and A. Needleman, *Material Rate Dependence and Localized Deformation in Crystalline Solids.* Acta Metallurgica, 1983. **31**(12): p. 1951-1976.
44. Zhao, Z., et al., *Investigation of three-dimensional aspects of grain-scale plastic surface deformation of an aluminum oligocrystal.* International Journal of Plasticity, 2008. **24**(12): p. 2278-2297.
45. Becker, R. and S. Panchanadeeswaran, *Effects of Grain Interactions on Deformation and Local Texture in Polycrystals.* Acta Metallurgica Et Materialia, 1995. **43**(7): p. 2701-2719.
46. Sarma, G.B. and P.R. Dawson, *Texture predictions using a polycrystal plasticity model incorporating neighbor interactions.* International Journal of Plasticity, 1996. **12**(8): p. 1023-1054.
47. Zhao, Z., et al., *Influence of in-grain mesh resolution on the prediction of deformation textures in fcc polycrystals by crystal plasticity FEM.* Acta Materialia, 2007. **55**(7): p. 2361-2373.
48. Zhao, Z., et al., *Introduction of a texture component crystal plasticity finite element method for anisotropy simulations.* Advanced Engineering Materials, 2001. **3**(12): p. 984-990.
49. Raabe, D. and F. Roters, *Using texture components in crystal plasticity finite element simulations.* International Journal of Plasticity, 2004. **20**(3): p. 339-361.
50. Melchior, M.A. and L. Delannay, *A texture discretization technique adapted to polycrystalline aggregates with non-uniform grain size.* Computational Materials Science, 2006. **37**(4): p. 557-564.
51. Toth, L.S. and P. Vanhoutte, *Discretization Techniques for Orientation Distribution-Functions.* Textures and Microstructures, 1992. **19**(4): p. 229-244.

52. Eisenlohr, P. and F. Roters, *Selecting a set of discrete orientations for accurate texture reconstruction.* Computational Materials Science, 2008. **42**(4): p. 670-678.
53. Suiker, A.S. and S. Turteltaub, *Computational modelling of plasticity induced by martensitic phase transformations.* International journal for numerical methods in engineering, 2005. **63**(12): p. 1655-1693.
54. Staroselsky, A. and L. Anand, *A constitutive model for hcp materials deforming by slip and twinning: application to magnesium alloy AZ31B.* International journal of Plasticity, 2003. **19**(10): p. 1843-1864.
55. Ma, A., F. Roters, and D. Raabe, *Studying the effect of grain boundaries in dislocation density based crystal-plasticity finite element simulations.* International Journal of Solids and Structures, 2006. **43**(24): p. 7287-7303.
56. Ma, A., F. Roters, and D. Raabe, *On the consideration of interactions between dislocations and grain boundaries in crystal plasticity finite element modeling - Theory, experiments, and simulations.* Acta Materialia, 2006. **54**(8): p. 2181-2194.
57. Bieler, T.R., et al., *The role of heterogeneous deformation on damage nucleation at grain boundaries in single phase metals.* International Journal of Plasticity, 2009. **25**(9): p. 1655-1683.
58. Dini, D., et al., *Residual strain analysis in polycrystalline aggregates using diffraction measurement and finite element modelling.* Journal of Strain Analysis for Engineering Design, 2009. **44**(1): p. 55-70.
59. Dini, D., A.M. Korsunsky, and F.P.E. Dunne, *Diffraction post-processor for polycrystalline plasticity modelling.* Residual Stresses Vii, 2006. **524-525**: p. 427-432.
60. Korsunsky, A.M., et al., *Comparative assessment of dissipated energy and other fatigue criteria.* International Journal of Fatigue, 2007. **29**(9-11): p. 1990-1995.
61. Song, X., et al., *Finite element modelling and diffraction measurement of elastic strains during tensile deformation of HCP polycrystals.* Computational Materials Science, 2008. **44**(1): p. 131-137.
62. Song, X., et al., *Inter-granular residual stresses in polycrystalline aggregates: finite element modelling and diffraction post-processing.* Stress Evaluation in Materials Using Neutrons and Synchrotron Radiation, 2008. **571-572**: p. 271-276.
63. Hill, R. and J.R. Rice, *Constitutive Analysis of Elastic-Plastic Crystals at Arbitrary Strain.* Journal of the Mechanics and Physics of Solids, 1972. **20**(6): p. 401-+.
64. Sarma, G.B., B. Radhakrishnan, and T. Zacharia, *Finite element simulations of cold deformation at the mesoscale.* Computational Materials Science, 1998. **12**(2): p. 105-123.
65. Kocks, U.F., *Laws for Work-Hardening and Low-Temperature Creep.* Journal of Engineering Materials and Technology-Transactions of the Asme, 1976. **98**(1): p. 76-85.
66. Kocks, U., *A statistical theory of flow stress and work-hardening.* Philosophical Magazine, 1966. **13**(123): p. 541-566.

67. Arsenlis, A. and D. Parks, *Crystallographic aspects of geometrically-necessary and statistically-stored dislocation density.* Acta Materialia, 1999. **47**(5): p. 1597-1611.
68. Cheong, K.S. and E.P. Busso, *Discrete dislocation density modelling of single phase FCC polycrystal aggregates.* Acta Materialia, 2004. **52**(19): p. 5665-5675.
69. Ma, A., F. Roters, and D. Raabe, *A dislocation density based constitutive model for crystal plasticity FEM including geometrically necessary dislocations.* Acta Materialia, 2006. **54**(8): p. 2169-2179.
70. Gao, H. and Y. Huang, *Geometrically necessary dislocation and size-dependent plasticity.* Scripta Materialia, 2003. **48**(2): p. 113-118.
71. Kucharski, S. and D. Jarzabek, *Depth Dependence of Nanoindentation Pile-Up Patterns in Copper Single Crystals.* Metallurgical and Materials Transactions a-Physical Metallurgy and Materials Science, 2014. **45A**(11): p. 4997-5008.
72. Wang, Y., et al., *Orientation dependence of nanoindentation pile-up patterns and of nanoindentation microtextures in copper single crystals.* Acta Materialia, 2004. **52**(8): p. 2229-2238.
73. Zaafarani, N., et al., *Three-dimensional investigation of the texture and microstructure below a nanoindent in a Cu single crystal using 3D EBSD and crystal plasticity finite element simulations.* Acta Materialia, 2006. **54**(7): p. 1863-1876.
74. Zaafarani, N., et al., *On the origin of deformation-induced rotation patterns below nanoindents.* Acta Materialia, 2008. **56**(1): p. 31-42.
75. Raabe, D., D. Ma, and F. Roters, *Effects of initial orientation, sample geometry and friction on anisotropy and crystallographic orientation changes in single crystal microcompression deformation: A crystal plasticity finite element study.* Acta Materialia, 2007. **55**(13): p. 4567-4583.
76. Weber, F., et al., *Texture evolution during bending of a single crystal copper nanowire studied by EBSD and crystal plasticity finite element simulations.* Advanced Engineering Materials, 2008. **10**(8): p. 737-741.
77. Fleck, N.A. and J.W. Hutchinson, *Strain gradient plasticity.* Advances in Applied Mechanics, Vol 33, 1997. **33**: p. 295-361.
78. Dunne, F.P.E. and D. Rugg, *On the mechanisms of fatigue facet nucleation in titanium alloys.* Fatigue & Fracture of Engineering Materials & Structures, 2008. **31**(11): p. 949-958.
79. Dunne, F.P.E., A. Walker, and D. Rugg, *A systematic study of hcp crystal orientation and morphology effects in polycrystal deformation and fatigue.* Proceedings of the Royal Society a-Mathematical Physical and Engineering Sciences, 2007. **463**(2082): p. 1467-1489.
80. Dunne, F.P.E., A.J. Wilkinson, and R. Allen, *Experimental and computational studies of low cycle fatigue crack nucleation in a polycrystal.* International Journal of Plasticity, 2007. **23**(2): p. 273-295.
81. Dunne, F.P.E., D. Rugg, and A. Walker, *Lengthscale-dependent, elastically anisotropic, physically-based hcp crystal plasticity: Application to cold-dwell fatigue in Ti alloys.* International Journal of Plasticity, 2007. **23**(6): p. 1061-1083.
82. Nye, J., *Some geometrical relations in dislocated crystals.* Acta metallurgica, 1953. **1**(2): p. 153-162.

83. AbdulLatif, A. and K. Saanouni, *Micromechanical modeling of low cycle fatigue under complex loadings .2. Applications.* International Journal of Plasticity, 1996. **12**(9): p. 1123-1149.
84. Toth, L.S., A. Molinari, and N. Zouhal, *Cyclic plasticity phenomena as predicted by polycrystal plasticity.* Mechanics of Materials, 2000. **32**(2): p. 99-113.
85. Manonukul, A. and F.P.E. Dunne, *High- and low-cycle fatigue crack initiation using polycrystal plasticity.* Proceedings of the Royal Society of London Series a-Mathematical Physical and Engineering Sciences, 2004. **460**(2047): p. 1881-1903.
86. Bennett, V.P. and D.L. McDowell, *Polycrystal orientation distribution effects on microslip in high cycle fatigue.* International Journal of Fatigue, 2003. **25**(1): p. 27-39.
87. Dunne, F.P.E., R. Kiwanuka, and A.J. Wilkinson, *Crystal plasticity analysis of micro-deformation, lattice rotation and geometrically necessary dislocation density.* Proceedings of the Royal Society a-Mathematical Physical and Engineering Sciences, 2012. **468**(2145): p. 2509-2531.
88. McHugh, P.E. and R. Mohrmann, *Modelling of creep in a Ni base superalloy using a single crystal plasticity model.* Computational Materials Science, 1997. **9**(1-2): p. 134-140.
89. Balasubramanian, S. and L. Anand, *Plasticity of initially textured hexagonal polycrystals at high homologous temperatures: application to titanium.* Acta Materialia, 2002. **50**(1): p. 133-148.
90. Bate, P., *Modelling deformation microstructure with the crystal plasticity finite-element method.* Philosophical Transactions of the Royal Society a-Mathematical Physical and Engineering Sciences, 1999. **357**(1756): p. 1589-1601.
91. Hull, D. and D.J. Bacon, *Introduction to dislocations*. 4th ed. 2001, Oxford Oxfordshire ; Boston: Butterworth-Heinemann. vii, 242 p.
92. Brown, L.M., *The self-stress of dislocations and the shape of extended nodes.* Philosophical Magazine, 1964. **10**(105): p. 441-466.
93. Bacon, D.J., *A Method for Describing a Flexible Dislocation.* physica status solidi (b), 1967. **23**(2): p. 527-538.
94. Foreman, A.J.E., *The bowing of a dislocation segment.* Philosophical Magazine, 1967. **15**(137): p. 1011-1021.
95. Amodeo, R.J. and N.M. Ghoniem, *Dislocation Dynamics .1. A Proposed Methodology for Deformation Micromechanics.* Physical Review B, 1990. **41**(10): p. 6958-6967.
96. Kubin, L.P., et al., *Dislocation microstructures and plastic flow: a 3D simulation.* Solid State Phenomena, 1992. **23**: p. 455-472.
97. Kocks, U.F. and H. Mecking, *Physics and phenomenology of strain hardening: the FCC case.* Progress in Materials Science, 2003. **48**(3): p. 171-273.
98. Lubarda, V.A., J.A. Blume, and A. Needleman, *An Analysis of Equilibrium Dislocation Distributions.* Acta Metallurgica Et Materialia, 1993. **41**(2): p. 625-642.

99. Vandergiessen, E. and A. Needleman, *Discrete Dislocation Plasticity - a Simple Planar Model.* Modelling and Simulation in Materials Science and Engineering, 1995. **3**(5): p. 689-735.
100. Groh, S. and H.M. Zbib, *Advances in Discrete Dislocations Dynamics and Multiscale Modeling.* Journal of Engineering Materials and Technology-Transactions of the Asme, 2009. **131**(4).
101. Madec, R., B. Devincre, and L.P. Kubin, *New Line Model for Optimized Dislocation Dynamics Simulations.* MRS Online Proceedings Library, 2000. **653**: p. null-null.
102. Devincre, B., et al., *Mesoscopic simulations of plastic deformation.* Materials Science and Engineering a-Structural Materials Properties Microstructure and Processing, 2001. **309**: p. 211-219.
103. Zbib, H.M., M. Rhee, and J.P. Hirth, *On plastic deformation and the dynamics of 3D dislocations.* International Journal of Mechanical Sciences, 1998. **40**(2-3): p. 113-127.
104. Ghoniem, N.M. and L.Z. Sun, *Fast-sum method for the elastic field off three-dimensional dislocation ensembles.* Physical Review B, 1999. **60**(1): p. 128-140.
105. Ghoniem, N.M., J.M. Huang, and Z.Q. Wang, *Affine covariant-contravariant vector forms for the elastic field of parametric dislocations in isotropic crystals.* Philosophical Magazine Letters, 2002. **82**(2): p. 55-63.
106. Schwarz, K.W., *Simulation of dislocations on the mesoscopic scale. I. Methods and examples.* Journal of Applied Physics, 1999. **85**(1): p. 108-119.
107. Schwarz, K.W., *Simulation of dislocations on the mesoscopic scale. II. Application to strained-layer relaxation.* Journal of Applied Physics, 1999. **85**(1): p. 120-129.
108. Rhee, M., et al., *Dislocation stress fields for dynamic codes using anisotropic elasticity: methodology and analysis.* Materials Science and Engineering: A, 2001. **309**: p. 288-293.
109. Cleveringa, H.H.M., E. Van der Giessen, and A. Needleman, *A discrete dislocation analysis of bending.* International Journal of Plasticity, 1999. **15**(8): p. 837-868.
110. Balint, D.S., et al., *A discrete dislocation plasticity analysis of grain-size strengthening.* Materials Science and Engineering a-Structural Materials Properties Microstructure and Processing, 2005. **400**: p. 186-190.
111. Kreuzer, H.G.M. and R. Pippan, *Discrete dislocation simulation of nanoindentation: the influence of obstacles and a limited number of dislocation sources.* Philosophical Magazine, 2005. **85**(28): p. 3301-3319.
112. Kreuzer, H.G.M. and R. Pippan, *Discrete dislocation simulation of nanoindentation.* Computational Mechanics, 2004. **33**(4): p. 292-298.
113. Polonsky, I.A. and L.M. Keer, *Simulation of microscopic elastic-plastic contacts by using discrete dislocations.* Proceedings of the Royal Society of London Series a-Mathematical Physical and Engineering Sciences, 1996. **452**(1953): p. 2173-2194.
114. Widjaja, A., E. Van der Giessen, and A. Needleman, *Discrete dislocation modelling of submicron indentation.* Materials Science and Engineering a-

Structural Materials Properties Microstructure and Processing, 2005. **400**: p. 456-459.

115. Widjaja, A., A. Needleman, and E. Van der Giessen, *The effect of indenter shape on sub-micron indentation according to discrete dislocation plasticity.* Modelling and Simulation in Materials Science and Engineering, 2007. **15**(1): p. S121-S131.
116. Kreuzer, H.G.M. and R. Pippan, *Discrete dislocation simulation of nanoindentation: the effect of moving conditions and indenter shape.* Materials Science and Engineering a-Structural Materials Properties Microstructure and Processing, 2004. **387**: p. 254-256.
117. Swadener, J.G., E.P. George, and G.M. Pharr, *The correlation of the indentation size effect measured with indenters of various shapes.* Journal of the Mechanics and Physics of Solids, 2002. **50**(4): p. 681-694.
118. Kreuzer, H.G.M. and R. Pippan, *Discrete dislocation simulation of nanoindentation: Indentation size effect and the influence of slip band orientation.* Acta Materialia, 2007. **55**(9): p. 3229-3235.
119. Yin, X. and K. Komvopoulos, *A Discrete Dislocation Plasticity Analysis of a Single-Crystal Half-Space Indented by a Rigid Cylinder.* Journal of Applied Mechanics-Transactions of the Asme, 2011. **78**(4).
120. Tarleton, E., et al., *A discrete dislocation plasticity study of the micro-cantilever size effect.* Acta Materialia, 2015. **88**: p. 271-282.
121. Shilkrot, L.E., W.A. Curtin, and R.E. Miller, *A coupled atomistic/continuum model of defects in solids.* Journal of the Mechanics and Physics of Solids, 2002. **50**(10): p. 2085-2106.
122. Jarvis, E.A.A., R.L. Hayes, and E.A. Carter, *Effects of oxidation on the nanoscale mechanisms of crack formation in aluminum.* Chemphyschem, 2001. **2**(1): p. 55-59.
123. Gall, K., et al., *Atomistic simulations on the tensile debonding of an aluminum-silicon interface.* Journal of the Mechanics and Physics of Solids, 2000. **48**(10): p. 2183-2212.
124. Cleveringa, H.H.M., E. VanderGiessen, and A. Needleman, *Comparison of discrete dislocation and continuum plasticity predictions for a composite material.* Acta Materialia, 1997. **45**(8): p. 3163-3179.
125. Gumbsch, P., et al., *Continuum Modeling of Dislocation Plasticity: Theory, Numerical Implementation and Comparison to Discrete Dislocation Simulations.* Advances in Heterogeneous Material Mechanics 2011, 2011: p. 7-15.
126. Kubin, L.P. and G. Canova, *The Modeling of Dislocation Patterns.* Scripta Metallurgica Et Materialia, 1992. **27**(8): p. 957-962.
127. Pettifor, D.G., et al., *Bond-order potentials: bridging the electronic to atomistic modelling hierarchies.* Computational Materials Science, 2002. **23**(1-4): p. 33-37.
128. Shilkrot, L.E., R.E. Miller, and W.A. Curtin, *Multiscale plasticity modeling: coupled atomistics and discrete dislocation mechanics.* Journal of the Mechanics and Physics of Solids, 2004. **52**(4): p. 755-787.

129. Tadmor, E.B., M. Ortiz, and R. Phillips, *Quasicontinuum analysis of defects in solids.* Philosophical Magazine a-Physics of Condensed Matter Structure Defects and Mechanical Properties, 1996. **73**(6): p. 1529-1563.
130. Curtin, W.A., et al., *Multi-scale plasticity modeling: Coupled discrete dislocation and continuum crystal plasticity.* Advances in Heterogeneous Material Mechanics 2008, 2008: p. 320-320.
131. Akasheh, F., H.M. Zbib, and T. Ohashi, *Multiscale modelling of size effect in fcc crystals: discrete dislocation dynamics and dislocation-based gradient plasticity.* Philosophical Magazine, 2007. **87**(8-9): p. 1307-1326.
132. Akarapu, S., H.M. Zbib, and D.F. Bahr, *Analysis of heterogeneous deformation and dislocation dynamics in single crystal micropillars under compression.* International Journal of Plasticity, 2010. **26**(2): p. 239-257.
133. Khan, S.M. and L.E. Levine, *Multi-scale Discrete Dislocation Plasticity Analysis: Application to Nano-indentation.* 2006.
134. Gao, Y., et al., *A hybrid multiscale computational framework of crystal plasticity at submicron scales.* Computational Materials Science, 2010. **49**(3): p. 672-681.
135. Wang, S., et al., *A virtual crystal plasticity simulation tool for micro-forming.* Mesomechanics 2009, 2009. **1**(1): p. 75-78.
136. Zhang, D.H. and S.Y. Li, *A Rate-Dependent Crystal Plasticity Analysis of Orientation Stability in Biaxial Tension of Magnesium.* Journal of Materials Science & Technology, 2011. **27**(2): p. 175-182.
137. Dong, H., et al., *Study of fcc metal tension behaviour by crystal plasticity finite element method.* Materials Science and Technology, 2012. **28**(7): p. 788-793.
138. Kiener, D., et al., *A further step towards an understanding of size-dependent crystal plasticity: In situ tension experiments of miniaturized single-crystal copper samples.* Acta Materialia, 2008. **56**(3): p. 580-592.
139. Deshpande, V.S., A. Needleman, and E. Van der Giessen, *Discrete dislocation plasticity analysis of single slip tension.* Materials Science and Engineering a-Structural Materials Properties Microstructure and Processing, 2005. **400**: p. 154-157.
140. Casals, O., J. Ocenasek, and J. Alcala, *Crystal plasticity finite element simulations of pyramidal indentation in copper single crystals.* Acta Materialia, 2007. **55**(1): p. 55-68.
141. Demir, E., et al., *Investigation of the indentation size effect through the measurement of the geometrically necessary dislocations beneath small indents of different depths using EBSD tomography.* Acta Materialia, 2009. **57**(2): p. 559-569.
142. Alcala, J., O. Casals, and J. Ocenasek, *Micromechanics of pyramidal indentation in fcc metals: Single crystal plasticity finite element analysis.* Journal of the Mechanics and Physics of Solids, 2008. **56**(11): p. 3277-3303.
143. Liu, Y., et al., *Combined numerical simulation and nanoindentation for determining mechanical properties of single crystal copper at mesoscale.* Journal of the Mechanics and Physics of Solids, 2005. **53**(12): p. 2718-2741.
144. Alcala, J., O. Casals, and J. Ocenasek, *Micromechanics of pyramidal indentation in fcc metals: Single crystal plasticity finite element analysis (vol 56, pg 3277, 2008).* Journal of the Mechanics and Physics of Solids, 2010. **58**(5): p. 751-751.

145. Tabor, D., *The hardness of metals*. Monographs on the physics and chemistry of materials. 1951, Oxford: Clarendon Press. ix, 175 p.
146. Johnson, K.L., *The correlation of indentation experiments.* Journal of the Mechanics and Physics of Solids, 1970. **18**(2): p. 115.
147. Stegall, D.E., et al., *Indentation size effect in FCC metals: An examination of experimental techniques and the bilinear behavior.* Journal of Materials Research, 2012. **27**(12): p. 1543-1552.
148. Chen, K., W.J. Meng, and G.B. Sinclair, *Size dependence of the plane-strain response of single-crystal Al to indentation by diamond wedges.* Acta Materialia, 2012. **60**(12): p. 4879-4887.
149. Korsunsky, A.M., et al., *On the hardness of coated systems.* Surface & Coatings Technology, 1998. **99**(1-2): p. 171-183.
150. Tuck, J.R., et al., *On the application of the work-of-indentation approach to depth-sensing indentation experiments in coated systems.* Surface & Coatings Technology, 2001. **137**(2-3): p. 217-224.
151. Eringen, A.C., *Nonlocal continuum field theories*. 2002, New York: Springer. xvi, 376 p.
152. Wei, Y.G. and J.W. Hutchinson, *Hardness trends in micron scale indentation.* Journal of the Mechanics and Physics of Solids, 2003. **51**(11-12): p. 2037-2056.
153. Qu, S., et al., *The indentation size effect in the spherical indentation of iridium: A study via the conventional theory of mechanism-based strain gradient plasticity.* International Journal of Plasticity, 2006. **22**(7): p. 1265-1286.
154. Guo, Y., et al., *Taylor-based nonlocal theory of plasticity: numerical studies of the micro-indentation experiments and crack tip fields.* International Journal of Solids and Structures, 2001. **38**(42-43): p. 7447-7460.
155. Eringen, A.C., *Theories of Nonlocal Plasticity.* International journal of engineering science, 1983. **21**(7): p. 741-751.
156. Lou, J., et al., *Nanoindentation study of plasticity length scale effects in LIGA Ni microelectromechanical systems structures.* Journal of Materials Research, 2003. **18**(3): p. 719-728.
157. Nicola, L., et al., *Surface versus bulk nucleation of dislocations during contact.* Journal of the Mechanics and Physics of Solids, 2007. **55**(6): p. 1120-1144.
158. Zhang, Y.H., Y.F. Gao, and L. Nicola, *Lattice rotation caused by wedge indentation of a single crystal: Dislocation dynamics compared to crystal plasticity simulations.* Journal of the Mechanics and Physics of Solids, 2014. **68**: p. 267-279.
159. Zhang, Y.H. and L. Nicola, *Effect of template shape on metal nanoimprinting: a dislocation dynamics study.* Journal of Zhejiang University-Science A, 2010. **11**(10): p. 722-726.
160. Zhang, Y.H., E. Van der Giessen, and L. Nicola, *Discrete dislocation simulations of the flattening of nanoimprinted surfaces.* Modelling and Simulation in Materials Science and Engineering, 2010. **18**(3).
161. Saha, R., et al., *Indentation of a soft metal film on a hard substrate: strain gradient hardening effects.* Journal of the Mechanics and Physics of Solids, 2001. **49**(9): p. 1997-2014.

162. Saha, R. and W.D. Nix, *Effects of the substrate on the determination of thin film mechanical properties by nanoindentation.* Acta Materialia, 2002. **50**(1): p. 23-38.
163. Saha, R. and W.D. Nix, *Soft films on hard substrates - nanoindentation of tungsten films on sapphire substrates.* Materials Science and Engineering a-Structural Materials Properties Microstructure and Processing, 2001. **319**: p. 898-901.
164. Han, S.M., R. Saha, and W.D. Nix, *Determining hardness of thin films in elastically mismatched film-on-substrate systems using nanoindentation.* Acta Materialia, 2006. **54**(6): p. 1571-1581.
165. Fivel, M.C., et al., *Three-dimensional modeling of indent-induced plastic zone at a mesoscale.* Acta Materialia, 1998. **46**(17): p. 6183-6194.
166. Nicola, L., et al., *Multi-asperity contact: A comparison between discrete dislocation and crystal plasticity predictions.* Philosophical Magazine, 2008. **88**(30-32): p. 3713-3729.
167. Bowden, F.P. and D. Tabor, *The friction and lubrication of solids*. Oxford classic texts in the physical sciences. 2001, Oxford: Oxford University Press. xviii, 374 p.
168. Tangena, A.G. and P.J.M. Wijnhoven, *Finite-Element Calculations on the Influence of Surface-Roughness on Friction.* Wear, 1985. **103**(4): p. 345-354.
169. Green, A., *Friction between unlubricated metals: a theoretical analysis of the junction model.* Proceedings of the Royal Society of London. Series A. Mathematical and Physical Sciences, 1955. **228**(1173): p. 191-204.
170. Ohmae, N., *Analysis of the Large Plastic-Deformation Involved in Wear Processes Using the Finite-Element Method with an Updated Lagrangian Formulation.* Journal of Tribology-Transactions of the Asme, 1987. **109**(2): p. 330-337.
171. Chang, W.R., I. Etsion, and D.B. Bogy, *An Elastic-Plastic Model for the Contact of Rough Surfaces.* Journal of Tribology-Transactions of the Asme, 1987. **109**(2): p. 257-263.
172. Kapoor, A., K.L. Johnson, and J.A. Williams, *A model for the mild ratchetting wear of metals.* Wear, 1996. **200**(1-2): p. 38-44.
173. Storakers, B., S. Biwa, and P.L. Larsson, *Similarity analysis of inelastic contact.* International Journal of Solids and Structures, 1997. **34**(24): p. 3061-3083.
174. Kogut, L. and I. Etsion, *A static friction model for elastic-plastic contacting rough surfaces.* Journal of Tribology-Transactions of the Asme, 2004. **126**(1): p. 34-40.
175. Dieterich, J.H., *Modeling of Rock Friction .1. Experimental Results and Constitutive Equations.* Journal of Geophysical Research, 1979. **84**(Nb5): p. 2161-2168.
176. Ruina, A., *Slip Instability and State Variable Friction Laws.* Journal of Geophysical Research, 1983. **88**(Nb12): p. 359-370.
177. Prakash, V. and R.J. Clifton, *Pressure-Shear Plate Impact Measurement of Dynamic Friction for High-Speed Machining Applications.* Proceedings of the Vii International Congress on Experimental Mechanics, Vols 1 and 2, 1992: p. 556-564.

178. Gearing, B.P., H.S. Moon, and L. Anand, *A plasticity model for interface friction: application to sheet metal forming.* International Journal of Plasticity, 2001. **17**(2): p. 237-271.
179. Kuhlmann-Wilsdorf, D., *Dislocation concepts in friction and wear.* Unknown, 1980. **1**.
180. Rigney, D.A., *Fundamentals of friction and wear of materials : papers presented at the 1980 ASM Materials Science Seminar 4-5 October 1980, Pittsburgh, Pennsylvania*. 1981, Metals Park, Ohio: ASM.
181. Rigney, D.A., *Large strains associated with sliding contact of metals.* Materials Research Innovations, 1998. **1**(4): p. 231-234.
182. Polonsky, I.A. and L.M. Keer, *Simulation of microscopic elastic-plastic contacts by using discrete dislocations.* Proceedings of the Royal Society a-Mathematical Physical and Engineering Sciences, 1996. **452**(1953): p. 2173-2194.
183. Polonsky, I.A. and L.M. Keer, *Scale effects of elastic-plastic behavior of microscopic asperity contacts.* Journal of Tribology-Transactions of the Asme, 1996. **118**(2): p. 335-340.
184. Bhushan, B. and M. Nosonovsky, *Scale effects in friction using strain gradient plasticity and dislocation-assisted sliding (microslip).* Acta Materialia, 2003. **51**(14): p. 4331-4345.
185. Hurtado, J.A. and K.S. Kim, *Scale effects in friction of single-asperity contacts. II. Multiple-dislocation-cooperated slip.* Proceedings of the Royal Society a-Mathematical Physical and Engineering Sciences, 1999. **455**(1989): p. 3385-3400.
186. Hurtado, J.A. and K.S. Kim, *Scale effects in friction of single-asperity contacts. I. From concurrent slip to single-dislocation-assisted slip.* Proceedings of the Royal Society a-Mathematical Physical and Engineering Sciences, 1999. **455**(1989): p. 3363-3384.
187. Rice, J.R. and R. Thomson, *Ductile Versus Brittle Behavior of Crystals.* Philosophical Magazine, 1974. **29**(1): p. 73-97.
188. Landman, U., et al., *Molecular-Dynamics Simulations of Adhesive Contact Formation and Friction.* Fundamentals of Friction : Macroscopic and Microscopic Processes, 1992. **220**: p. 463-510.
189. Gerde, E. and M. Marder, *Friction and fracture.* Nature, 2001. **413**(6853): p. 285-288.
190. Schijve, J., *Fatigue of structures and materials*. 2nd ed. ed. 2009, Dordrecht ; London: Springer.
191. Klesnil, M. and P. Luka\s\030C, *Fatigue of metallic materials*. 1992, Amsterdam ; Oxford: Elsevier.
192. Davidson, D.L. and K.S. Chan, *The Crystallography of Fatigue Crack Initiation in Coarse-Grained Astroloy at 20-Degrees-C.* Acta Metallurgica, 1989. **37**(4): p. 1089-1097.
193. Chan, K.S., *Roles of microstructure in fatigue crack initiation.* International Journal of Fatigue, 2010. **32**(9): p. 1428-1447.
194. Nowell, D., D. Dini, and D.A. Hills, *Recent developments in the understanding of fretting fatigue.* Engineering Fracture Mechanics, 2006. **73**(2): p. 207-222.

195. Szolwinski, M.P. and T.N. Farris, *Mechanics of fretting fatigue crack formation.* Wear, 1996. **198**(1–2): p. 93-107.
196. Warlow-Davies, E., *Fretting corrosion and fatigue strength: brief results of preliminary experiments.* Proceedings of the Institution of Mechanical Engineers, 1941. **146**(1): p. 32-38.
197. Tomlinson, G., P. Thorpe, and H. Gough, *An investigation of the fretting corrosion of closely fitting surfaces.* Proceedings of the Institution of Mechanical Engineers, 1939. **141**(1): p. 223-249.
198. Szolwinski, M.P. and T.N. Farris, *Mechanics of fretting fatigue crack formation.* Wear, 1996. **198**(1-2): p. 93-107.
199. Hills, D.A., *Mechanics of Fretting Fatigue.* Wear, 1994. **175**(1-2): p. 107-113.
200. Zhang, M., J. Zhang, and D.L. McDowell, *Micro structure-based crystal plasticity modeling of cyclic deformation of Ti-6Al-4V.* International Journal of Plasticity, 2007. **23**(8): p. 1328-1348.
201. Brinckmann, S. and E. Van der Giessen, *A discrete dislocation dynamics study aiming at understanding fatigue crack initiation.* Materials Science and Engineering a-Structural Materials Properties Microstructure and Processing, 2004. **387**: p. 461-464.
202. Cleveringa, H.H.M., E. Van der Giessen, and A. Needleman, *A discrete dislocation analysis of crack growth under cyclic loading.* Multiscale Phenomena in Materials-Experiments and Modeling, 2000. **578**: p. 293-302.
203. McCarthy, O.J., J.P. McGarry, and S.B. Leen, *The effect of grain orientation on fretting fatigue plasticity and life prediction.* Tribology International, 2014. **76**: p. 100-115.
204. Zhang, M., *Microstructure sensitivity of fretting fatigue based on computational crystal plasticity.* Tribology International, 2009. **42**(9): p. 1286-1296.
205. Hills, D.A. and M. Comninou, *An Analysis of Fretting Fatigue Cracks during Loading Phase.* International Journal of Solids and Structures, 1985. **21**(7): p. 721-730.
206. Nowell, D. and D.A. Hills, *Mechanics of Fretting Fatigue Tests.* International Journal of Mechanical Sciences, 1987. **29**(5): p. 355-365.
207. Hills, D.A., D. Nowell, and J.J. Oconnor, *On the Mechanics of Fretting Fatigue.* Wear, 1988. **125**(1-2): p. 129-146.
208. Kuno, M., et al., *Initiation and Growth of Fretting Fatigue Cracks in the Partial Slip Regime.* Fatigue & Fracture of Engineering Materials & Structures, 1989. **12**(5): p. 387-398.
209. Nowell, D. and D.A. Hills, *Crack Initiation Criteria in Fretting Fatigue.* Wear, 1990. **136**(2): p. 329-343.
210. Fellows, L.J., D. Nowell, and D.A. Hills, *On the initiation of fretting fatigue cracks.* Wear, 1997. **205**(1-2): p. 120-129.
211. Fellows, L.J., D. Nowell, and D.A. Hills, *Analysis of crack initiation and propagation in fretting fatigue: The effective initial flaw size methodology.* Fatigue & Fracture of Engineering Materials & Structures, 1997. **20**(1): p. 61-70.

212. Moobola, R., D.A. Hills, and D. Nowell, *Designing against fretting fatigue: crack self-arrest.* Journal of Strain Analysis for Engineering Design, 1998. **33**(1): p. 17-25.
213. Dini, D. and D.A. Hills, *A consideration of the effects of the slip displacement on fretting fatigue behaviour.* Journal of Strain Analysis for Engineering Design, 2004. **39**(4): p. 397-407.
214. Hills, D.A. and D. Dini, *A new method for the quantification of nucleation of fretting fatigue cracks using asymptotic contact solutions.* Tribology International, 2006. **39**(10): p. 1114-1122.
215. Goh, C.H., *Influence of microstructure in partial-slip fretting contacts based upon two-dimensional crystal plasticity simulations.* Journal of tribology, 2006. **128**(4): p. 735-744.
216. Goh, C.H., et al., *Polycrystal plasticity simulations of fretting fatigue.* International Journal of Fatigue, 2001. **23**: p. S423-S435.
217. Goh, C.H., D.L. McDowell, and R.W. Neu, *Characteristics of plastic deformation field in polycrystalline fretting contacts.* International Journal of Fatigue, 2003. **25**(9-11): p. 1047-1058.
218. Goh, C.H., R.W. Neu, and D.L. McDowell, *Crystallographic plasticity in fretting of Ti-6AL-4V.* International Journal of Plasticity, 2003. **19**(10): p. 1627-1650.
219. Zhang, M., R.W. Neu, and D.L. McDowell, *Microstructure-sensitive modeling: Application to fretting contacts.* International Journal of Fatigue, 2009. **31**(8-9): p. 1397-1406.
220. Deshpande, V.S., A. Needleman, and E. Van der Giessen, *Discrete dislocation modeling of fatigue crack propagation.* Acta Materialia, 2002. **50**(4): p. 831-846.
221. Balint, D.S., et al., *Discrete dislocation plasticity analysis of crack-tip fields in polycrystalline materials.* Philosophical Magazine, 2005. **85**(26-27): p. 3047-3071.
222. Motoyashiki, Y., et al., *A Study on Dislocation Movement and Stress Field near Fatigue Crack Tip by Discrete Dislocation Dynamics.* Journal of the Society of Materials Science, Japan, 2003. **52**(10): p. 1217-1224.
223. Mastorakos, I.N. and H.M. Zbib, *Dislocation-cracks interaction during fatigue: A discrete dislocation dynamics simulation.* Jom, 2008. **60**(4): p. 59-63.
224. Zeng, X.H. and A. Hartmaier, *Modeling size effects on fracture toughness by dislocation dynamics.* Acta Materialia, 2010. **58**(1): p. 301-310.
225. Reddy, G.V.P., et al., *Effect of grain disorientation on early fatigue crack propagation in face-centred-cubic polycrystals: A three-dimensional dislocation dynamics investigation.* Acta Materialia, 2013. **61**(14): p. 5300-5310.
226. Mayeur, J.R. and D.L. McDowell, *A three-dimensional crystal plasticity model for duplex Ti-6Al-4V.* International Journal of Plasticity, 2007. **23**(9): p. 1457-1485.
227. Chaboche, J.L., *Continuum Damage Mechanics .2. Damage Growth, Crack Initiation, and Crack-Growth.* Journal of Applied Mechanics-Transactions of the Asme, 1988. **55**(1): p. 65-72.

228. Chow, C.L. and J. Wang, *A Finite-Element Analysis of Continuum Damage Mechanics for Ductile Fracture.* International Journal of Fracture, 1988. **38**(2): p. 83-102.
229. Gao, H.J. and J.R. Rice, *Application of 3-D Weight-Functions .2. The Stress-Field and Energy of a Shear Dislocation Loop at a Crack Tip.* Journal of the Mechanics and Physics of Solids, 1989. **37**(2): p. 155-174.
230. Chaboche, J.L., *Continuum Damage Mechanics .1. General Concepts.* Journal of Applied Mechanics-Transactions of the Asme, 1988. **55**(1): p. 59-64.
231. Hirth, J.P. and J. Lothe, *Theory of dislocations*. Reprint of 2nd ed. 1992, Malabar, Fla: Krieger Publishing Company.
232. Evers, L.P., et al., *Crystal plasticity model with enhanced hardening by geometrically necessary dislocation accumulation.* Journal of the Mechanics and Physics of Solids, 2002. **50**(11): p. 2403-2424.
233. Numerical Recipes Software (Firm), *Numerical recipes P*. 1988, Numerical Recipes Software,: Cambridge, MA. p. 1 computer disk 3 1/2 in.
234. Golub, G.H. and C.F. Van Loan, *Matrix computations*. 3rd ed. Johns Hopkins studies in the mathematical sciences. 1996, Baltimore: Johns Hopkins University Press. xxvii, 694 p.
235. Strang, G., *Linear algebra and its applications*. 3rd ed. 1988, San Diego: Harcourt, Brace, Jovanovich, Publishers. xii, 505 p.
236. Zhang, P., et al., *A controlled Poisson Voronoi tessellation for grain and cohesive boundary generation applied to crystal plasticity analysis.* Computational Materials Science, 2012. **64**: p. 84-89.
237. Rose, M.E., *Elementary theory of angular momentum*. 1957, New York: John Wiley & Sons.
238. Aurenhammer, F., *Voronoi Diagrams - a Survey of a Fundamental Geometric Data Structure.* Computing Surveys, 1991. **23**(3): p. 345-405.
239. Britton, T.B. and A.J. Wilkinson, *Measurement of residual elastic strain and lattice rotations with high resolution electron backscatter diffraction.* Ultramicroscopy, 2011. **111**(8): p. 1395-1404.
240. Wilkinson, A.J., G. Meaden, and D.J. Dingley, *High-resolution elastic strain measurement from electron backscatter diffraction patterns: New levels of sensitivity.* Ultramicroscopy, 2006. **106**(4-5): p. 307-313.
241. Barbe, F., et al., *Intergranular and intragranular behavior of polycrystalline aggregates. Part 1: FE model.* International journal of plasticity, 2001. **17**(4): p. 513-536.
242. Barbe, F., S. Forest, and G. Cailletaud, *Intergranular and intragranular behavior of polycrystalline aggregates. Part 2: Results.* International journal of plasticity, 2001. **17**(4): p. 537-563.
243. Diard, O., et al., *Evaluation of finite element based analysis of 3D multicrystalline aggregates plasticity: Application to crystal plasticity model identification and the study of stress and strain fields near grain boundaries.* International Journal of Plasticity, 2005. **21**(4): p. 691-722.
244. Benzerga, A.A., *An analysis of exhaustion hardening in micron-scale plasticity.* International Journal of Plasticity, 2008. **24**(7): p. 1128-1157.

245. Deshpande, V.S., et al., *Size effects in single asperity frictional contacts.* Modelling and Simulation in Materials Science and Engineering, 2007. **15**(1): p. S97-S108.
246. Deshpandea, V.S., A. Needleman, and E. Van der Giessen, *Size dependence of energy storage and dissipation in a discrete dislocation plasticity analysis of static friction.* Materials Science and Engineering a-Structural Materials Properties Microstructure and Processing, 2005. **400**: p. 393-396.
247. Deshpande, V.S., A. Needleman, and E. Van der Giessen, *Discrete dislocation plasticity analysis of static friction.* Acta Materialia, 2004. **52**(10): p. 3135-3149.
248. Rice, J.R., *Tensile Crack Tip Fields in Elastic Ideally Plastic Crystals.* Mechanics of Materials, 1987. **6**(4): p. 317-335.
249. Friedman, J.H. and B.W. Silverman, *Flexible Parsimonious Smoothing and Additive Modeling.* Technometrics, 1989. **31**(1): p. 3-21.
250. Cleveringa, H.H.M., E. Van der Giessen, and A. Needleman, *A discrete dislocation analysis of rate effects on mode I crack growth.* Materials Science and Engineering a-Structural Materials Properties Microstructure and Processing, 2001. **317**(1-2): p. 37-43.
251. Segurado, J., J. LLorca, and I. Romero, *Computational issues in the simulation of two-dimensional discrete dislocation mechanics.* Modelling and Simulation in Materials Science and Engineering, 2007. **15**(4): p. S361-S375.
252. Uchic, M.D., et al., *Sample dimensions influence strength and crystal plasticity.* Science, 2004. **305**(5686): p. 986-989.
253. Greer, J.R. and W.D. Nix, *Size dependence of mechanical properties of gold at the sub-micron scale.* Applied Physics a-Materials Science & Processing, 2005. **80**(8): p. 1625-1629.
254. Greer, J.R. and W.D. Nix, *Nanoscale gold pillars strengthened through dislocation starvation.* Physical Review B, 2006. **73**(24).
255. Widjaja, A., et al., *Contact area and size effects in discrete dislocation modeling of wedge indentation.* Journal of Materials Research, 2007. **22**(3): p. 655-663.
256. Poon, B., D. Rittel, and G. Ravichandran, *An analysis of nanoindentation in linearly elastic solids.* International Journal of Solids and Structures, 2008. **45**(24): p. 6018-6033.
257. Cleveringa, H., E. Van der Giessen, and A. Needleman, *A discrete dislocation analysis of bending.* International Journal of Plasticity, 1999. **15**(8): p. 837-868.
258. Tarleton, E., et al., *A discrete dislocation plasticity study of the micro-cantilever size effect.* Acta Materialia, 2015. **88**: p. 271-282.
259. Matlab. *Curve Fitting Toolbox Documentation - MathWorks United Kingdom*. 2015; Available from: http://uk.mathworks.com/help/curvefit/index.html.
260. Conn, A.R., N.I.M. Gould, and P.L. Toint, *Trust-region methods*. MPS-SIAM series on optimization. 2000, Philadelphia, PA: Society for Industrial and Applied Mathematics. xix, 959 p.
261. Pippan, R., *Dislocation Emission and Fatigue Crack-Growth Threshold.* Acta Metallurgica Et Materialia, 1991. **39**(3): p. 255-262.
262. Bayley, C.J., W.A.M. Brekelmans, and M.G.D. Geers, *A comparison of dislocation induced back stress formulations in strain gradient crystal plasticity.* International Journal of Solids and Structures, 2006. **43**(24): p. 7268-7286.

263. Bao, Y.W., W. Wang, and Y.C. Zhou, *Investigation of the relationship between elastic modulus and hardness based on depth-sensing indentation measurements.* Acta Materialia, 2004. **52**(18): p. 5397-5404.
264. Musil, J., et al., *Relationships between hardness, Young's modulus and elastic recovery in hard nanocomposite coatings.* Surface & Coatings Technology, 2002. **154**(2-3): p. 304-313.
265. Oliver, W.C. and G.M. Pharr, *Measurement of hardness and elastic modulus by instrumented indentation: Advances in understanding and refinements to methodology.* Journal of Materials Research, 2004. **19**(1): p. 3-20.
266. Oyen, M.L., *Nanoindentation hardness of mineralized tissues.* Journal of Biomechanics, 2006. **39**(14): p. 2699-2702.
267. Koo, A. and J.F. Clare, *On the equivalence of generalized least-squares approaches to the evaluation of measurement comparisons.* Metrologia, 2012. **49**(3): p. 340-348.
268. Zhang, P., S.X. Li, and Z.F. Zhang, *General relationship between strength and hardness.* Materials Science and Engineering a-Structural Materials Properties Microstructure and Processing, 2011. **529**: p. 62-73.
269. Pavlina, E.J. and C.J. Van Tyne, *Correlation of Yield Strength and Tensile Strength with Hardness for Steels.* Journal of Materials Engineering and Performance, 2008. **17**(6): p. 888-893.
270. Busby, J.T., M.C. Hash, and G.S. Was, *The relationship between hardness and yield stress in irradiated austenitic and ferritic steels.* Journal of Nuclear Materials, 2005. **336**(2-3): p. 267-278.
271. Tuck, J.R., et al., *Indentation hardness evaluation of cathodic are deposited thin hard coatings.* Surface & Coatings Technology, 2001. **139**(1): p. 63-74.
272. Kim, J.-Y., et al., *Surface roughness effect in instrumented indentation: A simple contact depth model and its verification.* Journal of materials research, 2006. **21**(12): p. 2975-2978.
273. Franke, O., J.C. Trenkle, and C.A. Schuh, *Temperature dependence of the indentation size effect.* Journal of Materials Research, 2010. **25**(07): p. 1225-1229.
274. Jonsson, B. and S. Hogmark, *Hardness Measurements of Thin-Films.* Thin Solid Films, 1984. **114**(3): p. 257-269.
275. Korsunsky, A.M. and A. Constantinescui, *Work of indentation approach to the analysis of hardness and modulus of thin coatings.* Materials Science and Engineering a-Structural Materials Properties Microstructure and Processing, 2006. **423**(1-2): p. 28-35.
276. Curtin, W.A., et al., *Hybrid discrete dislocation models for fatigue crack growth.* International Journal of Fatigue, 2010. **32**(9): p. 1511-1520.
277. !!! INVALID CITATION !!!
278. Kysar, J.W., et al., *High strain gradient plasticity associated with wedge indentation into face-centered cubic single crystals: Geometrically necessary dislocation densities.* Journal of the Mechanics and Physics of Solids, 2007. **55**(7): p. 1554-1573.

279. Bouvier, S. and A. Needleman, *Effect of the number and orientation of active slip systems on plane strain single crystal indentation.* Modelling and Simulation in Materials Science and Engineering, 2006. **14**(7): p. 1105-1125.
280. Fischer, K.A. and P. Wriggers, *Frictionless 2D Contact formulations for finite deformations based on the mortar method.* Computational Mechanics, 2005. **36**(3): p. 226-244.
281. Hartmann, S. and E. Ramm, *A mortar based contact formulation for non-linear dynamics using dual Lagrange multipliers.* Finite Elements in Analysis and Design, 2008. **44**(5): p. 245-258.
282. Tur, M., F.J. Fuenmayor, and P. Wriggers, *A mortar-based frictional contact formulation for large deformations using Lagrange multipliers.* Computer Methods in Applied Mechanics and Engineering, 2009. **198**(37-40): p. 2860-2873.
283. Weyler, R., et al., *On the contact domain method: A comparison of penalty and Lagrange multiplier implementations.* Computer Methods in Applied Mechanics and Engineering, 2012. **205**: p. 68-82.
284. Fischer, K.A. and P. Wriggers, *Mortar based frictional contact formulation for higher order interpolations using the moving friction cone.* Computer Methods in Applied Mechanics and Engineering, 2006. **195**(37-40): p. 5020-5036.
285. Dawson, P.R., et al., *A Consistent Penalty Method for Contact between a Deforming Viscoplastic Workpiece and a Rigid Tool.* International Journal for Numerical Methods in Engineering, 1995. **38**(23): p. 3969-3987.
286. Hillerborg, A., M. Modéer, and P.-E. Petersson, *Analysis of crack formation and crack growth in concrete by means of fracture mechanics and finite elements.* Cement and concrete research, 1976. **6**(6): p. 773-781.
287. McCarthy, O.J., J.P. McGarry, and S.B. Leen, *A finite element study of microstructure-sensitive plasticity and crack nucleation in fretting.* Computational Materials Science, 2011. **50**(8): p. 2439-2458.
288. Hooputra, H., et al., *A comprehensive failure model for crashworthiness simulation of aluminium extrusions.* International Journal of Crashworthiness, 2004. **9**(5): p. 449-463.
289. Elices, M., et al., *The cohesive zone model: advantages, limitations and challenges.* Engineering Fracture Mechanics, 2002. **69**(2): p. 137-163.
290. Park, K. and G.H. Paulino, *Cohesive zone models: a critical review of traction-separation relationships across fracture surfaces.* Applied Mechanics Reviews, 2011. **64**(6): p. 060802.
291. Tijssens, M.G.A., E. van der Giessen, and L.J. Sluys, *Modeling of crazing using a cohesive surface methodology.* Mechanics of Materials, 2000. **32**(1): p. 19-35.
292. Lin, G., et al., *The effect of strength mis-match on mechanical performance of weld joints.* International Journal of Fracture, 1999. **96**(1): p. 37-54.
293. Homola, A.M., et al., *Fundamental experimental studies in tribology: The transition from "interfacial" friction of undamaged molecularly smooth surfaces to "normal" friction with wear.* Wear, 1990. **136**(1): p. 65-83.
294. Li, Q. and K.-S. Kim, *Micromechanics of friction: effects of nanometre-scale roughness.* Proceedings of the Royal Society A: Mathematical, Physical and Engineering Science, 2008. **464**(2093): p. 1319-1343.

295. Luan, B. and M.O. Robbins, *The breakdown of continuum models for mechanical contacts.* Nature, 2005. **435**(7044): p. 929-932.
296. Balint, D.S., et al., *Discrete dislocation plasticity analysis of the grain size dependence of the flow strength of polycrystals.* International Journal of Plasticity, 2008. **24**(12): p. 2149-2172.
297. Araujo, J.A. and D. Nowell, *Analysis of pad size effects in fretting fatigue using short crack arrest methodologies.* International Journal of Fatigue, 1999. **21**(9): p. 947-956.
298. Nowell, D., D. Hills, and R. Moobola, *Length scale considerations in fretting fatigue.* ASTM SPECIAL TECHNICAL PUBLICATION, 2000. **1367**: p. 141-153.
299. Tanaka, K. and T. Mura, *A Dislocation Model for Fatigue Crack Initiation.* Journal of Applied Mechanics-Transactions of the Asme, 1981. **48**(1): p. 97-103.
300. Stephens, R.I. and H.O. Fuchs, *Metal fatigue in engineering*. 2nd ed. 2001, New York: Wiley. xxi, 472 p.
301. Polák, J., *The effect of intermediate annealing on the electrical resistivity and shear stress of fatigued copper.* Scripta Metallurgica, 1970. **4**(10): p. 761-764.
302. Akahori, T., et al., *Effects of microstructure on the short fatigue crack initiation and propagation characteristics of biomedical alpha/beta titanium alloys.* Metallurgical and Materials Transactions a-Physical Metallurgy and Materials Science, 2000. **31**(8): p. 1949-1958.
303. Morris, W.L., M.R. James, and O. Buck, *Computer-Simulation of Fatigue Crack Initiation.* Engineering Fracture Mechanics, 1980. **13**(1): p. 213-221.
304. Manson, S.S., *Behavior of materials under conditions of thermal stress*. 1953: NACA TN 2933.
305. Coffin Jr, L., *The problem of thermal stress fatigue in austenitic steels at elevated temperatures*. 1954, Knolls Atomic Power Lab.
306. Ritchie, R.O. and A.W. Thompson, *On Macroscopic and Microscopic Analyses for Crack Initiation and Crack-Growth Toughness in Ductile Alloys.* Metallurgical Transactions a-Physical Metallurgy and Materials Science, 1985. **16**(2): p. 233-248.
307. Sadananda, K. and G. Glinka, *Dislocation processes that affect kinetics of fatigue crack growth.* Philosophical Magazine, 2005. **85**(2-3): p. 189-203.
308. Sangid, M.D., *The physics of fatigue crack initiation.* International Journal of Fatigue, 2013. **57**: p. 58-72.
309. Sangid, M.D., H.J. Maier, and H. Sehitoglu, *A physically based fatigue model for prediction of crack initiation from persistent slip bands in polycrystals.* Acta Materialia, 2011. **59**(1): p. 328-341.
310. Brown, L.M., *Cracks and extrusions caused by persistent slip bands.* Philosophical Magazine, 2013. **93**(28-30): p. 3809-3820.
311. Liu, Z.L., *A micropillar compression simulation by a multiscale plastic model based on 3-D discrete dislocation dynamics.* International Journal for Multiscale Computational Engineering, 2009. **7**(3): p. 217-225.
312. Tello, J.S. and W.A. Curtin, *A coupled discrete/continuum model for multiscale diffusion.* International Journal for Multiscale Computational Engineering, 2005. **3**(3): p. 257-265.

313. Wallace, J.M. and R.W. Neu, *Fretting fatigue crack nucleation in Ti-6Al-4V.* Fatigue & Fracture of Engineering Materials & Structures, 2003. **26**(3): p. 199-214.

Appendixes

Appendix I: The mathematical representation of Euler angle notation

Rotation Angle 1 (ϕ_1): Positive rotation of axes around the local z axis. This can be described through the matrix:

$$Z_1 = \begin{pmatrix} \cos\phi_1 & \sin\phi_1 & 0 \\ -\sin\phi_1 & \cos\phi_1 & 0 \\ 0 & 0 & 1 \end{pmatrix} \tag{I.1}$$

Rotation Angle 2 (Φ): Positive rotation of axes around the local rotated x axis; this aligns z with x3. The matrix:

$$X = \begin{pmatrix} 1 & 0 & 0 \\ 0 & \cos\Phi & \sin\Phi \\ 0 & -\sin\Phi & \cos\Phi \end{pmatrix} \tag{I.2}$$

Rotation Angle 3 (ϕ_2): Positive rotation of axes around the local rotated z axis, aligning the remaining axes, described by:

$$Z_2 = \begin{pmatrix} \cos\phi_2 & \sin\phi_2 & 0 \\ -\sin\phi_2 & \cos\phi_2 & 0 \\ 0 & 0 & 1 \end{pmatrix} \tag{I.3}$$

The global rotation from the local crystal system to the global one is then be given by:

$$R = Z_1 \cdot X \cdot Z_2 \tag{I.4}$$

And R is represented by Euler rotation angles as:

$$R = \begin{pmatrix} R_{11} & R_{12} & R_{13} \\ R_{21} & R_{22} & R_{23} \\ R_{31} & R_{32} & R_{33} \end{pmatrix} \tag{I.5}$$

With its elements as:

$$\begin{aligned} R_{11} &= \cos\phi_1 \cos\phi_2 - \sin\phi_1 \sin\phi_2 \cos\Phi \\ R_{12} &= \sin\phi_1 \cos\phi_2 + \cos\phi_1 \sin\phi_2 \cos\Phi \\ R_{13} &= \sin\phi_2 \sin\Phi \\ R_{21} &= -\cos\phi_1 \sin\phi_2 - \sin\phi_1 \cos\phi_2 \cos\Phi \\ R_{22} &= -\sin\phi_1 \sin\phi_2 + \cos\phi_1 \cos\phi_2 \cos\Phi \\ R_{23} &= \cos\phi_2 \sin\Phi \\ R_{31} &= -\sin\phi_1 \cos\phi_2 \cos\Phi + \sin\phi_1 \sin\Phi \end{aligned} \tag{I.6}$$

$$R_{32} = \cos\phi_1 \cos\phi_2 \cos\Phi + \cos\phi_1 \sin\Phi$$

$$R_{33} = \cos\Phi$$

Appendix II: Schmid's law

Schmid's law is illustrated in Figure Appendix-1. The shear force is the project of tensile force on the slip plane, and the corresponding area is the project of S. Thus, the shear stress is given by:

$$\tau = \frac{F\cos\alpha}{S/\cos\phi} = \sigma\cos\alpha\cos\phi \tag{I.7}$$

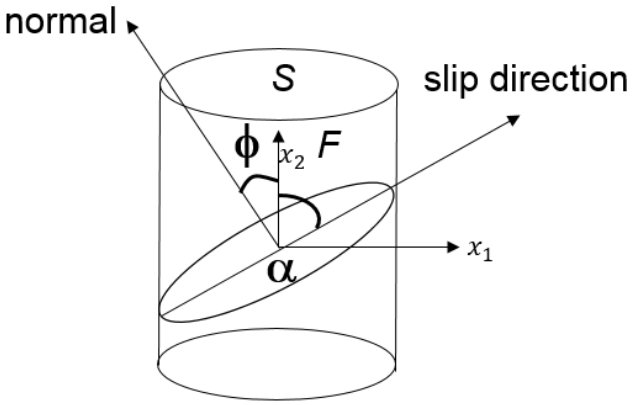


Figure Appendix-1. Schmid's law sketch

Appendix III: Parametric study on hardening parameters in CPFE formulations

Hardening parameters H_R and H_{exp} are varied to study their effects on the material performance under uniaxial tension in terms of stress strain response curves.

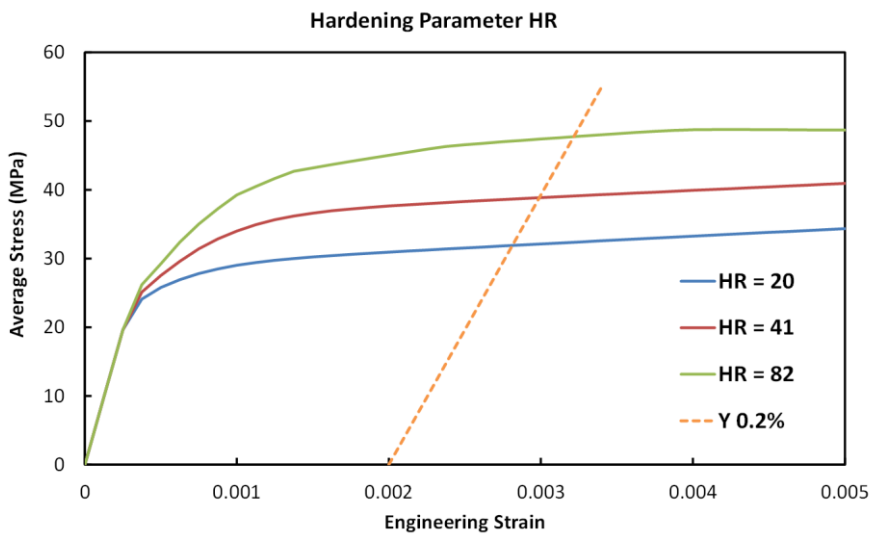


Figure Appendix-2. The stress strain response curves of three different values H_R of a single crystal specimen modelling with crystal plasticity finite element. The grain is with 9MPa as its critical resolved shear stress and 0 degree orientation. A 0.2% strain yield line is also included for reference.

The tensile stress σ versus applied strain U/L responses of the crystal plasticity finite element specimen with different values of hardening parameter H_R are shown in Figure Appendix-2. Parameter H_R shows no influence on the elastic response and the onset point of plastic flow. The main influence of the hardening parameter H_R on the material plastic performance is on the slope of the hardening part of stress strain curve. A larger H_R enables the corresponding polycrystalline material to exhibit a much stronger plastic response. For example, the curve $H_R = 82$ achieves 43 MPa under 0.2% engineering strain, much larger than the counterpart value with $H_R = 20$, only about 30 MPa subjected to the same strain level. In particular, H_R strongly affects the initial hardening slope near the onset of plastic flow while the final slope (when the accumulated plastic strain is large enough) is less dependent on H_R. This can also be verified from mathematical aspect in the hardening formula.

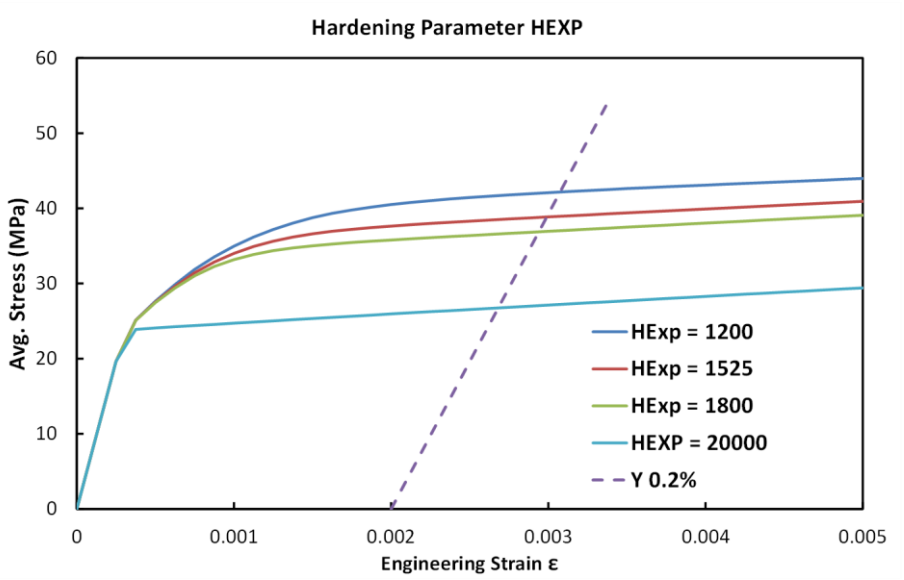


Figure Appendix-3. The stress strain response curves of three different values $\mathrm{H}_{\mathrm{exp}}$ of a single crystal specimen modelling with crystal plasticity finite element. The grain is with 9MPa as its critical resolved shear stress and 0 degree orientation. A 0.2% strain yield line is also included for reference.

The tensile stress σ versus applied strain U/L responses of the crystal plasticity finite element specimen with different values of hardening parameter $\mathrm{H}_{\mathrm{exp}}$ are shown in Figure Appendix-3. Parameter $\mathrm{H}_{\mathrm{exp}}$ shows no influence on the elastic response and the onset point of plastic flow. The main influence of the hardening parameter $\mathrm{H}_{\mathrm{exp}}$ on the material plastic performance is on the slope of the hardening part of stress strain curve. A smaller $\mathrm{H}_{\mathrm{exp}}$ enables the corresponding polycrystalline material to exhibit a much stronger plastic response. For example, the stress $\mathrm{H}_{\mathrm{exp}} = 1200$ achieves $40\ MPa$ under 0.2% engineering strain, much larger than the counterpart value with $\mathrm{H}_{\mathrm{exp}} = 20000$, only about $24\ MPa$ subjected to the same strain level. In particular, $\mathrm{H}_{\mathrm{exp}}$ strongly affects the hardening curve slope for the whole engineering range. This can also be verified from mathematical aspect in the hardening formula. A material with an extremely large value $\mathrm{H}_{\mathrm{exp}}$ would exhibit a perfect-elastic like behaviour.

Appendix IV: Step-time configuration for CPFE calculations in ABAQUS

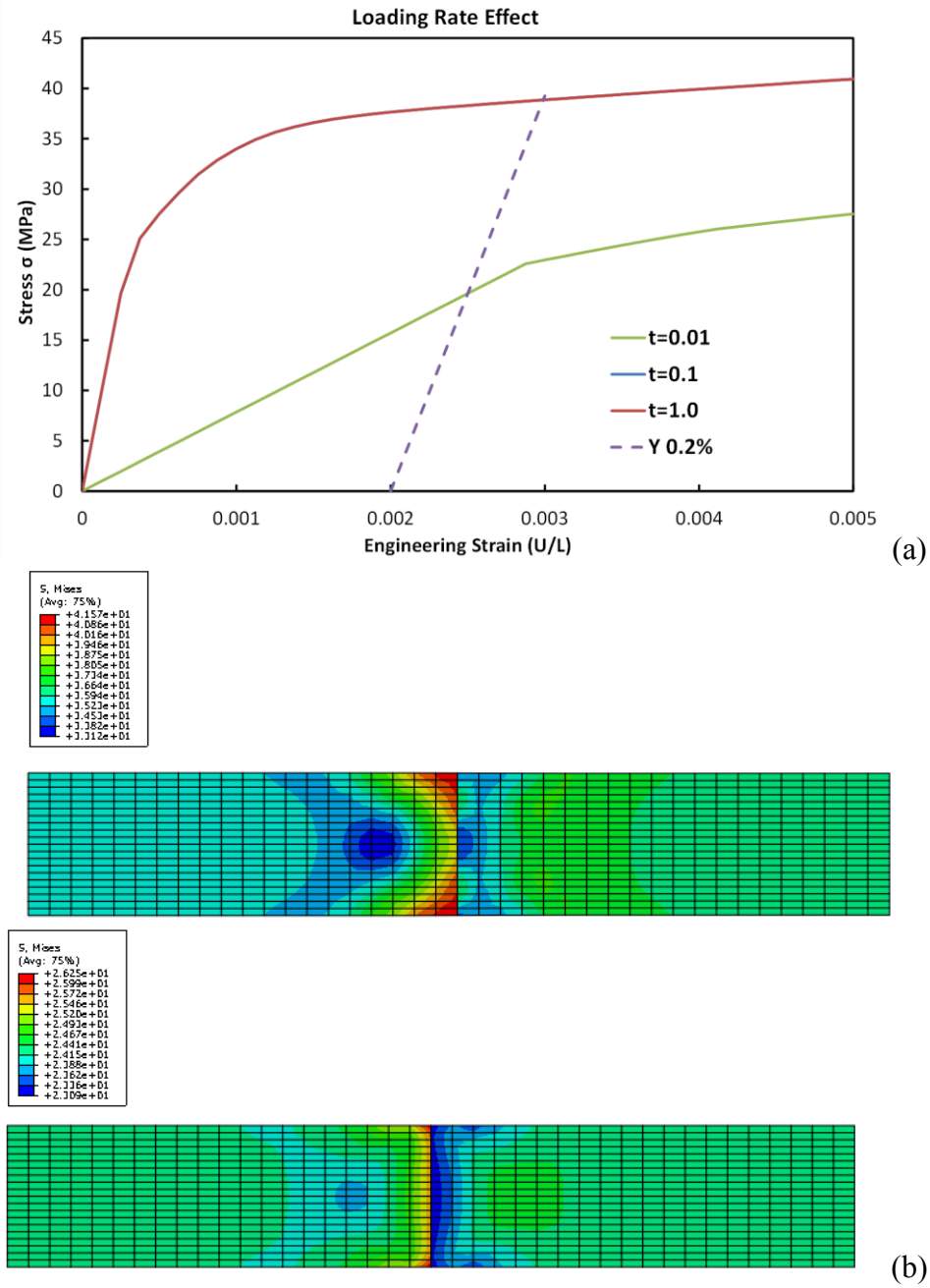


Figure Appendix-4. Uniaxial tensile response curves of the CPFE-Plastic bi-crystal film. (a) Overall Uniaxial tensile response curves of the CPFE-Plastic bi-crystal film. (a) Overall stress,σ, versus strain, U/L, and (b) von-Mises stress contour. Results are shown for specimens with a fixed geometry dimension $2L \times w = 12\mu m \times 2\mu m$ but subjecting from different loading rates respectively.

The tensile stress–strain responses of the reference single crystal specimens with the same geometry dimension $2L \times w = 12\mu m \times 2\mu m$ are reported in Figure Appendix-4(a) for three selected loading rates $\dot{U}/L$ (representing by step time t = 0.01s, 0.1s and 1s in ABAQUS) at the right boundary of specimens. It is clear seen in

Figure Appendix-4 (a) that the stress response is not affected by the loading rate if the loading step is sufficiently long. The stress performance could be changed a significantly if ABAQUS is not assigned sufficient step time to converge (see the difference in Figure Appendix-4(b) for more reference). The time is not enough in computation for plasticity flow fully expanding within grains during a time step. However, the loading step t = 0.1s is sufficiently long for CPFE calculations to generate a time-independent solution, and thus step time is also set for all other standard simulations. Therefore, the CPFE crystal response under uniaxial tension is considered as rate-independent.

Appendix V: Slip system effect on indentation pressure in DD calculations

The actual indentation pressure evolution curve versus the applied indentation depth δ is plotted in Figure Appendix-5 for $h = 10\ \mu m$ film with different slip systems indented by the $\omega = 5°$ wedge. The reference film with three slip systems $\phi^{(\alpha)}\ (\alpha = 1, 2\ 3) = \pm 35.3°$ and $90°$ with respect to the y-axis while other three films have only single slip system $\phi^{(\alpha)}\ (\alpha = 1,2) = \pm 35.3°$, $\phi^{(\alpha)}\ (\alpha = 1) = 0°$ or $\phi^{(\alpha)}\ (\alpha = 1) = 90°$. The dislocation nucleation source density is set same as $\rho_{nuc} = 8.28\ \mu m^{-2}$ in order to keep their indentation response from being affected by the density effect (shown before). As can be seen, the film with $\phi^{(\alpha)} = 90°$ slip system exhibits the weakest responses while the one with $\phi^{(\alpha)} = 0°$ shows the strongest response especially at the later stage of that indentation process $\delta = 0.3\ \mu m$. The indentation pressure of films with mixed and $\phi^{(\alpha)}\ (\alpha = 1,2) = \pm 35.3°$ slip systems fall between two extreme values given a certain indentation depth. This indicates that the preferable slip system that is parallel to the indentation direction shows the weakest resistance and hence yielding weakest crystal. Engineering materials composed by cubic crystalline aggregate with mixed slip systems exhibit an intermediate response.

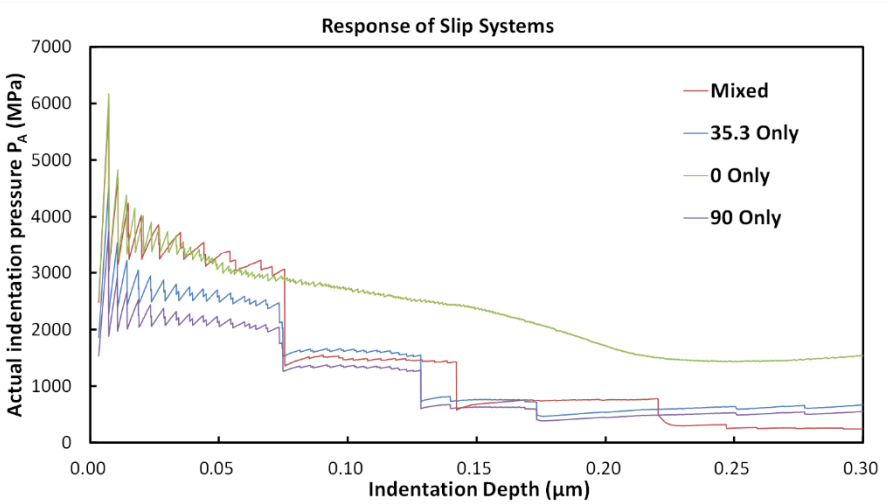
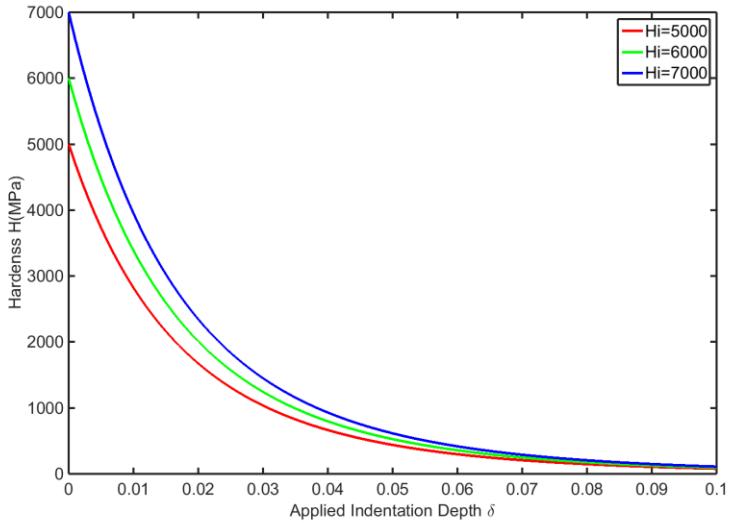


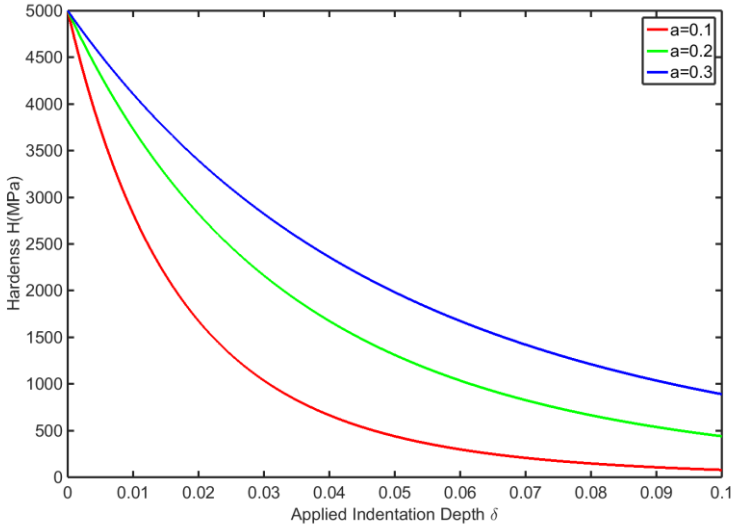
Figure Appendix-5. The actual hardness evolution H curve versus the applied indentation depth δ for $h = 10\ \mu m$ film with different slip systems indented by the $\omega = 5°$ wedge. Films involved are with different slip system, purely $\phi_i^\alpha = 35.3°$ labelled as 45 only, purely $\phi_i^\alpha = 0°$ labelled as 0 only, purely $\phi_i^\alpha = 90°$ labelled as 90 only. Mixed curve denotes the hardness response of the film with $\phi_i^\alpha = \pm 35.3°, 0°$ slip systems. All films studied are assigned the same dislocation source density $\rho_{nuc} = 8.28\ \mu m^{-2}$ to exclude the source density influence.

Appendix VI: Mathematical analysis on parameters in the proposed indentation pressure formula

Parametric study on the influence of fitting parameters in the proposed formula upon the indentation pressure variation are plotted with different values of H_i, a^* and α in Figure Appendix-6 (a), (b) and (c) respectively. From mathematical prospect, the new proposed formula shows that the indentation pressure exhibits a monotonic decrease with the increasing applied indentation depth δ because values of both a^* and α are positive, and the decreasing rate, i.e. the magnitude of its derivative also decreases. As seen in Figure Appendix-6 (a), the value of H_i determines the whole performance of the variation of H, especially when values of δ are close to 0. The domination of H_i decays as δ approaches infinity. As seen in Figure Appendix-6 (b) and (c), the decreasing rate of value of H are determined by fitting parameters a and α. In particular, lager values of parameter a and smaller values of parameter α result in a more rapid decay of p_A values.


Hi=5000
Hi=6000
Hi=7000
Hardenss H(MPa)
Applied Indentation Depth δ
0
1000
2000
3000
4000
5000
6000
7000
0.01
0.02
0.03
0.04
0.05
0.06
0.07
0.08
0.09
0.1

(a)


a=0.1
a=0.2
a=0.3
Hardenss H(MPa)
Applied Indentation Depth δ
0
500
1000
1500
2000
2500
3000
3500
4000
4500
5000
0.01
0.02
0.03
0.04
0.05
0.06
0.07
0.08
0.09
0.1

(b)

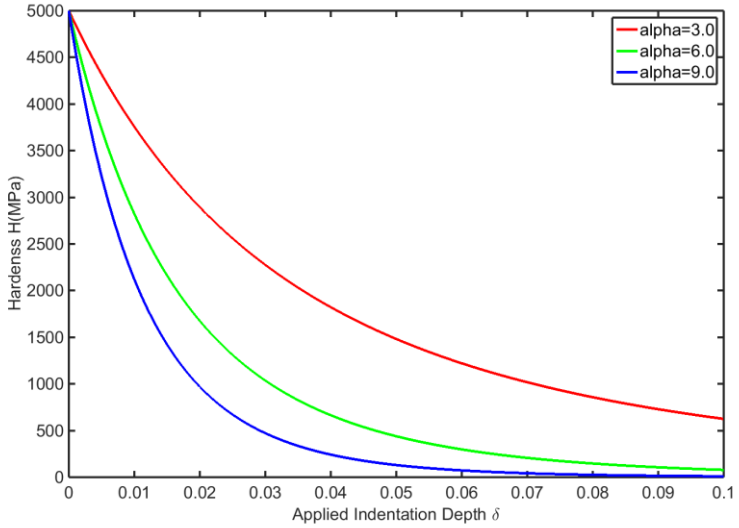


Figure Appendix-6. Parametric study of the influence of fitting parameters (a) H_i , (b) a^* and (c) α of the newly proposed formula upon the indentation pressure variation.

Appendix VII: Hardness value of an elastic film

Hardness evolution curves of specimens modelled as purely elastic material with same geometry dimensions and boundary conditions are shown Figure Appendix-7 (a) and (b). Purely elastic material modelling is obtained by setting critical resolved shear stress as an extremely large value, and keeping other parameters the same as the reference single crystal. Hardness evolution against relative indentation depth of purely elastic materials with two different Young's modulus $\mathrm{E} = 70\ \mathrm{GPa}$ and $\mathrm{E} = 700\ \mathrm{GPa}$ is shown in Figure Appendix-7 (a) and (b) respectively. The general trend of hardness evolution curves of purely elastic crystal is similar to that of crystal plasticity specimen. There is a fluctuation about a stable plateau hardness value and followed by a turning up to infinity due to rigid boundary effect. The average value of the stable zone (i.e. boundary effect free) of hardness evolution is considered as the hardness of the material. Thus the hardness values of the elastic crystal with Young's modulus $\mathrm{E} = 70\ \mathrm{GPa}$ and $\mathrm{E} = 700\ \mathrm{GPa}$ are obtained as $3500\ \mathrm{MPa}$ and $35000\ \mathrm{MPa}$ respectively, which indicates that the relationship between hardness and Young's modulus of an elastic material is given as:

$$H \cong 0.05 \times E \tag{I.8}$$

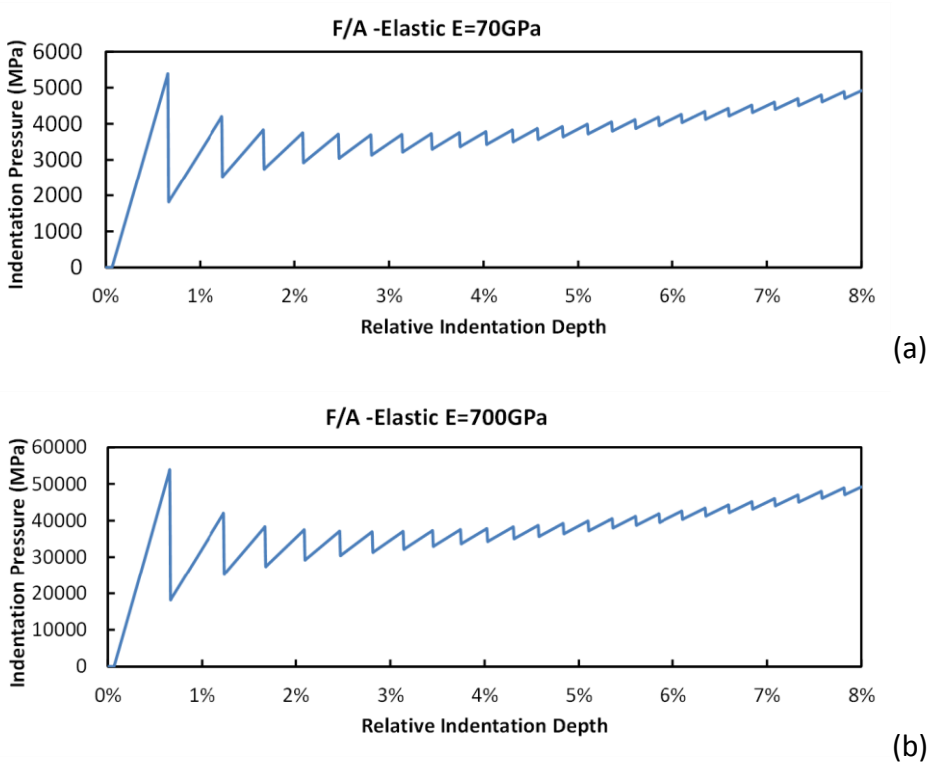


Figure Appendix-7. hardness evolution curves of the elastic materials against relative indentation depth. Results are shown for two crystals with different Young's modulus (a) $E = 70GPa$ and (b) $E = 700GPa$ respectively. The averaged stable value before turning up of hardness evolution is taken as the hardness of an elastic material.

Appendix VIII: Mathematical analysis of the proposed indentation pressure evolution

The formulas for describing the indentation pressure variation of two types of coating systems are depicted in Figure Appendix-8 (a) and (b) show the indentation pressure variation curves of the polycrystalline coating system with film being harder and softer than the substrate respectively. We can see that the indentation pressure depends totally on the indentation size effect of the coating film that is modelled as discrete dislocation plasticity when the relative indentation depth β is relatively small. However, the indentation curves start to turn up after a critical relative indentation depth due to the hardening effect of the grain boundary. It is noting that the hardening is not affected too much by the substrate hardness. Thus, the indention pressure of a polycrystalline coating material with internal grain boundaries is inevitably hardened, even though the hardness value of the substrate is smaller than the value of the coating film. For the indention pressure variation of a bulk coating system, Figure Appendix-8 (c) and (d) show the different situations where the film is harder and softer than the substrate respectively. Generally, we improve the conventional hardness transition formula eq.(6.1) by replacing the indentation size independent hardness of the coating film with the newly proposed indentation pressure variation within the indentation size effect regime. In details, the indention pressure continues to drop to

approach the continuum hardness of the substrate following the indentation size effect zone if the coating film is harder than the substrate. In contrast, the indention pressure turns up to arrive at the continuum hardness of the substrate if the coating film is softer than the substrate. It is noticing that there could be a minimum value of the composite material. This minimum hardness value is determinate by both hardness values of the coating film and substrate, as well as the fitting parameters in formula. We once tried to mathematically determine the minimum hardness value and its corresponding relatively indentation depth, but the analytical solution of the derivative of eq. (6.11) is not available.

The latter coupling model, i.e. the bulk coating system without internal grain boundaries, plays a potentially useful and numerical tool for predicting the indentation pressure and other mechanical properties of a coating system. As the physical interpretation of some fitting parameters has been given based on the microstructure, the new formula is suitable for determine the material normal performance in a nano-indentation process.

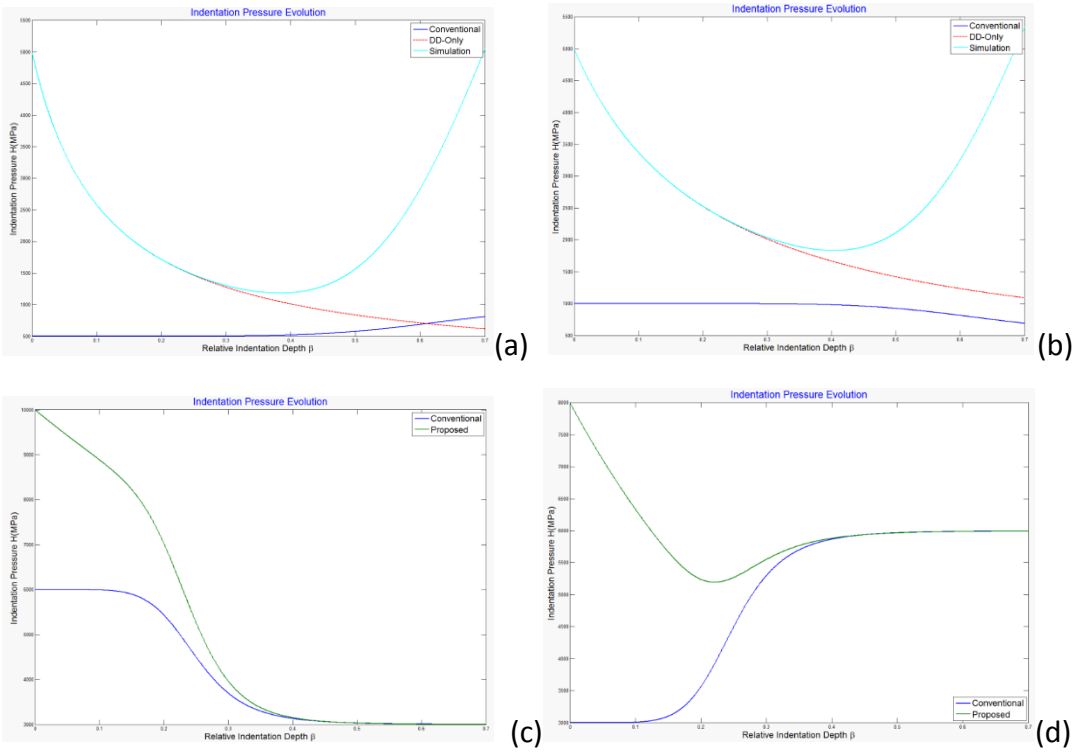


Figure Appendix-8. The indentation pressure evolution curves against the relative indentation depth schematically depicted by the proposed eq.(6.10) and (6.11) respectively. Results include the coupling methods with internal grain boundary ((a) and (b)) and with transparent coupling boundary to dislocations ((c) and (d)). Also, indentation pressure curves of two types of coating systems are predicted respectively.

Appendix IX: Dislocation source density effect on shear stress

The shear stress τ averaged along the contact with nominal contact size $a = 8.0\mu m$ between the asperity and $h = 10\ \mu m$ film with various microstructure are

illustrated in Figure Appendix-9. The general shape of shear stress response curve is observed as consistent as both experiments [293-295] and simulations [1, 4]. Of more significance, the dislocation source density is found to have a strong effect on the stress response of the film. A smaller value of source density is able delay the onset of sliding between the asperity and film. Meanwhile, it also hardens the shear response of the film in terms of the shear stress plateau. Both phenomenon is attributed to the dislocation source starvation effect. Local stress would further increase when there are no dislocation nucleation sources available locally. Therefore, films are hardened by a source-limited strengthening that is a universally observation in discrete dislocation simulations under various loading conditions [1, 258, 296]. Results of our sliding simulations show that a source density value $\rho_{nuc} = 48.53\ \mu m^{-2}$ is able to saturate the $h = 10\ \mu m$ film being contacted with $\mathrm{a} = 8.0\mu\mathrm{m}$ length.

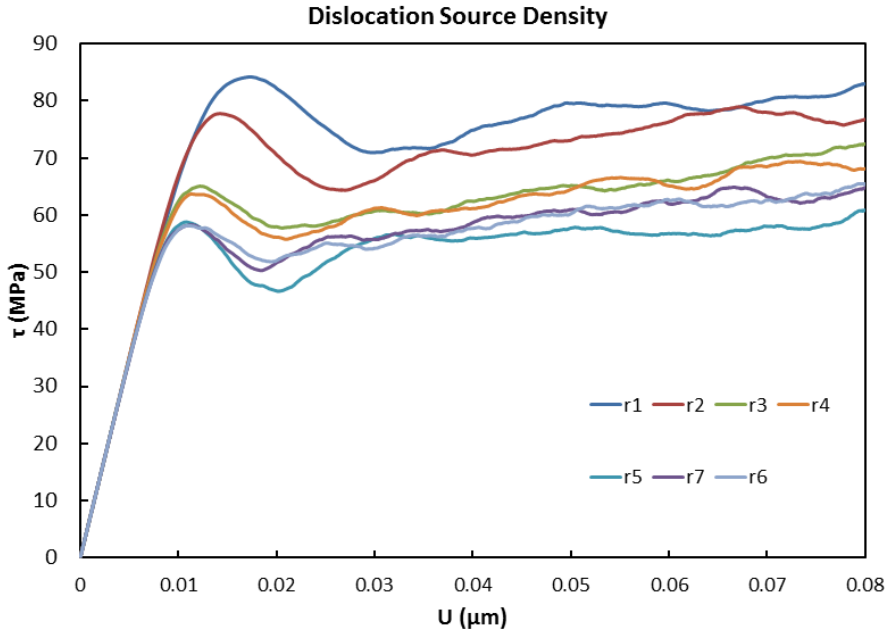


Figure Appendix-9. The shear stress τ versus sliding displacement U curves for the $h = 10\ \mu m$ film with contact size $\mathrm{a} = 8.0\mu\mathrm{m}$ for selected values of dislocation source density.

The averaged friction stress, τ_{ave}, is defined as the average value of τ over the range $0.015\mu\mathrm{m} \leq \mathrm{U} \leq 0.02\ \mu\mathrm{m}$ and $0.035\mu\mathrm{m} \leq \mathrm{U} \leq 0.040\ \mu\mathrm{m}$. For contact size $\mathrm{a} = 8.0\mu\mathrm{m}$, τ has attained a steady-state value for displacements in both of ranges. The $\tau - \mathrm{U}$ curve depends on the specific distribution of dislocation sources and obstacles and not just on the densities [3]. Here, calculations were carried out for three realizations, and the values obtained for these realizations differed by less than 5 % in all cases and the values of τ_{ave} reported are mean values. The averaged friction stress against the averaged dislocation source spacing is plotted in Figure Appendix-10. A linear relation between the average shear stress and the average source spacing is obtained when the source density does not saturate the film, i.e. $\rho_{nuc} < 48.53\ \mu m^{-2}$ nor too small $\rho_{nuc} > 19.41\ \mu m^{-2}$

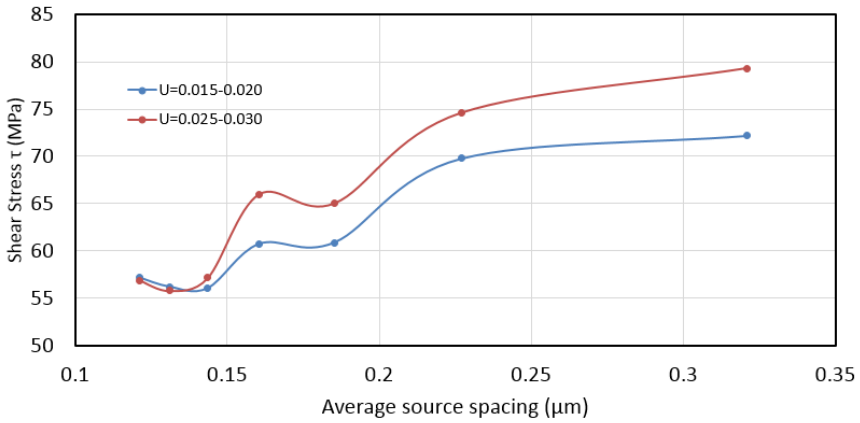


Figure Appendix-10. The averaged shear stress τ versus average source spacing $d_{avg.}$ curves for the $h = 10\ \mu m$ film with contact size $a = 4.0\mu m$ for selected values of dislocation source density.

Shear stress τ averaged along the contact with nominal contact size $a = 2.0\mu m$ between asperity and $h = 10\ \mu m$ film with various microstructure are illustrated in Figure Appendix-11. The quantitative dependence of shear stress on the dislocation source density still holds for density set $\rho_{nuc} = 9.71\ \ \mu m^{-2}$, $\rho_{nuc} = 19.41\ \ \mu m^{-2}$ and $\rho_{nuc} = 48.53\ \ \mu m^{-2}$. However, the shear stress response of the film with $\rho_{nuc} = 29.12\ \mu m^{-2}$ and $\rho_{nuc} = 67.94\ \mu m^{-2}$ unexpectedly exceeds the counterpart curve of $\rho_{nuc} = 19.41\ \ \mu m^{-2}$. Another set of calculations (results shown in Figure Appendix-12) where the obstacle density value is keep as constant for all microstructure are conducted to study the influence of obstacles. It is observed that shear response curves are not affected much by this decoupling of obstacle values.

This weaker dependence of shear stress on dislocation density (*i.e.* dislocation source spacing) results can be attributed to the relatively unstable response of films damaged by a small size contact, compared to mediate contact size.

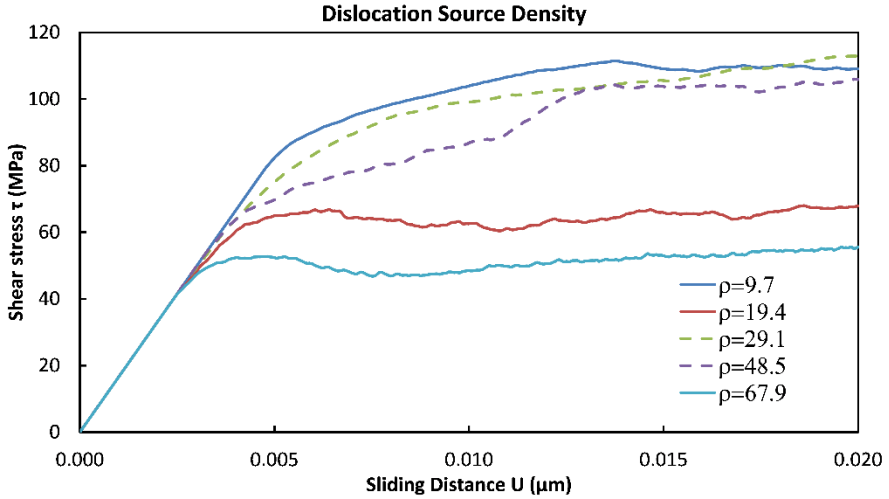


Figure Appendix-11. Shear stress τ versus sliding displacement U curves for the $h = 10\ \mu m$ film with contact size $a = 2.0\mu m$ for selected values of dislocation source density.

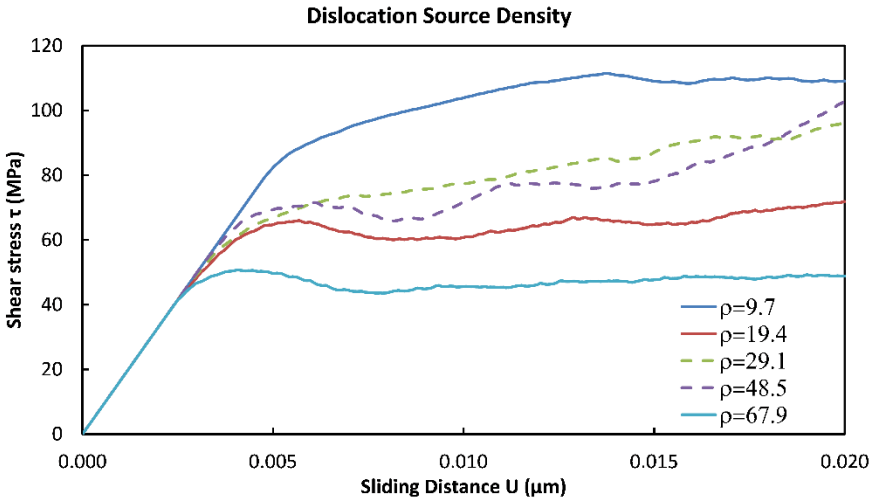


Figure Appendix-12. The shear stress τ versus sliding displacement U curves for the $h = 10\ \mu m$ film with contact size $a = 2.0\mu m$ for selected values of dislocation source density but the same obstacle density.

Shear stress τ averaged along contact with nominal contact size $a = 10.0\mu m$ between asperity and $h = 10\ \mu m$ film with various microstructure are illustrated in Figure Appendix-13. When sliding displacement is small, the dependence of shear stress on the dislocation density holds well. However, the shear stress τ of relative large dislocation source density (*i.e.* small average source spacing) converges to a uniform value when the sliding displacement approaches $U = 0.1\ \mu m$. This is a sign of saturation of dislocation activities where film behaviour does not reply on the initial dislocation source density any longer. This finding is explained as films are more prone to approach a continuum (i.e. independent of dislocation activity) status when contacted by a relative large contact size because plasticity flow is sooner introduced into films.

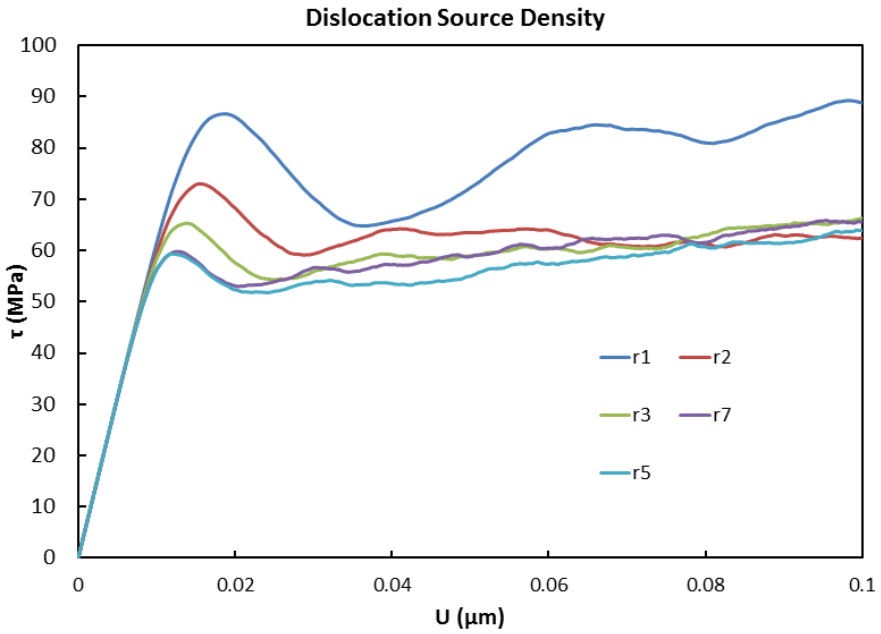


Figure Appendix-13. The shear stress τ versus sliding displacement U curves for the $h = 10\ \mu m$ film with contact size $a = 10.0\mu m$ for selected values of dislocation source density.

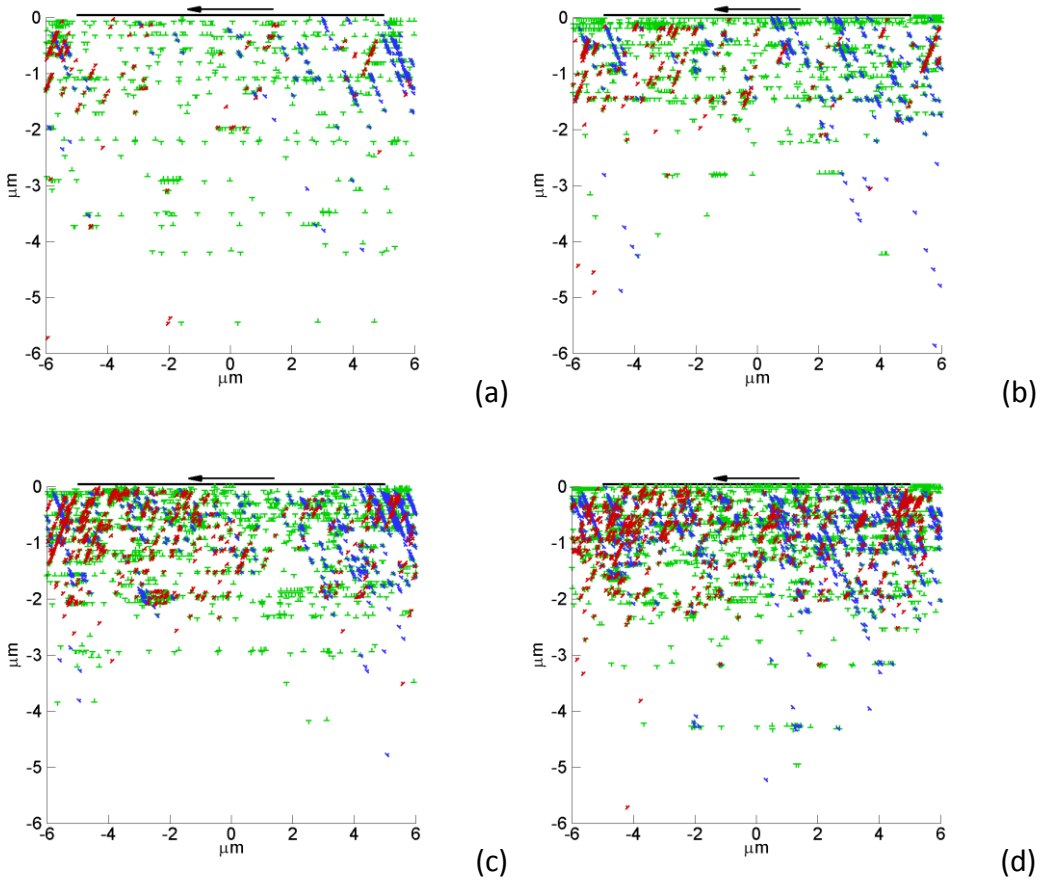


Figure Appendix-14. Dislocation structure in $h = 10\ \mu m$ film under $a = 10.0\mu m$ contact with the asperity. Results are obtained from the film with (a) $\rho_{nuc} = 9.71\ \ \mu m^{-2}$

(b) $\rho_{nuc} = 19.41\ \mu m^{-2}$ (c) $\rho_{nuc} = 48.53\ \mu m^{-2}$ (d) $\rho_{nuc} = 97.18\ \mu m^{-2}$ at the instant when sliding displacement $\mathrm{U} = 0.10\ \mu\mathrm{m}$

Figure Appendix-14 shows the dislocation structures in $h = 10\ \mu m$ film with four values of source density under contact size $\mathrm{a} = 10.0\mu\mathrm{m}$ respectively. Results are obtained at the instant when the asperity slides to the maximum stroke $\mathrm{U} = 0.1\ \mu\mathrm{m}$. There is a small number of dislocation observed in the film with the lowest source density $\rho_{nuc} = 9.71\ \ \mu m^{-2}$, which leads to the strongest shear response of these films. However, films with more nucleation sources yield similar dislocation structure, especially for dislocations piling up at the surface and subsurface along horizontal slip systems. This implies that dislocations occur to saturate near the contact when the source density is larger than a critical value ($\rho_{nuc} = 19.41\ \ \mu m^{-2}$ for the situation discussed herein). Thus the dislocation source factor is not able to play a crucial role in determining the shear response of films any longer when the contact size is relatively large.

Appendix X: Obstacle density effect on shear stress

Microstructure of films are also varied in terms of obstacle density with relevant parameters tabulated in Table Appendix-1.

Table Appendix-1. Parameters for realizing microstructure with different obstacle density in $\mathrm{h} = 10\mu\mathrm{m}$ film. The source density (i.e. the average source spacing $\mathrm{d_{avg}}$) is set as constant in this set of calculations.

label	# src/plane	# obs/plane	$\rho_{nuc}\ (\mu m^{-2})$	$\rho_{obs}\ (\mu m^{-2})$
Obs2	5	1	48.53	19.41
Obs5	5	1	48.53	48.53
Obs10	5	1	48.53	97.18

Shear stress τ averaged along contact with nominal contact size $\mathrm{a} = 4.0\mu\mathrm{m}$ between the asperity and $h = 10\ \mu m$ film with various microstructure are illustrated in Figure Appendix-15. The obstacle effect is not observed quite apparent when their values (e.g.$\rho_{obs} \leq 48.53\mu m^{-2}$) are not sufficiently enough. However, the shear stress response is significantly strengthened when the value of obstacle density is increased as$\rho_{obs} = 97.18\mu m^{-2}$. A sufficient number of obstacles are capable of preventing dislocations from further sliding as soon as they are about to pass obstacles. Thus films with larger obstacle density are observed with a stronger shear response.

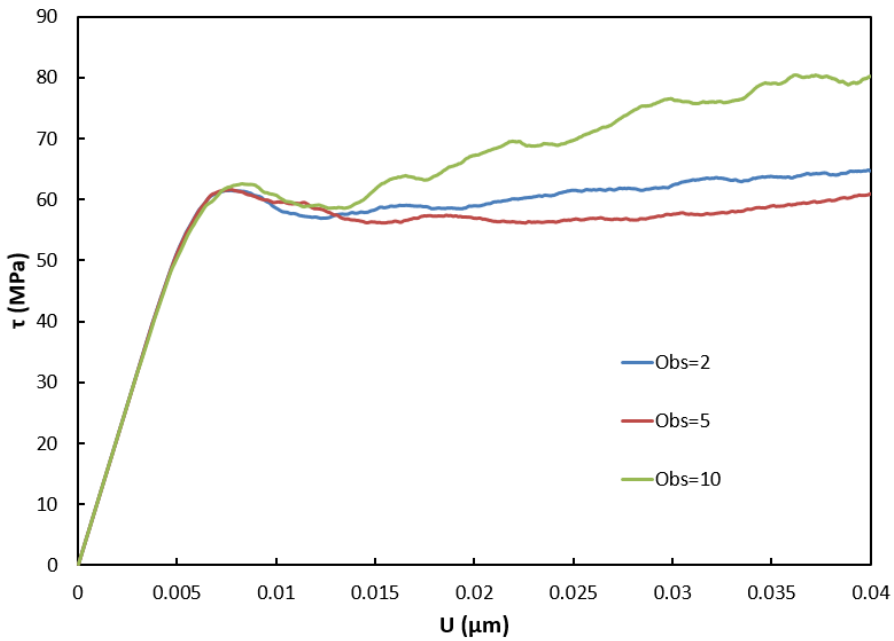
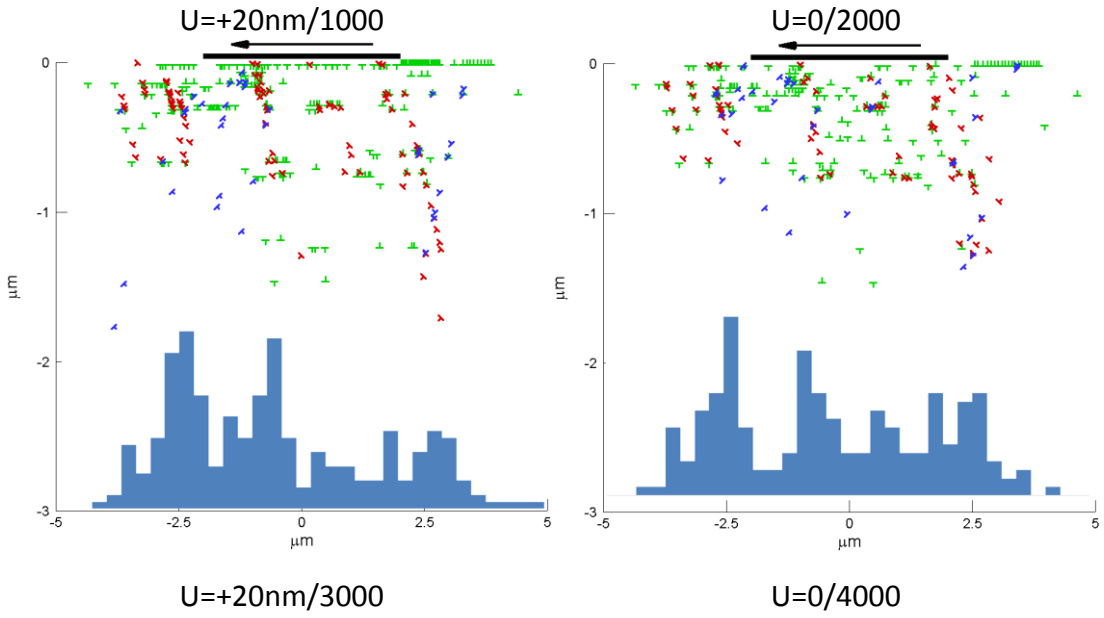


Figure Appendix-15. Shear stress τ versus sliding displacement U curves for the $h = 10\ \mu m$ film with contact size $a = 4.0\mu m$ for the same value of dislocation source density but selected values of obstacle density .

Appendix XI: Dislocation structure evolution in fretting simulations with various contact sizes

Figure Appendix-16 and Figure Appendix-17 show the dislocation structure evolution during the first cycles of fretting process with contact length $a = 4.0\ \mu m$ and $a = 10.0\ \mu m$, respectively.



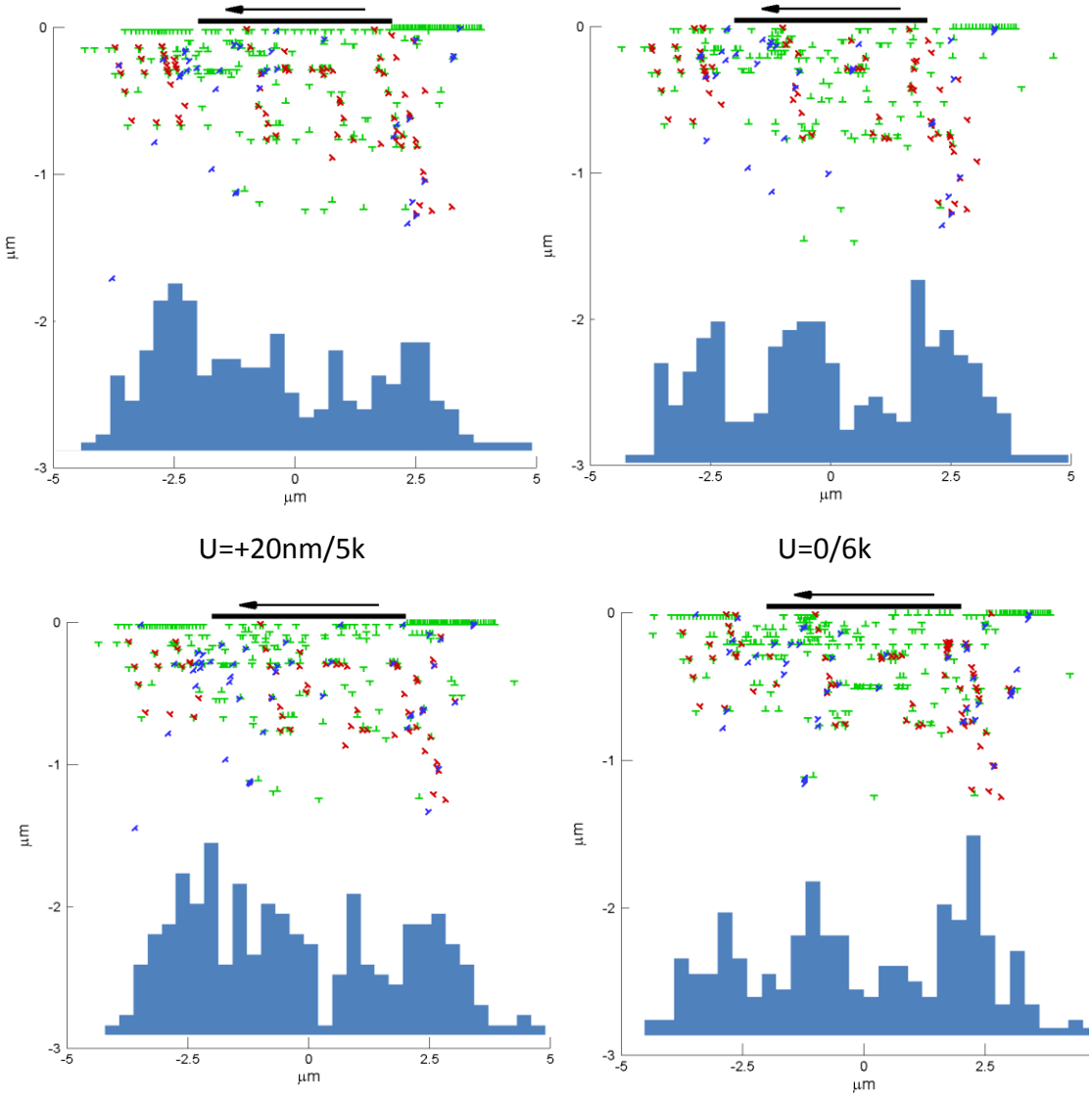
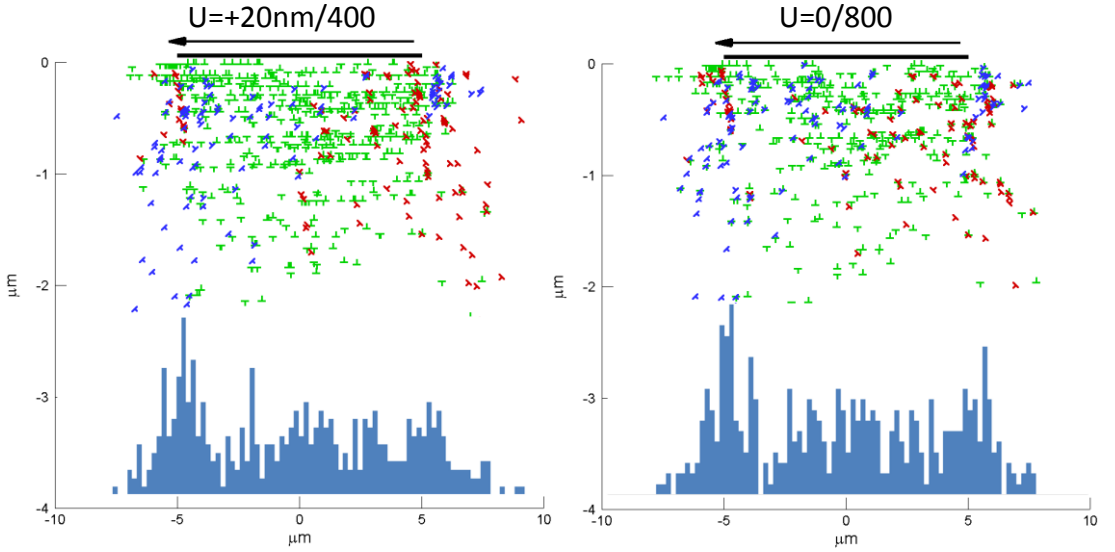


Figure Appendix-16. dislocation structure evolution during a fretting process. Results are obtained by cyclic sliding on the $h = 10\ \mu m$ film with a stress- and dislocation-free status initially. The contact length is set as $a = 4.0$ µm.



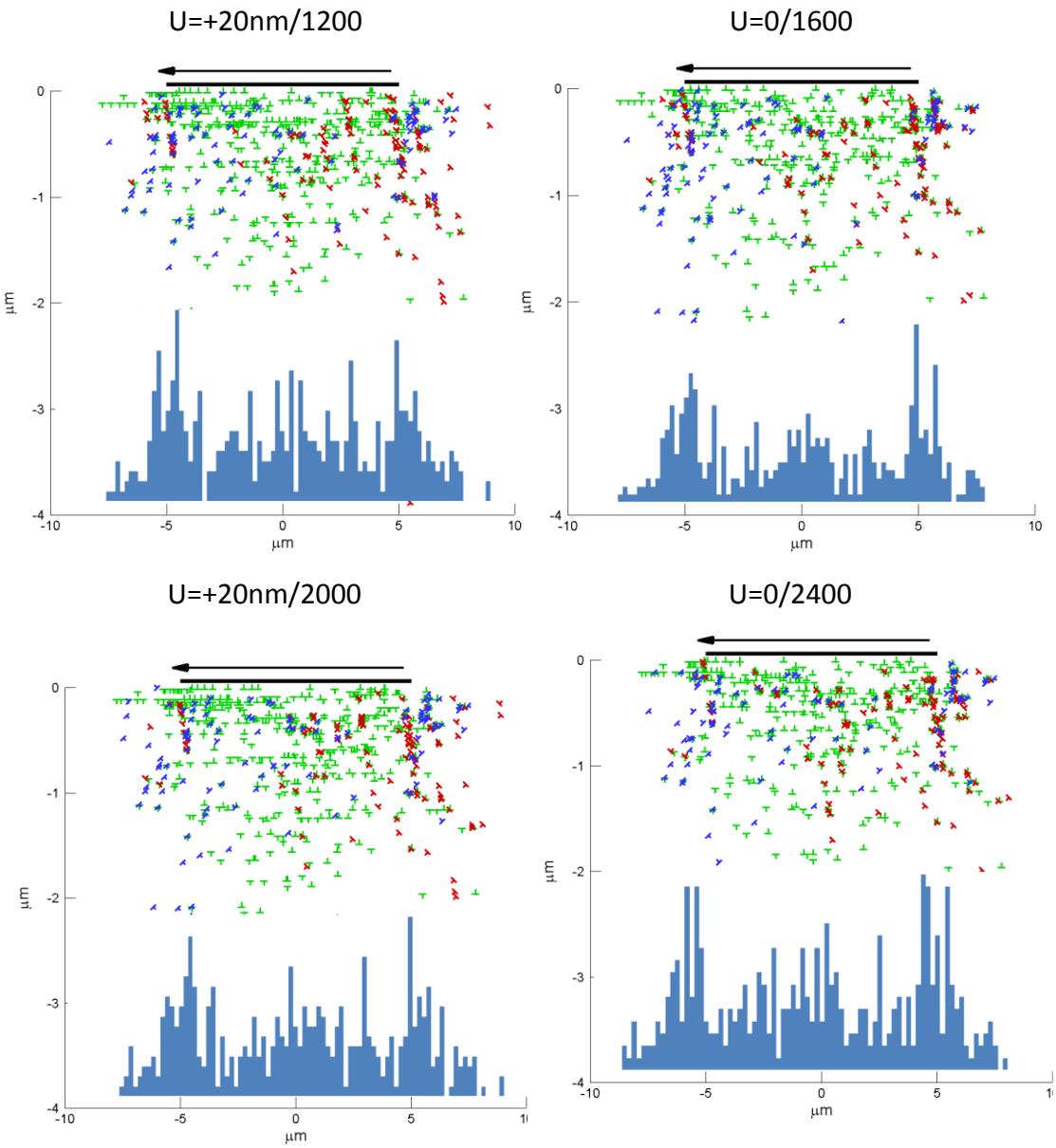


Figure Appendix-17. dislocation structure evolution during a fretting process. Results are obtained by cyclic sliding on the $h = 10\ \mu m$ film with a stress- and dislocation-free status initially. The contact length is set as $a = 10.0\ \mu m$.